A Submillimeter Imaging Survey of Ultracompact HII Regions

Thesis by

Todd R. Hunter

In Partial Fulfillment of the Requirements

for the Degree of

Doctor of Philosophy

California Institute of Technology

Pasadena, California

1997

(Submitted September 17, 1996)

© 1997
Todd R. Hunter
All Rights Reserved

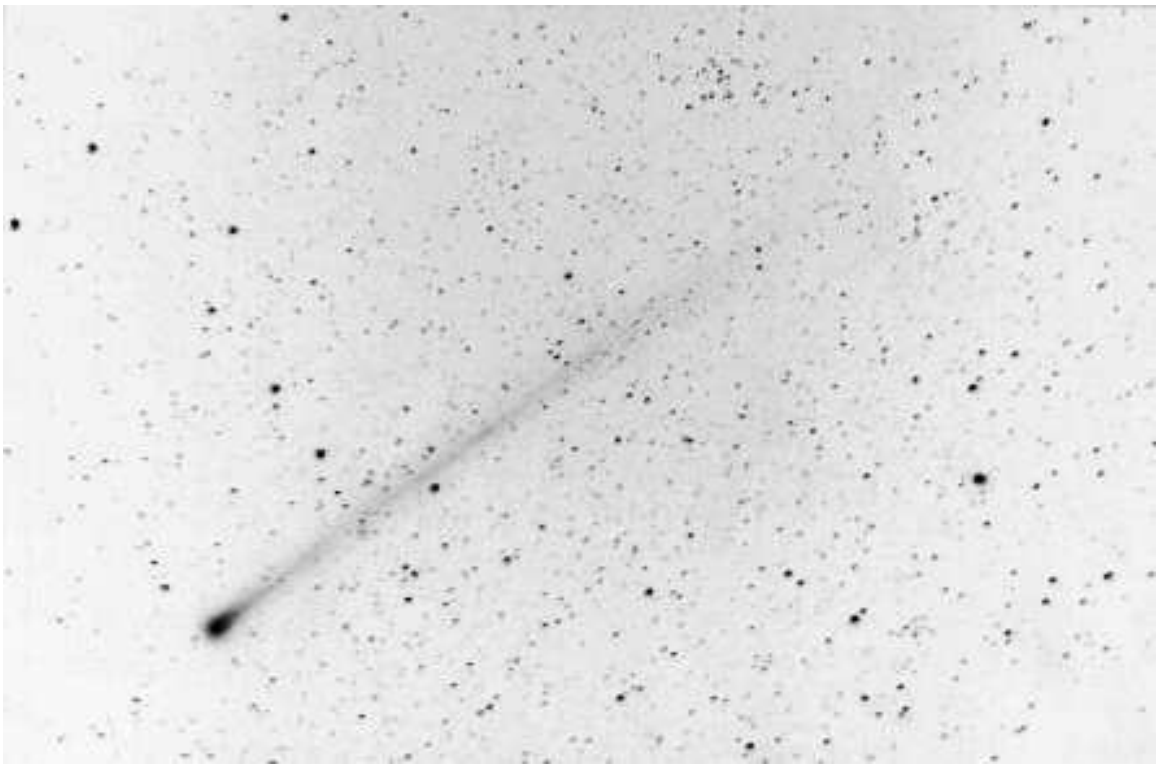

Comet Hyakutake

photographed on 25 March 1996
at Joshua Tree National Park, California

Acknowledgements

Much of the success of this thesis can be traced to Larry Ramsey and Jeff Hall for introducing me to instrumentation work at Penn State. My experience as a VLA summer student in 1990 also influenced me immeasurably by bringing radio astronomy to life in the Land of Enchantment, where I made some lifelong friends. Looking back, I am pleased that Craig Walker convinced me to apply to Caltech. I thank my graduate advisor Tom Phillips for teaching me how to tune SIS receivers at CSO and welcoming me into the submillimeter group, a unique collection of people that always manages to finish first when it counts. Thanks to Pat Schaffer and Jacob Kooi for the world's best receivers (and all those lab tools of theirs that I didn't steal). Special thanks go to Harvey Moseley's family and colleagues at NASA/Goddard for all their help and hospitality. For answering my frequent computer and scientific questions, Darek Lis deserves special mention. Similar recognition goes to Gene Serabyn for help with optics and for constructive comments on this manuscript, and to Ning Wang whose determination led to the timely commissioning of SHARC. Thanks also to Maryvonne Gerin and Peter Schilke for showing me all the neat features of GRAPHIC. For keeping the telescope running, thanks to the CSO staff, especially Taco, a dependable source of advice and humorous stories. To Greg Taylor, thanks for your lessons on VLA data and introducing me to the members of the Arcetri group. Thanks to Natalie Merchant and the 10kM for audio encouragement during long summer days of programming SHARC at the summit of Mauna Kea, where by the force of will my lungs were filled. Thanks to Eric Howard for his near-infrared data on S255, Chris DePree for his radio data on K3-50, and Debra Shepherd and Peter Hofner for sharing their millimeter and radio data on G45 and G75. Much of the research reported here was augmented by the patient advice and frequent noggin-usage of Dominic Benford and Robert Knop. Finally, with all the encouragement and help from my family back East, these past five years have been well worth the effort.

Abstract

This research explores the process of massive star formation in the Galaxy through submillimeter continuum and spectral line observations of ultracompact HII (UCHII) regions. First, I describe the design and operation of the Submillimeter High Angular Resolution Camera (SHARC)–a 24-pixel bolometer array camera for broadband continuum imaging at 350 and 450μm at the Caltech Submillimeter Observatory (CSO). Detailed information is included on the reflective off-axis optical design and the instrument control software interface. Second, I present 10″ to 12″ resolution SHARC images of 350 and 450μm continuum emission from a sample of 17 UCHII regions with different radio morphologies. Although the dust emission typically peaks at or near the UCHII region, additional sources are often present, sometimes coincident with the position of H_2O masers. The combination of submillimeter, millimeter and IRAS far-infrared flux densities forms the basis of greybody models of the spectral energy distributions. The average dust temperature is 40 ± 10 K and the average grain emissivity index (β) is 2.00 ± 0.25. Using a radiative transfer program that solves for the dust temperature versus radius, the distribution of dust around UCHII regions is modeled with a power-law spherical density profile to match the observed radial flux density profiles. By fixing the source boundary at the outer limit of the submillimeter emission, the resulting density profiles $n(r) \propto r^{-p}$ can be classified into four categories: 3 regions exhibit $p = 2$ (isothermal sphere), 4 exhibit $p = 1.5$ (dynamical collapse), 2 exhibit $p = 2$ in the outer regions and $p = 1.5$ in the inner regions, and 6 exhibit $p = 1$ (logatropic). Although these simplified models may not be unique, a good correlation between the dust luminosity-to-mass ratio and the temperature indicates that the more centrally-condensed sources exhibit higher star formation rates. Third, I present 20″ to 30″ resolution CO maps which reveal bipolar outflows from 15 out of 17 UCHII regions. The outflow mechanical luminosities and mass ejection rates follow the scaling relations with bolometric luminosity established

for less luminous pre-main sequence stars. However, in contrast to lower luminosity sources, the momentum from stellar radiation pressure is comparable to that required to drive the outflows. Many regions show evidence of separate, overlapping outflows. In a final detailed study, $2''$ resolution images obtained with the Owens Valley Millimeter Array reveal multiple outflows emanating from the molecular core containing the UCHII region G45.12+0.13, while simultaneous outflow and infall motion is seen toward the neighboring, less-evolved core containing G45.07+0.13.

Contents

Acknowledgements **iv**

Abstract **v**

1 Introduction and Background **1**

1.1 Massive star formation 1

1.2 Thesis outline 10

2 The Submillimeter High Angular Resolution Camera (SHARC) **12**

2.1 Instrument overview 13

2.2 Optical design 21

2.3 Optical performance 37

2.4 Instrument control system 42

2.5 Data reduction 48

2.6 Sensitivity 53

3 Submillimeter Continuum Images of UCHII Regions **56**

3.1 The characteristics of interstellar dust 56

3.2 Computation of dust column density and mass from submillimeter flux density 61

3.3 HIRES IRAS images 65

3.4 Calibration and pointing accuracy of the SHARC images 84

3.5 SHARC images of cometary UCHII regions 87

3.6 SHARC images of shell-like UCHII regions 106

3.7 SHARC images of unresolved UCHII regions 115

3.8 SHARC image of the G75 Complex (ON 2) 125

3.9 Greybody models 129

3.10 Density profiles 144
3.11 Luminosity to mass ratios 171
3.12 Summary 173

4 Molecular Outflows from UCHII Regions 176
4.1 Characteristics of molecular outflows 176
4.2 Possible mechanisms of jet-driven outflows 182
4.3 Outflows from high-mass star-forming regions 186
4.4 CO spectra 187
4.5 CO outflow maps 190
4.6 Calculation of outflow energetics 206
4.7 Scaling relations 211
4.8 Summary 217

5 Active Star Formation toward the G45.12+0.13 and G45.07+0.13 UCHII Regions 219
5.1 Introduction 220
5.2 Observations 224
5.3 Molecular outflows 226
5.4 Continuum emission 242
5.5 Discussion 245
5.6 Conclusions 248

6 Summary 250

References 252

Appendix A: SHARC Cryostat Manual 277

Appendix B: SHARC Software Manual 286

Appendix C: Input parameters for the OUTFLOW program 294

List of Figures

2.1 Photograph of the bolometer array detector 19
2.2 Layout of the ellipsoid re-imager 26
2.3 Strehl ratios versus chopper angle 28
2.4 Spot diagrams across the SHARC focal plane 30
2.5 Sketch of the internal cryostat optics 32
2.6 SHARC filter arrangement 34
2.7 Strehl ratio versus dewar rotation angle 38
2.8 CSO/SHARC beam map at 350μm 39
2.9 SHARC filter transmission curves 41
2.10 SHARC Server computer display 44
2.11 OTF map computer display 47
2.12 SHARC $NEFD$s achieved at 350 and 450μm 54
2.13 SHARC sensitivity vs. integration time at 450μm 55

3.1 Mean flux density-weighted grain radius for the $n(a) \propto a^{-3.5}$ distribution 62
3.2 HIRES IRAS maps of G19.61-0.23 71
3.3 HIRES IRAS maps of G29.96-0.02 72
3.4 HIRES IRAS maps of G34.26+0.14 73
3.5 HIRES IRAS maps of G45.1+0.1 74
3.6 HIRES IRAS maps of the K3-50 complex 75
3.7 HIRES IRAS maps of G75.8+0.4 76
3.8 HIRES IRAS maps of W3(OH) 77
3.9 HIRES IRAS maps of G138.30+1.56 78
3.10 HIRES IRAS maps of G139.909+0.197 79
3.11 HIRES IRAS maps of Monoceros R2 80
3.12 HIRES IRAS maps of GGD12-15 81

3.13 HIRES IRAS maps of the S255 complex 82
3.14 HIRES IRAS maps of G240.31+0.07 83
3.15 2.0 cm radio continuum image of G34.3+0.2 88
3.16 2.0 cm radio continuum image of G34.26+0.14 89
3.17 350 and 450μm images of G34.3+0.15 90
3.18 H_2CO $3_{1,2} - 2_{1,1}$ map around G34.3+0.2SE 92
3.19 H_2CO $3_{1,2} - 2_{1,1}$ spectrum of G34.3+0.2SE 93
3.20 2.0 cm radio continuum image of G29.96-0.02 94
3.21 800μm image of G29.96-0.02 95
3.22 450μm image of G29.96-0.02 96
3.23 6 cm radio continuum image of G19.61-0.23 97
3.24 800μm image of G19.61-0.23 98
3.25 450μm image of G19.61-0.23 99
3.26 3.6 cm VLA image of GGD12-15 100
3.27 350μm image of the GGD12-15 101
3.28 6 cm radio continuum image of Mon R2 103
3.29 350μm image of the Mon R2 complex 104
3.30 VLA 3.6 cm image of the K3-50 complex 107
3.31 800μm image of the K3-50 complex 109
3.32 SHARC 350μm image of the K3-50 complex 110
3.33 18 cm radio continuum image of W3(OH) 111
3.34 800μm image of W3(OH) 113
3.35 350μm image of W3(OH) 114
3.36 350μm image of G240.31+0.07 115
3.37 350μm image of G138.295+1.555 117
3.38 350μm image of the G139.909+0.197 complex 119
3.39 350μm image of the S255 complex 120
3.40 350μm image of the S255 complex 122
3.41 CS J=7$\rightarrow$6 image of the S255 complex 123
3.42 K-band & 350μm image of S255-FIR2 124

3.43 800μm image of G75.84+0.34 125
3.44 6 cm radio continuum image of G75.78+0.34 126
3.45 800μm image of the G75 complex 127
3.46 450μm image of the G75 complex 128
3.47 Histograms of the UCHII greybody models 133
3.48 Spectral energy distribution of G19.61-0.23 135
3.49 Spectral energy distribution of W3(OH) 136
3.50 Spectral energy distribution of G29.96-0.02 136
3.51 Spectral energy distribution of G34.3+0.2 137
3.52 Spectral energy distribution of K3-50A 137
3.53 Spectral energy distribution of K3-50C 138
3.54 Spectral energy distribution of Monoceros R2 138
3.55 Spectral energy distribution of GGD12-15 139
3.56 Spectral energy distribution of G192.584-0.041 139
3.57 Spectral energy distribution of S255-FIR2 140
3.58 Spectral energy distribution of G45.07+0.13 140
3.59 Spectral energy distribution of G45.12+0.13 141
3.60 Spectral energy distribution of G75.78+0.34 141
3.61 Spectral energy distribution of G75.84+0.40 142
3.62 Spectral energy distribution of G139.909+0.197 142
3.63 Spectral energy distribution of G138.295+1.555 143
3.64 Spectral energy distribution of G240.31+0.01 143
3.65 Flux profile of Uranus as the instrument response pattern 151
3.66 350μm image of Uranus in celestial coordinates 152
3.67 Flux profile of G240.31+0.07 153
3.68 Flux profile of G19.61-0.23 154
3.69 Flux profile of G29.96-0.02 155
3.70 Flux profile of W3(OH) 156
3.71 Flux profile of K3-50A 157
3.72 Flux profile of S255 FIR2 158

3.73 Flux profile of G75.78+0.34 159
3.74 Flux profile of G45.07+0.13 160
3.75 Flux profile of G34.3+0.2 161
3.76 Flux profile of K3-50C 162
3.77 Flux profile of G45.12+0.13 163
3.78 Flux profile of GGD12-15 164
3.79 Flux profile of G192.584-0.041 165
3.80 Flux profile of G138.295+1.555 166
3.81 Flux profile of G139.909-0.197 167
3.82 Predicted spectral energy distributions 169
3.83 Predicted temperature distributions 170
3.84 Dust core luminosity and $L_{\rm FIR}/M_{\rm dust}$ ratio vs. temperature 172

4.1 CO outflow spectra 189
4.2 CO J=2→1 map of K3-50 191
4.3 CO J=3→2 map of K3-50A 192
4.4 CO J=3→2 map of W3(OH) 193
4.5 CO J=3→2 map of G138.295+1.555 194
4.6 CO J=3→2 map of G139.909+0.197 195
4.7 CO J=3→2 map of G240.31+0.07 196
4.8 CO J=2→1 map of the G75.8+0.3 complex 197
4.9 CO J=2→1 map of G75.84+0.40 198
4.10 CO J=3→2 map of the S255 complex 199
4.11 CO J=2→1 map of G19.61-0.23 200
4.12 CO J=2→1 map of G29.96-0.02 201
4.13 CO J=3→2 map of G5.97-1.18 202
4.14 CO J=3→2 map of the Cepheus-A complex 204
4.15 CO J=3→2 map including G45.45+0.06 & G45.47+0.05 205
4.16 Outflow mechanical luminosity vs. bolometric luminosity 212
4.17 Outflow force vs. bolometric luminosity 214

4.18 Mass outflow rate vs. bolometric luminosity 216

5.1 CO J=3→2 map of G45.12+0.13 & G45.07+0.13 222
5.2 CO spectra of G45.12+0.13 and G45.07+0.13 227
5.3 CS 7→6 spectrum of G45.12+0.13 and G45.07+0.13 228
5.4 CO J=2→1 maps of G45.12+0.13 229
5.5 CO J=6→5 map of G45.12+0.13 230
5.6 CO J=6→5 map of G45.07+0.13 231
5.7 $C^{18}O$ J=1→0 map of G45.12+0.13 235
5.8 Channel maps of ^{13}CO J=1→0 toward G45.12+0.13 237
5.9 CO J=3→2 map of G45.12+0.13 238
5.10 CS J=7→6 map of G45.12+0.13 239
5.11 CS J=2→1 spectrum of G45.07+0.13 240
5.12 CS J=2→1 channel maps of G45.07+0.13 241
5.13 800, 450 and 350μm continuum maps of the G45 complex 242
5.14 110 GHz continuum map of G45.12+0.13 244
5.15 98 GHz continuum map of G45.07+0.13 246

List of Tables

3.1 UCHII regions analyzed with HIRES processing 66
3.2 Observed properties of the dust clumps toward G34.3+0.2 91
3.3 Observed properties of the dust clumps in Mon R2 105
3.4 Greybody model parameters of dust around UCHII regions 132
3.5 Comparison of the one- and two-component greybody models 134
3.6 Summary of dust density profiles 174

4.1 Observed and computed parameters of bipolar outflows 210

5.1 Summary of CSO spectroscopic observations of G45 224
5.2 Summary of OVRO observations of G45 226
5.3 Observed properties of the CS J=7→6 transition 228
5.4 Properties of the G45.12+0.13 molecular outflow 232
5.5 Properties of the G45.07+0.13 molecular outflow 234
5.6 Outflow masses derived from the ^{13}CO J=1→0 maps 236
5.7 Millimeter and submillimeter continuum fluxes of G45 243
5.8 Greybody model parameters of G45.12+0.13 and G45.07+0.13 . . . 243

Chapter 1 Introduction and Background

1.1 Massive star formation

Massive stars exert a dominant force on the interstellar medium throughout their lives. Powerful outflows, stellar winds, HII regions and supernova explosions combine to shape the appearance of galaxies, most notably the starbursts. With this fact in mind, the understanding of massive star formation in our Galaxy becomes an essential goal with universal application in astrophysics. Traditionally, this goal has been difficult to achieve due to the extreme optical extinction by interstellar dust in active star formation regions. In recent decades, the discovery of ultracompact HII (UCHII) regions at radio wavelengths has provided a promising target in this research. Observations indicate a link between UCHII regions, H_2O masers, dust emission, dense molecular gas, bipolar outflows and massive star formation. However, these different stages of activity cannot be explained in detail by the theoretical model of star formation that has developed from observations of nearby ($\lesssim 0.2$ kiloparsec) low-mass star-forming regions. In contrast, most of the high-mass star-forming regions in the Galaxy lie much further away, at kiloparsec distances. As a result, the bulk of the problem in interpreting observations of massive star formation originates in source confusion at the core of distant molecular clouds. The presence of a young stellar cluster in the near-infrared or an UCHII region in the radio must be considered in concert with the raw materials of star formation (molecular gas and dust) if the formation process is to be understood.

With the force of new technology, submillimeter observations promise to clarify the picture. The spatial distribution of interstellar dust and molecular gas, which emit a significant fraction of their energy in the submillimeter band, may help to explain the appearance of active star formation phenomena at other wavelengths. To explore this idea, both wide field and high resolution images will be needed. As bright

continuum sources at many wavelengths, UCHII regions provide a natural center of attention in this quest.

1.1.1 UCHII Regions

Stars with high surface temperatures emit a substantial number of photons at frequencies shortward of the Lyman edge, sufficient to ionize neutral hydrogen atoms in the ground state. The absorption of these photons by interstellar gas leads to ionized nebulae known as HII regions. UCHII regions are small versions of HII regions with diameters < 0.1 parsec (pc) believed to be produced by newly-formed O and early B-type stars at or near the dense cores of molecular clouds. The size and shape of the compact ionized gas has been studied in over 100 UCHII regions with the Very Large Array (VLA) via their free-free radio continuum emission (Wood & Churchwell 1989; Kurtz, Churchwell & Wood 1994). Several questions emerged from the radio surveys of UCHII regions: What is the physical nature of their frequent cometary morphology? Why are there so many of them (more than 50 per square degree in the Galactic plane)? How is their expansion affected by the molecular gas and dust in star formation regions?

1.1.1.1 Radio morphologies

Five different radio morphologies have been identified with UCHII regions: cometary (20%), core-halo (16%), multiply-peaked (17%), shell-like (4%) and spherical or unresolved (43%). Most of the theoretical work to date concerns the cometary UCHII regions. An early model of the cometary shape presumed a density gradient in the ambient gas into which the HII region expands asymmetrically, i.e. a non-spherical Strömgren model (Icke, Gatley & Israel 1980). Despite the plausibility of this model, the nearly perfect parabolic symmetry revealed by more recent observations of regions like G29.96-0.02 spurred the development of bow-shock models in which the young star moves through the ambient gas at high velocities of 10-20 km s^{-1} (Mac Low et al. 1991; Van Buren & Mac Low 1992). However, the discovery of a large

velocity gradient perpendicular to the head-tail axis of two cometary UCHII regions is incompatible with the bow-shock model predictions (Gaume, Fey & Claussen 1994; Gaume et al. 1995). Also, multi-frequency multi-configuration VLA images of W3 Main reveal velocity and linewidth gradients in the ionized gas which are indicative of turbulent expansion into highly anisotropic and clumpy molecular gas (Tieftrunk et al. 1996). As a consequence of findings such as these, current models have found renewed attraction in the idea of an initial density asymmetry in the gas surrounding UCHII regions (Williams, Dyson & Redman 1996).

1.1.1.2 Lifetime

Related to the morphological question of UCHII regions is their apparent longevity. The number of UCHII regions found in the Wood & Churchwell (1989) survey was quite large (75) compared to the small region of the first quadrant of the galactic plane that was imaged. 80 fields were observed with a $9'$ primary beam for a total coverage of ≈ 1.4 square degrees, yielding a detection rate of 54 per square degree. But because the Wood & Churchwell fields were chosen with prior knowledge of the presence of compact radio sources and strong far-infrared (FIR) emission, the detection rate could be anomalously high. In a volume-limited optical sample, Conti et al. (1983) found only 436 O stars within a 2.5 kiloparsec (kpc) radius of the Sun. Assuming a constant disk-like distribution of O stars within the central 10 kpc radius disk of the Milky Way, one could then expect roughly 200 O stars per square degree toward the inner half of the Galactic plane. Together, these results suggest that the lifetime of UCHII regions is a substantial fraction (1/4) of an O-star lifetime which is a few million years (Chiosi, Nasi & Sreenivasan 1978). Further evidence for the longevity of UCHII regions is the fact that their 48 parsec scale height above the Galactic plane (Churchwell, Walmsley & Cesaroni 1990) agrees well with the 50 parsec scale height of optically-identified O stars (Mihalas & Binney 1981). However, the Conti et al. (1983) survey reaches only far enough to include parts of the Perseus and Sagittarius arms adjacent to the local Orion-Cygnus arm. It misses most of the 5 kpc ring seen in CO surveys (Clemens, Sanders & Scoville 1988; Scoville & Solomon 1975) where

the concentration of O stars and UCHII regions is probably higher. A recent detailed analysis of the IRAS database indicates that the surface density of UCHII regions at galactocentric radii between 6.5 and 8.5 kpc is only 2 kpc^{-2} (Comerón & Torra 1996). Using the initial mass function of stars in the solar neighborhood (within 3 kpc) tabulated by Humphreys & McElroy (1984), the authors derive a birthrate of massive stars ($M > 15\ M_{\odot}$) to be 3.7×10^{-5} kpc^{-2} yr^{-1}. The ratio of these values yields an UCHII region lifetime of 5.4×10^4 yr, or about 2% of an O-star lifetime.

Though shorter than previous estimates, this lifetime is still difficult to reconcile with the rapid expansion timescale of standard HII regions (Spitzer 1978). The volume of ionized gas which a star can maintain is determined by its total rate of photon emission at frequencies above the Lyman limit ($N_{\rm L}$) compared to the recombination rate of the gas excluding captures into the $n = 1$ level ($\alpha^{(2)}$). (Captures into the $n = 1$ level emit photons of sufficient energy to ionize other excited hydrogen atoms). In the initial formation of an HII region, an ionization front proceeds rapidly into the neutral medium following the relations:

$$ {r_i}^3(t) = {r_S}^3[1 - \exp(-n_{\rm H}\alpha^{(2)}t)], \tag{1.1} $$

$$ {r_S}^3 = \frac{3N_{\rm L}}{4\pi n_e n_H \alpha^{(2)}}, \tag{1.2} $$

$$ N_{\rm L} = \int_{\nu_{\rm Lyman}}^{\infty} \frac{\pi F_\nu}{h\nu} d\nu, \tag{1.3} $$

where r_i is the radius of the ionization front, r_S is the radius of the Strömgren sphere, $n_{\rm e}$ is the electron density, n_H is the hydrogen ion density, $\alpha^{(2)} \sim 3 \times 10^{-13}$ cm^3 s^{-1} in gas of $T \sim 10000$ K and $\nu_{\rm Lyman} = 3.29 \times 10^{15}$ Hertz (Hz). Assuming an initial density of 10^5 cm^{-3}, and $N_{\rm L} \sim 10^{49}$ s^{-1} typical of an O6 star (Panagia 1973; Thompson 1984), r_i will reach $0.98 r_S = 0.03$pc $= 1''$ at 6 kpc in only 3 years. At this point a shock front forms and the HII region will expand slowly toward pressure equilibrium:

$$ \frac{r_i}{r_S} = \left(1 + \frac{7C_{\rm HII}t}{4r_S}\right)^{\frac{4}{7}}, \tag{1.4} $$

where $C_{\rm HII}$ is the sound speed ($\sim$ 10 km s^{-1}) in the ionized medium. For the O6

star, the dynamical timescale for the UCHII region to double its angular diameter is 4×10^3 yr, over an order of magnitude less than the average lifetime. From this remaining discrepancy, one is led to the possibility that UCHII regions reach pressure equilibrium with their surroundings because there is sufficient ambient gas to supply an essentially constant pressure at the ionization front (DePree, Rodríguez & Goss 1995; García-Segura & Franco 1996). For example, if the ambient gas outside the front has density $n_0 = 10^6$ cm^{-3} and temperature 200 K, then pressure equilibrium with the ionized gas requires:

$$P_{\rm UCHII} = P_{\rm ambient} \tag{1.5}$$

$$2n_i kT_i = n_0 kT_0 \tag{1.6}$$

$$n_i = 1.0 \times 10^4 \text{ cm}^{-3}. \tag{1.7}$$

In equilibrium, the stagnation radius of the UCHII region equals the radius of the Strömgren sphere with density n_i:

$$r_{\rm stagnation} = \left(\frac{3N_{\rm L}}{4\pi {n_i}^2 \alpha^{(2)}} \right)^{\frac{1}{3}} = 0.14 \text{ pc}. \tag{1.8}$$

Therefore, for the O6 star at 6 kpc, the UCHII region will stagnate at an angular diameter of $\sim 9''$ as long as there is sufficient material present to keep $n_0 \gtrsim 10^6$ cm^{-3}.

1.1.1.3 Molecular gas

To explore the problem of UCHII region expansion, studies of the molecular gas around them have been initiated. Measurements of optically-thin molecular transitions toward UCHII regions yield typical column densities of $N_{\rm H_2} \geq 10^{23}$ cm^{-2} (Cesaroni et al. 1991; Cesaroni, Walmsley & Churchwell 1992; Churchwell, Walmsley & Wood 1992; Olmi, Cesaroni & Walmsley 1993). Millimeter interferometric observations of G34.3+0.2 and G5.89-0.39 reveal gas densities of 10^6 cm^{-3} toward the molecular cores (Akeson & Carlstrom 1996). In a survey of massive star-forming regions, many of the UCHII regions were detected in the CS J=7→6 transition which

exhibits a critical density of $\sim 2 \times 10^7$ cm^{-3} (Plume, Jaffe & Evans 1992). These high densities support the pressure equilibrium scenario as a solution to the problem of UCHII lifetimes. Furthermore, additional ram pressure may be applied by the infalling motion of molecular gas as suggested by the redshifted NH_3 absorption features seen toward the UCHII regions G10.6-0.4 (Ho & Haschick 1986) and W3(OH) (Keto 1987; Reid, Myers & Bieging 1987).

1.1.1.4 Dust cocoons

Mixed with the molecular gas are dust grains which absorb short wavelength photons from the central stars and in turn emit bright thermal radiation in the FIR and submillimeter. In fact, the three brightest 100μm sources in the IRAS Point Source Catalog (PSC) coincide with UCHII regions in the cores of well known molecular clouds (Sgr B2, NGC2024, and G34.26+0.14). Although the dust comprises only about 1% of the mass, its broadband emission dominates the bolometric luminosity (typically $10^5 - 10^6 L_\odot$) escaping from these clouds. In their survey of the IRAS PSC, Wood & Churchwell (1989) found that the dust around radio-identified UCHII regions exhibits characteristic FIR colors which distinguish them from other classes of objects. Specifically, they identify 1717 candidate massive embedded stars satisfying the following criteria: $\log(\frac{F_{60}}{F_{12}}) \geq 1.30$ and $\log(\frac{F_{25}}{F_{12}}) \geq 0.57$. The emission typically increases steeply from 12μm to 100μm, indicative of cool dust ($T \lesssim 30$ K). A simple model based on the IRAS data and 1.3 millimeter flux densities of UCHII regions proposes a small central region of warm dust (T$\sim$ 150 K) near the star enveloped by a large cloud of cool dust (T$\sim$ 26 K) (Garay et al. 1993).

Luminosity estimates of the embedded young stellar sources have been made from the relative flux densities in the four IRAS bands and from the ionizing photon rate derived from radio continuum observations. However, the IRAS PSC suffers from poor spatial resolution so it is possible that infrared emission from more than one young object contributes to the flux density of sources in the PSC. Given this confusion, it is not surprising that IRAS luminosity estimates are higher than the luminosity inferred from radio continuum emission in 10 out of 13 massive star-forming regions

studied by Hughes & Macleod (1993). Also, within HII regions, dust likely absorbs many of the stellar ultraviolet photons resulting in a lower gas ionization rate and less free-free emission than expected in a dust-free region. Estimates for ultraviolet (UV) absorption by dust within UCHII regions run as high as 50-90% (Wood & Churchwell 1989; Armand et al. 1996). Further observations of thermal dust *emission* at high angular resolution are necessary to determine the amount of dust within UCHII regions.

1.1.1.5 Embedded protostars

Optical and infrared surveys of young clusters in the Milky Way such as NGC6611 reveal a strong population of $3 - 8 M_{\odot}$ pre-main-sequence stars among OB clusters (Hillenbrand et al. 1993; Massey, Johnson & Degioia-Eastwood 1995). These observations indicate that high mass and low mass stars form simultaneously (at least to some degree) in clusters. However, to understand the formation process we must identify protostellar clusters in an earlier stage of development when they are still too embedded to be seen at wavelengths shorter than 100μm. The dust in young massive protostellar cores should be cooler than the dust in and around UCHII regions since the strong ionizing radiation has either not begun or not had time to substantially heat the surroundings (even if the central luminosity source may already be present). Protostellar cores in this stage and in the initial contraction stage should present their peak emission at wavelengths longward of 100μm (cooler than 30 K). Of course, lower mass protostars which never develop significant ionizing radiation should lie in cool cores of lower mass which should be detectable at submillimeter wavelengths. Deep surveys in the submillimeter will improve our knowledge of the number of young protostars of all masses forming in these environments.

In order to interpret submillimeter flux densities, an important quantity to know is the dust emissivity $Q(\nu)$ which varies as ν^{β}. This property causes the observed emission to appear as a modified Planck spectrum, with $I_{\nu} \propto \nu^{2+\beta}$ in the submillimeter range (when the cloud is optically thin and in the Rayleigh-Jean limit such that $h\nu << kT$). Current models of the dust emission around UCHII regions are forced

to estimate β by interpolation between the measured the 100μm and 1 millimeter (mm) flux densities (Chini et al. 1986; Chini, Krügel & Wargau 1987). Clearly, submillimeter fluxes need to be gathered in order to get more accurate measurements of β, the color temperature and the mass of the dust. Furthermore, if the emission can be spatially resolved, much better constraints can be set on the size of the dust cores in relation to the ionized gas.

1.1.2 H_2O Masers and pre-UCHII regions

Interstellar masers are sources of intense line radiation amplified by stimulated emission from molecules and radicals excited into population inversion via collisional or radiative pumping (Elitzur 1992). Twenty years ago, the association of H_2O masers with compact HII regions was firmly established through single-dish surveys in the 22 GHz $6_{1,6} \rightarrow 5_{2,3}$ transition. (Genzel & Downes 1977; Cesarsky et al. 1978; Genzel & Downes 1979). However, the first radio interferometric studies of star-forming regions found that H_2O maser spots were offset typically by several arcseconds ($\sim 0.02 - 0.1$ pc) from compact HII regions (Forster & Caswell 1989). These findings led to the speculation that the masers were actually tracing gas at the location of massive stars in an earlier stage of formation, prior to the time when the UCHII region becomes detectable. More sensitive high resolution ($\sim 0\farcs1$) VLA maps have revealed several sources in which the maser emission is *directly* coincident with very weak ($\sim$1 mJy), unresolved ($\lesssim 0\farcs1$) UCHII regions such as W75N-B (Hunter et al. 1994). Also, from the continuing single-dish H_2O maser surveys (Brand et al. 1994; Palla et al. 1991), there is evidence that the lifetime of the maser phase is quite short ($\lesssim 10^4$ yr). In the case of a massive protostar (> 10 $M_\odot$), the maser occurs during a brief stage of evolution before the new UCHII region has had time to expand significantly (e.g., Codella et al. 1995). To explore this idea, Jenness, Scott & Padman (1995) surveyed 44 known H_2O/IRAS sources with no associated HII regions or OB clusters and found submillimeter continuum emission from 40 of them (91%). Furthermore, in a near-infrared imaging survey of 17 H_2O masers, all of the fields contain a high density

of K-band sources (Testi et al. 1994). These high detection rates suggest a population of deeply embedded sources in an early protostellar phase. In the UCHII region Cepheus A HW2 (Hughes & Wouterloot 1984), 39 H_2O maser spots have been resolved, spatially and kinematically, into a disk-like structure surrounding the UCHII region and perpendicular to its associated thermal radio jet (Torrelles et al. 1996; Rodríguez et al. 1994). This finding confirms the intimate connection between water masers and protostars.

1.1.3 Bipolar Outflows

Further evidence that H_2O masers trace protostars comes from their association with bipolar molecular outflows. Using very-long baseline interferometry, H_2O maser proper motions have been measured directly and indicate outflow motion (Genzel et al. 1981; Reid et al. 1988). In addition, single-dish CO surveys of H_2O maser sources have found a high detection rate of broad CO lines, indicative of outflowing gas (Fukui 1989; Fukui 1991). Surveys of CO outflow sources also tend to reveal new H_2O masers (Henning et al. 1992; Xiang & Turner 1995). Furthermore, the linewidths of CS and NH_3 transitions have been found to scale with the H_2O maser luminosity, suggesting that masers trace regions undergoing a general increase in turbulent energy, as can be expected from a molecular outflow (Anglada et al. 1996).

An important development in the study of UCHII regions has been the recent detection of massive molecular outflows apparently associated with them. The earliest examples are G5.89-0.39 (Harvey & Forveille 1988), DR 21 (Garden & Carlstrom 1992), and AFGL 2591 (Mitchell, Hasegawa & Schella 1992). Dividing the length scale of these outflows by the mean outflow velocity in the CO line wings yields a typical dynamical timescale of $\sim 2\times10^4$ yr. However, a recent survey of a well-defined sample of IRAS sources from the Class I or Class II-D phase of low-mass young stellar objects (as defined by Adams, Lada & Shu (1987)) revealed a 70% detection rate of molecular outflows (Parker, Padman & Scott 1991). Similar high detection rates are found by Fukui (1993). Because the combined duration of the Class I and II-D

phases is believed to be 2.5×10^5 yr (Beichman et al. 1986; Myers et al. 1987), this statistical evidence suggests that outflows in low-mass star-forming regions are much older ($\gtrsim 1.5 \times 10^5$ yr) than their dynamical timescale. Since the outflows observed in more massive regions exhibit timescales similar to their low mass counterparts, they may also be older than they appear. A dedicated single-dish search for high-velocity CO emission from UCHII regions has recently been completed with a 90% success rate (Shepherd & Churchwell 1996a). Further single-dish mapping and interferometric imaging is needed to determine if this CO emission corresponds to outflows from the UCHII regions or from younger, nearby sources and to compare the dynamical and statistical ages of these outflows.

1.2 Thesis outline

This thesis explores the appearance of high-mass star-forming regions by examining two components of the UCHII region phenomenon: dust cocoons and bipolar outflows. As part of my research, I helped to build the first facility bolometer array camera for the Caltech Submillimeter Observatory (CSO). This instrument, called the Submillimeter High Angular Resolution Camera (SHARC), is described in Chapter 2, including details of my contribution to the optical design and software interface. Images at 350 and/or 450μm of 17 UCHII regions taken with this camera are presented in Chapter 3 along with IRAS HIRES images. The physical conditions of the dust (grain emissivity, temperature, column density, mass, and luminosity) are derived from greybody models of the FIR to submillimeter spectral energy distributions. The submillimeter continuum flux density profiles of the dust cores are compared to predicted profiles from radiative transfer models. Also, the positions of the submillimeter continuum sources are compared to radio continuum maps and H_2O maser positions from the literature in order to search for new sources in the pre-UCHII phase. Maps of bipolar molecular outflows from many of these UCHII regions are presented in Chapter 4, some of which are new detections. Finally, Chapter 5 presents a detailed study of a young cluster of outflows and UCHII regions in the G45 star-forming region

using data from the CSO and the Owens Valley Millimeter Array.

Chapter 2 The Submillimeter High Angular Resolution Camera (SHARC)

The successful deployment of array detectors on infrared telescopes has revolutionized astronomy over the past two decades (McLean 1994; Elston 1991) and driven the development of longer wavelength arrays. Beyond the mid-infrared atmospheric windows, the longest infrared wavelengths observable from the ground are in the 350-1000 μm range, often referred to as the submillimeter band. A current goal in astronomy is to gather high spatial resolution images using the new class of large aperture ($\geq$ 10m) ground-based submillimeter telescopes. This includes the Caltech Submillimeter Observatory (CSO), located near the summit of Mauna Kea, Hawaii. The CSO consists of a 10.4-meter parabolic primary dish with excellent surface accuracy and a hyperbolic secondary mirror which together form a classical Cassegrain telescope. Operating at frequencies from 200 to 1000 GHz, the telescope employs numerous cryogenic heterodyne and bolometric instruments.

During the past five years, the Caltech submillimeter group has developed a bolometer array camera in collaboration with Dr. S. Harvey Moseley and his colleagues in the infrared, X-ray, and microelectronics fabrication groups at the National Aeronautics and Space Administration's Goddard Space Flight Center (NASA/GSFC) in Greenbelt, Maryland (Wang et al. 1996). Installed at the CSO in Fall 1995, the camera has been in active use monthly since this date and has been opened for external proposals beginning in September 1996. The numerous advantages of the 24-pixel linear bolometer camera over the single channel bolometer system will revolutionize the field of ground-based submillimeter continuum observations. Its main advantages include: 1) A nearly twenty-fold increase in mapping speed of extended sources such as nearby external galaxies and Galactic molecular clouds; 2) Improved sky subtraction by removing correlated noise and noise spikes from all pixels; 3) Doubling of the

on/off integration time on point sources when performing pointed observations. In this chapter, I give a brief overview of the instrument followed by a more detailed description of the opto-mechanical design, which has been accepted for publication in the November 1996 issue of *Publications of the Astronomical Society of the Pacific* under the authorship of T.R. Hunter, D.J. Benford, & E. Serabyn. Finally, I explain the camera control interface and data reduction software now in use at the CSO.

2.1 Instrument overview

2.1.1 Bolometer theory

Bolometer can be classified as thermal detectors. Upon the absorption of incident radiation, the temperature of a bolometer rises, causing a change in electrical resistance of the active element (Langley 1881). A bolometer has a heat capacity

$$C \equiv \frac{dQ}{dT} \tag{2.1}$$

where dQ is the additional thermal energy stored in the device after a temperature change of dT. Because it is connected to a heat sink of fixed temperature $T_{\rm sink}$, the heat will be conducted away from the bolometer at temperature $T_{\rm bolo}$ at the rate

$$P = G(T_{\rm bolo} - T_{\rm sink}) \tag{2.2}$$

where G is the thermal conductance. The magnitude of the bolometer's temperature response can be increased by making G as small as possible with the constraint that C is also reduced in order that the response time, defined as

$$\tau \equiv \frac{C}{G}, \tag{2.3}$$

remains below the value required in the experiment. The change in resistance of the active element is governed by its temperature coefficient of resistance defined by

$$\alpha \equiv \frac{1}{R}\frac{dR}{dT}. \tag{2.4}$$

Unlike normal metals, the resistance of ion-implanted thermometers in silicon bolometers at $T < 10\text{K}$ has empirically been found to increase as T decreases (e.g., Downey et al. 1984):

$$R = R_0 \exp\left[\left(\frac{T_0}{T}\right)^{\frac{1}{2}}\right], \tag{2.5}$$

$$\alpha = -\frac{1}{2}\left(\frac{T_0}{T^3}\right)^{\frac{1}{2}}, \tag{2.6}$$

where R_0 and T_0 are constants depending on the level of implantation. This behavior is consistent with the prediction of the model for variable-range hopping with a Coulomb gap (Pignatel et al. 1994; Zhang et al. 1993). Hence, incident radiation on the bolometer causes a change in resistance

$$\Delta R = \alpha R \Delta T = -\frac{1}{2} R_0 \exp\left[\left(\frac{T_0}{T}\right)^{\frac{1}{2}}\right]\left(\frac{T_0}{T^3}\right)^{\frac{1}{2}} \Delta T, \tag{2.7}$$

which can be measured as a change in voltage at constant bias current I

$$\Delta V = -\frac{1}{2} I R_0 \exp\left[\left(\frac{T_0}{T}\right)^{\frac{1}{2}}\right]\left(\frac{T_0}{T^3}\right)^{\frac{1}{2}} \Delta T. \tag{2.8}$$

This equation simply illustrates the advantage of low temperature operation of ion-implanted silicon bolometers. The bolometer responsivity R

$$R \equiv \Delta V / \Delta T, \tag{2.9}$$

increases with decreasing temperature as long as the self-heating effect of the bias current remains small.

The fundamental sensitivity limit of a bolometer is determined by temperature fluctuations in the active element (Jones 1953; Low 1961; Mather 1981; Mather 1984). In an optimal bolometer, the dominant source of temperature fluctuations will be in the rate of absorption and emission of photons, called the background limit. In the case of a practical submillimeter telescope observation, the detected radiation is typically dominated by the atmosphere emitting as a greybody (a blackbody of finite optical depth) into the telescope beam (Phillips 1988). The Noise Equivalent Power (NEP) of a detector is defined as the signal power required to obtain a unity signal to noise ratio in the presence of some known noise. The background noise consists of two terms: the fluctuations in the incident photon rate (the "particle" term) and the fluctuations in the squared amplitude of the incident electromagnetic waves (the "wave" term) (Lewis 1947; Fellgett, Jones & Twiss 1959). A detailed formula for the background limit to the noise equivalent power of a bolometer operating at the focus of a submillimeter telescope has been compiled by Benford, Hunter & Phillips (1996) valid in the limit that $\epsilon(\nu)$, the emissivity of the atmosphere at the observed frequency ν, is constant across the detection bandpass $\Delta\nu$:

$$NEP = \sqrt{\frac{4\epsilon kTh\nu\Delta\nu}{\eta_{\rm optics}\eta_{\rm MB}^2\eta_{\rm bolo}(1-\epsilon)^2}\left[1+\epsilon\eta_{\rm optics}\eta_{\rm bolo}\frac{kT}{h\nu}\right]}, \tag{2.10}$$

where T is the temperature of the emitting material in the atmosphere, $\eta_{\rm MB}$ is the telescope main beam efficiency, $\eta_{\rm optics}$ is the net efficiency of the filters and foreoptics, and $\eta_{\rm bolo}$ is the fractional absorptivity of the detector. With the appropriate values for SHARC:

$$\eta_{\rm optics} = 0.85, \qquad \eta_{\rm bolo} = 0.35, \tag{2.11}$$

$$\Delta\nu_{\rm 850GHz} = 103 \text{ GHz}, \qquad \Delta\nu_{\rm 650GHz} = 68 \text{ GHz}, \tag{2.12}$$

$$\eta_{\rm MB:850\ GHz} \approx 0.30, \qquad \eta_{\rm MB:650\ GHz} \approx 0.40, \tag{2.13}$$

$$\epsilon \approx 0.6, \qquad T \approx 260 \text{ K}, \tag{2.14}$$

the calculated background NEPs in the two highest frequency submillimeter windows

(referenced to a position above the atmosphere) become:

$$NEP_{650\mathrm{GHz}} = 9.1 \times 10^{-15}\ \mathrm{Watt}/\sqrt{\mathrm{Hz}} \tag{2.15}$$

$$NEP_{850\mathrm{GHz}} = 1.6 \times 10^{-14}\ \mathrm{Watt}/\sqrt{\mathrm{Hz}} \tag{2.16}$$

In computing these values, it is interesting to note that the contributions to the background NEP from the "particle" and "wave" terms (the additive terms in brackets in Eq. 2.10) are comparable at a frequency of 850 GHz: 1 and 1.1, respectively. With appropriate consideration, the NEP can be related to a useful observational parameter to the practicing astronomer, the Noise Equivalent Flux Density ($NEFD$). The $NEFD$ provides a measure of the expected integration time required to attain signal to noise ratio of 1 on a source with a given flux density in Janskys (Jy). The $NEFD$ can be estimated given the bandwidth of detection $\Delta\nu$ and the telescope geometric collecting area A:

$$NEFD = \frac{2\ NEP}{A\Delta\nu\eta_{\mathrm{demod}}\eta_{\mathrm{chop}}} \tag{2.17}$$

where η_{demod} is the electronic demodulation efficiency of the lock-in detection process and η_{chop} is the mechanical efficiency of the chopping secondary mirror beyond the factor of 2 explicitly introduced for standard optical chopping ($\sqrt{2}$ because the on-source time is half the total time, and $\sqrt{2}$ because the result is a differenced measurement).

In periods of good submillimeter transparency on Mauna Kea (about 20% of the time), ϵ can be as low as 0.6 across most of the 350 and 450μm filter bands. Under these conditions, with $A = 85\ \mathrm{m}^2$, $\eta_{\mathrm{demod}}\eta_{\mathrm{chop}} = 0.58$, the background-limited $NEFD$ becomes:

$$NEFD_{650\mathrm{GHz}} = 0.53\ \mathrm{Jy}/\sqrt{\mathrm{Hz}}, \tag{2.18}$$

$$NEFD_{850\mathrm{GHz}} = 0.62\ \mathrm{Jy}/\sqrt{\mathrm{Hz}}. \tag{2.19}$$

However, because ϵ varies with frequency within the filter bandpass (increasing near the edges and at several significant absorption lines as can be seen in Fig. 2.9),

Eq. 2.10 must be integrated properly over frequency. The resulting background-limited $NEFD$s can easily become a factor of 2 higher than those listed in equations 2.18 and 2.19. In addition, correlated sky noise not removed by the optical chopping technique will raise the $NEFD$ further.

The background-limited $NEFD$ available to broadband bolometric detectors can be compared to that of the current generation of high frequency heterodyne receivers (e.g., Kooi et al. 1994). Using the Dicke radiometer equation (Kraus 1986), a system noise temperature of 1000 K, a bandwidth of 1 GHz, and the same telescope efficiencies listed above, the background-limited $NEFD$s are 9 and 12 Jy/$\sqrt{\text{Hz}}$ at 650 and 850 GHz, respectively. The advantage of a broad bandwidth is clearly evident in this comparison.

2.1.2 Optical coupling vs. concentrating horns

Because photoconductive detectors are not available beyond a wavelength of $\sim 200\mu$m, continuum detectors used in the submillimeter range have traditionally been composite bolometers. A composite bolometer consists of a separate thermistor physically attached to a radiation-absorbing substrate which is suspended from the cold bath by leads of low thermal conductance (e.g., Nishioka, Richards & Woody 1978). Due to the crowding of suspension leads, it is difficult to construct a closely-packed array of composite bolometers. In addition, the low absorptivities of the bolometers typically required the use of compound parabolic concentrating horns and integrating cavities in order to collect light over a sufficient diameter in the focal plane and deliver it to the bolometer (Winston 1970; Hildebrand 1982). At the same time, these horns, commonly referred to as Winston cones, limit the solid angle of ambient radiation viewed by the detectors. In a similar vein, straight-sided conical horns can be used to produce nearly Gaussian beam profiles with the appropriate horn aperture ($d \sim 2F\lambda$) chosen to deliver high efficiency (Cunningham & Gear 1990; Kreysa et al. 1993). In both cases, however, the large horn input diameter conflicts by a large factor with the goal of full sampling of the highest spatial frequencies available in the focal plane

pattern of a large aperture submillimeter telescope ($d \sim F\lambda/2$).

On the other hand, it is now possible to construct monolithic bolometer arrays using microelectronic fabrication techniques (Moseley, Mather & McCammon 1984). In a monolithic bolometer array, the substrate and thermal/mechanical leads are etched from a silicon wafer. The thermistor and electrical leads are ion-implanted directly into the silicon substrate. This technology allows large bolometers (~ 1 mm) to be manufactured in linear arrays on a single silicon wafer. The closely-packed pixels allow an optical configuration which fully samples the spatial frequencies available in the focal plane. With a proper impedance-matching coating, the large size of the pixels enables them to efficiently absorb radiation with $\lambda \leq d_{\rm pixel}$. As at optical and infrared wavelengths, there is no inherent throughput limitation to this type of coupling (Richards & Greenberg 1982). This characteristic eliminates the earlier requirement for a concentrating cone, and indicates that the pixels can be optically coupled in the focal plane with geometric optics techniques.

2.1.3 Monolithic bolometer array

The bolometer array detector used in SHARC is a monolithic silicon package of linear geometry developed and fabricated by Harvey Moseley, Christine Allen, Brent Mott and their colleagues at NASA/GSFC. Similar arrays have been constructed there for instruments flown on the Kuiper Airborne Observatory (KAO) (Moseley 1995) and the Advanced X-ray Astronomical Facility (AXAF) (Moseley, Mather & McCammon 1984; McCammon et al. 1987; McCammon et al. 1989). Each array originates on a silicon wafer large enough to supply several arrays. Because the final dopant concentration is difficult to predict, a series of wafers are doped by increasing amounts in order to obtain wafers with a range of values of R_0 and T_0. Specifically, the SHARC array came from the MIRA-2 series (Mid-InfraRed Array) of 1 by 24 pixel arrays. After cutting and mounting the arrays, a measurement of R_0 and T_0 determines their optimum operating temperature for photon sensitivity. In order that the background photon noise dominate over thermal noise in the detector during broadband submil-

limeter continuum observations, the SHARC array was selected to operate at 0.3 K.

A thin bismuth film (110 nm) is applied as an absorber to match the impedance of free space. Each of the 24 pixels is rectangular (1 mm by 2 mm by 12μm) with four thermally-conducting support legs of size 2 mm by 12μm by 14μm (see Fig. 2.1). The total thermal conductance of the four legs at 0.3 K was measured to be 10^{-9} W

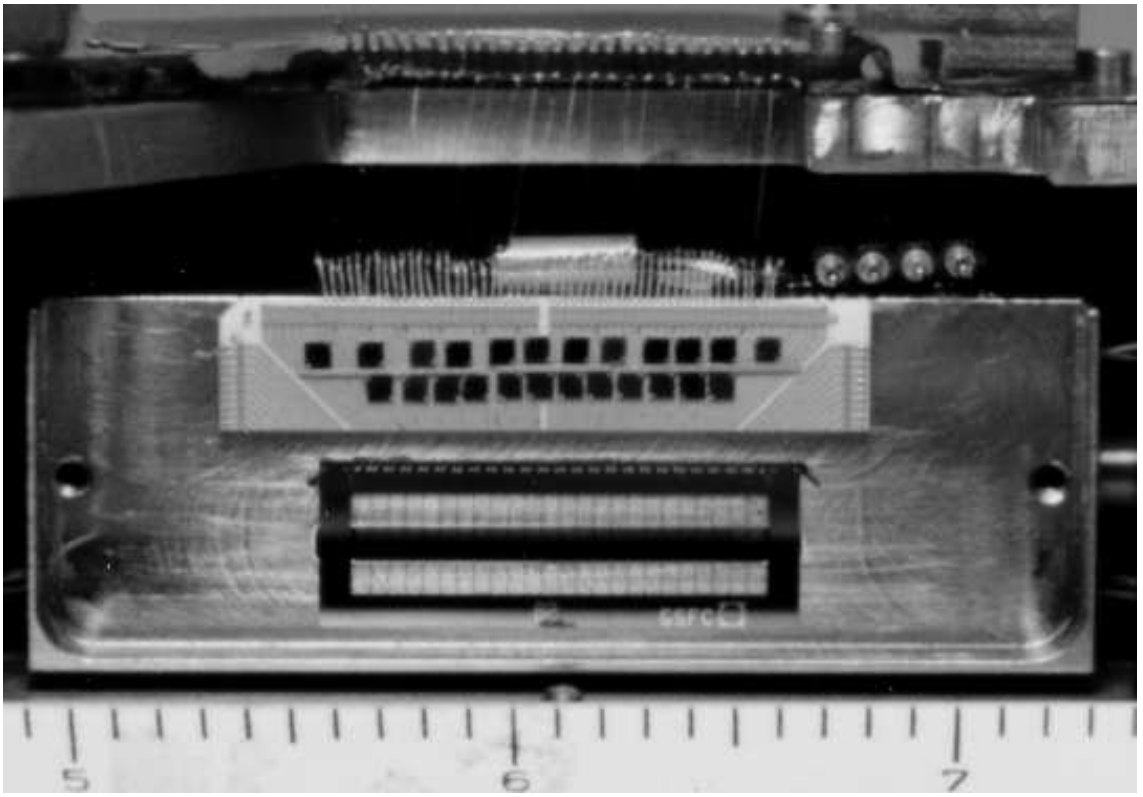

Figure 2.1: A close-up photograph showing the configuration of the bolometer array detector in SHARC. The minor divisions on the ruler at the bottom are tenths of inches. Just above the ruler is the rectangular invar block cooled to 0.3 K and suspended from the rest of the housing via Kevlar cords for thermal isolation. Mounted in two rows near the top of the invar block are the square 30 MΩ load resistors. Below these resistors lies a rectangular annulus of silicon with all of the interior etched away except for the bisecting line of pixels and their narrow support legs. Manganin leads (0.001 inch diameter) under tension bridge the thermal stages near the top and carry the signals to the JFET stage mounted nearby.

K^{-1} (Wang 1994). The heat capacity of the silicon plus the bismuth coating plus the arsenic contact leads is estimated to be approximately 2×10^{-12} J K^{-1} (Benford 1996). These two values yield a time constant of $\sim$ 2 millisecond which is much shorter than the typical telescope beam switching rate of several Hz. Four of the

pixels were damaged during fabrication, so there are 20 working pixels in the current version of the camera (as of Summer 1996).

2.1.4 Cryogenics and electronics

The bolometer array has been installed in a ^{3}He cryostat backed by liquid ^{4}He and liquid N_2 cooled shields. The cryostat operating manual is provided in Appendix A. The first stage electronics are three eight-channel FET (field effect transistor) packages which operate at 130 K inside the dewar and serve as impedance transformers of the signal. Located just outside the dewar are three four-layer, eight-channel, battery-powered, low-noise preamplifier boards. These boards yield a nominal gain of 500 from 3 to 300 Hz, with a high gain setting of 8000 used for most astronomical sources. The amplified signals are subsequently sent to 16-bit A/D boards with a ± 3 volt range and a sampling rate of 1 kHz. The digitized signals are transferred via fiber optic cables to a DSP (digital signal processor) board inside a Macintosh Quadra 950 computer which performs digital lock-in detection at the chopping frequency.

During my graduate study at Caltech, I have worked on several technical aspects of the bolometer array which will be described in detail in this chapter. With Gene Serabyn, a senior research associate in the submillimeter group, I designed the helium-cooled off-axis reflecting optics and the mechanical support structure for these optics. Building on the Macintosh data display software package written for bolometer arrays by Kevin Boyce of Goddard, I extended the package onto an Ethernet and digital input/output interface with the CSO control computer and antenna computer. Finally, I wrote, tested and installed the complementary software interface on the telescope computer with helpful pointers from Ken Young (Raoul Taco Machilvich), the CSO staff astronomer and computer engineer. The software manual is provided in Appendix B.

2.2 Optical design

Obviously, in designing the optics for a new camera, one must consider all of the optical elements beginning with the telescope primary and secondary mirrors, and including any relay optics. Here we briefly describe the tertiary relay optics at the CSO, the details of which are presented elsewhere (Serabyn 1996).

2.2.1 Tertiary relay optics system

Array instruments, including SHARC, are mounted at the Cassegrain area of the CSO where a large unvignetted field of view is possible (Padman 1994; Serabyn 1994). However, because of the large focal ratio (f/12.96) at the Cassegrain focus, a system of relay optics was designed to reduce the focal ratio to a value (f/4.48) more suitable for illuminating millimeter-sized detectors with an appropriate-sized diffraction spot. As constructed, the relay optics provide dual mounting ports, each of which can support an instrument cryostat simultaneously. A flat steering mirror selects one of the two ports and an off-axis ellipsoidal mirror creates a tertiary image (of diameter 32 mm) of the primary mirror that lies 50.8 mm above the instrument mounting surface. The tertiary image of the farfield lies 142.2 mm beyond the image of the primary mirror.

2.2.2 Design requirements for the camera

Many constraints on the camera optical design were necessary due to the imaging requirements, the geometry and cryogenic requirements of the detectors, and the limited volume available in cryostats. First I briefly describe the array detector to be used in the camera, as this sets the plate scale and sampling geometry.

2.2.2.1 Optical requirements

Because the array detector is monolithically etched from a silicon wafer, the detector elements are closely spaced. 24 array elements of size 1 mm by 2 mm are aligned with their long axes adjacent (Wang et al. 1996). There is only a small ($\sim$ 15 μm) gap

between the pixels so that the total size of the array is 24.34 mm by 2 mm. In order to provide Nyquist sampling of the sky brightness distribution along the array axis, the plate scale of the final image must provide $\sim$ 2 pixels per telescope diffraction beamsize in the focal plane. For simplicity and quick implementation, the camera is designed to operate only in the 350 and 450μm atmospheric windows, but an 870μm filter is available for limited observing and testing purposes. With this restriction, a single, fixed plate scale is sufficient for the optical design. In order for the CSO diffraction beamsize at 400μm ($9\farcs7$) to be roughly 1 mm in radius at the detectors ($1.22F\lambda \sim 2$ mm), they must be illuminated by an f/4.0 beam. Thus, the camera optics must transform the f/4.48 relay optics input beam to f/4.0. With a 10.4 meter telescope the f/4.0 plate scale is $4\farcs95$ per mm. Hence, the 24.34 mm bolometer array subtends $120'' = 2'$ on the sky.

In addition to the plate scale requirement, the quality of the final focus must be excellent (Strehl ratio > 0.95 for secondary chop angles $< 2'$ off-axis) over a field of view as large as the available and foreseeable detector arrays. To allow for expansion of future arrays in the perpendicular direction, it was decided that the optics should maintain high quality imaging over a square field corresponding to the linear size of the current array: $2' \times 2'$, or about 25 by 25 mm in linear units (which translates to a maximum radius of $\sim$ 18 mm). Also, the distortion of the focal plane must be negligible with respect to the diffraction beamsize; i.e. the separation of two point source images must be linear across the $2'$ field with respect to the angular separation of the sources on the sky.

2.2.2.2 Thermal requirements

Background radiative loading of the cold bolometer array must be reduced to an absolute minimum by proper cold stops, baffling, and bandpass and blocking filters. Operating at 0.3 K, the array is cooled by a ^{3}He refrigerator. With the exception of a selected bandpass originating from the small solid angle of the sky targeted by the bolometer array, all ambient temperature radiation entering the dewar window must be rejected by filters at liquid nitrogen and helium temperatures. Because they emit

as blackbodies, the stops and camera optics must lie within the helium work space of the cryostat.

2.2.2.3 Geometrical requirements

The total volume available to the camera optics is limited by the size of the helium work space of the cryostat. The diameter of the cold plate is 25 cm and the height of the helium stage radiation shield, although extendable, is limited to ~ 50 cm due to mechanical stability concerns and cryogen usage. In effect, these sizes limit the focal lengths of the optical imaging components. The use of folding mirrors must be avoided in order to minimize the number of optical elements, and to reduce the effect of stray light in the system. Fewer elements also allow easier alignment.

2.2.3 Rejected designs

In order to match the extensive requirements for the camera, several reimaging designs were explored. All of the optical designs were modeled on a VAXStation with the software package CODE V (Optical Research Associates 1995) in order to determine image quality and ray clearance. The models included all of the optical elements beginning with the CSO primary surface. The automatic design features of CODE V were used in many cases to vary the curvature of optical surfaces in order to optimize the quality of the final focal plane. In the course of designing the camera optics, three general configurations were explored: standard spherical lenses, a pair of off-axis paraboloidal mirrors, and a single off-axis ellipsoid. In this section we briefly describe our reasons for rejecting the first two of these configurations.

2.2.3.1 On-axis lenses

Recently, germanium lenses have been successfully used in the reimaging optics of mid-infrared cameras (Cowan et al. 1995). Although cold lenses can provide distortion-free fields with good imaging off-axis, they require additional folding mirrors inside a cryostat because the focusing elements are transmissive. When using transmissive lenses

at submillimeter wavelengths, an important consideration is the thickness and absorption coefficient of the lens material. When cooled to 1.5 K, both standard optical quality germanium and silicon have fairly low but non-negligible absorption coefficients ($\alpha_{\rm Ge} \sim \alpha_{\rm Si} \sim 0.1$ cm^{-1}) and high indices of refraction ($n_{\rm Ge} = 3.928, n_{\rm Si} = 3.3818$) at 333 μm (Loewenstein, Smith & Morgan 1973). The high refractive index of these materials allows for lens surfaces with relatively large radii of curvature (and thus small thicknesses) for a specified focal length. These qualities make them candidates for submillimeter lenses. Perhaps the biggest problem with using lenses is the difficulty of applying an anti-reflection (AR) coating. Recent work has been done to coat hemispherical Si lenses with Stycast 2850FT fiber-epoxy (produced by Emerson & Cuming, Inc.), which has a refractive index $n = 2.0$ at 4 K at millimeter/submillimeter wavelengths (Halpern et al. 1986), and to machine the cured layer to quarter wave thickness (Kaneshiro 1994). Although possible, it is an expensive process requiring a diamond tool lathe, and the resulting root-mean-square (RMS) surface accuracy of the coating is not well measured. Despite the good imaging quality, designs including lenses were rejected due to the reflective and absorptive losses and the need for additional flat mirrors.

2.2.3.2 Off-axis paraboloidal mirrors

After our research on lenses, we grew to favor a mirror design for the camera because mirrors can redirect the incident beam to a suitable location in the cryostat while also focusing. In fact, paraboloidal mirrors have been used as the focusing element in mid-infrared cameras (Gezari et al. 1992). However, with our f/# requirement, a single paraboloid exhibits significant coma on fields larger than $\sim 1'$. By using two off-axis paraboloids in the proper orientation, as in an Ebert-Fastie spectrometer mounting, one can correct for the effects of coma in the final image (James & Sternberg 1969). In order to cancel coma in a planar arrangement, the two concave off-axis mirrors must face each other with their respective vertices both off to the same side of the chief ray. In this configuration, the emergent chief ray crosses its incident path, hence we label it the "crossed" orientation for convenience. This arrangement of paraboloids was

successfully used in the previous generation of relay optics at the CSO and provided a Strehl ratio of > 0.95 over a $4'$ diameter field of view at a wavelength of 350μm (Serabyn 1994). The first design considered for the bolometer array optics consisted of a pair of crossed paraboloidal mirrors inside the cryostat.

In order to fit into the limited volume of a cryostat, relatively short focal lengths (< 100 mm) and large bounce angles ($\sim 45^\circ$) are required. Several crossed paraboloid configurations were considered with separations of up to 254 mm. We found that although this mirror configuration produces good Strehl ratios, the focal plane exhibits a large barrel distortion across the $2'$ field. If this design were implemented, the resultant mapping of the bolometer array detectors onto the sky would be significantly curved ($\sim 30''$ spread in azimuth with the array aligned in elevation). In addition, the plate scale varies across the field. Both of these effects would necessitate detailed measurements and corrections during optical alignment and astronomical observations. Although longer focal length paraboloids may be ideal for small fields of view ($\sim 1'$) they are not suitable in limited cryostat volumes.

2.2.4 Selected design: off-axis ellipsoidal mirror

The third design we considered for the array optics began with the realization that larger mirrors can be used if we include the relay optics ellipsoidal mirror in our conception of the "camera." Since the tertiary relay optics already incorporate one off-axis ellipsoid, potentially superior imaging quality is then obtainable by using a second off-axis ellipsoid in the camera optics, similar to the crossed paraboloid case. However, because a farfield focus and primary image lie between two ellipsoids, cold aperture and field stops can be provided with only one of the ellipsoidal mirrors inside the cryogenic dewar (see Fig. 2.2). Hence this single, cold mirror can be made much larger. As in the case of the paraboloids, one can expect the aberrations induced by the first surface to be partially cancelled by aberrations of opposite sign induced by the second surface (the cancellation is only partial in the case of unmatched F numbers). However, in this case, a farfield focus exists between the two ellipsoids

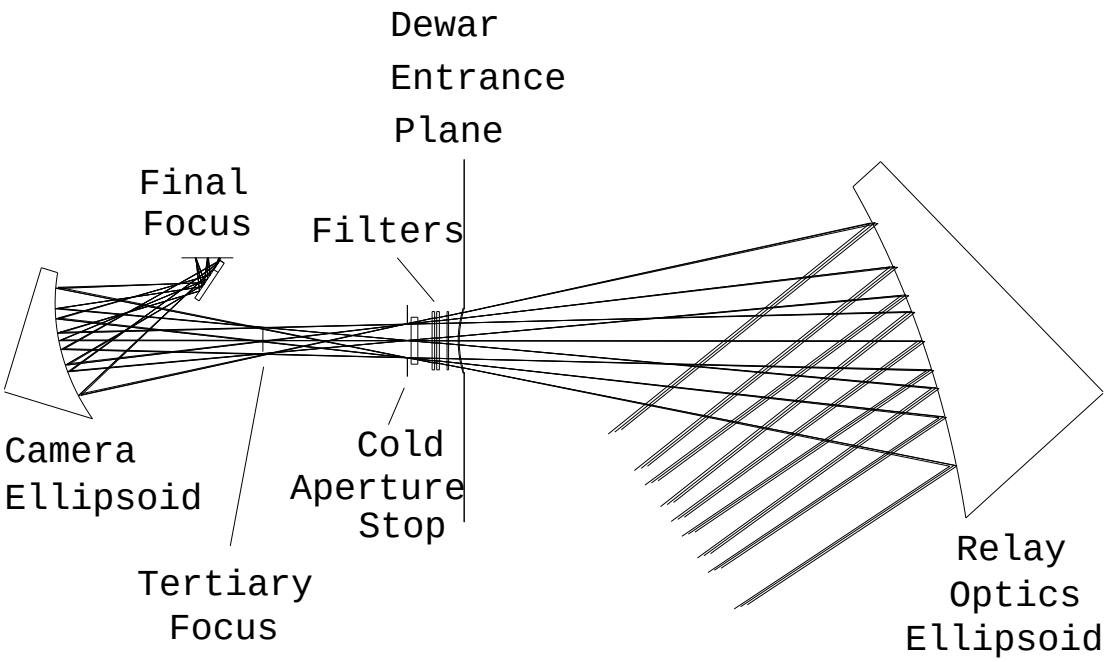

Figure 2.2: Layout of the uncrossed ellipsoidal mirror re-imager used for SHARC. The large ellipsoidal mirror is part of the CSO relay optics and the rest of the optics are cryogenically cooled. The rays plotted span a angle of $2'$ on the sky.

rather than a collimated beam as in the case of the two paraboloids. Since all the rays cross the chief ray axis at the focus, one expects the best imaging to be achieved with the ellipsoid surfaces in the "uncrossed" configuration, opposite to the case with paraboloids.

Before discussing the shape of the ellipsoidal mirror in the camera, it is important to review the shape and illumination of the relay optics ellipsoid. In geometric terms, elliptical surfaces can be defined by two foci. Optically, rays emergent from one geometrical focus of the ellipse are reflected by the surface to the second focal point. But the imaging characteristics of the ellipse are not limited to these two points. Moving the object point closer to the surface along the incident chief ray will displace the image further from the surface along the reflected chief ray. This effect provides an interesting flexibility in using elliptical mirrors in which degradation of the on-axis image is traded for improvements in the off-axis imaging.

For example, if it is required that the input and output focal ratios of the beam be identical, then using an ellipse in the standard configuration would require illuminat-

ing the portion of the surface 90° off the major axis, where the curvature is maximally different in the two perpendicular directions. However, by moving the object point relative to the geometric focus, one can choose a different ellipse in which the portion of the surface used is much closer to the axis, and hence more symmetric. This ellipse is likely to achieve better imaging with the same position of the beam foci. Of course, the displacement of the object point introduces separate aberrations; thus there should exist a best compromise between moving closer on-axis and deflecting the object point. Requiring a 37° deflection for mechanical clearances in the relay optics, the best surface was found using CODE V optimization. We carried out calculations for nine field angles located at the center and on the corners and edge-centers of a $2'$ square grid. The resulting relay optics ellipsoid has an eccentricity of 0.7606, an input focal length of 3500 mm, and an output focal length of 547.5 mm. The object distance (the Cassegrain focus) is 1803 mm.

Since the camera optics require a small focal ratio change from f/4.48 to f/4.0, focal displacement was again exploited in designing the camera optics ellipsoid. In this case, a shorter focal length was necessary in order to fit into the available cryostat length. Thus, we chose 300 mm as the focal length of the generating ellipse. We also required a deflection angle on 22.5° on the ellipsoidal surface to yield sufficient clearance for the detector assembly at the focal plane. Determined from CODE V optimization, the ellipsoid giving best imaging in this configuration has an eccentricity of 0.4129, an input focal length of 200.0 mm and an output focal length of 178.5 mm. With 10% for clearance, the required size of the off-axis section of the ellipsoidal mirror for the entire $2'$ field is 13.5 cm square. For two 24-pixel linear arrays separated by 10 mm (a feasible expansion of the current detector), the required size is only 13.5 by 8.4 cm which easily fits on the 25 cm diameter cold plate. This smaller section was constructed for SHARC at Caltech with an automated milling machine performing successive circular cuts about the axis of the ellipsoid.

From analysis in CODE V, the uncrossed ellipsoidal mirror configuration described above provides excellent diffraction-limited imaging (Strehl > 0.95) in the final focal plane across a $2' \times 2'$ square field even with the secondary mirror chopping (rotated)

at angles up to $\pm 2'$ ($4'$ throw) in the farfield. Even with chopper throws up to $8'$, the Strehl remains > 0.85, but this degradation is more due to the secondary mirror than the camera optics. The Strehl ratios as a function of secondary chop angle at the field center, four edges, and four corners of the field are plotted in Fig. 2.3. All the Strehl ratios reported in this paper are taken at the best composite focus of the nine fields (corners, edge-centers and center of a $2'$ square) and hence the effects of field curvature are directly included. However, since the depth of focus $\sim F^2\ \lambda$ is ~ 6 mm, a small to moderate amount of field curvature is not a critical problem in this application.

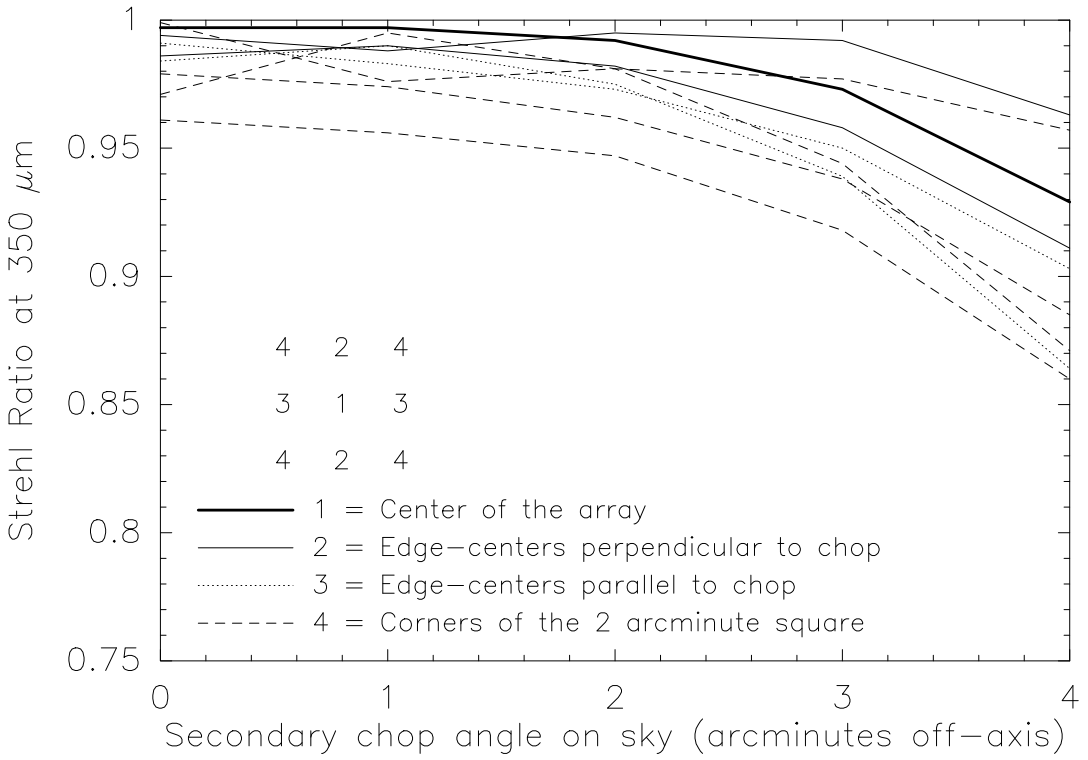

Figure 2.3: Strehl ratios across the $2'$ field of view of the camera focal plane as a function of the secondary chopper angle. The solid and dashed lines represent, respectively, the center and edges of the current linear array (which is oriented in zenith angle). The graph shows the performance at the best composite focus of the nine fields at each setting of the chopper.

Spot diagram footprints of the $2'$ by $2'$ focal plane are given in Fig. 2.4. To envision the diffraction beam, these spot diagrams must be convolved with a spot size of $\sim$ 1.6 mm (at a wavelength of 350μm). There is essentially no distortion

in direction along the array. A small distortion ($\sim 2''$ over $120''$) exists across the field in the direction perpendicular to the array but it is negligible compared to the diffraction beamsize ($8\farcs5$ at the shortest operating wavelength of 350μm). Distortion becomes the most significant aberration at focal lengths less than 300 mm (for the final ellipse) but the Strehl ratios also degrade.

2.2.5 Optical stops

The pair of ellipsoidal mirrors is not the entire optical design, however. As shown in Fig. 2.2, upon entering along the axis of the cylindrical cryostat, the converging f/4.48 beam delivers an image of the secondary mirror (the secondary sub-illuminates the primary) lying 5 cm inside the mounting surface. The farfield focus lies an additional 14.2 cm beyond the primary image. After this focus, the beam re-expands to fill the cold ellipsoid. Upon reflection, the chief ray moves away from the dewar axis at 22.5° and is redirected by a small folding mirror onto the bolometer array mounted perpendicular to the helium work surface.

With direct illumination, as in any optical or infrared camera, the aperture must be carefully defined (to avoid spillover past the edge of the primary mirror) by using a cold physical stop in the optics (Hildebrand 1986). For this reason, we place a 32 mm diameter cold aperture stop at the primary image to define the illumination pattern of the array pixels, i.e. to ensure that each pixel sees radiation originating only from the secondary mirror. Scattered ambient radiation, which lowers bolometer sensitivity and degrades the detector angular response pattern (beam), must be prevented as much as possible from entering the optical path after the stop. To achieve this goal, we completely surround the reimaging optics with absorptive baffling. A special case of baffling is the field stop which lies at a farfield image (of the sky) in order to precisely define the solid angle of the astronomical object from which radiation is admitted to the detector. We place a field stop in the form of a thin aluminum plate with a rectangular slit machine-punched to match the scaled size of the bolometer array at the farfield focus. In this configuration, the field stop also limits the background

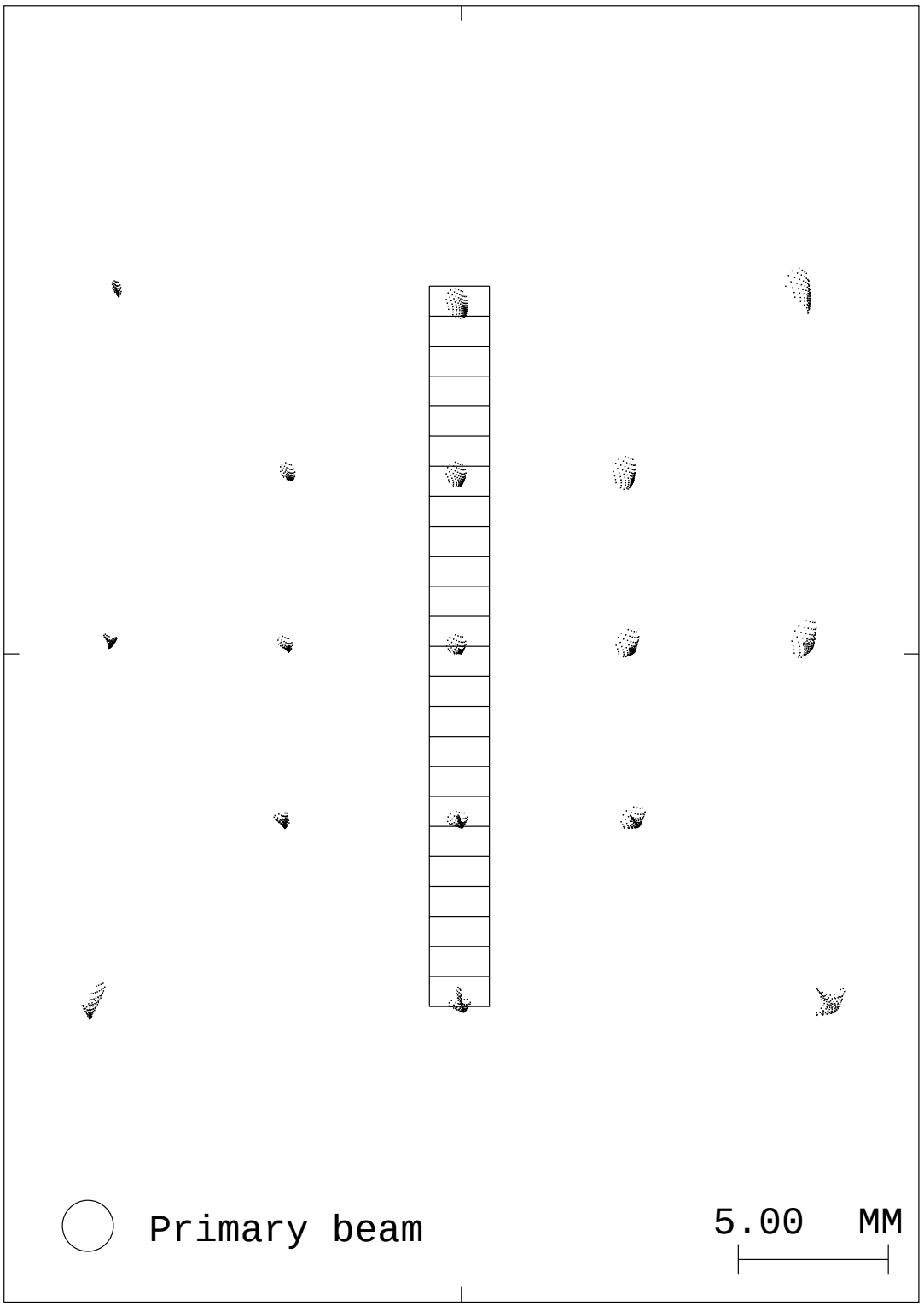

Figure 2.4: Spot diagram of the SHARC focal plane. The spots lie at the center, corners and edges of a $1'$ and a $2'$ square field, corresponding in the focal plane to 12 mm and 24 mm respectively. The diameter of the primary diffraction beamsize of $8''.5$ is shown.

radiation transmitted to the detector. By design, the field stop slit plate can be easily replaced by suitable plates as larger arrays become available. Because they lie beyond the bandpass filtering, both the aperture and field stop must be cooled to $T < 4$K in order to minimize the blackbody emission reaching the detector.

2.2.6 Mechanical design

Because the optical design requires both the aperture and field stops to be at low temperature, a significant mechanical support structure is needed to align and fix these elements with respect to the ellipsoidal and flat mirrors and the detector array. The mechanical support was designed to be symmetric about a plane in order to simplify the optical arrangement as much as possible and to allow for accurate positioning of the mirrors and stops. Thus the optical system is reflection-symmetric about the plane defined by the linear array and the mid-line of the off-axis ellipsoid.

In order to minimize the required dewar length without adding extra folding mirrors, the ellipsoidal mirror was placed directly on the helium work surface with the chief ray aligned with the entrance window along the dewar axis (see Fig. 2.5). All of the optical elements, including the rotation of the flat mirror are fixed in place. Thus there is no alignment to perform other than the lateral positioning of the bolometer array housing which is accomplished by means of a sliding surface. As all mirror surfaces are polished, this adjustment is performed with visible light.

To insure proper alignment of the aperture stop and field stop with the ellipsoidal mirror, the support structure attaches directly to the mirror with self-consistent stop locations defined by tapped holes machined to specification. This arrangement also allows easy removal of the entire optics assembly including the detector housing, either with or without the ellipsoidal mirror. All sides of the main optics assembly (which resembles a shoe box with the ellipsoid at one end and the aperture stop at the other) are covered with thin metal baffle sheets to block stray light from reaching the detectors. The baffles are constructed from 0.625 mm OFHC copper sheet to insure good thermal coupling to the helium bath.

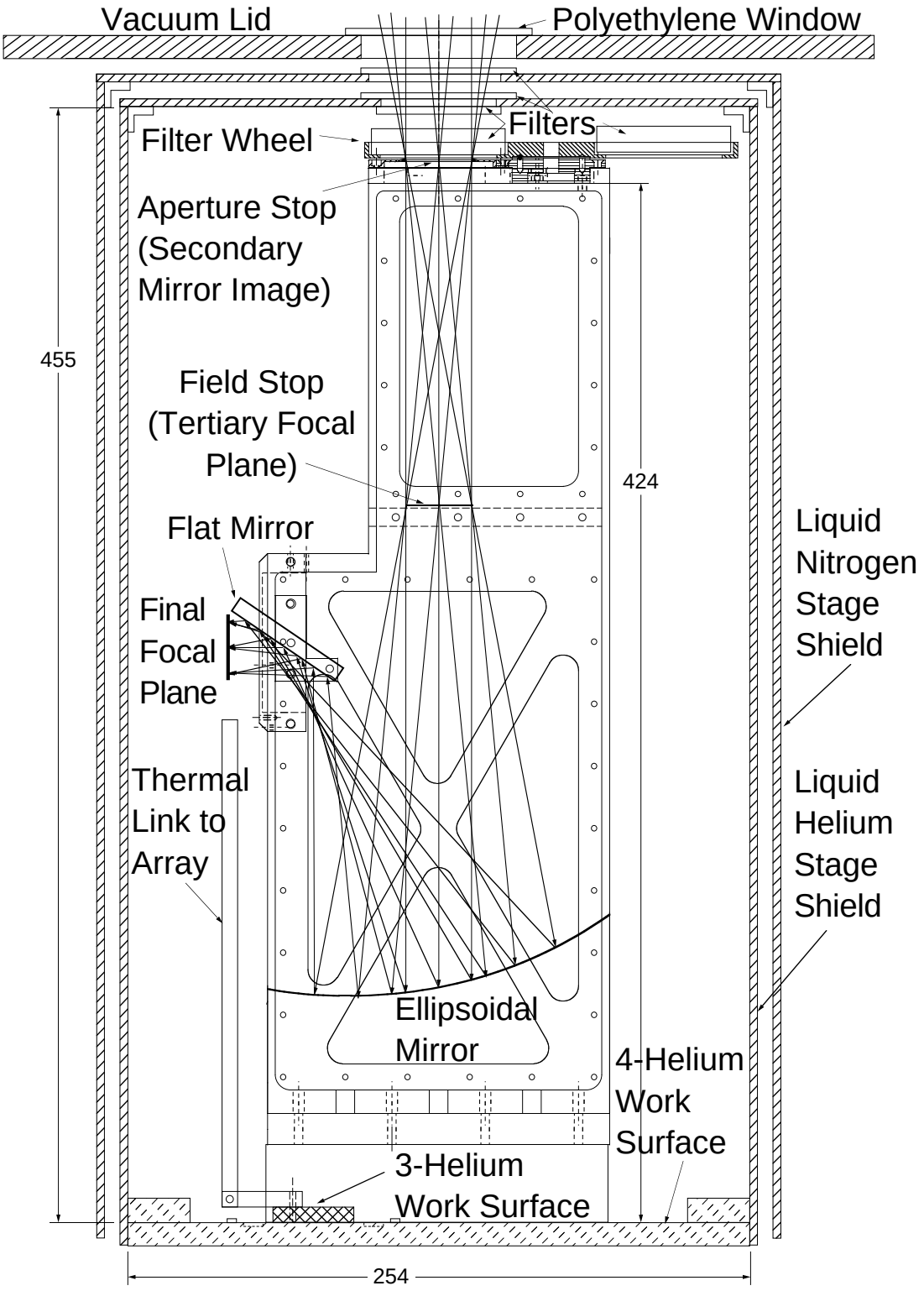

Figure 2.5: A scale drawing of the cryostat optics with dimensions in units of millimeters.

2.2.7 Filtering

Optical filtering is important in a submillimeter camera for two main reasons: 1) to define the bandpass of the observations, and 2) to limit the radiative heat load on the cryogenic detectors. The bandpass of the camera is defined by one of a pair of narrow-band metal mesh filters mounted on a liquid He-cooled filter wheel which is located just above the aperture stop. According to measurements made by the manufacturer (Cochise Instruments 1995), the bandpass filters effectively block all wavelengths $\lambda > 150\mu$m (outside of their specified bandpass). The bandpass filter wheel is a 152 mm diameter geared circular plate with four round milled slots that can hold metal-mesh bandpass filters of 46 mm clear aperture. The filter wheel is mounted at the top of the optics chamber just below the lid of the He temperature shield. Manually operated from the outside, the wheel drive shaft extends from the bottom of the dewar up along the inside of the helium shield to a 9.5 mm diameter gear. The gear drives the filter wheel with a 16:1 turn ratio.

However, because of the broad wavelength response of the detectors, far-infrared through optical radiation must be rejected by a stack of pre-filters. The pre-filtering occurs at the entrance to the liquid N_2 and He shields of the cryostat. A schematic of the filter arrangement is shown in Fig. 2.6. First, the vacuum window of the cryostat is a 1.0 mm thick disk of high density clear polyethylene which provides long-term durability and water impermeability (Bussone 1989) coupled with low loss at submillimeter wavelengths (Birch, Dromey & Lesurf 1981; Stützel, Tegtmeier & Tacke 1988; Birch 1990). Next, a long-wavelength-pass quartz filter (64 mm diameter, 1.5 mm thick) with a black polyethylene AR coating on both sides is mounted at the window of the nitrogen shield lid. At this temperature, quartz is essentially opaque to radiation between 5 and 40μm (Eldridge 1991), becoming transmissive at longer wavelengths (Loewenstein, Smith & Morgan 1973; Randall & Rawcliffe 1967). The black polyethylene also serves to block optical and near-infrared radiation. A second long-wavelength-pass quartz filter (57 mm diameter, 2.5 mm thick) is mounted as the window of the helium shield. On its top surface is a diamond scattering layer opaque

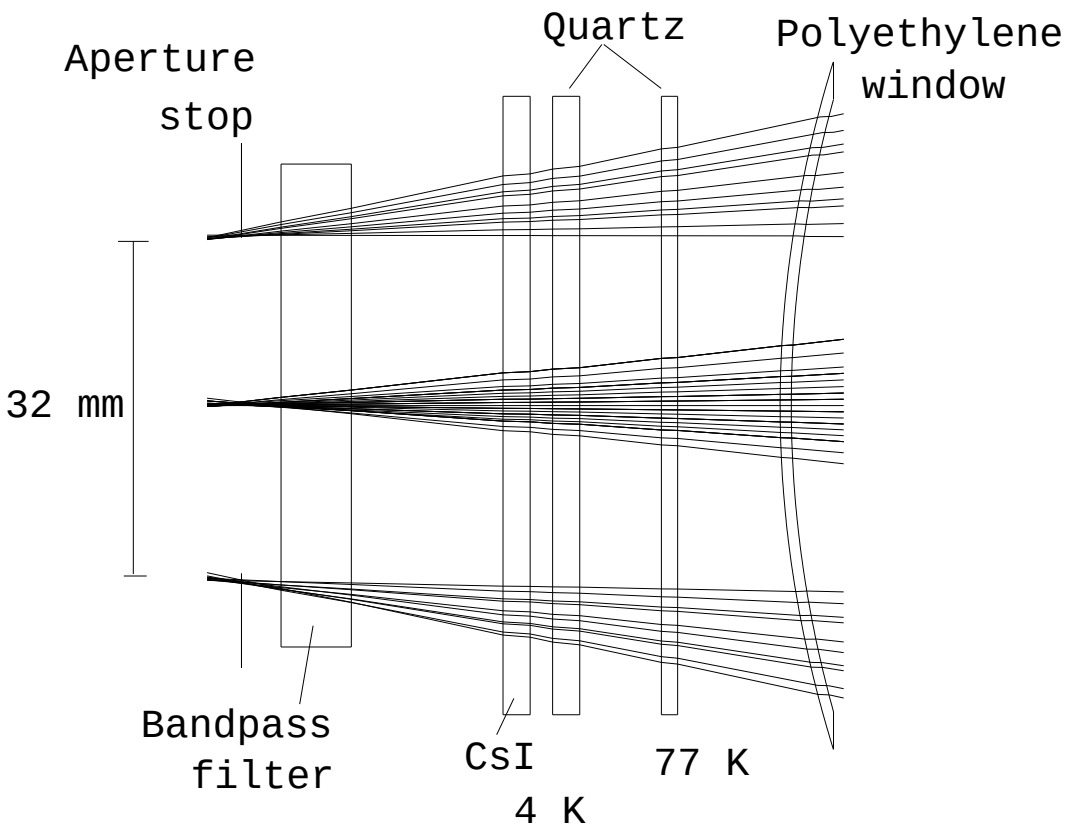

Figure 2.6: The filter arrangement at the entrance of the SHARC cryostat. The filters (and thicknesses) are: high density clear polyethylene vacuum window (1.01 mm); quartz (1.5 mm) with black polyethylene AR coating; quartz (2.5 mm) with a diamond scattering layer on the top and a black polyethylene AR coating on the bottom, Cesium Iodide (2.5 mm) with a clear polyethylene AR coating on both sides; metal-mesh bandpass filter (6.5 mm). The bandpass filters lie in a manually-driven filter wheel with space for four different filters.

from about 5 to 100μm (Infrared Laboratories 1995). Again, a black polyethylene AR coating is applied on the bottom surface of the quartz to block the near-infrared photons originating from the 77 K filter and shield. At this point, photons shortward of 100μm are completely blocked.

The quartz filter, on the helium shield lid, is followed by a crystalline cesium iodide (CsI) filter (57 mm diameter, 2.5 mm thick) with clear polyethylene anti-reflection coating (Josse, Gerbaux & Hadni 1993) on both sides. The clear polyethylene also serves to protect the CsI from hydration. As an ionic crystal, CsI exhibits a reflective band in the far-infrared ($\sim$100-170 μm) due to lattice vibrations (Mitsuishi, Yamada & Yoshinaga 1962; Eldridge 1991). At 4 K, the CsI filter yields nearly zero transmission of incident radiation between 100 and 150μm while rising to 90% transmission at 350μm (Hadni et al. 1962). This combination of filters thus cuts off all radiation shortward of 150μm, eliminating any possible third harmonic response of the metal mesh bandpass filters.

2.2.8 Submillimeter black paint

As in all sensitive cameras, it is important to minimize unwanted reflections and scattered light inside the optical train. When the detector pixels are similar in size to the telescope diffraction beam, scattered light reaching the pixels will cause sidelobes in their angular response pattern and distort the instrument beamshape. In addition, with cryogenic bolometers sensitive to broadband radiation, all of the low temperature surfaces must be highly absorptive so that only emission from low temperature materials can be seen by the detector. To ensure this property, we coated the inner surfaces of the optics support and baffles with a specially-mixed "submillimeter" black paint. The far-infrared properties of various types of optical black coatings have been measured (Smith 1984; Pompea et al. 1984). The base of the mixture we chose is a black polyurethane paint, Aeroglaze Z-306 (Lord Corporation Industrial Coatings 1995). A 2-part wash primer was applied to the roughened (400 grit sandpaper) metal surfaces prior to the black topcoat. Tests of the submillimeter absorptivity of the paint, per-

formed by inserting metal samples coated with a layer of thickness ~ 0.1 millimeter into the beam of the 650 GHz heterodyne receiver at the CSO (Kooi et al. 1994), revealed that the paint absorbs less than 10% of incident submillimeter radiation. To improve the absorption of the topcoat base, we added (3% by volume) carbon black powder (Fisher Scientific 1995) filtered to remove large congealed clumps that could clog the air brush used to apply the paint, and solid glass beads (10% by volume) with a distribution of diameters from 50-200 microns (Potters Industries 1995). Carbon black effectively absorbs optical and infrared radiation while dielectric glass beads of radius a extend the attenuation to longer wavelengths $\lambda < 2\pi a$ (Sato et al. 1989). A significant amount of Aeroglaze 9958 paint thinner (25% by volume) was also added to lower the viscosity of the total mixture sufficiently to be sprayed with the air brush. Multiple coats were required to obtain sufficient thickness of ~ 0.3 mm (0.010 inch). With these additives, the submillimeter absorptivity of the metal samples was raised to $\sim 65\%$. The paint adheres well to aluminum and copper surfaces of thickness over 0.5 mm (0.020 inch). When applied to thinner sheet metal, thermal cycling causes the paint to buckle and peel.

2.2.9 Field rotation

The current observing method employed with millimeter and submillimeter bolometers relies on rapid beam switching in the azimuth direction in order to subtract sky emission. At the CSO, this switching is accomplished by chopping the secondary mirror at a rate of several Hz. Raster scan "on-the-fly" maps are acquired by scanning the telescope in azimuth at successive elevation settings and restoring the individual dual beam pixel measurements to a single beam image in celestial coordinates. Because this rapid scanning method works well to combat correlated sky fluctuations, the preferred observing mode for SHARC is to align the array axis in the elevation direction and have the CSO secondary mirror chop in azimuth. Deep integrations are performed by repeated mapping scans. This on-the-fly mapping technique also avoids the problem of field rotation of altitude-azimuth-mount telescopes.

The option does exist to maintain fixed alignment of a linear detector array along a special position angle on the source by rotating the dewar on its mounting plate as the telescope tracks. However, because the optics contain off-axis elements, this rotation varies the imaging performance. Best imaging is obtained when the two ellipsoidal mirrors lie uncrossed in the same plane as discussed above. However, to align the linear bolometer array with the elevation direction, the dewar must be rotated 14° with respect to this configuration, in order to compensate for an angular offset introduced by the two flat mirrors of the relay optics which send the beam out of the symmetry plane of the primary mirror. The imaging quality across the bolometer array remains excellent in the elevation-aligned configuration, despite the small disalignment of the mirror axes. A plot of the Strehl ratios as a function of dewar rotation is given in Fig. 2.7. The nine graphs plotted represent Strehl ratios at the same nine fields as in Fig. 2.3 and with the secondary mirror rotated off-axis by $2'$ on the sky. The allowance for dewar rotation was not a major concern during the original design given our fixed orientation observing mode. However, we note that the Strehl ratios across the central line of the focal plane remain above 0.8 over $\pm 60°$ of position angle, and because sources are typically observed only within a few hours of local transit time (with parallactic angles between $\pm 45°$), this range of performance is satisfactory for observations relying on field de-rotation.

2.3 Optical performance

Shown in Fig. 2.8 is a beam map of SHARC obtained at the CSO at a wavelength of 350μm. The map was constructed by scanning the bolometer array through the planet Uranus in the azimuth direction at a rate of $3\farcs0$ s^{-1}, stepping the array in elevation by 1 pixel ($5''$) and repeating to allow all pixels to pass through the planet. A total of 31 scans were added. The sample size in azimuth was $2\farcs93$ per 0.976 second integration. Because of the small angular size of Uranus ($\theta = 3\farcs6$) and its large flux density, it is a good source with which to measure the beam pattern. The brightness temperature ($T_{\rm B}$) of Uranus varies with wavelength such that at 350, 450,

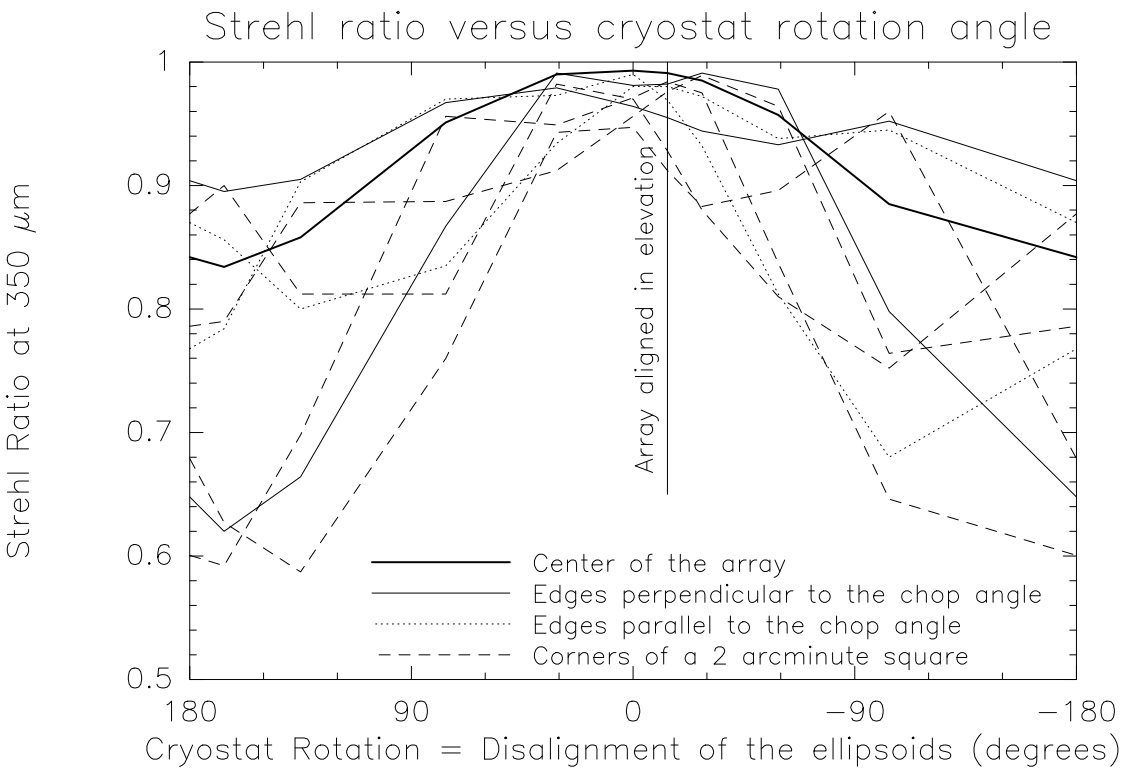

Figure 2.7: The Strehl ratio of the camera optics across the 2′ field of view in the focal plane as a function of the dewar rotation angle. The heavy and solid lines represent, respectively, the center and edges of the currently-installed array detector. The results plotted are with the secondary mirror rotated off-axis by 2′ on the sky.

and 1300μm, $T_{\rm B} = 64$, 73 and 94 K, respectively (Hildebrand 1985; Orton et al. 1986; Serabyn & Weisstein 1996); and at 3300μm (90 GHz), $T_{\rm B} = 134$ K (Ulich 1981). Thus, the expected blackbody flux density from Uranus at 350μm (849 GHz) can be computed from the Planck function:

$$F_\nu = B_\nu(T_{\rm B})\Omega = \frac{2h\nu^3}{c^2\left[\exp\left(\frac{h\nu}{kT_{\rm B}}\right)-1\right]}\frac{\pi\theta^2}{4} = 2.4\times10^{-21}\ \mathrm{erg\ cm^{-2}\ s^{-1}\ Hz^{-1}} = 240\ \ \mathrm{Jy}. \tag{2.20}$$

Because SHARC uniformly illuminates the secondary mirror, the response to a point source should be an Airy pattern. With a 10.4-meter telescope operating at 350μm, the theoretical full-width at half-maximum (FWHM) of the main lobe of the Airy disk is 7.″2. The under-illumination of the primary by the secondary widens the

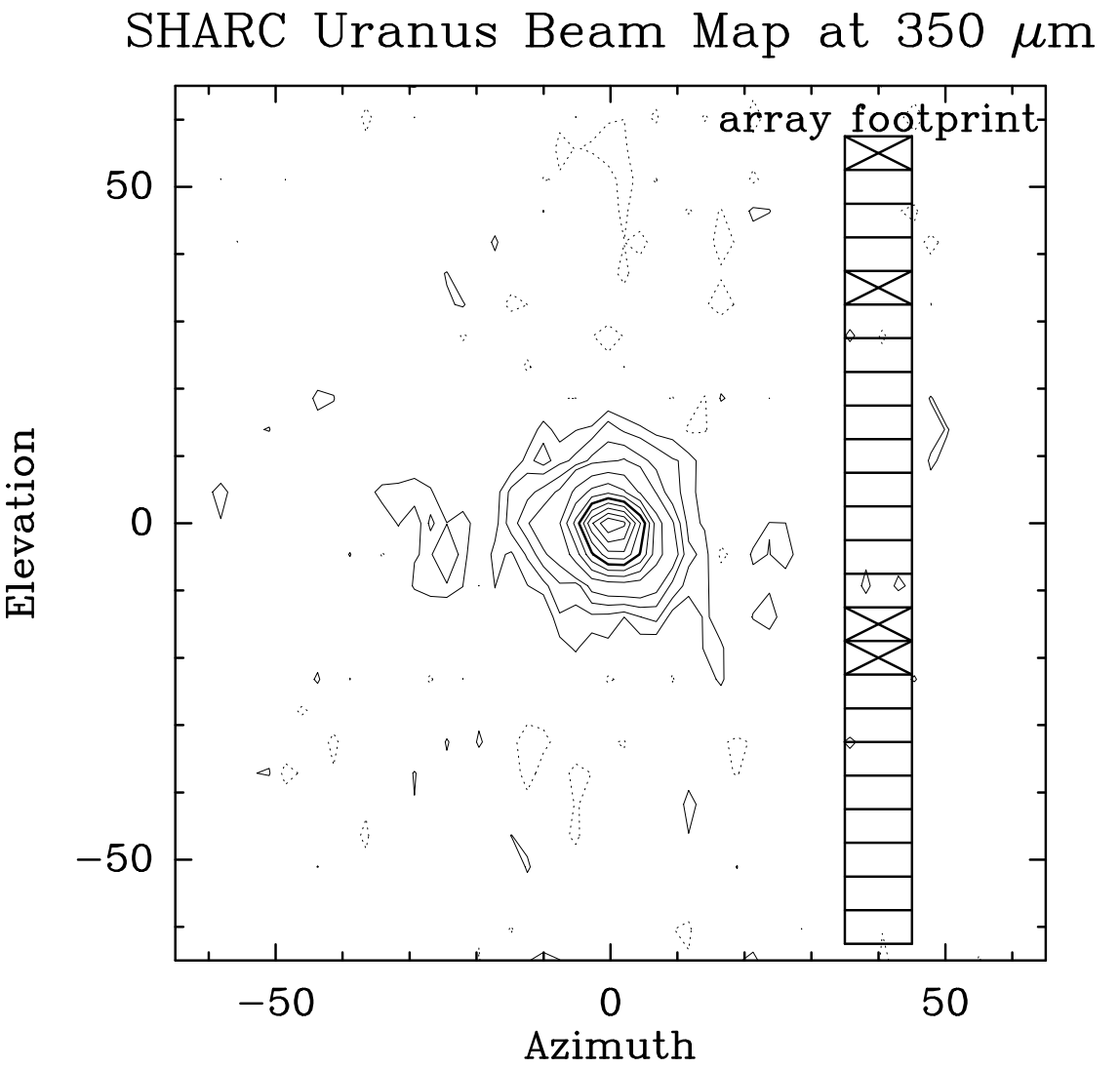

Figure 2.8: A CSO/SHARC beam map at 350μm constructed from a sum several SHARC scans recorded while the telescope was driven across the planet Uranus at a rate of 3 arcseconds per second. The secondary mirror was chopping 86 arcseconds in azimuth at 4.09 Hz during the scans. The solid contour levels are 2,4,7,10-90% by 10% of the peak flux density. The dashed contour is -2%. The array footprint is shown with non-functioning pixels marked by an X.

CSO's Airy disk slightly, while its central obstruction of roughly 12% (linear) narrows it slightly (Schroeder 1987). In the case of the CSO, these effects virtually cancel each other, so they are neglected here. If we convolve the $7''.2$ FWHM Airy disk over the area of the rectangular detector, the expected half power beamwidths become $10''.5$ along the long axis (azimuth) by $7''.7$ along the short axis (elevation).

Fitting a single Airy pattern to the image of Uranus yields a size of $12''.4$ in azimuth by $10''.7$ in elevation. However, the low level wings of beam pattern evident in the contour plot are not well fitted by the single Airy-like components because at this short wavelength, the surface roughness of the CSO primary and secondary mirrors degrades the imaging performance. Surface inaccuracies (on the scale of $\sim \lambda/20$), flexure, obstruction from the feed legs, defocus and decenter of the secondary divert a portion of the flux into sidelobes, called the telescope error pattern, which can have a complex shape. We attempt to account for this error pattern by fitting the azimuth and elevation cuts through the image of Uranus with the sum of two components: an Airy-like "main beam," and a wider and weaker Gaussian (the "error pattern") constrained to lie at the same position. In this model, the fitted FWHM of the main Airy lobe is $10''.3$ in azimuth by $8''.8$ in elevation, containing 32% of the flux, while the FWHM of the Gaussian component is $24''$ in azimuth by $21''$ in elevation. The fitted size of the Airy disk closely matches the theoretical prediction in azimuth and is only $\sim 1''$ larger than expected in elevation.

Several effects could cause $\sim 1''$ smoothing of the beam in elevation, including a slow pointing drift between successive scans or a slight offset between the + and − beams, implying that this broadening may not be significant. However, the spatial sampling of the current Uranus data set is not sufficient to distinguish between the causes. Finer sampling ($\leq 1''$ per integration) of the signal in the in-scan direction, together with smaller elevation increments between scans ($4''$, or $1''$ less than the pixel-to-pixel spacing) will improve the spatial sampling of the beam pattern in the future, allowing further refinement of our understanding of SHARC's performance. However, it is already clear that SHARC's ultimate imaging performance will be limited largely by the quality of the telescope surface, rather than the camera optics. The approach

of applying geometric optics and planar arrays at submillimeter wavelengths has thus been quite successfully demonstrated.

The SHARC filter transmission curves are plotted in Fig. 2.9 along with the atmospheric transmission over Mauna Kea as a function of frequency. The bandwidths and effective frequencies of the filters are also listed for sources with different submillimeter spectral indices $2 + \beta$, where $F_\nu \propto \nu^{2+\beta}$. Blackbodies correspond to $\beta = 0$, while dust grains with power-law emissivities generally correspond to $\beta = 1$ or 2.

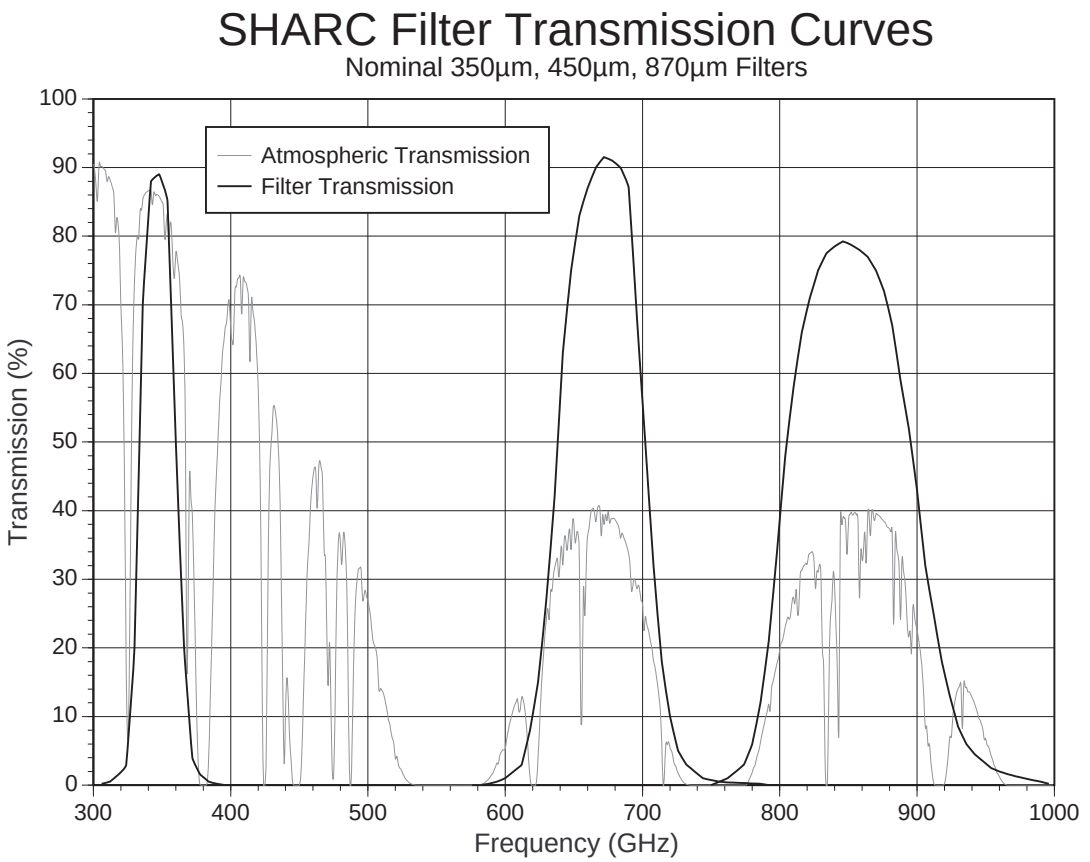

Figure 2.9: The SHARC filter transmission curves superimposed on the atmospheric transmission over Mauna Kea during good weather ($\tau_{225\mathrm{GHz}} = 0.05$). The computed bandwidths and effective frequencies of the filters are also listed for different submillimeter spectral indices $2 + \beta$. Figure courtesy of D.J. Benford.

2.4 Instrument control system

The other instrument-related project of my thesis is the development and implementation of the control software for the CSO bolometer array camera. Traditionally, the heterodyne spectrometers on millimeter and submillimeter telescopes have been managed by a small "backend computer" responsible for setting system parameters, and processing and delivering data to the main telescope computer. In the case of the continuum bolometer array system at the CSO, the instrument control computer, or "camera computer," is an Apple Macintosh.

2.4.1 System requirements

The requirements of the software package for the CSO bolometer array camera were well defined at the outset of the project. First, the digital signal processing board (DSP) that performs digital lock-in of the bolometer signals was designed by engineers at the Goddard Space Flight Center (GSFC) on a Macintosh NuBus board and thus required a Macintosh computer for operation. Second, much of the low level communication to the DSP board was written by Kevin Boyce (GSFC) in the Labview software package, a graphical programming language originally written for the Macintosh (but now available for PC and Unix platforms). Rather than recreate this code, the control software was based on the existing Labview architecture. Third, the main CSO control program, the User Interface Program (UIP) runs under the VMS operating system on a VAXStation 3100 located in the telescope building. The UIP exerts ultimate control over the 68000-based computer which controls the antenna computer as well as the Power-PC (Cetia) backend computer for the acousto-optic spectrometers used with the heterodyne instruments. For uniformity, it was decided in consultation with the CSO staff that the Macintosh computer that operates the DSP board would also be controlled by the UIP over Ethernet in a manner similar to the backend computer. Finally, since the Macintosh performs the actual data gathering, rapid communication with the antenna computer is required in order to know when the antenna has reached and acquired the selected position.

2.4.2 Hardware

The control computer for SHARC is a Macintosh Quadra 950 computer outfitted with 24 Megabytes of RAM, a 1 Gigabyte hard drive and a SuperMatch 20 inch color monitor. The CPU in the Quadra 950 is a 33 MHz 68040 which currently runs Labview version 3.0.1 (National Instruments 1995). The extra memory was required to compile and run the complex virtual instruments (VIs) that communicate with the VAX and display the data on the Mac. Also purchased was a multi-purpose analog and digital I/O board, the AT-MIO-32 board from National Instruments, Inc., to allow the source acquisition status bit (the "acquire bit") and the telescope tracking status bit (the "idle bit") generated by the antenna computer to be monitored in real time by the Macintosh software. The Quadra 950 allows space for 5 NuBus boards of which at least 2 are required: the DSP board and the I/O board. Since this computer is planned to also run a bolometer spectrometer system, or an upgraded camera with a larger number of pixels, additional boards may be required in the near future. The extra slots available in the Quadra plus its high processor speed influenced the decision to buy it. One important modification was needed to the mechanical housing of the Quadra itself. A second fan was added inside the case in order to increase the convective cooling rate of the microprocessors on the mother board and the NuBus boards in order to prevent the overheating problems frequently faced by visiting groups using Macintosh computers at the CSO.

2.4.3 Communication between the various computers

The communication between the Macintosh and the CSO control computer (the VAXStation 3100) is modeled after the system configured for the heterodyne receivers by Ken Young at the CSO. All of the communication occurs asynchronously using the Transmission Control Protocol/Internet Protocol (TCP/IP) implemented over a local Ethernet. Fortunately, the Labview package supplies built-in VIs for TCP/IP communication. On the VAX side, the communication software is written in C in order to use the built-in TCP/IP socket routines for VAX C in the Multinet software package

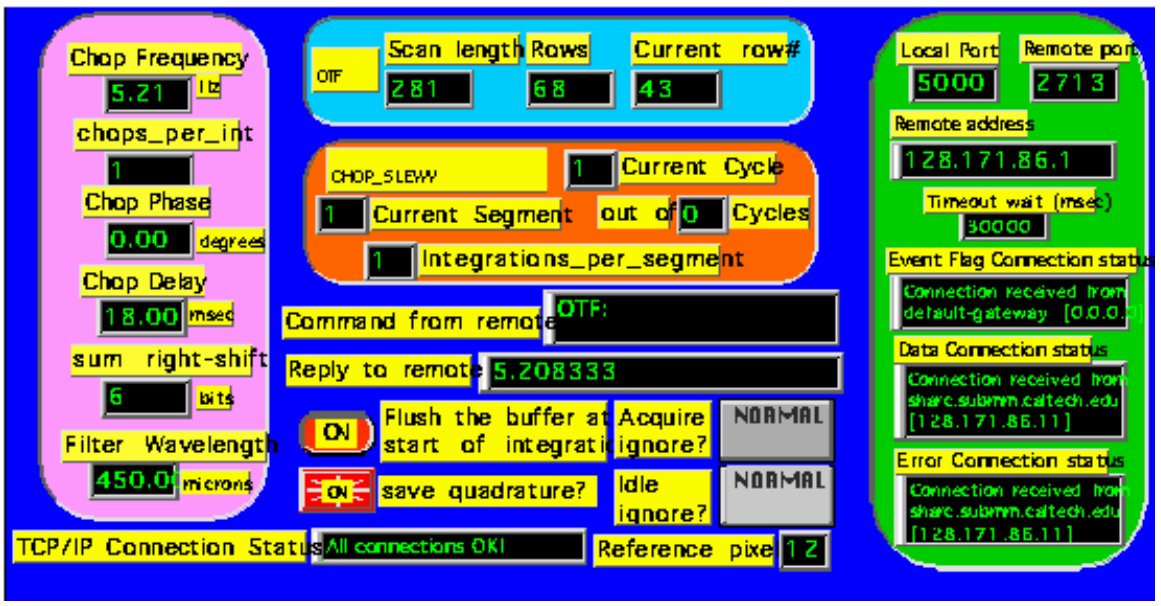

Figure 2.10: A sample of the SHARC Server display on the Macintosh Quadra at CSO. (The font overruns in this image are an artifact of the screen dump process.)

(TGV, Inc. 1992). To initialize observing with the bolometer array, the server VI must be started within Labview on the Macintosh, which is configured as a Startup item upon reboot of the system. After initializing the display panel on the Macintosh (shown in Fig. 2.10), the server sits and waits for a connection to be made on the TCP/IP port 5000 of the Macintosh. Sometime later, the observer issues the SHARC command in the UIP, which spawns a client program called SHARC_CLIENT, written in VAX C. The client program creates two VMS mailboxes called TO_SHARC and FROM_SHARC which are used to transfer commands to and receive responses from the Macintosh (the server). The client also assigns a communications channel to a socket to be used for TCP/IP communication to the remote Macintosh and initiates a connection to port 5000 on the Macintosh. When the server receives this connection request it opens the connection and returns a prompt character (>) which the client perceives as the "Connection OK" response. The client then enters a permanent loop waiting for a message to appear in the TO_SHARC mailbox (as will occur when SHARC-related commands are issued in the UIP). When a message appears, it searches for the termination character (~) and relays the message as a string to the Macintosh over TCP/IP, then waits for a return string message(s). When the

client receives the prompt symbol (>) it stops waiting for further messages from the Macintosh and instead waits for or acts upon the subsequent mailbox message from other UIP commands.

Once the client has connected to the server, the Mac initiates three more TCP connections to the VAX: one for error messages (through port 5001 on both machines), event flags (port 5002), and data (port 5003). Multinet is configured on the VAX so that when the Mac sends a connection request to these ports, the appropriate server program will be initiated on the VAX. The connection to port 5001 starts the program SHARC_EVENT_FLAG_SERVER, port 5002 starts the SHARC_ERROR_SERVER, and port 5003 starts the SHARC_SCAN_WRITER. All error conditions on the Mac are sent to the error server process on the VAX and appear as messages on the UIP operator's terminal. The event flag channel is used to clear the backend wait (BEWAIT) status on UIP observing commands when the Mac has gathered the appropriate number of data. Finally, data are sent to the scan writer process along with some header variables when appropriate.

2.4.4 Data display on the Macintosh

The two main data acquisition modes for bolometer observing at CSO are the scanning mode (known as OTF_MAP) and the pointed observation mode (known as CHOP_SLEWY). Both modes involve the use of the CSO's chopping secondary.

2.4.4.1 OTF_MAP

The term OTF_MAP ("on-the-fly" mapping) refers to the observing mode in which the antenna computer directs the telescope to scan across the source at a constant rate, usually in azimuth at a rate of a few arcseconds per second, while data is gathered "on-the-fly". Because rapid sampling of the lock-in signal allows for the best possible sky noise subtraction, we sample after each chop period of the secondary mirror which is the maximum rate possible. This method allows extended maps to be constructed more rapidly than with a series of pointed observations. The raw signal is sampled

by the A/D system at 1 kHz and sent to the DSP via a fiber optic link. Performing digital lock-in detection, the DSP demodulates the data with a sine wave template function and reports a signal level at the chopping rate. The demodulated bolometer signals are displayed in real time on the Macintosh in the form of 24 separate strip chart graphs (see Fig. 2.11). The basic display is modeled on the "Display Data" module written by Kevin Boyce of GSFC. As integrations are obtained they are sent back to the VAX over Ethernet in real time. The data are accumulated at the socket on the VAX and written to disk all at once at the end of each row of the map. This strategy has the advantage of requiring only a single open and close of the data file for each OTF_MAP row. The data consist of 4 byte integers in DSP units. The data header of each scan contains the scale factor for the proper conversion from DSP units to millivolts. The conversion from DSP units to actual voltage (post-amplification) is:

$$V(\text{volts}) = \left(\frac{\text{DSP units}}{32 \times 10^6}\right)\left(\frac{f}{c}\right)\left(\frac{750}{T}\right)2^{s-6} \tag{2.21}$$

where f is the chopping frequency in Hz, c is the number of chop cycles per integration (usually 1), T is the unitless amplitude of the sine wave template (defaults to 750), and s is the right shift (in bits) applied to the data by the DSP (defaults to 6). The chopping frequency is generated on the DSP board in the Macintosh in the form of a 0 to 5 volt square wave and can take on quantized values satisfying the equation:

$$f(\text{Hz}) = \frac{1000}{n} \text{ where } 2 \leq n \leq 512. \tag{2.22}$$

The chopper throw is determined by the amplification and offset applied to the square wave signal by the chopping secondary control circuitry built by Martin Houde at CSO. Currently, the throw must be tuned manually. However, a simple closed-loop circuit has been designed and is being built that will interface with the I/O board in the Macintosh to enable it to automatically set and monitor the chopper throw (via the standard UIP command SECONDARY on the VAX).

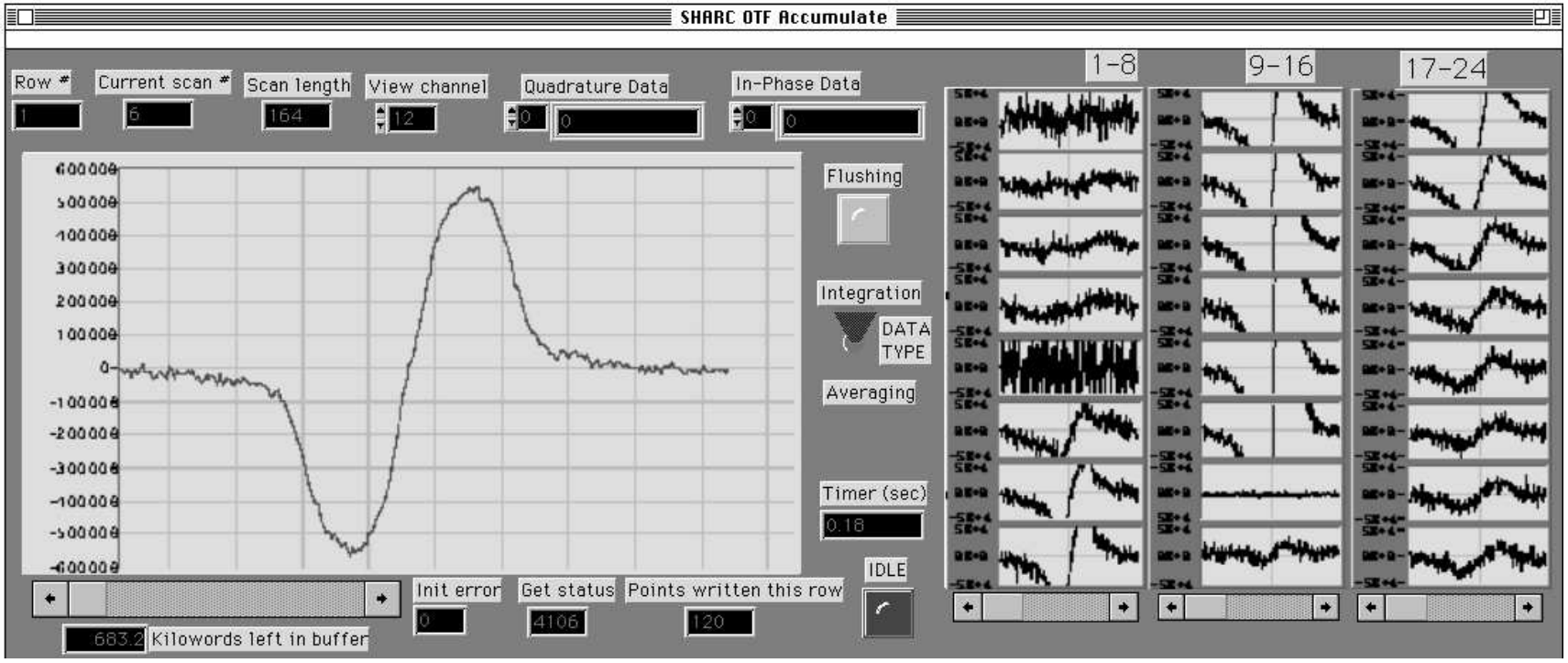

Figure 2.11: This scan of Jupiter is a sample of the SHARC OTF mapping display on the Macintosh Quadra at CSO. The large sweep auto-scales with the signal from the reference pixel while the grid of 24 sweeps shows the signals from the entire array on the same scale. The graphical layout of the display was originally conceived by Kevin Boyce at NASA Goddard.

2.4.4.2 CHOP_SLEWY

The term CHOP_SLEWY refers to the standard pointed observation combining two motions: constantly chopping the secondary mirror (at a few Hz) while frequently nodding the telescope (every few seconds) to move the target source between the positive and negative beams and provide better subtraction of atmospheric fluctuations and beam asymmetries. As in OTF_MAP mode, the demodulated bolometer signals are displayed on the Macintosh as strip charts. Upon the completion of each nodding segment, data are sent to the VAXStation which immediately appends it to the current file. At the conclusion of the specified number of chopping cycles, the average and RMS value of the data in each channel are written to the file after the scan data. Since the multiplex advantage of a (continuum) linear array is best exploited in mapping mode, the pointed observing mode of SHARC was not fully-commissioned until August 1996. It is expected to be used more in the future for deep integrations on point sources.

2.5 Data reduction

Since all demodulated SHARC data are stored on the VAX, it is most convenient for this machine to run the data reduction software. Using the NOD-2 dual beam restoration algorithm (Haslam 1974; Emerson, Klein & Haslam 1979), Darek Lis has written an OTF data reduction program called CAMERA. The program interactively proceeds through the various steps of data reduction: 1) pixel-to-pixel gain calibration, 2) automatic or manual de-spiking, 3) de-striping, 4) constant offset or linear baseline removal, 5) airmass correction, 6) dual beam restoration, 7) azimuth/elevation pointing correction, and 8) transformation to equatorial celestial coordinates. In standard mode, images of the source are created by restoring a map from each pixel of the array separately. A separate mode of the software is available for automatically analyzing pointing scans and pixel gain scans. In a separate FORTRAN program called REGRID, the restored images written by CAMERA are summed together into a regular

grid in equatorial coordinates with sigma-weighting and flux calibration applied. The output image file from REGRID is in FITS format (Wells, Greisen & Harten 1981) and can be read into a variety of software packages.

2.5.1 Pixel gain calibration

Because of small differences in the thermal properties of each pixel and in the optical efficiency across the focal plane, each pixel of the bolometer array exhibits a slightly different level of response when centered on a given source. Although the magnitude of the effect is generally less than 10% in the SHARC pixels, it is a good practice to measure and remove it from the data. The relative gains of the pixels are measured at the CSO by scanning a bright planet quickly through the array such that atmospheric changes are minimal during the scan. This is accomplished with elevation scans invoked by the UIP command OTF/SIDEWAYS. The planet is placed in the positive beam for several scans followed by the negative beam for several scans. Each scan is analyzed in the gain mode of CAMERA which writes out a file with the computed gains normalized to unity. These gains are then averaged to create the gain file named CAMERA.DAT to be subsequently used in data reduction.

2.5.2 Despiking

Cosmic ray hits and static electronic glitches are occasionally manifest in the data as temporal spikes in the scans. Spikes may appear in a single pixel or in all pixels at once. Fortunately, these spikes can be automatically identified and flagged in CAMERA by their magnitude with respect to the RMS background level. The value of the spike is replaced by the average of four values: the two adjacent integrations from that pixel and the integration from the two adjacent pixels (if they are not already flagged). An avoidance range can be specified within which spikes will not be removed by the automatic procedure. Alternatively, spikes can be flagged manually in CAMERA.

2.5.3 Destriping

After despiking, any correlated noise remaining on the array appears as stripes in the scan data along the direction of the array. On nights of unstable or windy conditions, the dominant source of correlated noise originates above the telescope. Most likely the correlation is due to cells of water vapor blowing through the two beams faster than the chopping period (~ 0.25 seconds). Removal of these stripes is a riskier process than despiking, especially when extended emission is present. For this reason, an avoidance region in the scan can be specified in CAMERA within which the data will not contribute to the calculation of the destriping correction *and* within which no destriping correction will be made. This feature enables one to ensure that the structure of specified sources will not be altered by this noise reduction algorithm.

2.5.4 Offset or baseline removal

During long scans, a drift in the signal zero level may occur. Although this effect is usually not detectable in SHARC scans, CAMERA allows the removal of a constant offset or a baseline computed from a specified number of integrations on each end of the scan. Of course, if destriping has already been invoked, no offset should remain at this point.

2.5.5 Airmass correction

Even in excellent conditions on Mauna Kea, the zenith optical depth of the atmosphere τ at 350 and 450μm is always greater than 0.5. (This optical depth τ corresponds to an emissivity $\epsilon = 0.39$ via the relation: $\epsilon = 1 - e^{-\tau}$). As a source rises and sets, the airmass $A(t)$ through which it is observed changes, causing the signal strength $S(t)$ to rise and fall significantly as a function of time t:

$$S(t) = S_0 \exp\left[-A(t)\tau\right] \text{ where } A(t) = \sec\left[\text{zenith_angle}(t)\right], \tag{2.23}$$

where S_0 is the signal that would be recorded above the atmosphere. In order to properly calibrate the continuum flux density of all the sources observed, it is essential to measure the optical depth each night, preferably on several sources observed at many different airmasses. Once the optical depth has been computed, the scans of each source can be calibrated to a fixed airmass with CAMERA before summing into a map.

2.5.6 Dual beam restoration

Once the scans are calibrated, they can be restored from a dual beam response pattern into a single beam sky intensity. This is accomplished in CAMERA with the NOD2 libraries. The raw dual beam scan is essentially a derivative of the sky intensity. The restoration process uses the edges of the scan as a zero level which is propagated across the scan (introducing some additional noise) in order to properly reconstruct the extended emission. Both before and after the restoration, the scans are written to GREG format RGDATA files named CAMERA.DUAL and CAMERA.REST.

2.5.7 Pointing correction

Occasionally it necessary and valid to correct the pointing offsets listed in the scan header. For example, if the pointing is not rechecked after a change in reference pixel, the operator may have erred in the sign of the change to the fixed zenith angle offset of the telescope. Or, a thermal pointing shift of the telescope may have occurred since the most recent pointing scan. Because the OTF scans are recorded in azimuth-elevation coordinates, these telescope-based pointing shifts can be corrected in data reduction after the observation. The offsets to shift the image should be specified in CAMERA as the direction you wish the image to move in azimuth and elevation.

2.5.8 Coordinate transformation

After restoration, each integration of each scan is transformed by CAMERA from azimuth-elevation coordinates to celestial equatorial coordinates using the appropriate

header information of the local sidereal time and telescope offsets. Space exists in the raw data file header for individual motor encoder readings, but these are not currently written by the antenna computer. The data are treated as if the telescope was pointed at the requested location during the scan. The transformed integrations are then output to the file CAMERA.RADEC.

2.5.9 Regridding, summing and flux calibration

Multiple maps of a given source (in the form of multiple CAMERA.RADEC files) can be summed by the program REGRID. A center position in right ascension and declination and a grid of pixels about that point must be specified. Each integration of each map is placed into the appropriate pixel and added in with sigma weighting. Each map can be given an absolute flux calibration conversion from millivolts (mV) to Jy which will be applied individually. The flux calibration changes smoothly with opacity, with larger opacities causing fewer mV per Jy. Like the optical depth, it is vital that the flux calibration be computed for each night at some consistent reference airmass (typically 1.0). In REGRID, additional pixels can be flagged in any or all maps if necessary. The pixel-to-pixel gain calibration can also be invoked at this point if it has not already been applied. The output of REGRID is a FITS image. At the CSO, smoothing and customized display of these images is achieved in the GRAPHIC package developed at the Insitut de Radio Astronomie Millimétrique (IRAM).

2.5.10 CHOP_SLEWY data reduction

A software package called the Bolometer Array Data Analysis Software has been developed by Dominic Benford to read, sum, display and calibrate data obtained in CHOP_SLEWY mode. The command line interface resembles the CLASS package developed at IRAM for heterodyne spectroscopy.

2.6 Sensitivity

Finally, this chapter concludes with a demonstration of the sensitivity achieved with SHARC at the telescope in the case of short and long integrations.

2.6.1 Short integrations

Shown in Fig. 2.12 are SHARC OTF scans taken with the same pixel (22) under stable atmospheric conditions on 27 April 1996. With calibration based on Uranus, the $NEFD$ achieved in a one second integration on blank sky adjacent to the planet is 3.8 Jy at 350μm and 2.2 Jy at 450μm. These values are about a factor of five above the most optimistic background limits computed in Eq. 2.18 and 2.19.

2.6.2 Long integrations

In order to test the camera sensitivity during long integrations, it is necessary to consider a series of data taken during constant sky conditions. The longest integration performed to date with SHARC is the CSO deep field survey for protogalaxies which contains the sum of 1,007,270 0.244-second pixel integrations. This corresponds to 4370 seconds of integration in each 10$''$ resolution element in the map. Therefore the RMS noise achieved in the final map (95 mJy at 450μm) implies an average $NEFD$ = 6.2 Jy/$\sqrt{\text{Hz}}$, However, these data are spread over a large field (3$'$) and acquired over many nights with varying weather conditions and may not represent the effective $NEFD$ for long integrations on a single position with the CHOP_SLEWY mode.

Because the CHOP_SLEWY observing mode mode was only recently commissioned, no comprehensive sensitivity measurements exist yet. However, we can construct long OTF integrations by adding together scans from different pixels over adjacent patches of sky during the same map; thereby insuring that the data are taken during similar sky conditions. For this purpose we use a map of Uranus for intrinsic calibration and use only those scans which do not pass near the planet ($> 25''$

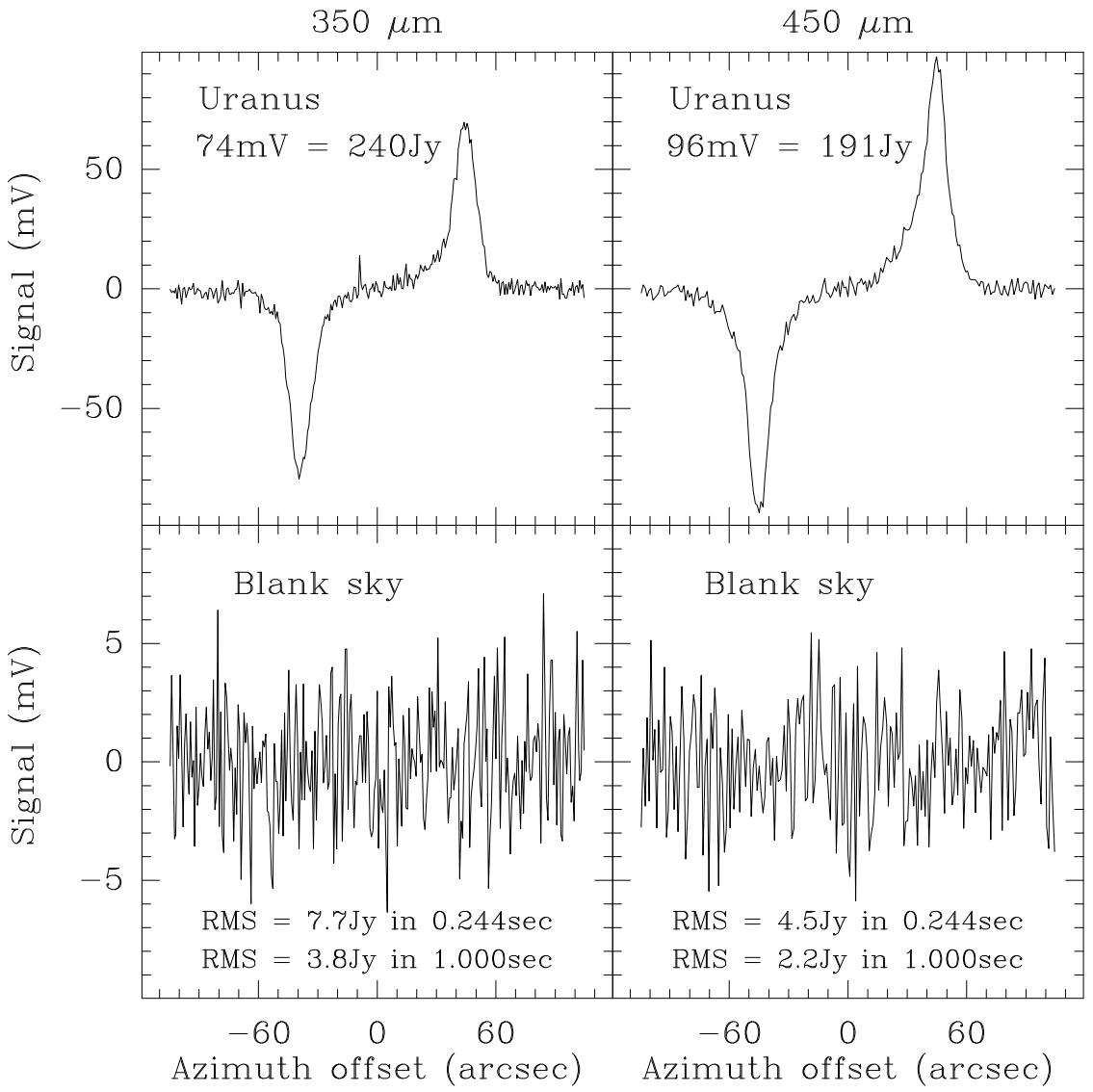

Figure 2.12: The SHARC *NEFD* measured at CSO on the night of 27 April 1996 (UT) during which the optical depth in the 450μm filter band was 0.95. The integration time along the x-axis is 0.244 seconds corresponding to one secondary mirror chop cycle at 4.09 Hz.

away). A plot of the RMS noise versus integration time on the blank sky in this map is shown in Fig. 2.13. For the timescales probed by these data, the decrease of inte-

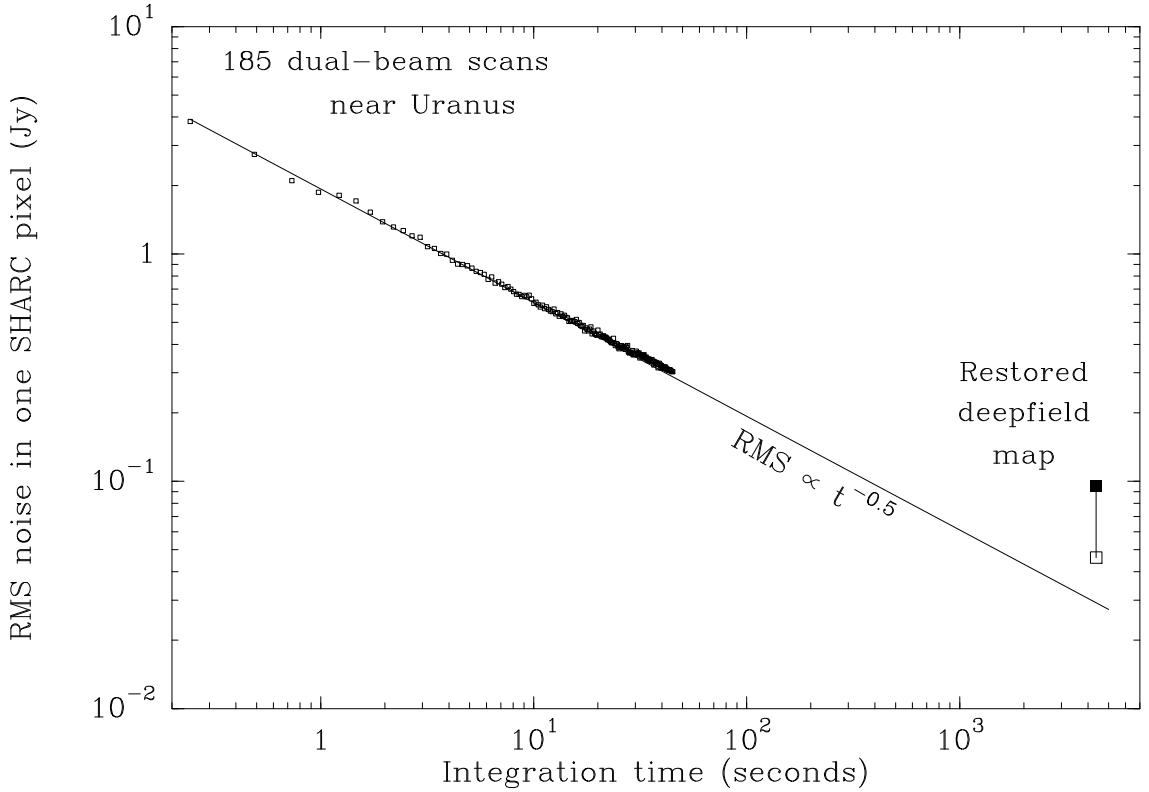

Figure 2.13: The RMS noise in a single SHARC pixel is plotted as a function of integration time at 450μm. The data at the upper left come from raw dual beam scans of Uranus taken within the same hour. The solid square at the right marks the RMS noise achieved in the final restored map of the deep field survey. The open square represents the estimated noise prior to single beam restoration.

grated noise with time closely follows the theoretical prediction. Representing a much longer integration time, the deep field point lies above the trend, partly due to added noise from the dual beam restoration process (explained further in section 2.5.6) and partly due to the fact that the data were taken during varying weather conditions.

Chapter 3 Submillimeter Continuum Images of UCHII Regions

3.1 The characteristics of interstellar dust

Over the past decade, the development of large infrared and submillimeter telescopes along with sensitive detectors has allowed astronomers to measure thermal emission from cool interstellar clouds. Composed primarily of invisible molecular hydrogen gas, these clouds can be studied only through emission from other molecules or dust. Contrary to many common spectral lines from molecular species, thermal dust emission has an optical depth of much less than one at wavelengths longer than 200μm in most interstellar clouds (Hildebrand 1983). Hence the total submillimeter continuum flux density is proportional to the number of grains present in the telescope beam. With instruments like the Submillimeter High Angular Resolution Camera (SHARC) at the CSO, the spatial distribution of dust can now be mapped at high resolution. However, the determination of the mass of dust from flux density measurements depends critically on the far-infrared emissivity of dust grains. Thus in order to quantify the physical conditions of dust in interstellar clouds it is necessary to understand the composition and shape of individual grains and how they respond to incident radiation. For this purpose, a brief review of cosmic dust grains is presented in the following subsections.

3.1.1 Dust composition

The shape and composition of interstellar dust grains have been inferred from astronomical observations and laboratory measurements of their probable constituents. A review of the observed extinction from dust at UV to FIR wavelengths is given by (Mathis 1990). The detailed composition of grains, such as the presence or absence of

ice mantles, likely varies between different types of regions. To explain the bulk of the observations, standard ingredients in dust grain models of the interstellar medium include graphite and silicate particles. One of the early and often-quoted models of dust includes a mixture of six different materials: graphite, silicon carbide (SiC), enstatite ($[Fe,Mg]SiO_3$), olivine ($[Fe,Mg]_2SiO_4$), iron and magnetite (Fe_3O_4) (Mathis, Rumpl & Nordsieck 1977, hereafter referred to as MRN). In order to calculate the extinction due to a spherical grain of a given material, one must know the complex indices of refraction at each wavelength considered. Of the six materials listed, graphite exhibits the additional complexity of anisotropic refraction. The geometry of graphite is described by two axes in the basal plane with a third axis (the c-axis) perpendicular to this plane. The refractive indices for light with the electric field (E-vector) parallel to the c-axis ($\epsilon_{\parallel}$) are different from that for light with the E-vector perpendicular to the c-axis ($\epsilon_{\perp}$) (Taft & Philipp 1965; Tosatti & Bassani 1970). Although no rigorous theory exists for computing the optical cross sections of such a material, the common approximation (as in the MRN model) is to assume that 1/3 of the grains exhibit $\epsilon_{\parallel}$ and 2/3 exhibit $\epsilon_{\perp}$. In general, the response of a grain to incident radiation is modeled with the dipole approximation, as the grain radius $a \lesssim 0.1\lambda$. (Note that this approximation likely fails in the inner parts of protostellar and protoplanetary accretion disks.) The result of the MRN model for both spherical and cylindrical grains is that of the six materials, graphite is present in all the mixtures which provide the best fit to the observed interstellar extinction in diffuse clouds from UV wavelengths to 1μm. The required distribution of grain sizes follows the power law distribution $n(a) \propto a^{-3.5}$ over the range 0.005μm to $\sim 0.25\mu$m.

3.1.2 Dust extinction in the infrared

The extinction predictions of the MRN graphite-silicate grain mixture have been computed and extended to longer wavelengths. In a comprehensive paper, Draine & Lee (1984) compiled the dielectric properties of graphite and silicate dust grains including the scattering and absorption cross sections as a function of wavelength

from $0.03 - 1000\mu$m. They find that the MRN model matches the observed near-infrared extinction of diffuse clouds with graphite grains (mostly the $\epsilon_\perp$ component) contributing a factor of several more extinction than the silicate grains. At longer wavelengths ($8 - 50\mu$m), silicate grains dominate the extinction, particularly in the 9.7 and 18μm bands in which absorption features have been confirmed observationally (Dyck & Simon 1977). By 70μm, extinction due to graphite grains (mostly the $\epsilon_\parallel$ component) again exceeds silicate grains. Draine & Lee (1984) predict the 100μm thermal emission from the MRN mixture and show that it matches the IRAS flux density observed toward clouds of infrared cirrus (Low 1984). Thus the MRN mixture has proved to be successful in predicting dust extinction and thermal emission across the infrared range.

3.1.3 Dust extinction in the submillimeter

At submillimeter wavelengths, the extinction from both graphite and silicate grains increases as a power-law with frequency (ν),

$$\frac{\tau_{ext}}{N_{\mathrm{H_2}}} \propto \nu^{\beta}, \tag{3.1}$$

where $N_{\mathrm{H_2}}$ is the column density of molecular hydrogen gas. In the model of Mathis, Mezger & Panagia (1983), graphite grains exhibit $\beta = 1.9$, silicate grains exhibit $\beta = 2.3$, and a mixture of the two yields $\beta = 2.25$. Draine & Lee (1984) predict $\beta = 1.9$ for both species. Recent laboratory measurements of millimeter-wave absorption in silicate grains yield values of β between 1.5 and 2.5 (Agladze et al. 1996). The essential reason for this steep drop in extinction is that as the wavelength becomes much larger than the radius, the dust grain becomes a poor radiator. Purcell (1969) notes the correspondence of this effect to the difficulty of constructing an efficient broad-band long-wavelength radio antenna of small size. The absorption efficiency Q of a grain is defined as the ratio of the absorption cross section σ_{abs} to the projected

geometric area:

$$Q \equiv \frac{\sigma_{\rm abs}}{\pi a^2}. \tag{3.2}$$

Often, $\sigma_{\rm abs}$ is re-written in terms of a mass opacity coefficient κ and the grain mass density ρ assuming spherical grains:

$$Q = \frac{m_{\rm grain}\kappa}{\pi a^2} = \frac{\frac{4}{3}\pi a^3 \rho \kappa}{\pi a^2} = \frac{4}{3} a \rho \kappa. \tag{3.3}$$

A simple derivation of the expected power law drop-off of the absorption efficiency of a grain is given by Knacke & Thomson (1973) and Wright (1982) using formulae from van de Hulst (1957) for small ellipsoids. In this derivation, Q can be approximated by the expansion:

$$Q = -4\chi {\rm Im}\left(\frac{\epsilon - 1}{\epsilon + 2}\right) - \frac{4}{15}\chi^3 {\rm Im}\left[\left(\frac{\epsilon - 1}{\epsilon + 2}\right)^2 \left(\frac{\epsilon^2 + 27\epsilon + 38}{2\epsilon + 3}\right)\right] + \frac{8\chi^4}{3} {\rm Re}\left(\frac{\epsilon - 1}{\epsilon + 2}\right)^2 \tag{3.4}$$

where $\chi = 2\pi a\nu/c, a$ is the particle radius, ϵ is the complex index of refraction, and ν is the frequency. The first term represents the Rayleigh absorption cross section which dominates in the low frequency limit. In a dissipative model of atomic oscillators where the restoring force is proportional to velocity, the imaginary part of the dielectric constant is proportional to ν. With another factor of ν coming from χ, the emissivity Q is then proportional to ν^2 (Andriesse 1974). This relation can be expected to hold for frequencies lower than the structural resonant frequencies of the grains which are generally above 3000 GHz (Gezari, Joyce & Simon 1973). Measurements of the emissivity of interstellar grains as a function of frequency should be compared to the expected value of $\beta = 2$ derived here.

3.1.4 Measurements of dust emissivity in the submillimeter

Despite the expected value of $\beta = 2$, measurements of β at submillimeter wavelengths exhibit a broad range from ~ 1 to over 3 (Helou 1989). Why is there such a variation?

One explanation for objects with low values of β is that the emission comes from very fine grains in which surface vibration modes dominate the bulk vibration modes, leading to $\beta = 1$ (Seki & Yamamoto 1980). Laboratory measurements confirm this result for grains of olivine, obsidian and fused quartz with $a \lesssim 0.01\mu$m (Koike, Hasegawa & Hattori 1987). A possible explanation for the values of $\beta > 2$ is the presence of ice on grains. The absorptivity of ice has been measured from 2.5 to 330μm (Bertie, Labbé & Whalley 1969). At the longest wavelengths, from about 160 to 330μm, the absorptivity scales as ν^4, much steeper than the expected value of 2. This dependence is predicted by a theory of light absorption by the vibrational modes of the crystal in which the density of states and the vibration intensity are both proportional to ν^2 (Whalley & Labbé 1969).

The relevance of ice to dust grains was established by the detection in dense clouds of absorption features at 3.08 (Soifer, Russell & Merrill 1976), 4.67, 6.0 & 6.85μm in combination with the silicate band at 9.7μm. These lines have been attributed to ice in the form of a mantle surrounding the silicate core of a grain (Tielens 1989). Calculations on olivine, quartz and lunar rocks by Aannestad (1975) show that the presence of ice mantles of radii $\gtrsim 1.5a_{\rm core}$ on grains of these materials steepen β to values of 2.9 to 3.5. For this reason, ice mantles have been invoked to explain measurements of $\beta > 2$ at millimeter wavelengths (Schwartz 1982). The presence of ice is likely to be augmented on colder grains and there is some evidence that β is inversely correlated with dust temperature in dust clouds around HII regions (Gordon 1988). A good overview of the optical constants and opacity of ice, organic, metallic and composite grains compiled by Pollack et al. (1994) shows that the expected value of β varies significantly with the grain material. Thus, the large variation in observed values of β may be real and may reveal the underlying composition and physical condition of the grains. Also, fractal models of dust grains suggest that the long wavelength absorption of grains depends strongly on their shape and aspect ratio (Wright 1987). Further accurate measurements of β in the submillimeter range (such as the data presented in this thesis) are necessary to explore these possibilities.

3.2 Computation of dust column density and mass from submillimeter flux density

The general result of the dust models discussed in the previous section is that the emissivity of the grains decreases with decreasing frequency, causing them to emit a modified Planck spectrum. With this information, the flux density F_ν at frequency ν from a optically-thin cloud of N dust grains at uniform temperature T_d with a geometric cross sectional area σ can be immediately written (Hildebrand 1983) as follows:

$$F_\nu = \frac{N\sigma Q_\nu B_\nu(T_d)}{D^2} = \frac{N\sigma Q_\nu}{D^2}\frac{2h\nu^3}{c^2[\exp{(h\nu/kT_d)}-1]}, \tag{3.5}$$

where D is the distance to the source. As seen in Eq. 3.4, $Q_\nu \propto a$ and thus $F_\nu \propto \sigma a \propto v_{grain}$, the volume of a single grain. As mentioned in section 3.1.1, a distribution of dust grain radii $n(a) \propto a^{-3.5}$ is present in an interstellar cloud. Truncating this distribution at $a_l = 0.01\mu$m and $a_u = 0.25\mu$m, the dust model of Mathis, Mezger & Panagia (1983) finds good agreement with the observed interstellar extinction A_V at optical and infrared wavelengths. One can compute a flux density-weighted mean grain radius $\bar{a}$ over this size distribution:

$$\bar{a} = \frac{\int_{a_l}^{a_u} an(a)a^3da}{\int_{a_l}^{a_u} n(a)a^3da} = \frac{\int_{a_l}^{a_u} aa^{-3.5}a^3da}{\int_{a_l}^{a_u} a^{-3.5}a^3da} \tag{3.6}$$

$$= \frac{\int_{a_l}^{a_u} a^{0.5}da}{\int_{a_l}^{a_u} a^{-0.5}da} = \frac{1}{3}\left(\frac{a_u^{1.5}-a_l^{1.5}}{a_u^{0.5}-a_l^{0.5}}\right) \tag{3.7}$$

$$= 0.103\ \mu\text{m for } a_u = 0.25\mu\text{m and } a_l = 0.01\mu\text{m}. \tag{3.8}$$

A contour plot of $\bar{a}$ as a function of a_l and a_u is included in Fig. 3.1.

The value of $\bar{a}$ can be used as an effective grain radius in the formula for flux density. Essentially, a cloud of N identical grains of radius $\bar{a}$ would emit the same flux density as N grains having the specified power-law distribution of radii. Assuming spherical grains, one can then compute the total flux density-weighted volume of dust

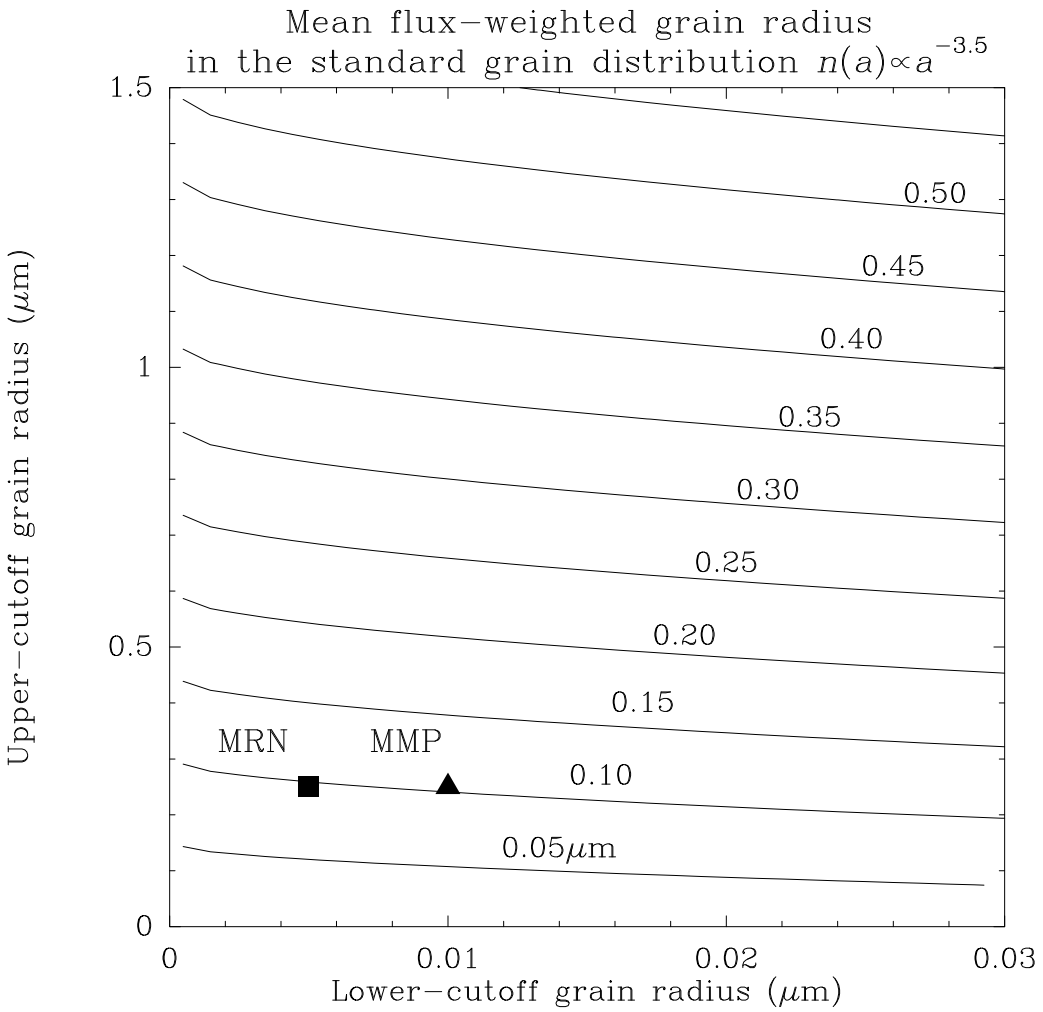

Figure 3.1: Mean flux density-weighted grain radius for the $n(a) \propto a^{-3.5}$ grain distribution as a function of the lower-cutoff radius a_l and the upper-cutoff radius a_u. The points labelled MRN and MMP correspond to the models of Mathis, Rumpl & Nordsieck (1977) and Mathis, Mezger & Panagia (1983), respectively.

in the cloud

$$V = N v_{grain} = 4N\pi\bar{a}^3/3. \tag{3.9}$$

This relation can be used to eliminate N from Eq. 3.5 and arrive with

$$V = \frac{M_d}{\rho} = \frac{4\pi\bar{a}^3/3}{\pi\bar{a}^2}\frac{F_\nu D^2}{B_\nu(T_d)Q_\nu}, \tag{3.10}$$

where ρ is the grain mass density. The total mass of a cloud with flux density F_ν becomes

$$M_d = \frac{4\bar{a}\rho}{3}\frac{F_\nu D^2}{B_\nu(T_d)Q_\nu}, \tag{3.11}$$

$$M_{\rm H_2} = \frac{4R\bar{a}\rho}{3}\frac{F_\nu D^2}{B_\nu(T_d)Q_\nu}, \tag{3.12}$$

$$= \frac{1.3\times10^4}{Q_\nu J_\nu(T_d)}\left(\frac{\bar{a}}{0.1\mu m}\right)\left(\frac{\rho}{3\ \mathrm{g\ cm^{-3}}}\right)\left(\frac{R}{100}\right)\left(\frac{F_\nu}{\mathrm{Jy}}\right)\left(\frac{D}{\mathrm{kpc}}\right)^2\left(\frac{\nu}{\mathrm{GHz}}\right)^{-3} M_\odot, \tag{3.13}$$

where R is an empirically-determined gas to dust mass ratio and $J_\nu \equiv [\exp(h\nu/kT_d)-1]^{-1}$. Using the telescope beam size Ω, this equation can be rewritten in terms of the gas column density

$$N_{\rm H_2} = \frac{M_{\rm H_2}}{m_{\rm H_2}\Omega D^2} \tag{3.14}$$

$$= \frac{8.1\times10^{17}}{Q_\nu J_\nu(T_d)\Omega}\left(\frac{\bar{a}}{0.1\mu m}\right)\left(\frac{\rho}{3\ \mathrm{g\ cm^{-3}}}\right)\left(\frac{R}{100}\right)\left(\frac{F_\nu}{\mathrm{Jy}}\right)\left(\frac{\nu}{\mathrm{GHz}}\right)^{-3} \mathrm{cm^{-2}}. \tag{3.15}$$

By applying the following empirical expression for Q_ν valid at submillimeter and longer wavelengths (Hildebrand 1983),

$$Q_\nu = 7.5\times10^{-4}\left(\frac{\nu}{2.4\ \mathrm{THz}}\right)^\beta \tag{3.16}$$

the formulas for column density and mass become:

$$N_{\mathrm{H_2}} = \frac{7.8 \times 10^{10}}{J_\nu(T_d)\Omega}\left(\frac{\bar{a}}{0.1\mu m}\right)\left(\frac{\rho}{3\ \mathrm{g\ cm^{-3}}}\right)\left(\frac{R}{100}\right)\left(\frac{F_\nu}{\mathrm{Jy}}\right)\left(\frac{\nu}{2.4\ \mathrm{THz}}\right)^{-3-\beta}\ \mathrm{cm^{-2}}, \tag{3.17}$$

$$M_{\mathrm{H_2}} = \frac{1.3 \times 10^{-3}}{J_\nu(T_d)}\left(\frac{\bar{a}}{0.1\mu m}\right)\left(\frac{\rho}{3\ \mathrm{g\ cm^{-3}}}\right)\left(\frac{R}{100}\right)\left(\frac{F_\nu}{\mathrm{Jy}}\right)\left(\frac{D}{\mathrm{kpc}}\right)^2\left(\frac{\nu}{2.4\ \mathrm{THz}}\right)^{-3-\beta} M_\odot. \tag{3.18}$$

In reality, a distribution of dust temperatures will be present in a star-forming cloud with the warmest grains lying near the young embedded stars and coolest grains lying in the outer parts of the cloud (in the absence of external heating sources). For this reason, we cannot expect to be able to fit the entire infrared through submillimeter spectrum with a modified Planck function of a single temperature. Multi-temperature models have been constructed to fit the continuum spectra of star-forming dust cores (Hobson & Padman 1994; Xie et al. 1993; Gürtler et al. 1991; Pajot et al. 1986). These models include a component of small, warm grains ($T \sim 200$K) which significantly increase the emission in the 12 and 25μm bands of IRAS. As discussed later in section 3.10.4, radiative transfer models indicate a smooth distribution of temperature with cloud radius (Goldreich & Kwan 1974; Scoville & Kwan 1976). However, because the bulk of the luminosity from UCHII regions emerges at $\lambda > 60\mu$m, accurate estimates of the dust mass can be obtained by fitting only the cold component of dust. Measurements at 100, 350/450, 800 and 1300μm are essential to characterize this component of the spectrum. Many 1300μm flux density measurements of UCHII regions exist in the literature (e.g., Chini et al. 1986), and low resolution 100μm data are available from the IRAS database. IRAS images of UCHII regions are presented in the next section, followed by new high resolution submillimeter images in the subsequent sections.

3.3 HIRES IRAS images

In order to link the new submillimeter images presented in this thesis to the far-infrared, analysis of the IRAS database was undertaken. With the ultimate goal of spatially resolving the dust surrounding UCHII regions, I conducted a HIRES survey of 75 fields surrounding the UCHII regions in the Wood & Churchwell survey along with others from the literature. A NASA Astrophysics Data Program (ADP) grant was obtained in order to pursue the research. The HIRES algorithm employs the maximum correlation method to enhance the spatial resolution of IRAS images beyond the standard IRAS Sky Survey Atlas (ISSA) plates, which have $4'$ to $5'$ resolution, and approach the diffraction limit of the telescope (Aumann, Fowler & Melnyk 1990). The processed fields are one square degree in size with $15''$ pixels, at the wavelengths of 100, 60, 25, and 12μm. The images were analyzed using the Skyview software package developed at the NASA Infrared Processing and Analysis Center (IPAC). The effective resolution achieved by HIRES is approximately $90''$ at 100μm and $50''$ at 60μm with significant variation from field to field. Aperture photometry was performed on the 126 sources in these fields which could be identified with radio-detected UCHII regions. The list of these sources, together with their measured IRAS flux densities (within a $2'$ radius of the centroid) and blackbody color temperatures between 60 and 100μm are given in Table 3.1.

In general, the FIR emission remains unresolved at the two longest wavelengths despite the improved resolution of the HIRES maps. In a few cases, including G45.12+0.13 & G45.07+0.13, G75.84+0.40 & G75.78+0.34, and K3-50A & K3-50C, the FIR flux has been resolved between a pair of adjacent UCHII regions. This allows more accurate blackbody fits when combined with submillimeter data. However, the overall lack of real detail in the HIRES images emphasized the need for higher resolution submillimeter studies at CSO. As a sample of the HIRES results, contour plots of the sources later imaged with SHARC are included as Figs. 3.2 through 3.14. All of the maps are in presented in equatorial (B1950) coordinates.

Table 3.1: UCHII regions analyzed with HIRES processing

	Coordinates (1950.0)		IRAS flux density (Jy)				$T_{\rm col}$
Source	R.A.	Dec.	100μm	60μm	25μm	12μm	K
W3(OH)	$02^h21^m34.^s0$	$61°52'25''$	35249	26140	10792	1274	54
G133.947+1.064	$02^h23^m15.^s5$	$61°38'57''$	12569	9828	752	100	57
G138.30+1.56	$02^h57^m36.^s2$	$60°17'24''$	1376	1002	291	55	53
G139.909+0.197	$03^h03^m31.^s3$	$58°19'04''$	1441	1267	504	73	60
G206.543-16.35	$05^h39^m09.^s3$	$-01°57'40''$	30326	18085	12485	1299	49
MONR2IRS2	$06^h05^m21.^s0$	$-06°22'25''$	20652	17649	5072	634	59
G189.03+0.784	$06^h05^m40.^s8$	$21°31'28''$	2924	2097	470	145	53
G188.949+0.915	$06^h05^m52.^s6$	$21°38'58''$	1745	1233	269	78	53
G188.793+1.030	$06^h06^m06.^s6$	$21°51'13''$	1288	1141	268	77	60
G189.876+0.516	$06^h06^m21.^s8$	$20°40'05''$	2592	2063	291	128	57
I06068+2030	$06^h06^m53.^s9$	$20°30'50''$	1456	1240	208	102	59
GGD12-15	$06^h08^m24.^s1$	$-06°11'08''$	4975	3721	726	63	55
G192.584-0.041	$06^h09^m59.^s3$	$18°00'16''$	6247	4647	701	237	55
G240.31+0.07	$07^h42^m45.^s1$	$-24°00'24''$	780	613	64	2	54
NGC6334A	$17^h16^m58.^s9$	$-35°52'00''$	26543	21731	3433	694	59
NGC6334B	$17^h16^m58.^s9$	$-35°51'30''$	22187	19198	3081	765	60
NGC6334C	$17^h17^m15.^s0$	$-35°48'15''$	22783	18924	6215	1325	59
NGC6334D	$17^h17^m27.^s3$	$-35°47'30''$	21220	19089	6201	1226	62
NGC6334E	$17^h17^m33.^s5$	$-35°42'15''$	23743	19177	2798	458	57
NGC6334F	$17^h17^m33.^s5$	$-35°42'15''$	24239	20944	2786	480	60
G351.78-0.54	$17^h23^m21.^s6$	$-36°06'44''$	17607	9720	392	86	46
G1.13-0.11	$17^h45^m33.^s3$	$-28°00'29''$	9320	4396	921	223	42
G5.48-0.24	$17^h56^m00.^s0$	$-24°20'25''$	2082	1537	260	47	53
AFGL 5425	$17^h56^m52.^s9$	$-23°45'12''$	1950	1766	269	38	62
G5.89-0.39	$17^h57^m27.^s8$	$-24°03'57''$	21735	15872	2664	330	53
G6.55-0.01	$17^h57^m46.^s4$	$-23°20'26''$	3604	2581	276	59	53
AFGL 5176S	$17^h58^m53.^s2$	$-23°58'41''$	3146	2430	275	112	55

Source	Coordinates (1950.0) R.A.	Dec.	IRAS flux density (Jy) 100μm	60μm	25μm	12μm	$T_{\rm col}$ K
G7.47+0.06	$17^h59^m11.^s9$	-22°28′02″	3339	1499	227	108	42
G8.14+0.23	$18^h00^m00.^s2$	-21°48′15″	6451	5137	957	171	57
G5.97-1.18	$18^h00^m37.^s6$	-24°22′36″	10135	15407	5470	808	102
G9.62+0.19	$18^h03^m15.^s9$	-20°31′52″	7617	4620	403	63	48
G8.67-0.36	$18^h03^m18.^s6$	-21°37′43″	5122	2338	198	33	42
I18035-2126	$18^h03^m36.^s9$	-21°26′13″	916	730	79	30	57
G10.47+0.03	$18^h05^m41.^s1$	-19°52′26″	9895	4754	190	36	42
G10.30-0.15	$18^h06^m00.^s2$	-20°06′11″	11251	11119	2742	402	66
G10.15-0.34	$18^h06^m25.^s7$	-20°19′56″	26177	22250	6109	1013	59
G9.876-0.750	$18^h07^m21.^s4$	-20°45′52″	3541	1898	134	134	46
G10.62-0.38	$18^h07^m30.^s6$	-19°56′25″	21222	13024	582	83	48
G11.110-0.399	$18^h08^m34.^s4$	-19°31′23″	3327	1443	271	105	41
I18089-1837	$18^h08^m57.^s3$	-18°36′56″	1785	1545	283	57	60
G12.21-0.10	$18^h09^m45.^s8$	-18°25′26″	5125	3199	236	41	50
G12.68-0.18	$18^h11^m00.^s2$	-18°01′49″	6542	3382	302	56	44
G11.95-0.03	$18^h11^m04.^s0$	-18°54′25″	4275	2399	274	10	46
G13.19+0.04	$18^h11^m10.^s6$	-17°29′19″	4417	3625	667	152	59
G12.81-0.20	$18^h11^m18.^s0$	-17°56′19″	31018	22339	3166	329	53
G13.87+0.28	$18^h11^m42.^s5$	-16°46′30″	5657	4402	753	141	55
G12.91-0.26	$18^h11^m44.^s3$	-17°53′03″	6425	3569	331	29	46
G13.21-0.15	$18^h11^m54.^s7$	-17°33′33″	2518	1134	84	14	42
I18134-1652	$18^h13^m26.^s9$	-16°51′31″	4795	4140	648	175	60
G10.841-2.592	$18^h16^m13.^s0$	-20°48′48″	3802	3305	533	116	60
G15.04-0.68	$18^h17^m26.^s7$	-16°14′46″	19560	23149	4451	835	77
G16.94-0.07	$18^h19^m05.^s8$	-14°14′51″	2633	1149	207	109	41
G18.146-0.284	$18^h22^m13.^s3$	-13°17′34″	9859	9779	1798	390	66
G18.302-0.391	$18^h22^m52.^s3$	-13°12′04″	3355	2270	440	53	51
G19.491+0.135	$18^h23^m14.^s3$	-11°54′23″	2556	1465	158	36	46

	Coordinates (1950.0)		IRAS flux density (Jy)				$T_{\rm col}$
Source	R.A.	Dec.	100μm	60μm	25μm	12μm	K
G19.07-0.27	$18^h23^m58.^s9$	-12°28′07″	5785	4486	521	105	55
G19.61-0.23	$18^h25^m04.^s6$	-11°54′09″	1025	498	30	12	42
G20.08-0.14	$18^h26^m12.^s9$	-11°26′08″	507	310	21	12	48
G20.99+0.09	$18^h26^m17.^s9$	-10°36′09″	1645	1237	130	31	55
G23.70+0.17	$18^h31^m08.^s7$	-08°09′39″	2841	2101	354	58	55
G24.47+0.49	$18^h31^m28.^s4$	-07°20′21″	7218	6052	1231	296	59
G25.650+1.050	$18^h31^m39.^s2$	-06°02′06″	2696	1097	220	82	41
G23.96+0.15	$18^h31^m42.^s1$	-07°57′09″	4053	3550	670	89	60
G23.43-0.21	$18^h32^m03.^s3$	-08°35′39″	9680	6022	572	130	50
G23.87-0.12	$18^h32^m30.^s6$	-08°09′09″	1922	1574	139	39	59
I18328-0735	$18^h32^m50.^s0$	-07°35′51″	3848	2358	183	48	48
I18341-0727	$18^h34^m09.^s7$	-07°27′21″	5297	3202	304	71	48
G25.72+0.05	$18^h35^m22.^s0$	-06°27′11″	4211	3006	367	78	53
G25.38-0.18	$18^h35^m29.^s1$	-06°49′11″	12834	13875	3493	506	71
G26.54+0.42	$18^h35^m34.^s3$	-05°32′20″	2180	1855	336	99	59
G26.10-0.07	$18^h36^m29.^s4$	-06°09′11″	1841	1287	112	30	53
G27.28+0.15	$18^h37^m54.^s9$	-05°00′30″	1963	1037	96	22	44
G27.49+0.19	$18^h38^m08.^s9$	-04°47′45″	2542	2001	219	48	57
G28.198-0.050	$18^h40^m19.^s9$	-04°17′00″	3953	2031	199	27	44
I18406-0338	$18^h40^m38.^s0$	-03°38′30″	2872	2261	290	77	57
G28.288-0.364	$18^h41^m38.^s1$	-04°21′00″	3918	3456	977	101	60
G28.60-0.36	$18^h42^m10.^s2$	-04°04′30″	1968	1305	138	43	51
G29.96-0.02	$18^h43^m27.^s0$	-02°42′51″	12937	11832	2169	330	62
G30.53+0.02	$18^h44^m25.^s0$	-02°10′32″	1503	1404	156	25	64
G31.41+0.31	$18^h44^m58.^s5$	-01°16′08″	2013	775	50	-6	39
G30.78-0.02	$18^h45^m01.^s0$	-01°58′32″	23611	25105	5750	1073	69
G31.28+0.06	$18^h45^m37.^s5$	-01°29′38″	3638	1703	134	16	42
G32.15+0.13	$18^h46^m58.^s9$	-00°41′33″	1243	766	169	30	50

Source	Coordinates (1950.0) R.A.	Dec.	IRAS flux density (Jy) 100μm	60μm	25μm	12μm	$T_{\rm col}$ K
G31.396-0.257	$18^h46^m59.^s5$	-01°32′38″	3392	2297	311	53	51
G32.80+0.19	$18^h47^m18.^s0$	-00°22′45″	523	328	43	8	50
G33.133-0.092	$18^h49^m25.^s0$	00°11′00″	1839	1274	199	49	51
G33.91+0.11	$18^h50^m18.^s0$	00°51′45″	3165	1827	275	45	48
G34.26+0.14	$18^h50^m46.^s0$	01°11′00″	28752	18686	2291	342	50
G35.57+0.06	$18^h53^m31.^s0$	02°19′13″	3024	1397	186	87	42
G35.578-0.030	$18^h53^m52.^s0$	02°16′43″	4661	2990	323	106	50
G37.55-0.11	$18^h57^m46.^s4$	03°59′15″	3706	2288	275	92	50
G35.200-1.741	$18^h59^m14.^s1$	01°08′48″	15612	13366	2309	380	60
G37.874-0.399	$18^h59^m23.^s7$	04°08′30″	6266	4276	465	122	51
G41.52+0.04	$19^h04^m40.^s0$	07°34′15″	1585	763	132	69	42
G41.71+0.11	$19^h04^m49.^s0$	07°48′00″	1017	499	114	58	44
G42.46-0.26	$19^h07^m27.^s0$	08°14′33″	2941	1698	269	99	48
W49N	$19^h07^m49.^s6$	09°01′34″	30782	21796	3135	481	53
G43.237-0.045	$19^h08^m01.^s7$	09°01′19″	6219	3439	258	90	46
G43.795-0.127	$19^h09^m30.^s6$	09°30′40″	2761	1893	213	61	51
G43.18-0.52	$19^h09^m46.^s0$	08°47′11″	1903	1064	196	77	46
G45.12+0.13	$19^h11^m06.^s0$	10°48′30″	7603	7668	1742	350	68
G45.48+0.13	$19^h11^m46.^s8$	11°07′15″	4562	3805	472	100	59
G45.45+0.06	$19^h12^m01.^s0$	11°04′00″	8539	7188	1120	184	59
G43.89+0.14	$19^h12^m03.^s7$	09°17′26″	1873	1082	262	78	48
I19139+1113	$19^h14^m00.^s3$	11°13′59″	1102	736	71	28	51
G48.609+0.027	$19^h18^m11.^s7$	13°49′38″	6956	5330	570	154	55
G50.31+0.68	$19^h19^m11.^s0$	15°38′29″	1214	774	149	57	50
G53.605+0.046	$19^h28^m09.^s6$	18°14′04″	2594	1372	142	98	44
G54.10-0.06	$19^h29^m31.^s8$	18°36′19″	3390	1848	261	101	46
G60.884-0.128	$19^h44^m14.^s8$	24°28′20″	5855	4585	820	159	57
G61.48+0.09	$19^h44^m40.^s8$	25°05′07″	13897	13575	1841	279	66

Source	Coordinates (1950.0) R.A.	Dec.	IRAS flux density (Jy) 100μm	60μm	25μm	12μm	$T_{\rm col}$ K
K3-50A	$19^h59^m50.^s8$	$33°24'22''$	14386	14444	2391	516	68
G69.540-0.975	$20^h08^m09.^s8$	$31°22'41''$	3516	1536	105	27	41
G78.438+2.659	$20^h17^m53.^s0$	$40°47'06''$	3864	3223	765	130	59
G75.84+0.40	$20^h19^m48.^s3$	$37°21'29''$	8376	9045	2004	699	71
G75.78+0.34	$20^h19^m50.^s9$	$37°16'29''$	9418	7297	891	150	55
G76.18+0.10	$20^h22^m05.^s6$	$37°28'29''$	2143	1474	189	50	51
G76.38-0.621	$20^h25^m33.^s8$	$37°12'50''$	14281	14353	3479	496	68
G79.321+1.291	$20^h26^m20.^s2$	$40°42'15''$	4972	4743	915	193	64
G77.965-0.006	$20^h27^m47.^s3$	$38°51'16''$	4251	3702	716	150	60
G79.297+0.281	$20^h30^m42.^s8$	$40°06'04''$	11715	14800	2103	398	82
G106.80+5.31	$22^h17^m41.^s1$	$63°03'42''$	14064	12105	1641	347	60
G109.872.11	$22^h54^m17.^s8$	$61°45'50''$	22544	15473	961	27	51
G110.209+2.630	$22^h55^m07.^s3$	$62°21'40''$	4068	3157	324	148	55
NGC7538S	$23^h11^m36.^s6$	$61°11'50''$	16882	13554	2554	432	57
G111.612+0.374	$23^h13^m19.^s2$	$60°51'03''$	3724	3168	779	112	59
G111.282-0.663	$23^h13^m54.^s6$	$59°45'38''$	2977	2286	402	98	55
I23139+5939	$23^h13^m58.^s5$	$59°39'23''$	1208	624	111	45	44
Average							54

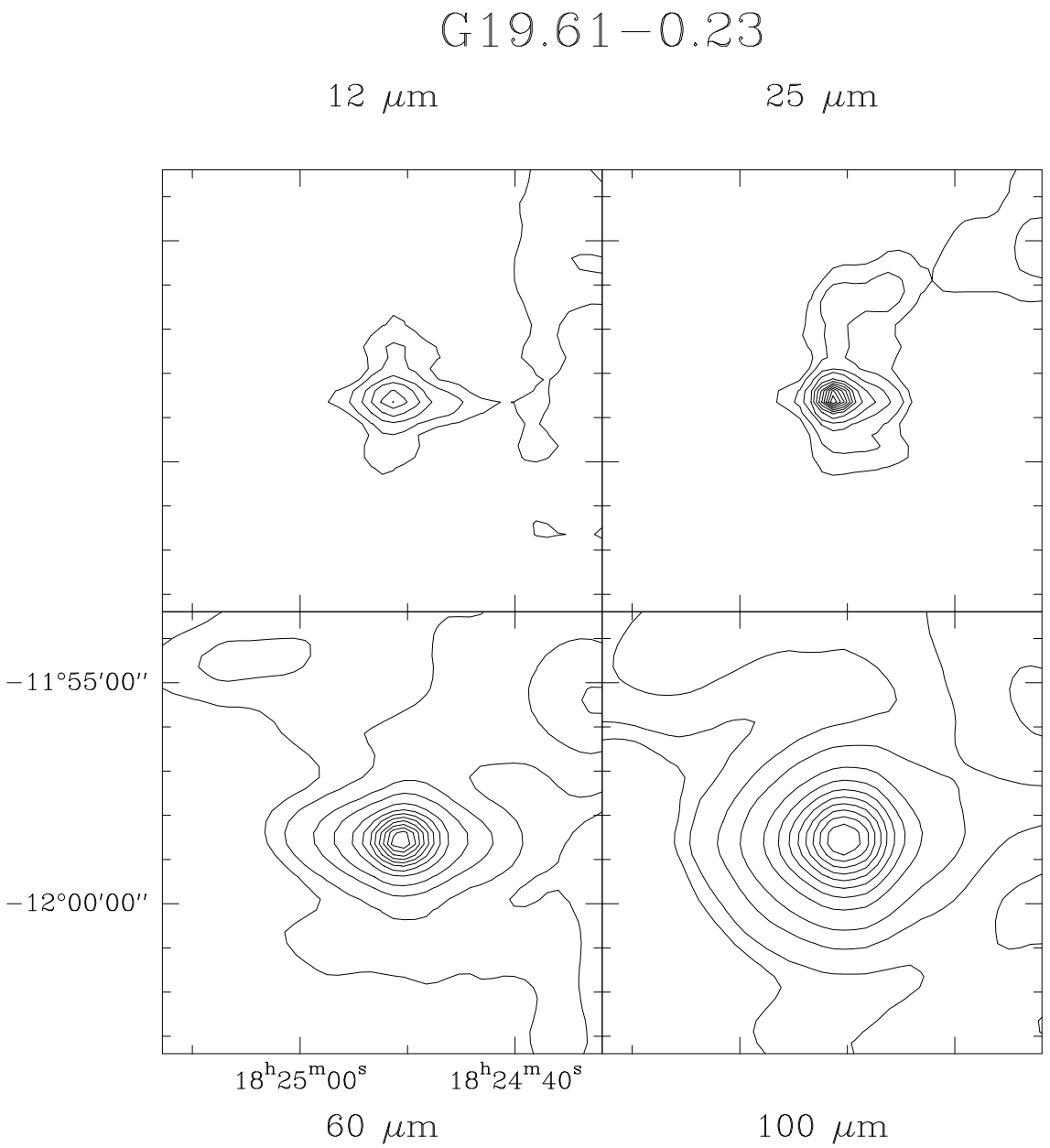

Figure 3.2: HIRES processed IRAS maps of G19.61-0.23. Contour levels are 1, 2, 5, 10 to 100 by 10% of the peak intensity in each 1° field (12μm: 4073; 25μm: 13956; 60μm: 35728.9; 100μm: 20081.9 MJy/sr).

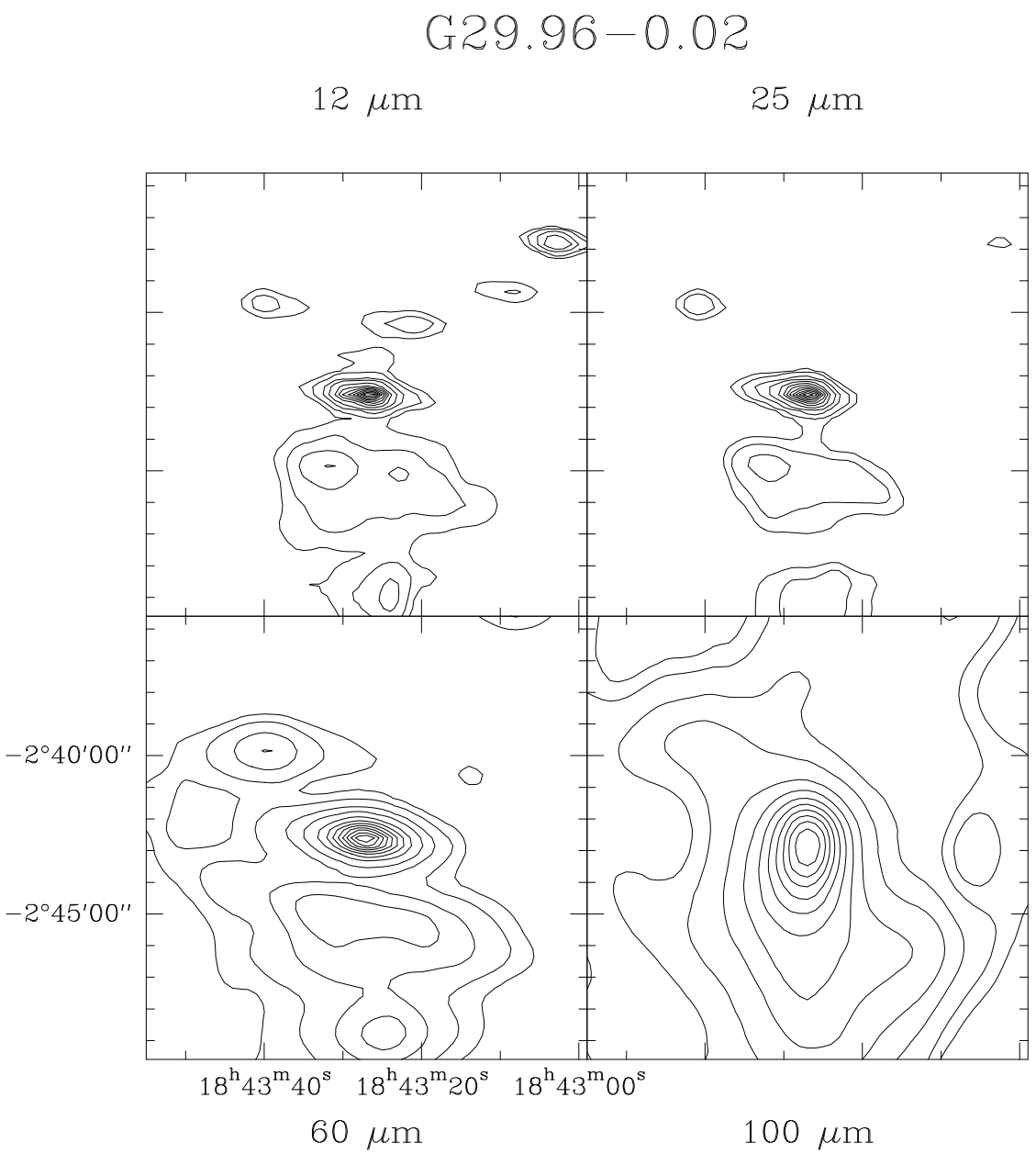

Figure 3.3: HIRES processed IRAS maps of G29.96-0.02. Contour levels are 1, 2, 5, 10 to 100 by 10% of the peak intensity in each 1° field (12μm: 5516; 25μm: 37686; 60μm: 71062; 100μm: 25276 MJy/sr).

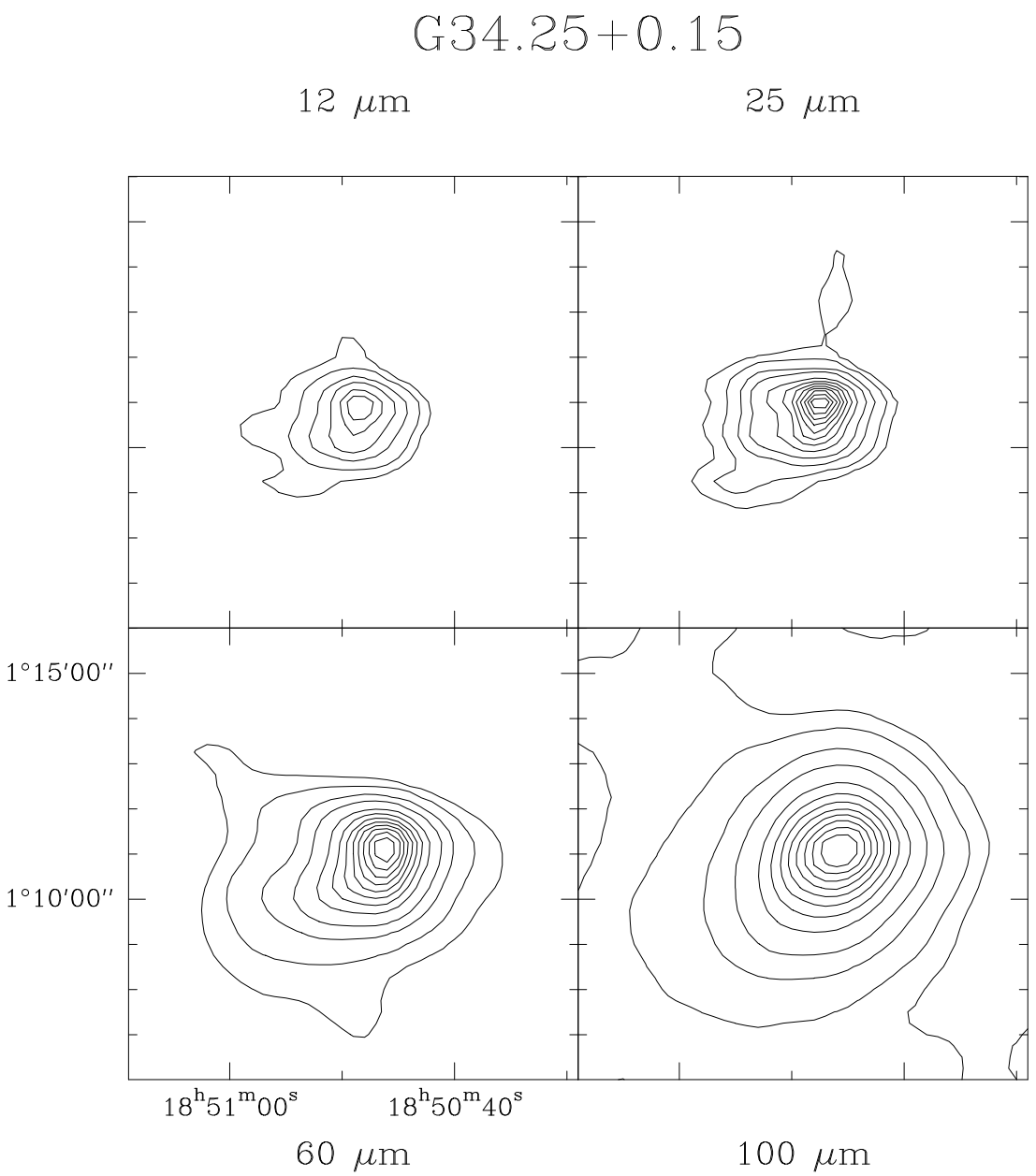

Figure 3.4: HIRES processed IRAS maps of G34.26+0.14. Contour levels are 1, 2, 5, 10 to 100 by 10% of the peak intensity in each 1° field (12μm: 7651; 25μm: 19003; 60μm: 85429; 100μm: 77272 MJy/sr).

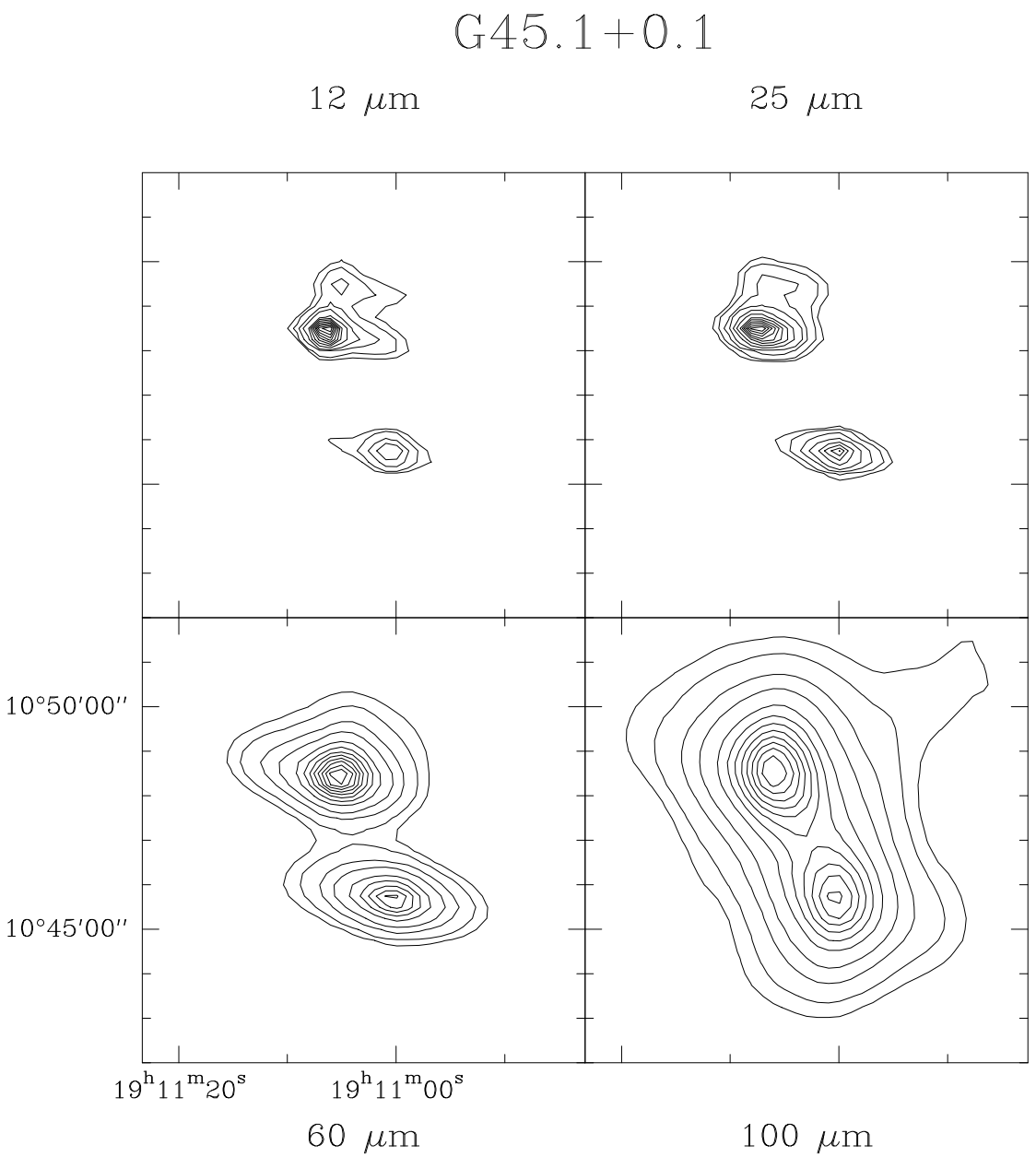

Figure 3.5: HIRES processed IRAS maps of G45.1+0.1. The two UCHII regions G45.12+0.13 and G45.07+0.13 have been resolved. Contour levels are 1, 2, 5, 10 to 100 by 10% of the peak intensity in each 1° field (12μm: 10794; 25μm: 34889; 60μm: 66149; 100μm: 24283 MJy/sr).

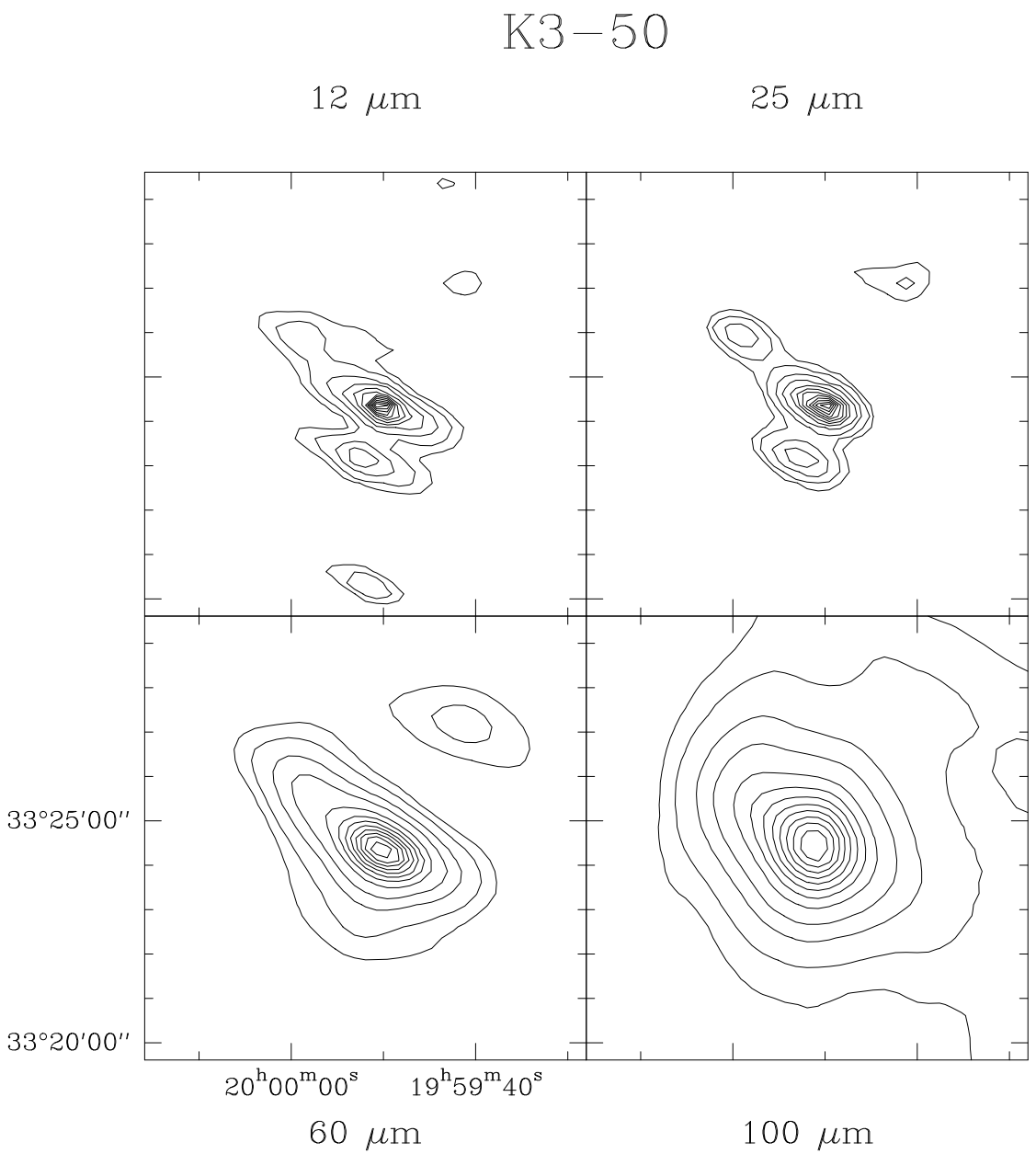

Figure 3.6: HIRES processed IRAS maps of the K3-50 complex. Radio components A, B and C have been resolved. Contour levels are 1, 2, 5, 10 to 100 by 10% of the peak intensity in each 1° field (12μm: 9769; 25μm: 43208; 60μm: 90814; 100μm: 44942 MJy/sr).

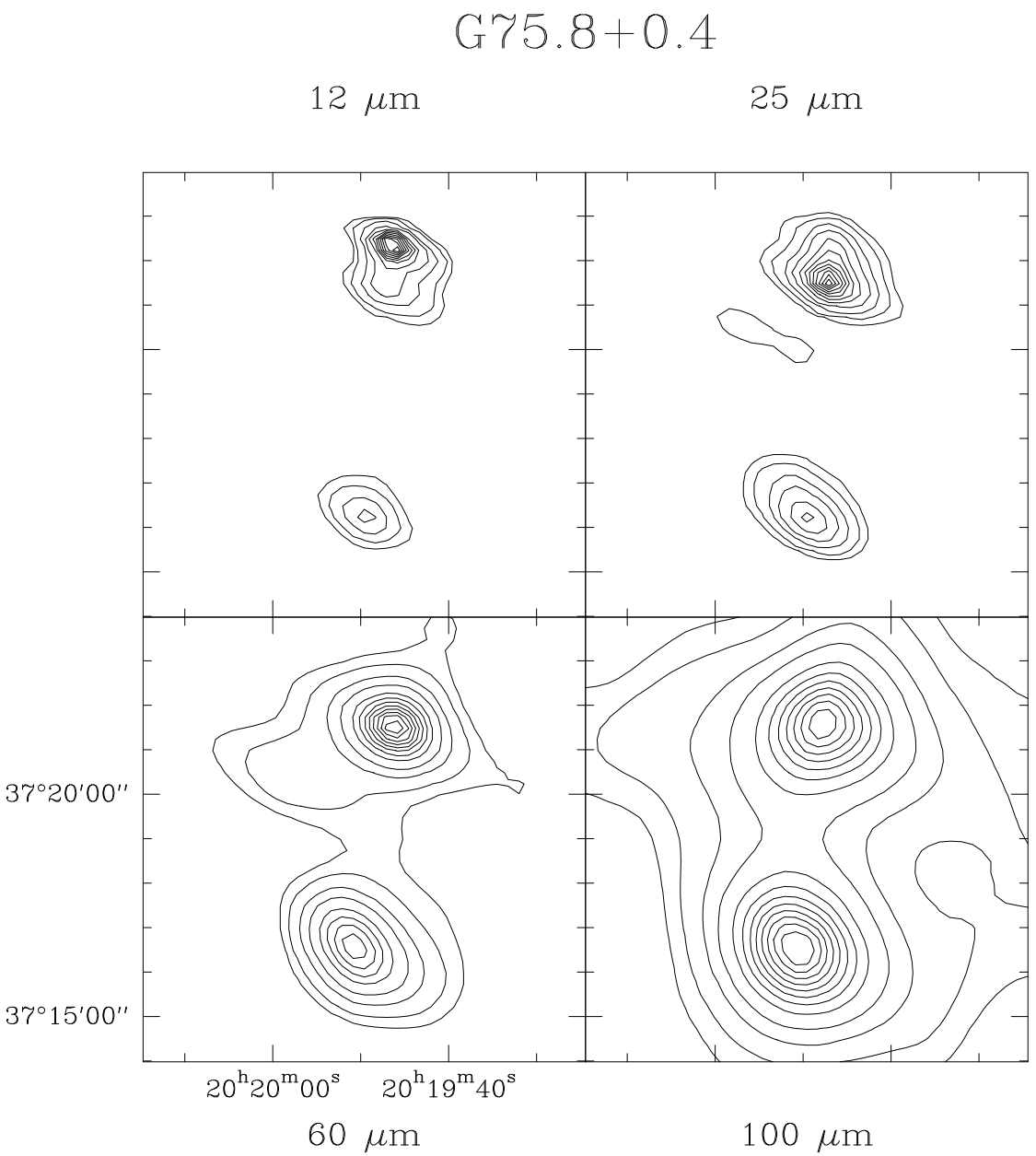

Figure 3.7: HIRES processed IRAS maps of G75.8+0.4. The two UCHII regions G75.78+0.34 and G75.84+0.40 have been resolved. Contour levels are 1, 2, 5, 10 to 100 by 10% of the peak intensity in each 1° field (12μm: 14105; 25μm: 29131; 60μm: 73016; 100μm: 27409 MJy/sr).

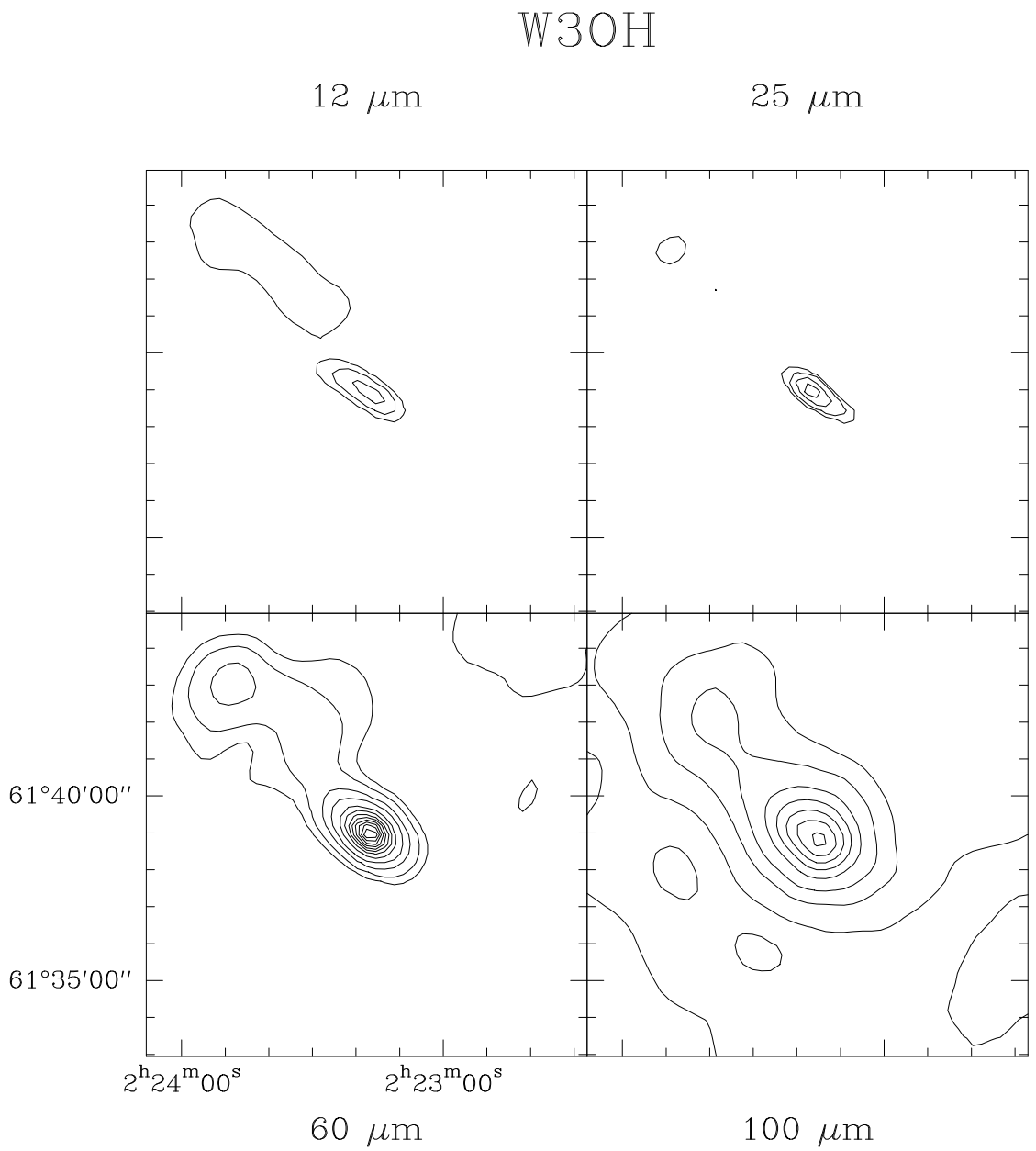

Figure 3.8: HIRES processed IRAS maps of W3(OH). Contour levels are 1, 2, 5, 10 to 100 by 10% of the peak intensity in each 1° field (12μm: 11259; 25μm: 116263; 60μm: 111077; 100μm: 59204 MJy/sr).

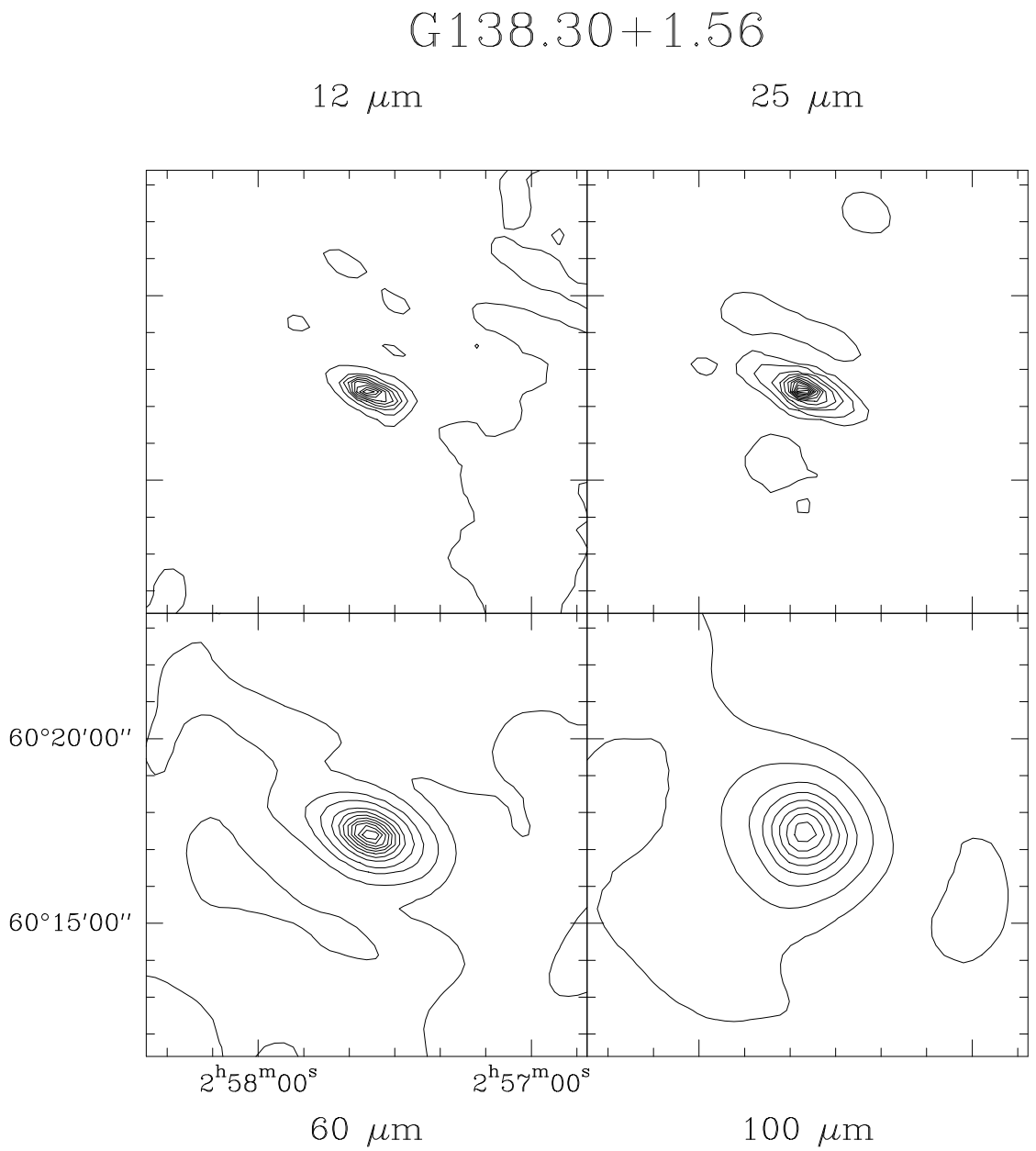

Figure 3.9: HIRES processed IRAS maps of G138.30+1.56. Contour levels are 1, 2, 5, 10 to 100 by 10% of the peak intensity in each 1° field (12μm: 465; 25μm: 6986; 60μm: 8224; 100μm: 5102 MJy/sr).

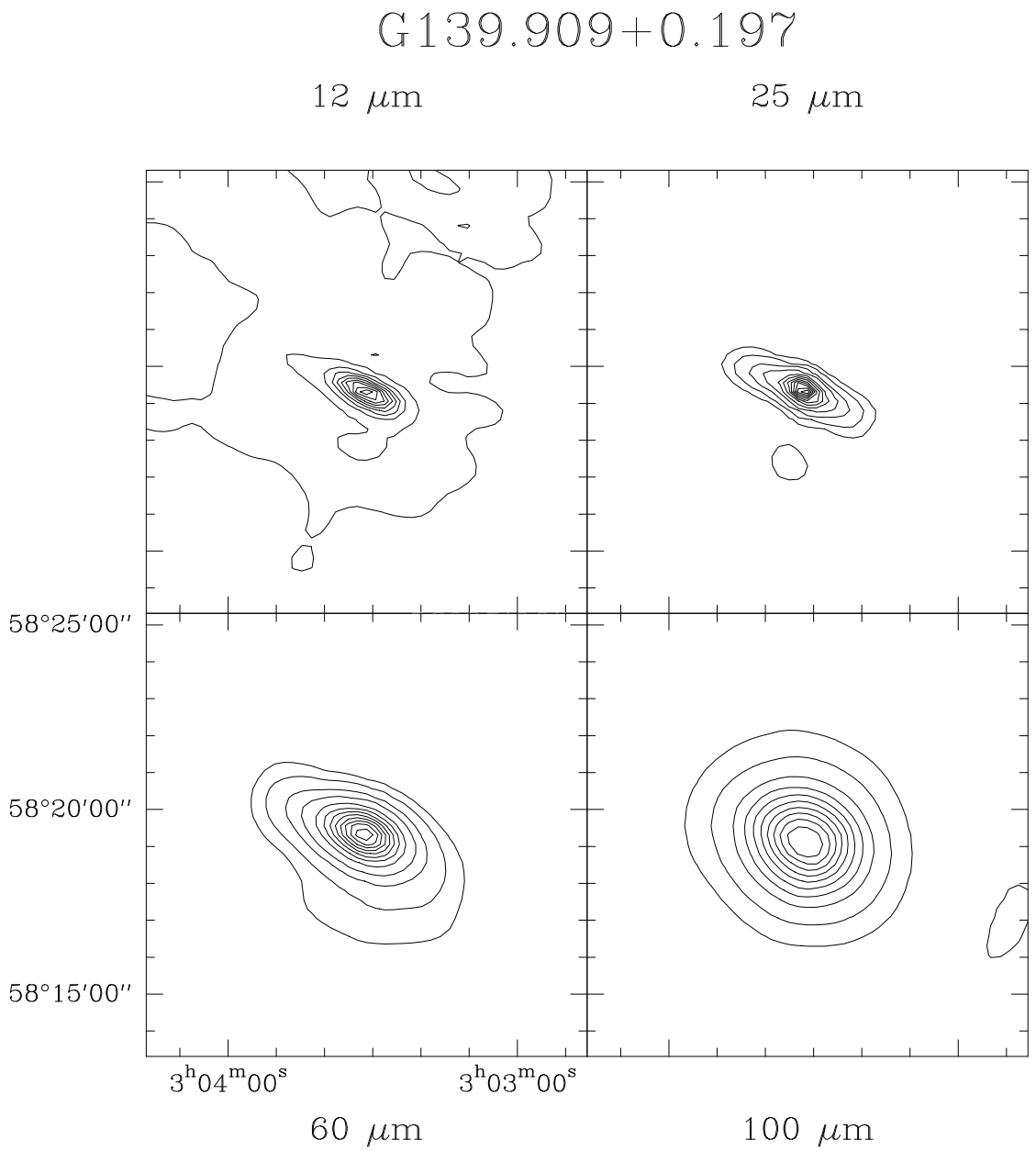

Figure 3.10: HIRES processed IRAS maps of G139.909+0.197. Contour levels are 1, 2, 5, 10 to 100 by 10% of the peak intensity in each 1° field (12μm: 522; 25μm: 9455; 60μm: 7928; 100μm: 3207 MJy/sr).

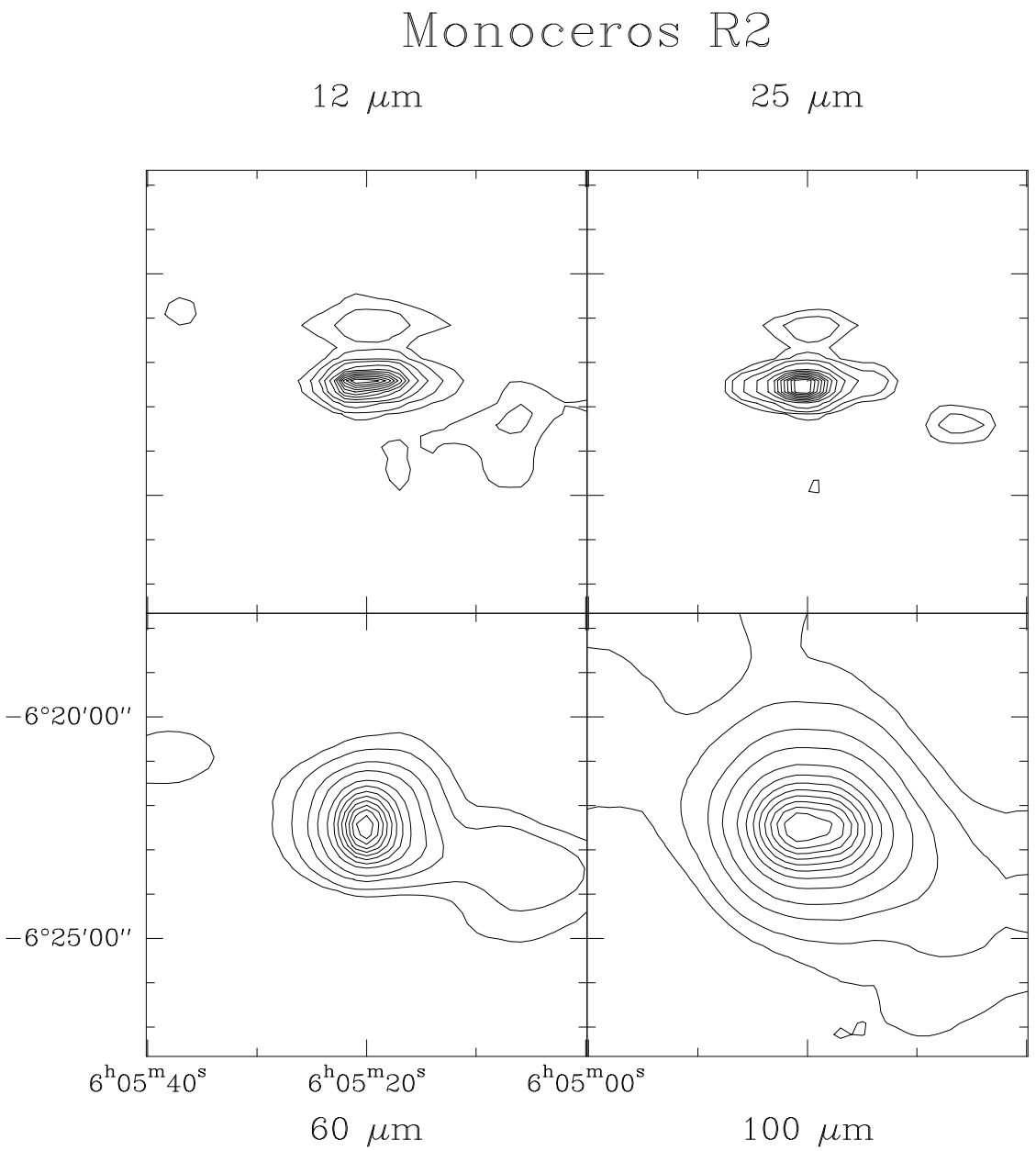

Figure 3.11: HIRES processed IRAS maps of Monoceros R2. Contour levels are 1, 2, 5, 10 to 100 by 10% of the peak intensity in each 1° field (12μm: 10093; 25μm: 83071; 60μm: 109584; 100μm: 58851 MJy/sr).

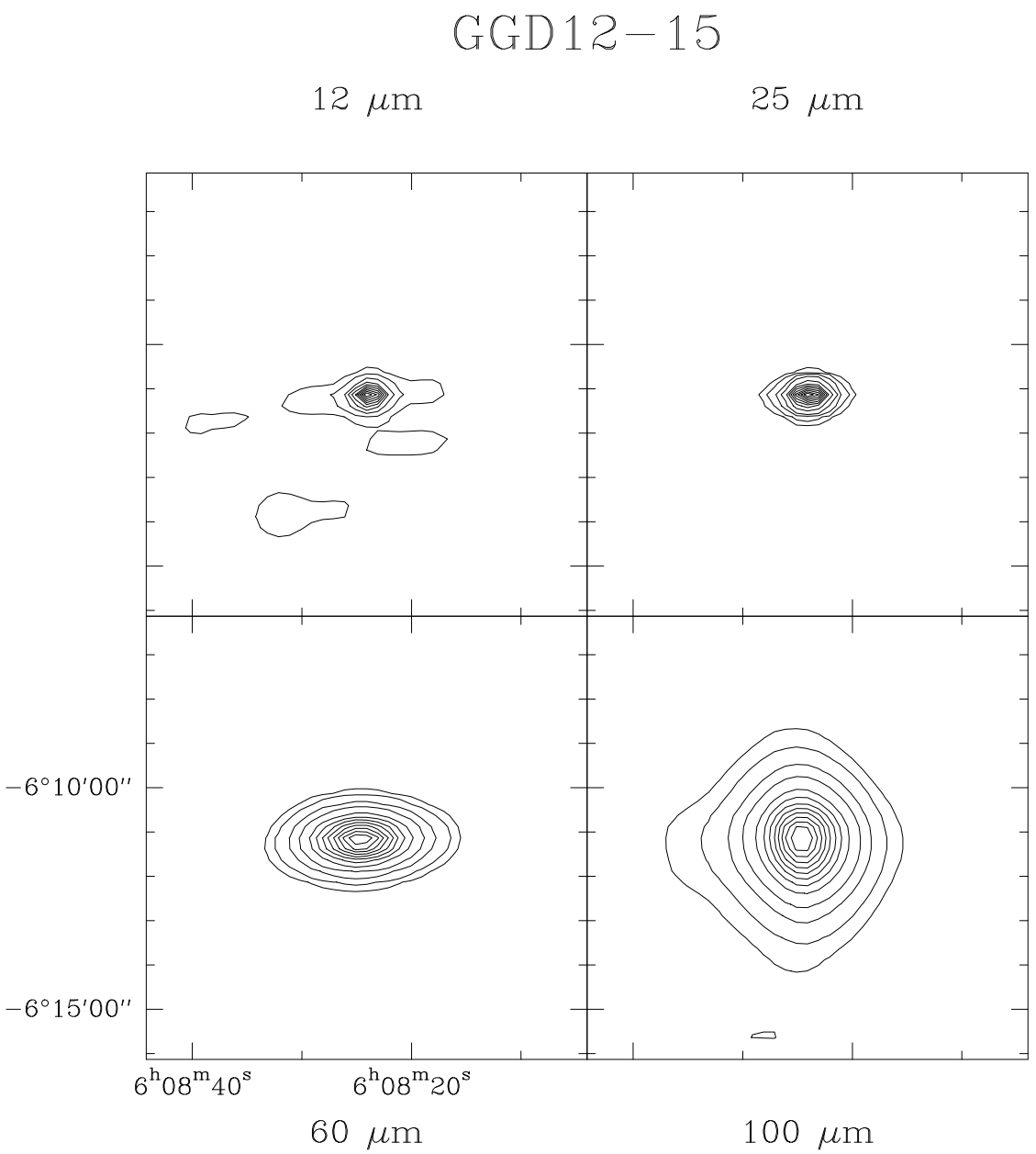

Figure 3.12: HIRES processed IRAS maps of GGD12-15. Contour levels are 1, 2, 5, 10 to 100 by 10% of the peak intensity in each 1° field (12μm: 993; 25μm: 24816; 60μm: 33049; 100 μm: 25241 MJy/sr).

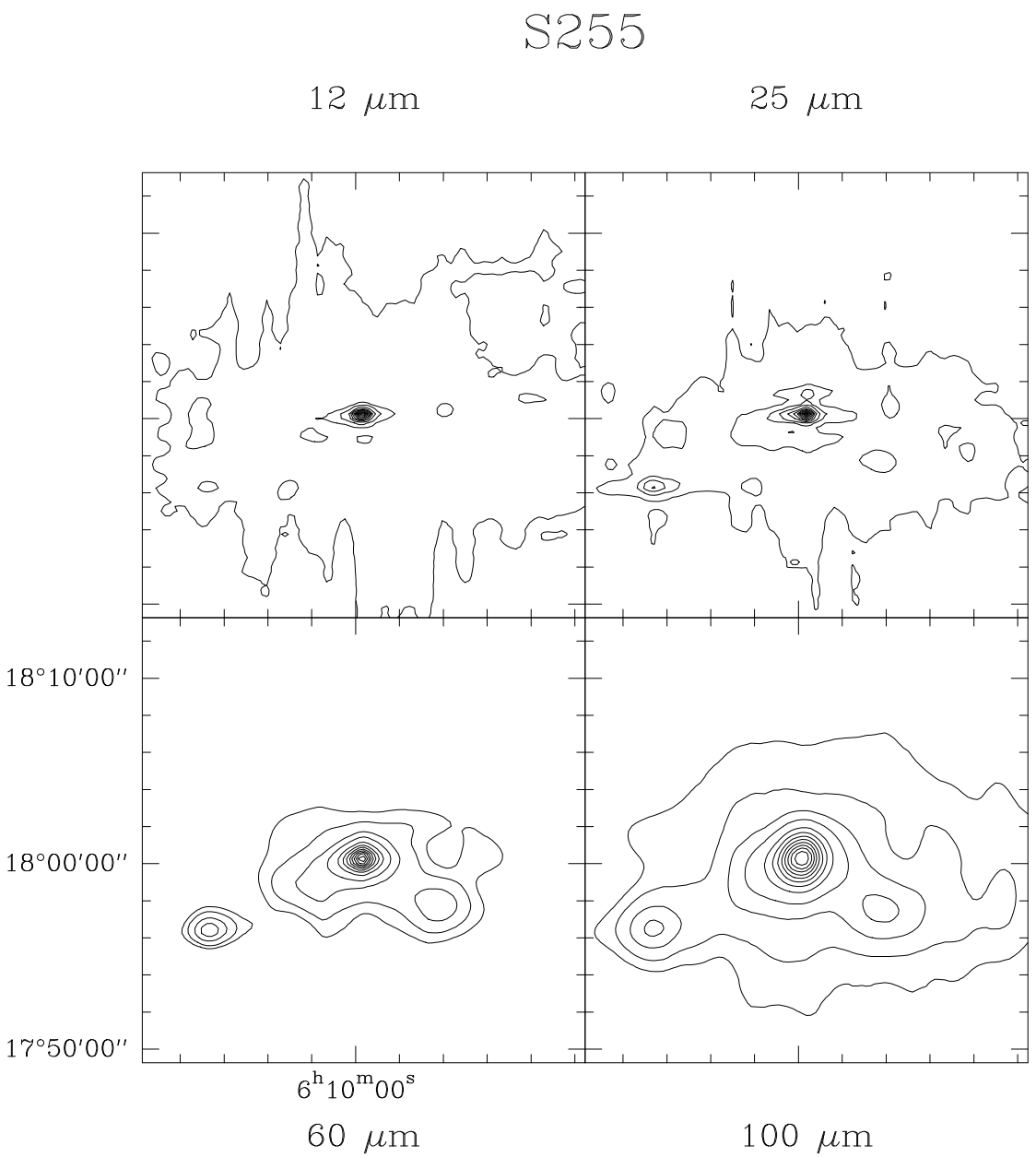

Figure 3.13: HIRES processed IRAS maps of the S255 complex. The extension to the southwest of the field center coincides with S256. Contour levels are 1, 2, 5, 10 to 100 by 10% of the peak intensity in each 1° field (12μm: 3101; 25μm: 11339; 60μm: 26675; 100μm: 15907 MJy/sr).

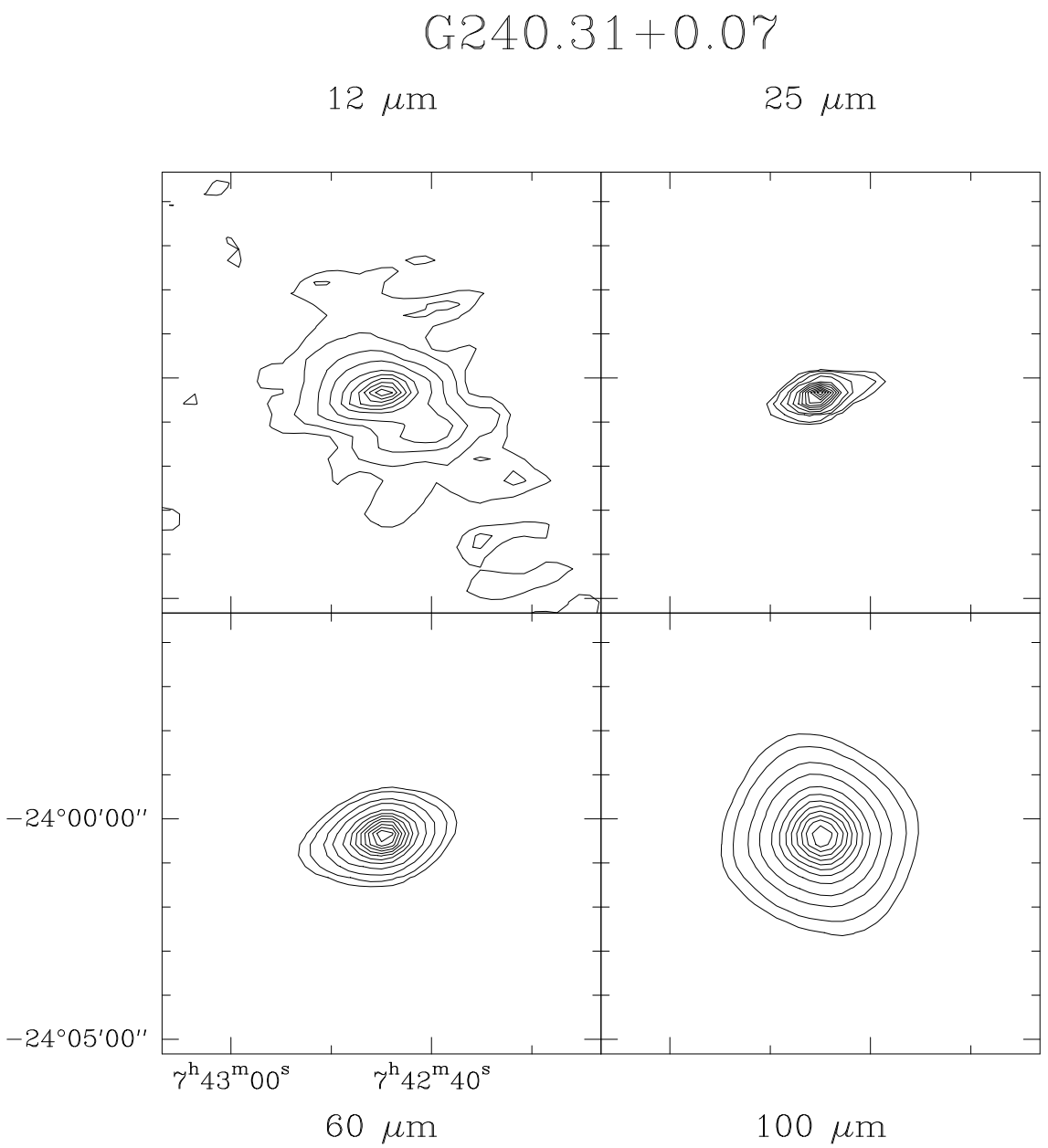

Figure 3.14: HIRES processed IRAS maps of G240.31+0.07. Contour levels are 1, 2, 5, 10 to 100 by 10% of the peak intensity in each 1° field (12μm: 54.8; 25μm: 2140; 60μm: 7580; 100μm: 4032 MJy/sr).

3.4 Calibration and pointing accuracy of the SHARC images

The data reduction scheme used to prepare the SHARC images was described in Chapter 2. Before presenting and interpreting the images, a discussion of the flux calibration, dynamic range and pointing accuracy should be considered.

3.4.1 Flux calibration

The absolute flux calibration of ground-based submillimeter continuum observations is ultimately limited by the stability and uniformity of the atmosphere. Even on relatively calm nights, the zenith optical depth τ across the frequency band of the filter can change significantly ($\sim 20\%$) on short timescales (minutes to hours). Beyond the regular increase with airmass, τ can be a significant function of azimuth and elevation depending on the position of clouds and weather systems. The most accurate method of measuring τ through the desired filter is to record the signal strength of a source as it rises or sets through different airmasses. By nature, this measurement requires several hours during which τ can be changing. In the 350 and 450μm bands, $\tau \sim 1$ in good weather. Thus a 20% change in τ will cause $\sim 20\%$ change in the signal strength. The calibration conversion factor from volts to Janskys depends on the signal recorded from a standard source including planets and secondary sources previously calibrated to planets (e.g., Sandell 1994), taking into account the fact that planetary brightness temperatures vary as a function of frequency (Hildebrand 1985; Orton et al. 1986). So if τ changes by 20% between the observation of the calibrator and the observation of the source, then the source flux density will be in error by $\sim 20\%$ plus the additional measurement uncertainties. Several scans of the source taken at different times and interspersed with the calibrator can help reduce this uncertainty. If the source is extended spatially, the extended flux has additional uncertainty because the response of the telescope beam to an extended source differs from the response to a point source. The best estimate of the accuracy of the flux calibration on a given night can

be made from the dispersion in several measurements of τ on different sources. The frequent readings from the CSO 225 GHz τ-meter can also be considered (if it was operating dependably at the time). With these effects, the flux calibration of a single OTF map recorded in one session is probably no better than 30% accurate. Since the images in the following sections were constructed from a sum of 1, 2 or 3 maps, the estimated calibration accuracy is $\sim 30\%$.

3.4.2 Dynamic range

Due to the presence of sidelobe response in the 350 and 450μm beams, there is a dynamic range limit for genuine features surrounding bright sources in the SHARC maps. As can be seen in the 350μm beam map in Fig. 2.8, the brightest feature outside the central beam lies at the $\sim 4\%$ intensity level. Consistent results have been found with maps of bright compact galaxies such as Arp 220. When several maps taken at different parallactic angles are summed, the effect of the sidelobes will tend to smear which will raise the dynamic range further. Thus the dynamic range is at least 25:1. All of the sources identified in the maps presented in the following sections easily fall within this criterion. It should be noted that the beam is significantly cleaner at 450μ than at 350μm (due to the telescope surface accuracy) and hence the dynamic range in maps at the longer wavelength is nearly a factor of 2 larger.

3.4.3 Pointing accuracy

The CSO is an altitude-azimuth mount telescope. Pointing correction is accomplished with two sets of offsets in this coordinate system: tilt terms which vary as a function of elevation, and fixed terms which remain constant (in the ideal case) and vary only due to small differences in the mounting position of the selected instrument. Additional corrections in azimuth and elevation result from a formula containing several constants designed to account for deviations between the radio and optical pointing of the telescope. These so-called "optical pointing constants" are periodically measured and updated using an optical telescope attached to the radio telescope backing structure

and looking through a hole in the primary. Finally, a significant refraction correction ($\lesssim 1'$) to the elevation angle is computed from the current humidity reading. The details of these formulas will not be discussed, but they provide an idea of the level of complexity required in the pointing of a submillimeter telescope.

Even when these systematic terms correct well for pointing errors, other effects can disturb the pointing accuracy of the telescope. Thermal changes at sunset and sunrise can cause small distortions in the telescope surface which cause $\sim 10''$ changes in the fixed terms. For this reasons, observations during these times cannot be relied upon for absolute pointing accuracy. The best pointing accuracy is achieved when the fixed terms are measured on a calibrator located near the target source in both axes of motion, particularly in elevation. Unfortunately, in the 350 and 450μm wavebands, very few bright point-like sources exist. Planets of small angular size ($< 10''$) such as Uranus, Neptune and (much of the time) Mars are best. Nearby evolved stars with dust shells and well-known positions (such as IRC+10216) are also good pointing sources. Bright star-forming regions with a dominant component of compact emission have also been used by assuming the submillimeter emission peak coincides with infrared or radio positions (Sandell 1994). UCHII regions have been used for this purpose, even though the presence of extended emission and the lack of *a priori* knowledge of the submillimeter position makes them less reliable pointing sources.

Because UCHII regions themselves are the subject of this work, I chose to use only sources with the most reliable peak positions (Uranus, IRC+10216, Orion KL, IRAS16293-2422 and K3-50A) for correction of the fixed pointing terms. For this reason, the angular distance between the pointing source and the target source was in many cases larger than recommended ($> 90^\circ$ in azimuth or $> 20^\circ$ in elevation). The absolute pointing accuracy of a single map is estimated to be $\pm 5''$. For many of the regions studied, more than one map was acquired and summed, which should improve the accuracy of the peak positions of sources in the map.

3.5 SHARC images of cometary UCHII regions

Since the installation of SHARC at CSO in September 1995, over a dozen UCHII regions have been imaged at 350 and/or 450μm. The sample includes regions of various radio morphology. The cometary UCHII regions studied are G19.61-0.23A, G29.96-0.02, G34.3+0.2, G45.12+0.13, and GGD12-15. Similar to the cometary shape is the classic blister-type HII region Monoceros R2 (Mon R2). The shell-like or spherical UCHII regions studied are W3(OH), K3-50A and K3-50C. Also studied are a group of UCHII regions unresolved at radio wavelengths including G45.07+0.13, G138.300+1.558, G139.909+0.197, G240.31+0.07 and a group of sources in the S255 complex. The final object presented is the G75 complex which contains several UCHII regions of cometary and core-halo shapes. These sources will be discussed individually in the following sections with the exception of the two G45 sources which are presented in greater detail in Chapter 5. Also, prior to the installation of SHARC, maps of 800μm emission from many of these UCHII regions were made at the CSO with the single channel bolometer equipped with a 20$''$ Winston cone. These maps are included in the following sections. Although most of the sources are unresolved at the limited signal to noise level of these maps, they do provide 800μm fluxes which are used in the greybody models computed in section 3.9. All of the maps in the following sections are in presented in equatorial (B1950) coordinates.

3.5.1 G34.3+0.2 Complex (W44, AFGL 2271, I18507+0110)

At a distance of 3.8 kpc (Kuchar & Bania 1994), G34.25+0.14 is a 90$''$ (1.7 pc) extended, shell-like HII region as seen in Fig. 3.15 (Fey et al. 1994; Fey et al. 1992). Just beyond the northwest edge of the extended HII region lies the prototypical cometary UCHII region G34.26+0.14 (see Fig. 3.16). The discovery of this source prompted speculation that the cometary tail was due to relative motion of the central ionizing source with respect to the interstellar medium (Reid & Ho 1985). Higher sensitivity observations show that the tail is at least 15$''$ (0.28 pc) in length and that it curves back on itself (Gaume, Fey & Claussen 1994). Theoretical models propose that this

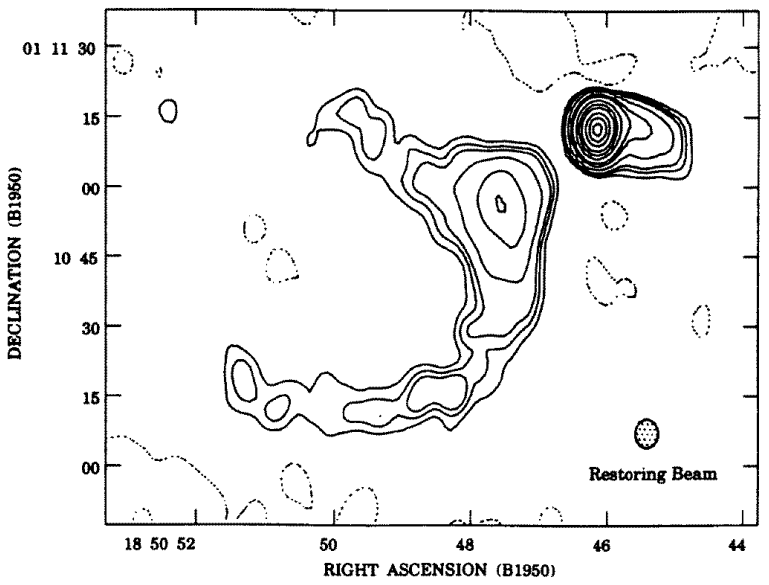

Figure 3.15: 2.0 cm radio continuum image of the G34.3+0.2 complex reproduced from Fig. 2 of Fey et al. (1994).

kind of cometary shape could be explained if the young O star was moving at a rate of 10-20 km s^{-1} through the natal molecular cloud (Mac Low et al. 1991; Van Buren & Mac Low 1992). Also, two unresolved radio components labelled "A" and "B" lie $3''$ southeast and $2''$ northeast of the cometary region "C", respectively. The location of the OH masers (Garay, Reid & Moran 1985) and the primary concentration of H_2O masers (Benson & Johnston 1984; Downes et al. 1979) lie between the 3 radio components directly opposite to the direction of the cometary tail. VLA images of the NH_3(3,3) and (1,1) inversion transitions indicate a concentration of dense gas intimately associated with the H_2O masers (Heaton, Little & Bishop 1989; Keto 1987) reaching densities of $\sim 7 \times 10^7$ cm^{-3} in the central region (Garay & Rodríguez 1990). Such high densities are confirmed by the presence of a CH_3CN core (Akeson & Carlstrom 1996). Maser emission has also been observed in the 325 ($5_{1,5} \rightarrow 4_{2,2}$), 439 ($6_{4,3} \rightarrow 5_{5,0}$) and 471 GHz ($6_{4,2} \rightarrow 5_{5,1}$) transitions of H_2O (Melnick et al. 1993). In a JCMT 330-360 GHz spectral line survey, 14 transitions of ethanol have been detected indicating a rotational temperature of 125 K and a large column density (2×10^{15} cm^{-2}) consistent with grain surface chemistry (Macdonald, Habing & Millar 1995). Observed with the Berkeley-Illinois-Maryland Array (BIMA) millimeter

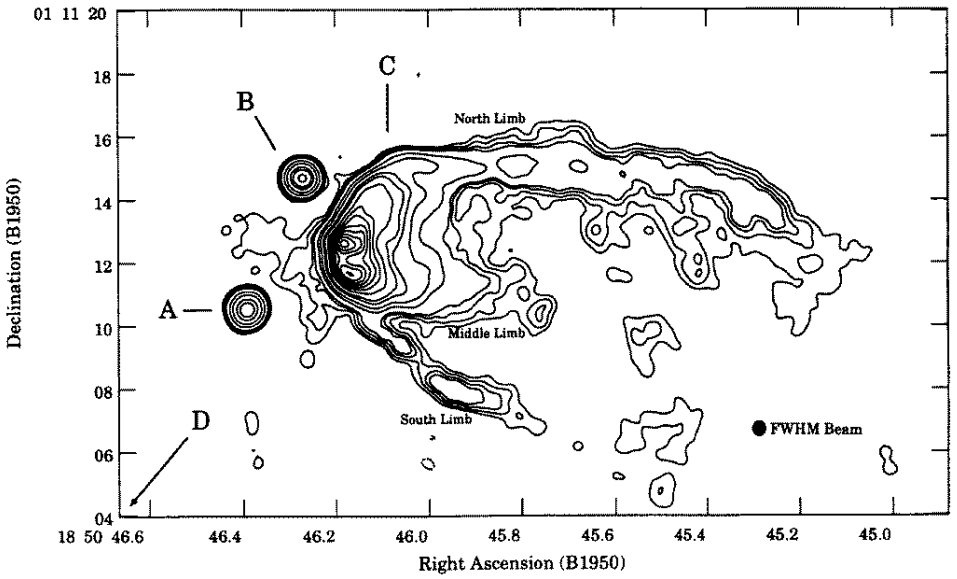

Figure 3.16: 2.0 cm radio continuum image of G34.26+0.14 reproduced from Fig. 1 of Gaume, Fey & Claussen (1994).

interferometer, the position of the complex molecules in the region also lies a few arcseconds east of the UCHII region (Mehringer & Snyder 1996). Together, these observations suggest that the UCHII region expands preferentially to the west away from the dense molecular gas. Additional H_2O maser spots lie at an offset $(-40'', +18'')$ from the UCHII region (Fey et al. 1994) and probably trace a separate center of star formation activity at a projected distance of 0.8 pc.

Shown in Fig. 3.17 are 350μm and 450μm images of the G34.3+0.2 complex. The position of the cometary UCHII region is marked by a triangle and the two sites of H_2O maser emission are marked by crosses. Essentially, the dust emission peaks on the UCHII region. The half power width of the dust core is $34''$ (0.63 pc), identical to the size of the CS J=5$\rightarrow$4 emission mapped with the IRAM 30m telescope (Churchwell, Walmsley & Wood 1992). Extensions of dust emission protrude to the southwest and northwest bracketing the ionized tail of the cometary UCHII region on a large scale. The dust clump northwest of the UCHII region coincides with the secondary concentration of H_2O masers (Fey et al. 1994). Blueshifted ^{13}CO emission near this position was once interpreted as an extension of an outflow from the UCHII region (Matthews et al. 1987) but the coincidence of the dust clump and

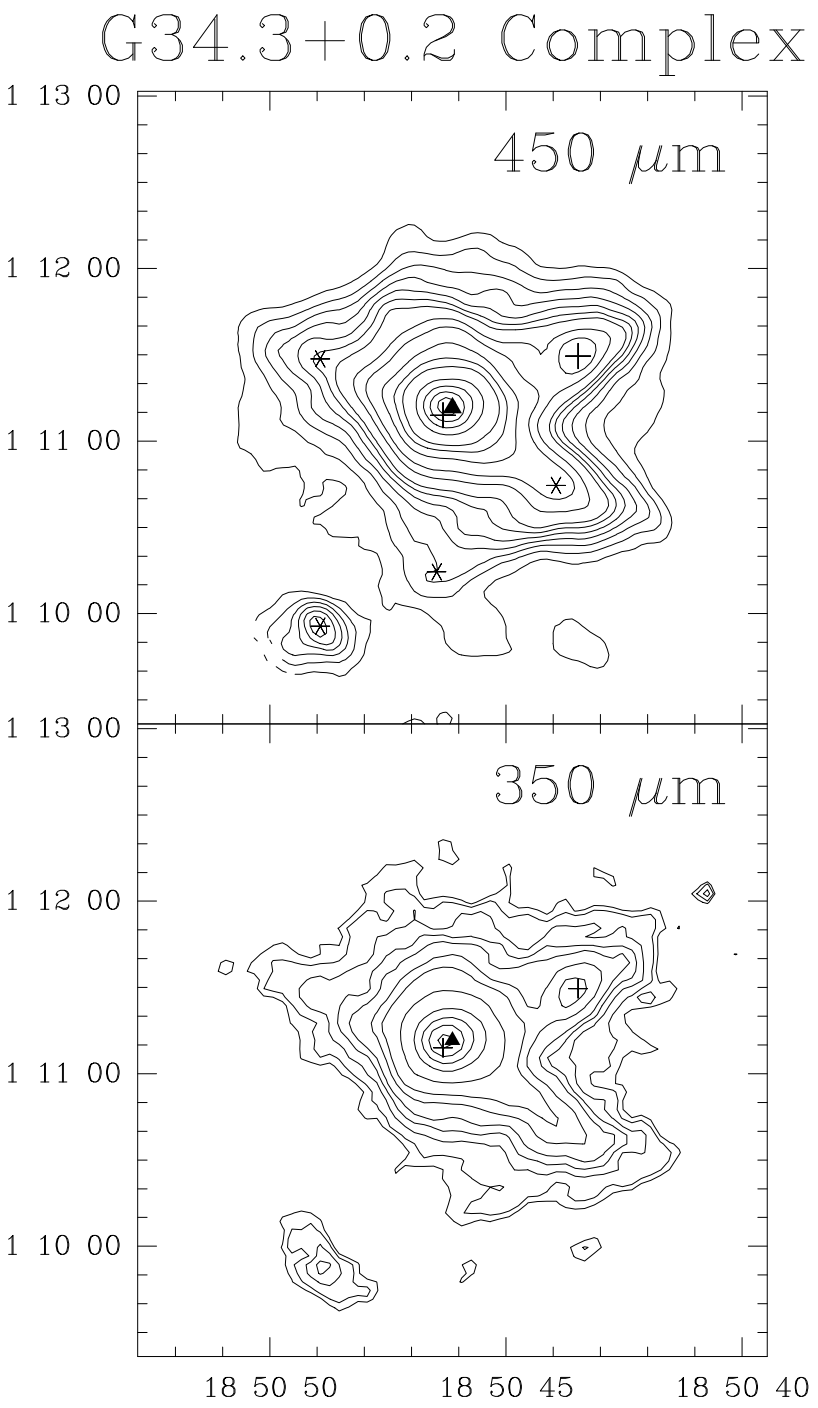

Figure 3.17: *Bottom panel:* 350μm image of G34.3+0.15 (d = 3.8 kpc) with the position of the UCHII region marked by the triangle, and the two H_2O maser concentrations marked by crosses. The contour levels are 25, 30, 40, 50, 60, 80, 100, 150, 250, 350, 450 and 550 Jy/beam. *Top panel:* 450μm image of the same region with contour levels 8, 10, 12, 14, 16, 18, 20, 25, 30, 40, 50, 60, 90, 120, 150 and 180 Jy/beam. The asterisks mark the position of the submillimeter sources identified in Table 3.2.

masers provides overwhelming evidence that it is a separate core. Two additional dust sources (G34.3+0.2SE and G34.3+0.2SW) lie to the southeast and southwest of the UCHII region. There is no compact radio continuum nor maser emission at these positions. However, the flux in these objects imply large molecular masses, 1700 and 560 $M_\odot$, respectively (see Table 3.2). Thus they may contain younger massive protostars forming on the outskirts of the dust core containing the UCHII region.

Table 3.2: Observed properties of the dust clumps toward G34.3+0.2

Src #	UCHII offset ($\Delta\alpha''$,$\Delta\delta''$)	B1950.0 Coordinates R.A.	Dec.	$S_{350\mu m}$ Jy	$S_{450\mu m}$ Jy	M_{gas} $M_\odot$
1	$(0,0)$	$18^h50^m46.^s1$	$+01°11'10''$	1060	410	6500
2	$(-33,-27)$	$18^h50^m43.^s9$	$+01°10'44''$	300	96	1700
3	$(-40,+18)$	$18^h50^m43.^s5$	$+01°11'29''$	260	90	1500
4	$(+42,+17)$	$18^h50^m48.^s9$	$+01°11'28''$	170	55	940
5	$(+42,-76)$	$18^h50^m48.^s9$	$+01°09'54''$	83	39	560
6	$(+5,-57)$	$18^h50^m46.^s5$	$+01°10'13''$	51	35	440
Sum of 6 clumps				1900	730	11500
Total emission				4700	1700	27000

To confirm the protostellar nature of the isolated continuum source G34.3+0.2SE, a map of the H_2CO ($3_{1,2} - 2_{1,1}$) transition at 225.6777 GHz around its position was obtained with the CSO (see Fig. 3.18). Emission in this transition indicates a high volume density of molecular gas (Wang et al. 1995; Mangum & Wooten 1993). G34.3+0.2SE (clump 5 in Table 3.2) was chosen because it is sufficiently separated from the UCHII region to avoid confusion in the 30″ CSO beam at this frequency. The position of an H_2CO core coincides with the 350/450μm source, confirming the presence of a dense star-forming molecular core associated with the dust core. The spectrum closest to the peak is shown in Fig. 3.19. The core of emission on the northwest edge of the map originates from the vicinity of the UCHII region.

3.5.2 G29.96-0.02 (W43S, AFGL 2245, I18434-0242)

At a distance of 7.4 kpc (Churchwell, Walmsley & Cesaroni 1990), G29.96-0.02 is a cometary UCHII region similar in appearance to G34.26+0.14. The main radio component lies on the edge of a shell-like envelope about 8″ (0.3 pc) in diameter

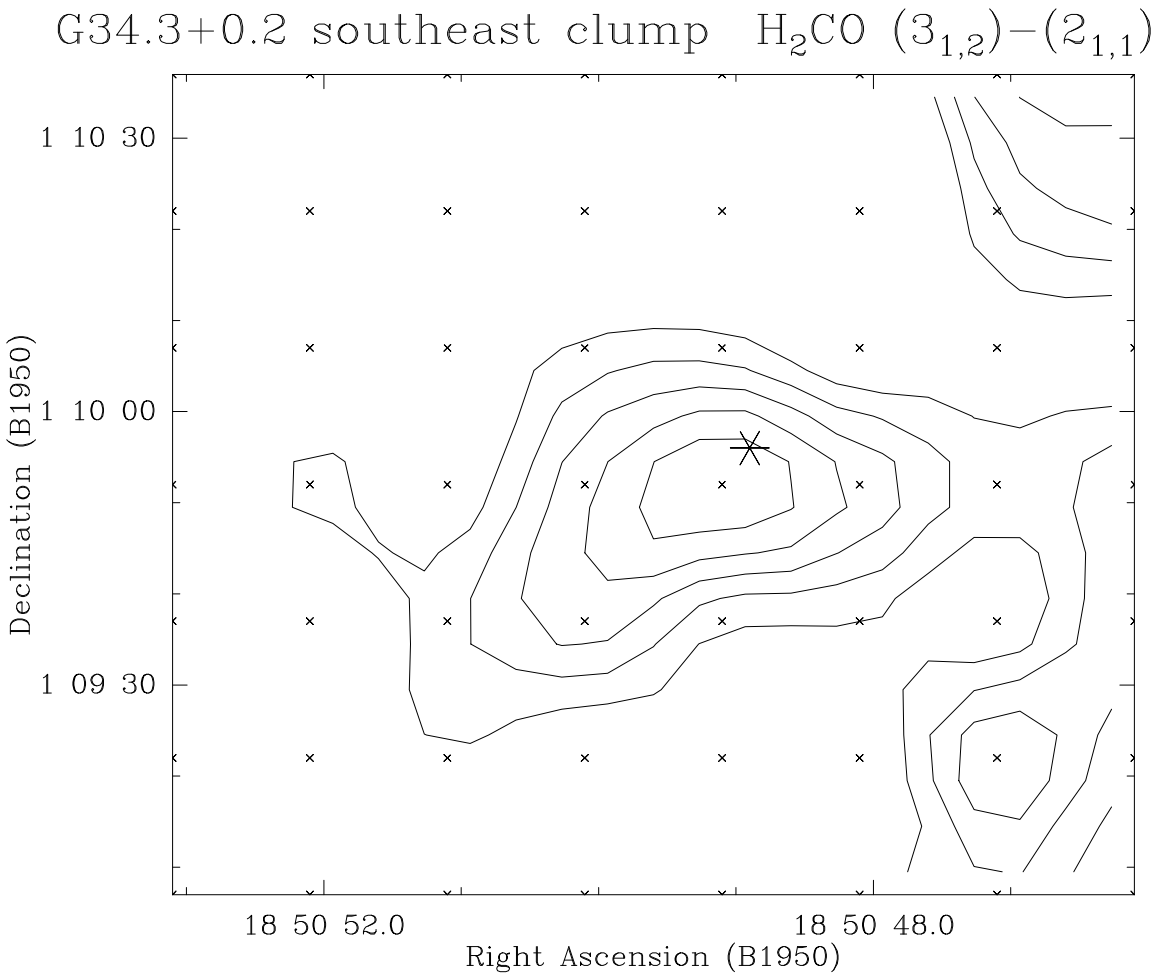

Figure 3.18: H_2CO $3_{1,2} - 2_{1,1}$ map integrated over the velocity range 53 to 62 km s^{-1} of the submillimeter dust clump that lies southeast of G34.3+0.2 (d = 3.8 kpc) in Fig. 3.17. The position of the dust clump is marked by the asterisk. Contour levels are 2.5 to 5.0 by 0.5 K km s^{-1} on the main beam brightness temperature scale.

(Megeath et al. 1990; Cesaroni et al. 1994). As seen in Fig. 3.20, diffuse radio emission extends up 40″ (1.4 pc) to the north where a faint filament about 16 (0.6 pc) in length turns toward the west (Fey et al. 1995). Another filamentary structure emerges from the southern edge of the shell and extends 10″ to the east.

The 800μm CSO single channel bolometer map shows a compact dust core (Fig. 3.21). The total FIR (IRAS) luminosity of the dust core is $10^{6.30} L_\odot$ (Wood & Churchwell 1989).

Strong emission from the molecular species CH_3CN, CS and ^{13}CO is present toward the core. Observed with an 11″ beam at the IRAM 30m telescope, the half

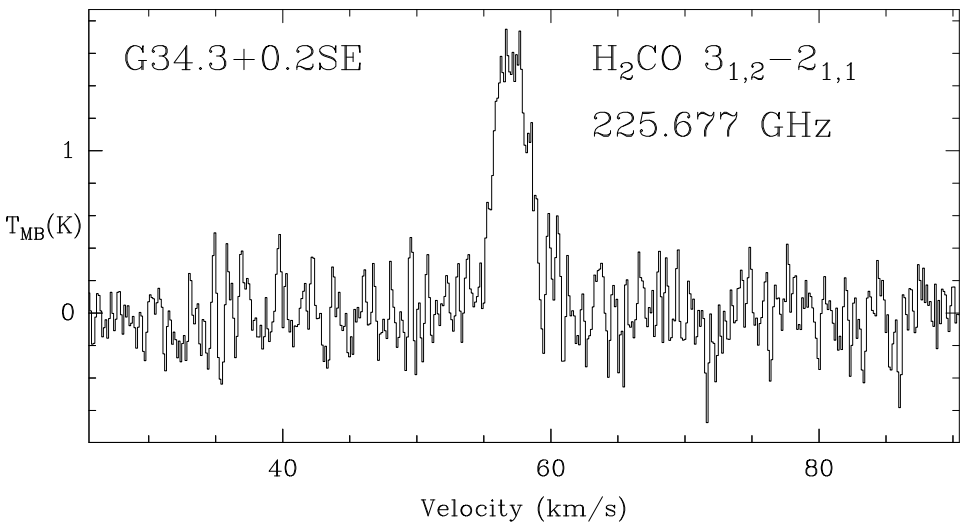

Figure 3.19: The H_2CO $3_{1,2} - 2_{1,1}$ spectrum observed with a $30''$ beam at the CSO at the offset of $(+45'', -80'')$ from G34.3+0.2, within a few arcseconds of the peak dust emission from G34.3+0.2SE. The vertical axis is main beam brightness temperature in units of Kelvin.

power width of the core in the CS J=5→4 transition is $31'' \times 20''$ in RA-Dec coordinates (1.1×0.7 pc) (Churchwell, Walmsley & Wood 1992). The core contains a near-infrared cluster of stars roughly $30''$ across and centered on the UCHII region (Fey et al. 1995). In the other direction, $2''$ (0.07 pc) west of the core lies a dense NH_3 clump (Cesaroni et al. 1994) coincident with two H_2O maser spots (Hofner & Churchwell 1993) and a rare 6 cm H_2CO maser (Pratap, Menten & Snyder 1994). The Brγ line exhibits large linewidths both ahead of the bow and in the tail (Lumsden & Hoare 1996). This velocity structure is inconsistent with the bow shock model but can be explained by the streaming motions toward low density regions in a "champagne" flow, in which the ionization front reaches the edge of the cloud in one direction causing the ionized gas to flow away at velocities of order 30 km s^{-1} (Bodenheimer, Tenorio-Tagle & Yorke 1979; Tenorio-Tagle 1979). In this picture, the G29.96-0.02 UCHII region encounters a high density medium on its western side. The photoevaporated material is swept back to the east along the cometary tail where it expands into a less dense but anisotropic medium (Fey et al. 1995).

The 450μm image of G29.96-0.02 shown in Fig. 3.22 reveals that the dust emission peaks near the core of the UCHII region. The half power diameter is $17''$ (0.61 pc),

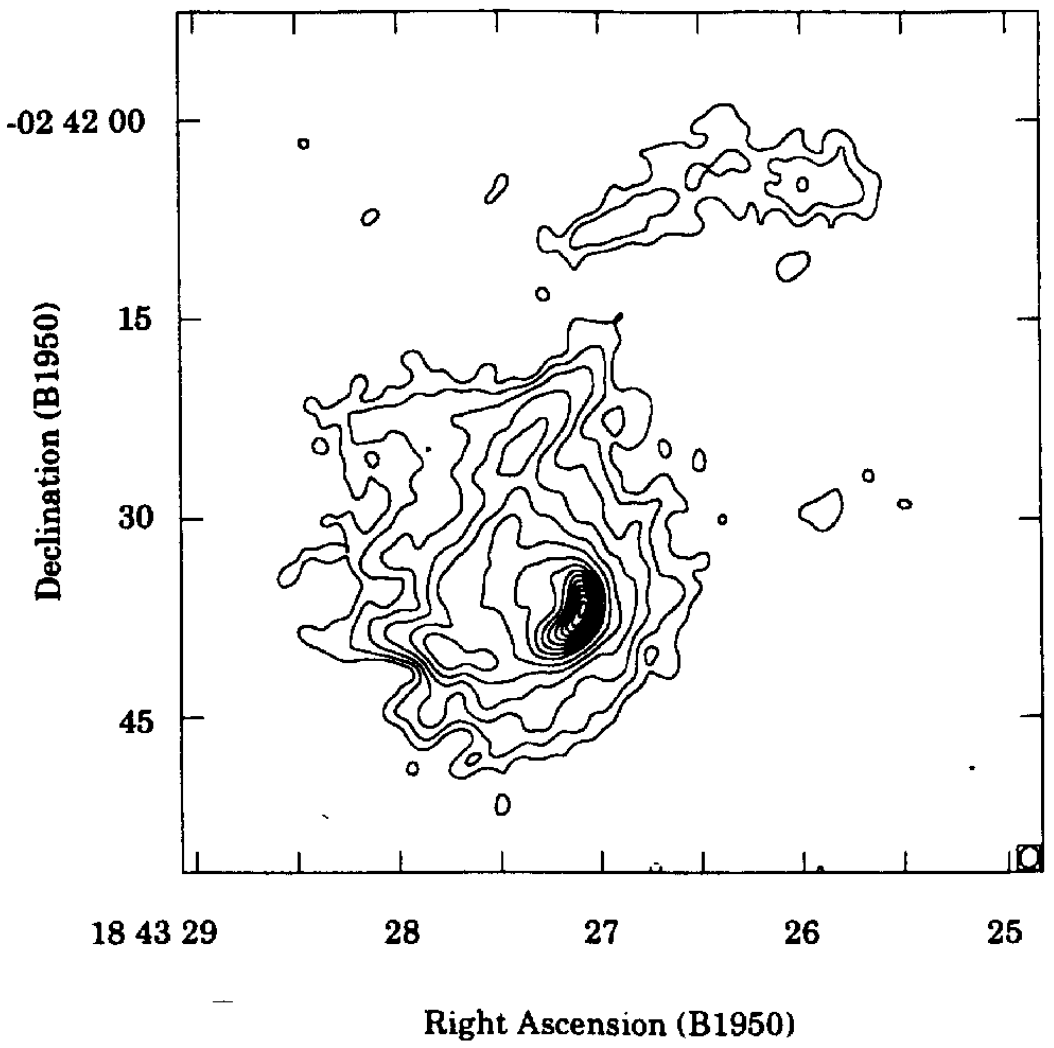

Figure 3.20: 2.0 cm radio continuum image of G29.96-0.02 reproduced from Fig. 2 of Fey et al. (1995).

slightly smaller than the CS core. But as in G34.26+0.14, an extended component of dust emission lies along the general direction of the ionized cometary tail to the east and also to the north along the extended radio filament. Looking back at the 800μm map (Fig. 3.21), the faint clump of emission in the east matches the northeast tail of emission seen in the 450μm image. The coincidence of the extended radio and submillimeter continuum suggests that there exists a diffuse component of warm dust associated with the expanding HII region. The diffuse 450μm emission to the southwest is not identified with any radio continuum emission.

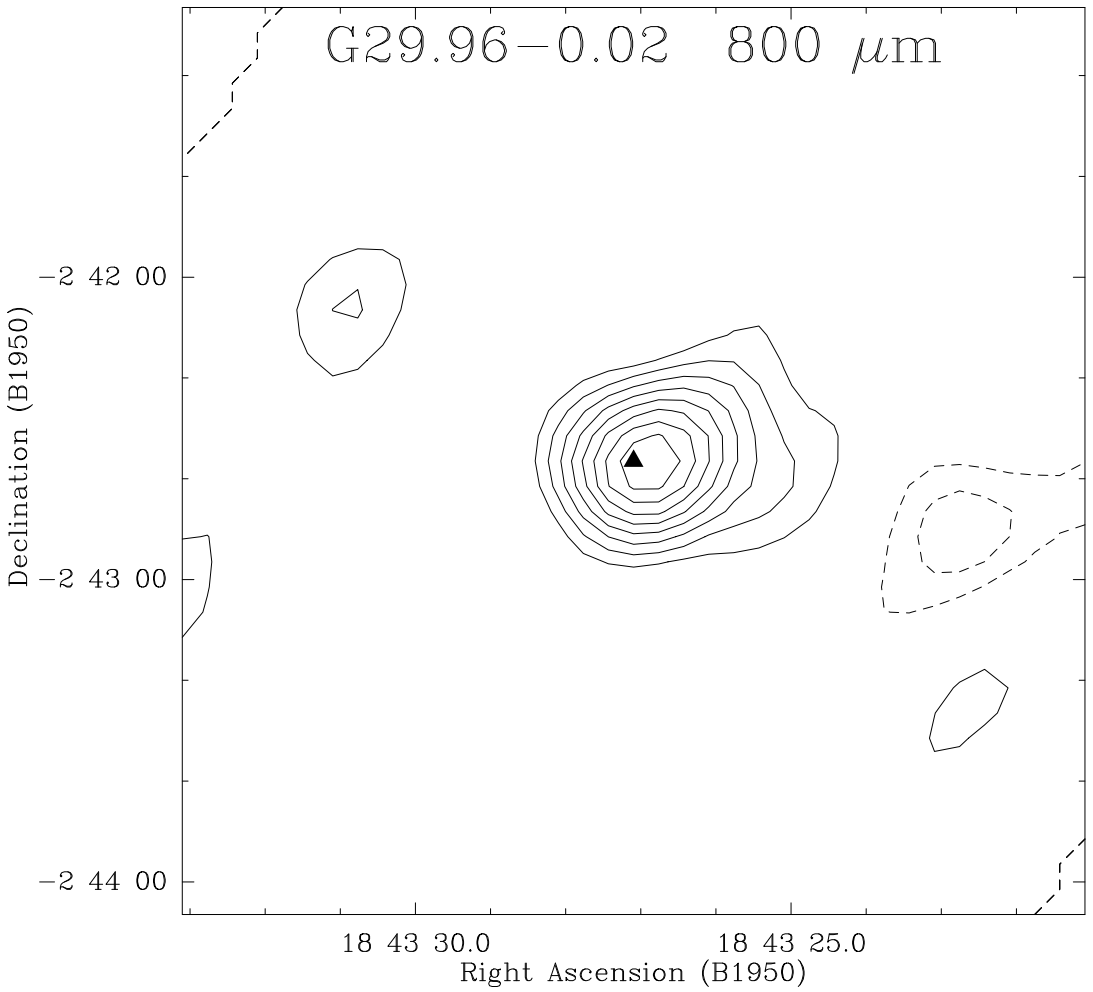

Figure 3.21: 800μm image of G29.96-0.02. Contour levels are 6 to 30 by 3 Jy/beam. The position of the UCHII region is marked by the cross (Wood & Churchwell 1989).

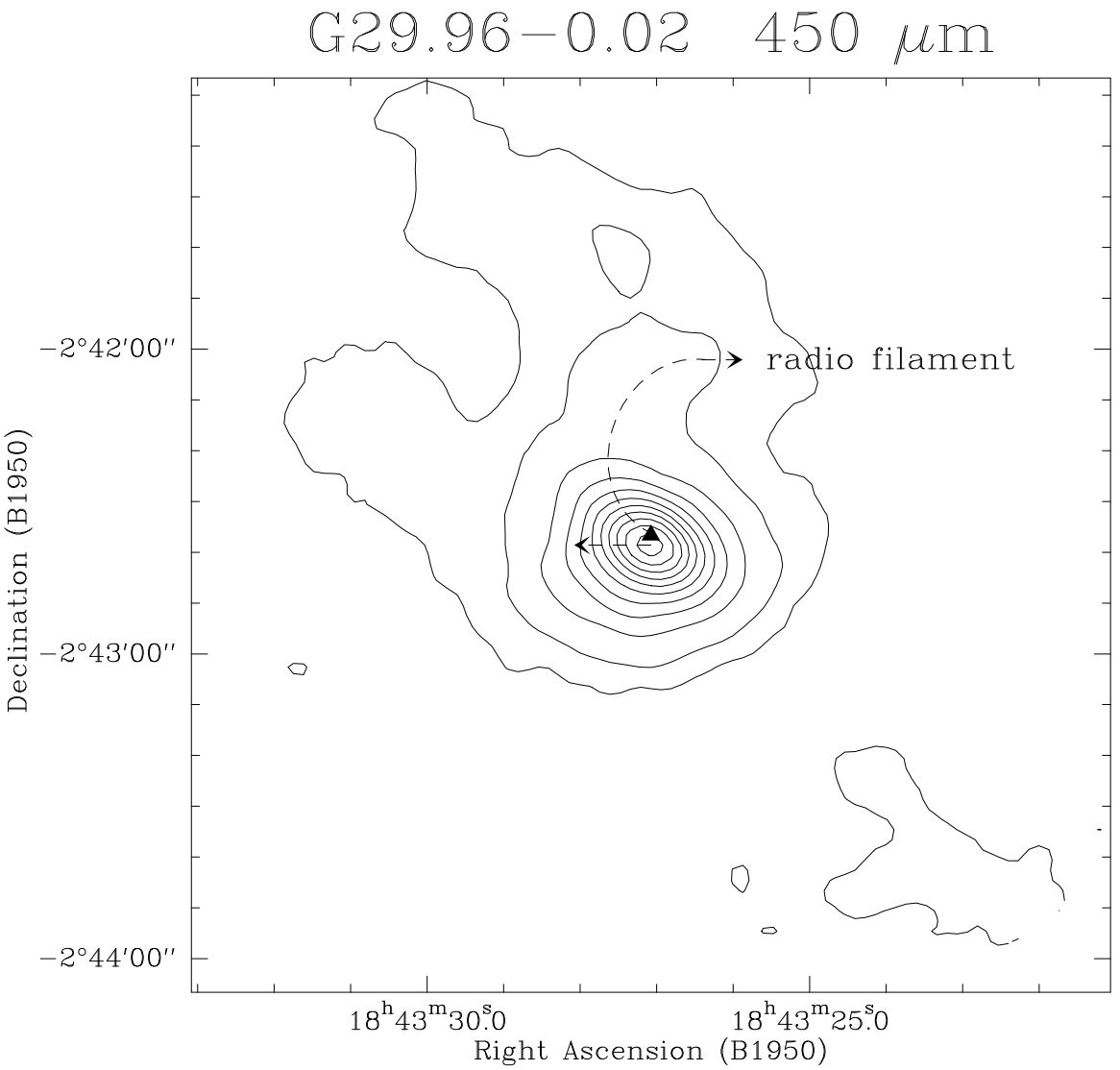

Figure 3.22: 450μm image of G29.96-0.02 (d = 7.4 kpc). Contour levels are 5, 10 to 100 by 10 Jy/beam. The position of the UCHII region is marked by the triangle and the direction of the cometary filaments are indicated by arrows (Fey et al. 1995).

3.5.3 G19.61-0.23 (I18248-1158)

G19.61-0.23 is a compact cluster of 5 UCHII regions (see Fig. 3.23), the most prominent of which is component A, a cometary UCHII region associated with strong H_2O maser emission (Churchwell, Walmsley & Cesaroni 1990). The UCHII regions lie within a compact core of 800μm continuum emission as seen in the CSO single channel bolometer map in Fig. 3.24. At a distance of 4.5 kpc (Wood & Churchwell 1989), the total FIR (IRAS) luminosity of the region is $10^{5.42} L_{\odot}$ (Wood & Churchwell 1989).

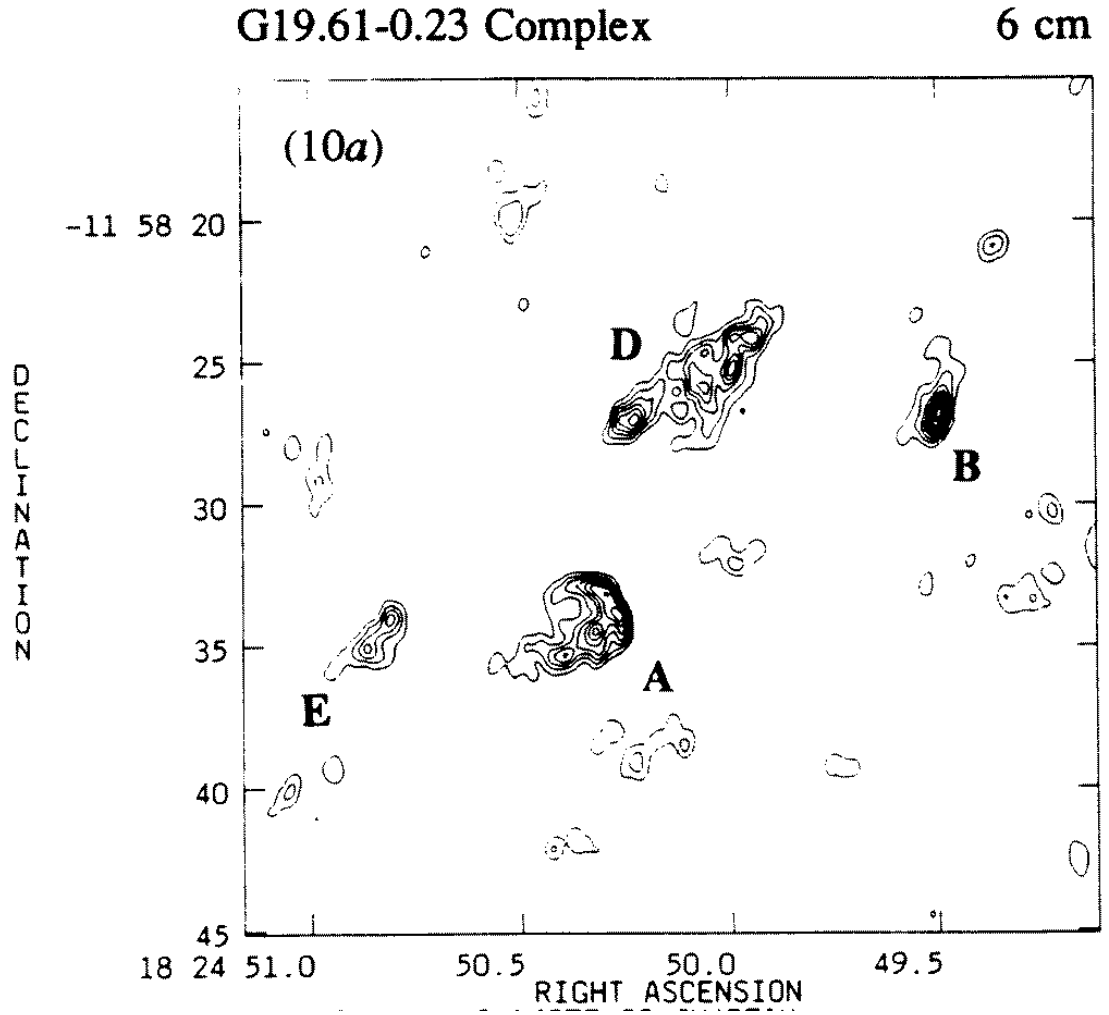

Figure 3.23: 6 cm VLA radio continuum image of G19.61-0.23 reproduced from Wood & Churchwell (1989).

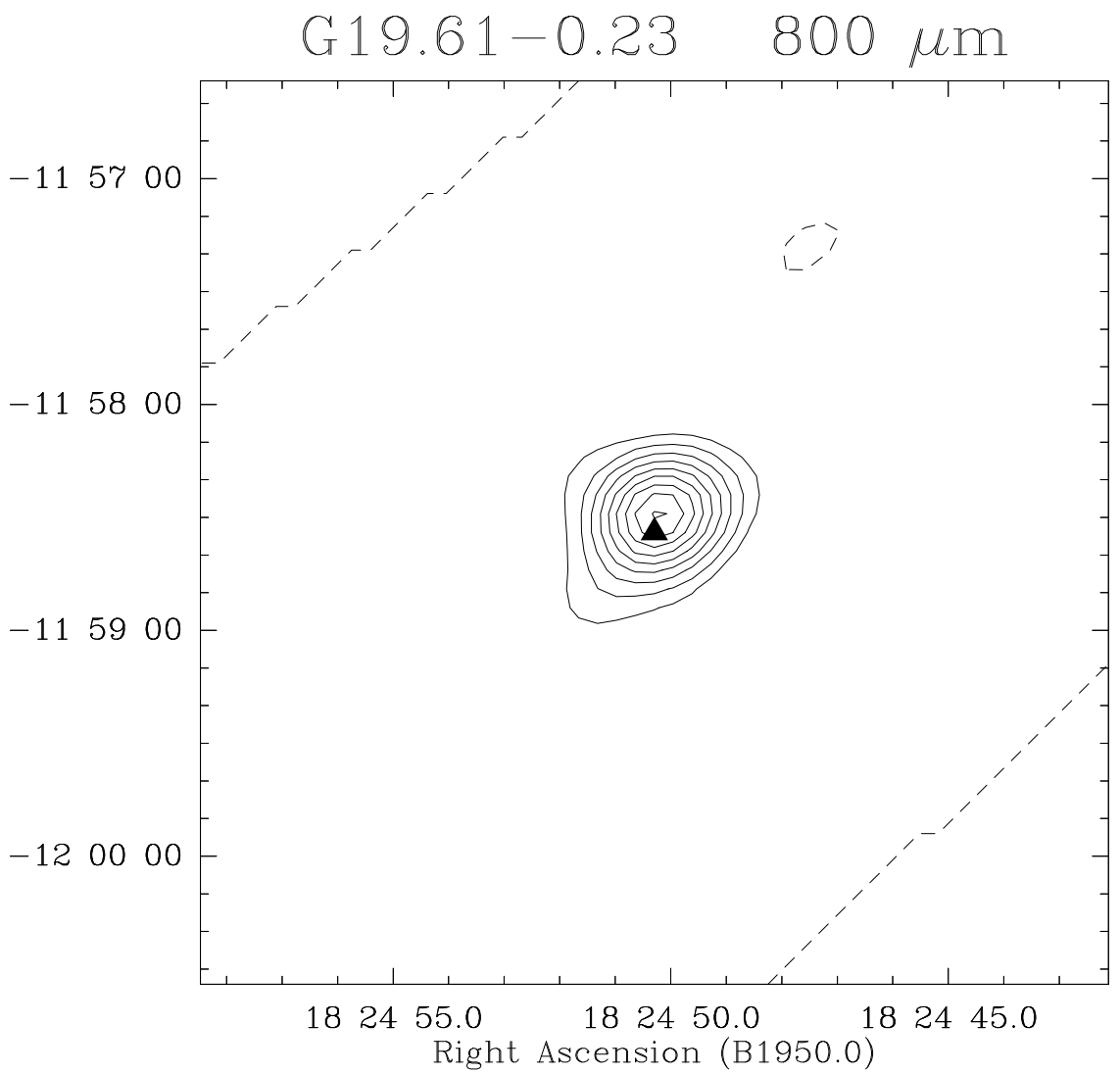

Figure 3.24: 800μm image of G19.61-0.23. Contour levels are 8 to 40 by 4 Jy/beam. The position of radio component A is marked by the triangle (Wood & Churchwell 1989).

The position angle of the cometary radio tail of component A is 60° as indicated by the arrow on the SHARC 450μm image in Fig. 3.25. Analogous to G34.26+0.14 and G29.96-0.02, the radio position of the main UCHII region is consistent with the peak dust position with a slight extension of dust along the radio tail. In this case, all five radio components lie within the 20 Jy contour.

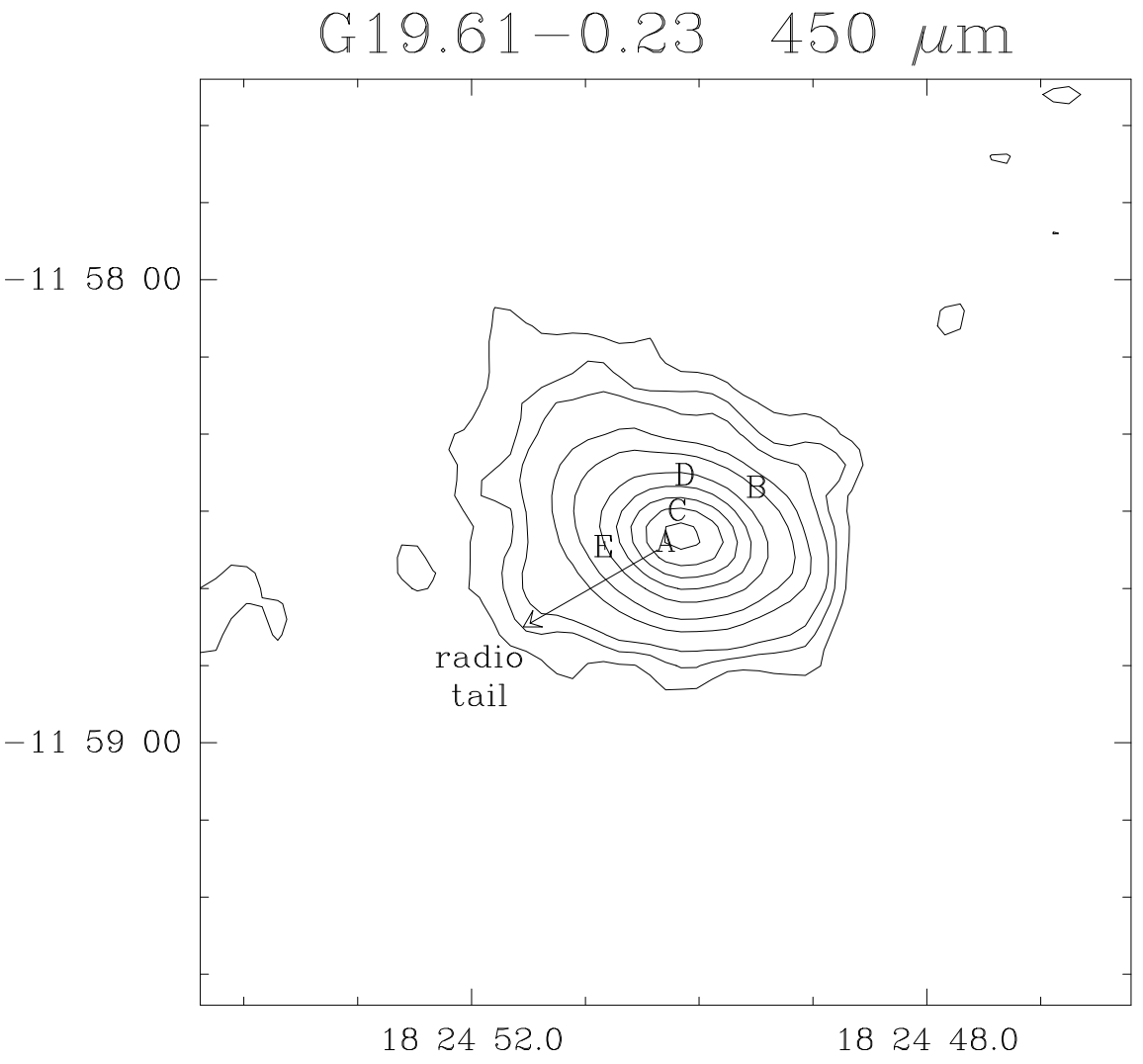

Figure 3.25: 450μm image of G19.61-0.23 ($d = 4.5$ kpc). Contour levels are 6, 8, 10, 15, 20 to 70 by 10 Jy/beam. The position of the five UCHII components are marked by letters (Wood & Churchwell 1989).

3.5.4 GGD12-15 complex (I06084-0611)

GGD12-15 is a cluster of Herbig-Haro objects identified from the Palomar Sky Survey (Gyulbudaghian, Glushokov & Denisyuk 1978). A large molecular outflow originating from these objects was first identified in the CO J=1→0 transition by Rodríguez, Cantó & Torrelles (1982). A cometary UCHII region (see Fig. 3.26) powered by a B0.5 star lies at the core of GGD12-15 with a water maser located $\sim 30''$ (0.15 pc) to the northeast (Tofani et al. 1995). OH maser emission has also been detected in this region (Rodríguez et al. 1980) along with a core of NH_3 with a molecular gas mass of $\sim 100 M_\odot$ (Torrelles et al. 1983). Despite higher resolution CO J=2→1 maps obtained at the James Clerk Maxwell Telescope (JCMT), the powering source of the molecular outflow remains uncertain (Little, Heaton & Dent 1990) but the outflow axis lies closer to the H_2O maser source than the UCHII region. Although the UCHII region dominates the FIR emission, it does not have a prominent counterpart in the near-infrared. At a distance of 1 kpc (Rodríguez, Cantó & Torrelles 1982), the FIR and submillimeter luminosity of the entire region is $10^{4.15} L_\odot$ (Little, Heaton & Dent 1990).

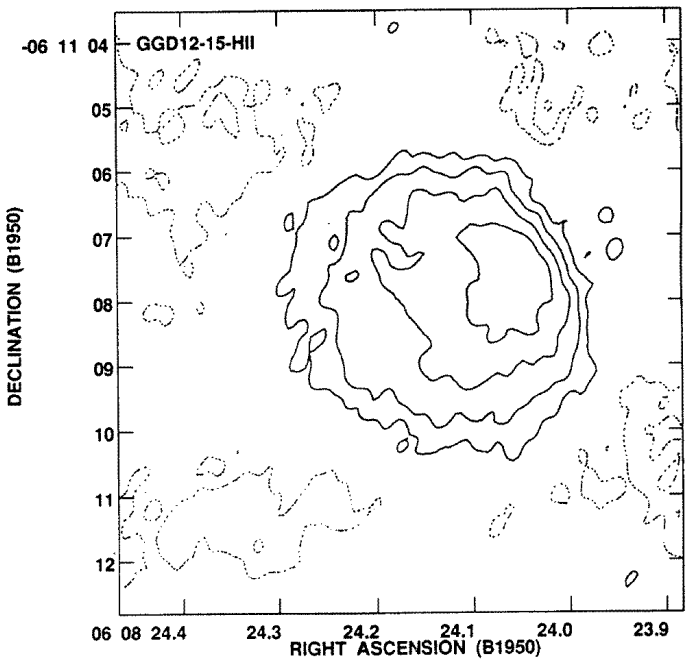

Figure 3.26: A 3.6 cm VLA image of GGD12-15 reproduced from Tofani et al. (1995).

An 800μm JCMT map peaks on the UCHII region with some extended emission surrounding the H_2O maser position. A cluster of near-infrared sources lies around the lower contours of the submillimeter emission including the $200L_\odot$ source 9M coincident with the H_2O maser (Harvey et al. 1985). With higher angular resolution than the JCMT map, the 350μm SHARC image of GGD12-15 reveals a distinct subpeak of emission at the position of the maser source (see Fig. 3.27).

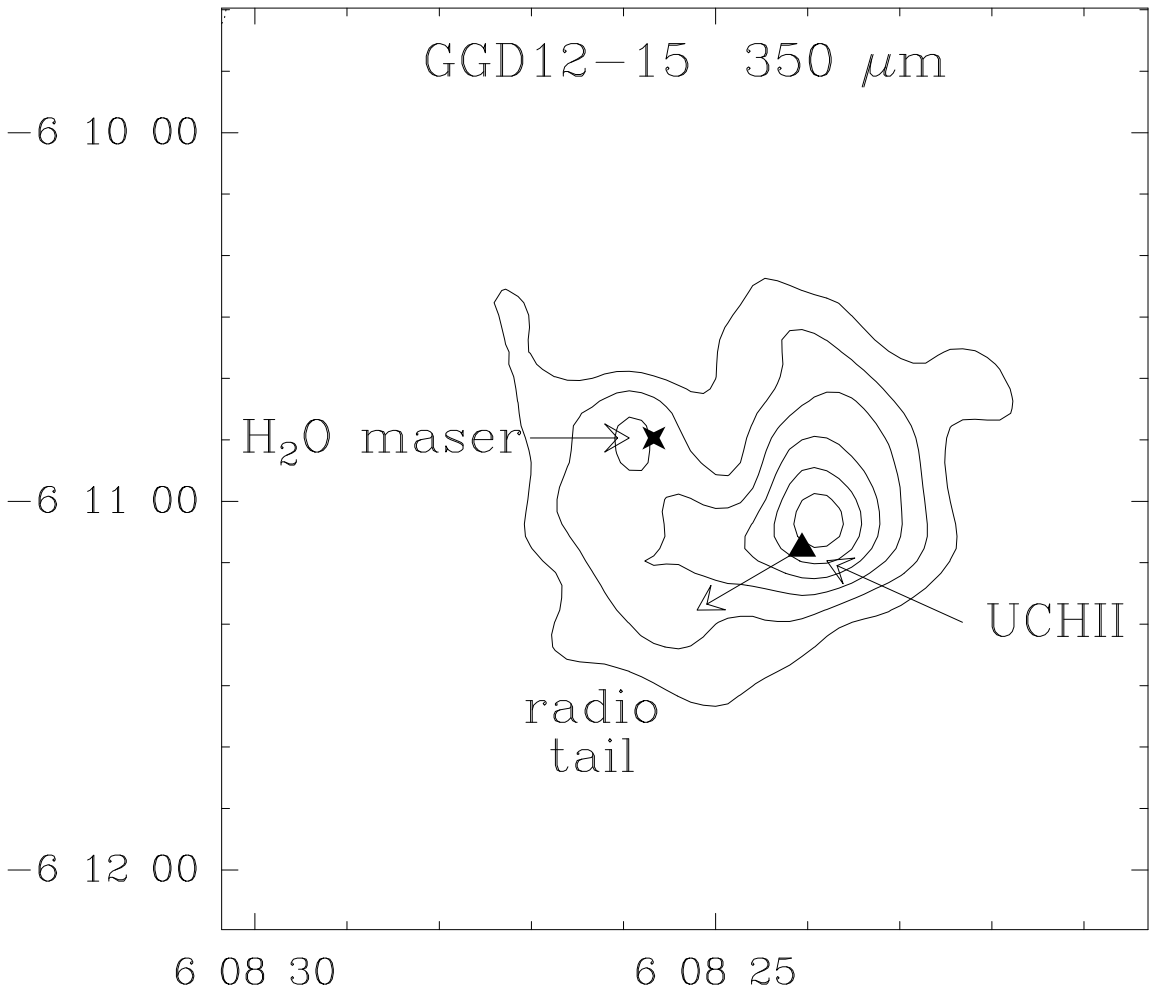

Figure 3.27: 350μm image of the GGD12-15 complex (d = 1 kpc). Contour levels are 10 to 35 by 5 Jy/beam. The positions of the H_2O maser and UCHII region are marked (Tofani et al. 1995).

Matching an extended 20μm source (Harvey et al. 1985), the main submillimeter peak occurs a few arc seconds northwest of the UCHII region, in front of the cometary head of ionized gas. As in G34.3+0.2, the absolute pointing of the SHARC image

is strengthened by the good correspondence of the H_2O maser and the sub-peak of continuum emission. Hence the magnitude and direction of the offset from the UCHII region is likely to be real. This offset supports the model of cometary UCHII regions (discussed in section 3.5.1) as the result of a streaming motions in an asymmetric medium. As in G29.96-0.02 and G19.61-0.23, faint extended dust emission lies along the direction of expansion of the HII region.

3.5.5 Monoceros R2 complex (I06053-0622)

At a distance of 830 pc (Henning, Chini & Pfau 1992), Mon R2 is a reflection nebulosity containing a blister-type UCHII region (see Fig. 3.28) imaged at the VLA by Massi, Felli & Simon (1985). Early FIR observations revealed a young cluster of infrared sources with a total FIR luminosity of $10^{4.70} L_{\odot}$ (Beckwith et al. 1976; Thronson et al. 1980). Infrared polarimetric studies have been performed (Hodapp 1987; Aspin & Walther 1990). More sensitive near-infrared observations revealed the ionizing source to be $IRS1_{SW}$, consistent with a B0 star (Howard, Pipher & Forrest 1994). The infrared cluster is associated with a core of dense gas identified in maps of the CS J=5→4 and 2→1 transitions (Heyer et al. 1986) and in NH_3 (Torrelles et al. 1983). A gas kinetic temperature of 55 K was derived from observations of the NH_3 (1,1) and (2,2) transitions in a 40″ beam, (Takano 1986).

The brightest near-infrared source in the cluster is IRS3, a pre-main sequence object undetected in radio continuum or in Brγ emission. VLA observations pinpoint an H_2O maser coincident with IRS 3 (Tofani et al. 1995). Previously, H_2O maser emission was detected at another location offset $(-34'', +17'')$ from IRS3 (Rodríguez & Cantó 1983) but this source was not detected in the more recent observations of Tofani et al. (1995). IRS3 has been resolved into two components at near-infrared wavelengths including a conical reflection nebula 500 AU in length and a possible circumstellar disk (Koresko et al. 1993). A giant molecular outflow 28′ (6.8 pc) in extent has been mapped in CO J=1→0 (Wolf, Lada & Bally 1990). Due to the large dimensions of the outflow, it is unclear whether $IRS1_{SW}$, IRS3 or some other source is

the source of the outflow. High resolution CS and ^{13}CO observations indicate dense clumps in the outflow (Tafalla, Bachiller & Wright 1994).

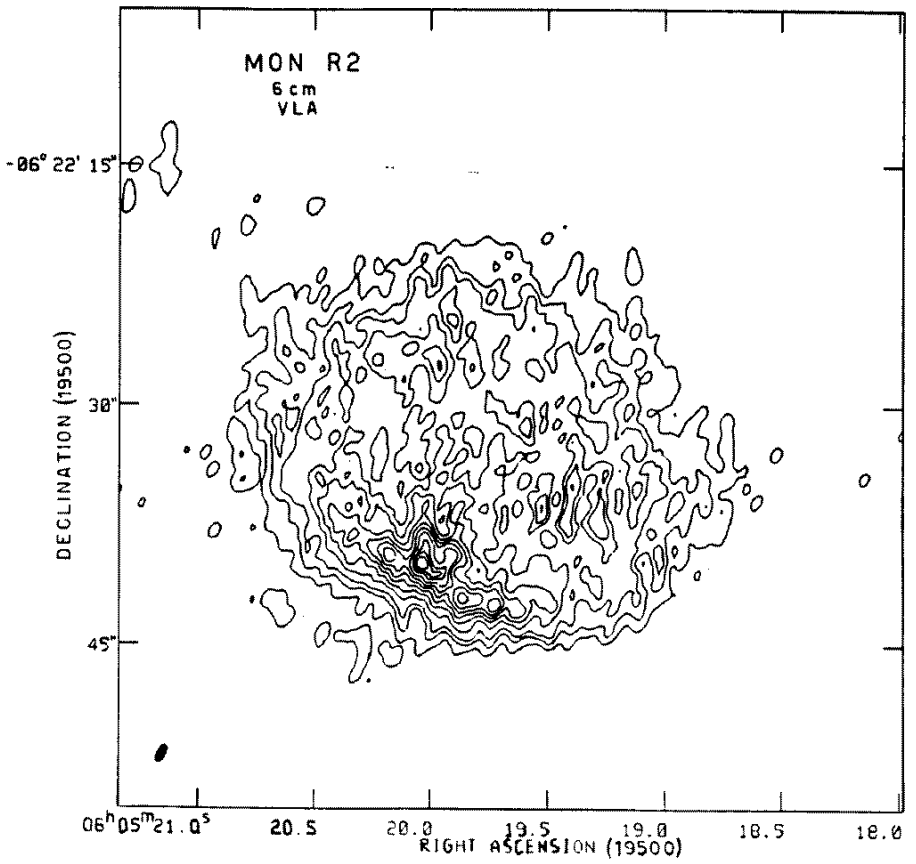

Figure 3.28: 6 cm radio continuum image of Mon R2 reproduced from Fig. 1 of Massi, Felli & Simon (1985).

An early submillimeter map at 870μm with 18$''$ (0.072 pc) resolution obtained at the Swedish ESO Submillimeter Telescope (SEST) revealed seven dust clumps in the Mon R2 cluster (Henning, Chini & Pfau 1992) which were interpreted as remnants of star formation. The SHARC 350μm image of Mon R2 is shown in Fig. 3.29. The peak emission occurs southeast of the UCHII region whose cometary tail expands to the northwest along a minimum ridge in the dust emission. As in the case of G34.3+0.2 and GGD12-15, the confidence in the absolute pointing accuracy of the SHARC map is better than 3$''$ judging by the good correspondence of the H_2O maser (coincident with IRS3) and the sub-peak of continuum emission. Thus the magnitude and direction of the offset from the UCHII region is significant and strongly confirms

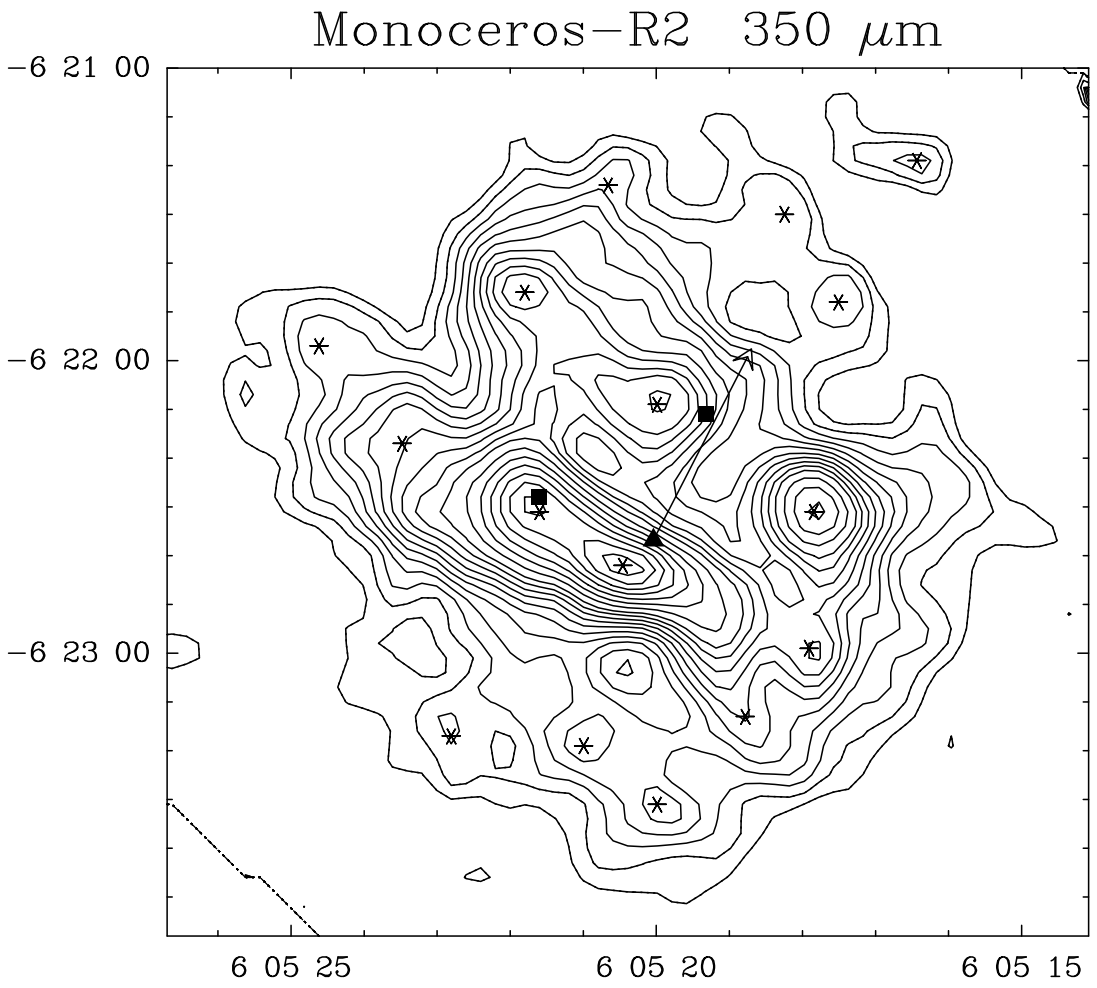

Figure 3.29: 350μm image of the Mon R2 complex (d = 0.83 kpc). Contour levels are 10 to 52 by 2 Jy/beam. The arrow marks the expansion direction of the blister UCHII region whose cometary peak is marked by the triangle (Massi, Felli & Simon 1985). The squares mark the position of the two H_2O masers (Tofani et al. 1995; Rodríguez & Cantó 1983), the eastern one being coincident with IRS3. The asterisks mark the position of submillimeter sources identified in Table 3.3.

the blister model for the HII region. In addition to the two main sources, a dozen other dust clumps surround the cloud core. Some of the clumps can be identified with the Henning, Chini & Pfau (1992) sources. A list of source positions and fluxes is compiled in Table 3.3. Some of the sources have no infrared counterpart in a deep K-band image of the region (Carpenter 1996). As this is the nearest UCHII region in the survey, the complex submillimeter structure evident here suggests that similar structure may be present (but unresolved) in the submillimeter images of the more distant sources.

Table 3.3: Observed properties of the dust clumps in Mon R2

Src	Offset*	B1950.0 Coordinates		$S_{350\mu\mathrm{m}}$	M_{gas}
#	$\Delta\alpha'', \Delta\delta''$	R.A.	Dec.	Jy	$M_\odot$
1	$-55, -31$	$06^h05^m17.^s9$	$-06°22'59''$	49	11
2	$-56, -3$	$06^h05^m17.^s8$	$-06°22'31''$	39	9
3	$-42, -45$	$06^h05^m18.^s8$	$-06°23'13''$	74	16
4	$-24, +19$	$06^h05^m20.^s0$	$-06°22'09''$	61	13
5	$-17, -14$	$06^h05^m20.^s5$	$-06°22'42''$	98	22
6	$0, -3$	$06^h05^m21.^s6$	$-06°22'31''$	92	20
7	$+3, 42$	$06^h05^m21.^s8$	$-06°21'46''$	56	12
8	$-24, -63$	$06^h05^m20.^s0$	$-06°23'31''$	36	8
9	$-9, -51$	$06^h05^m21.^s0$	$-06°23'19''$	36	8
10	$+28, +11$	$06^h05^m23.^s5$	$-06°22'17''$	44	10
11	$-61, +40$	$06^h05^m17.^s5$	$-06°21'48''$	30	7
12	$-50, +58$	$06^h05^m18.^s3$	$-06°21'30''$	26	6
13	$+18, -49$	$06^h05^m22.^s8$	$-06°23'17''$	26	6
14	$+45, +31$	$06^h05^m24.^s6$	$-06°21'57''$	29	6
15	$-14, +64$	$06^h05^m20.^s6$	$-06°21'24''$	30	7
16	$-77, +69$	$06^h05^m16.^s5$	$-06°21'19''$	28	6
Sum of 16 clumps				757	168
Total emission				2180	480

*Offsets measured from the H_2O maser associated with IRS 3

3.5.6 Summary of cometary UCHII regions

The dust surrounding cometary UCHII regions is generally extended on arc minute scales. In most cases, the position of the peak dust emission coincides with the dominant compact radio source with extended emission present along the direction of

the tail. One exception is the blister-type HII region in Mon R2 which clearly expands asymmetrically from the edge of the dust core of IRS 1 into a cavity relatively empty of dust. In most sources, additional sub-peaks of dust emission have also been identified, some of which are associated with known H_2O maser clusters and some of which are heretofore unknown sources.

3.6 SHARC images of shell-like UCHII regions

3.6.1 K3-50 complex (I19598+3324)

At a distance of 8.7 kpc (Roelfsema, Goss & Geballe 1988), K3-50 is a complex of compact HII regions associated with the W58 molecular cloud (Neugebauer & Garmire 1970). VLA observations with $0''.14$ (0.006 pc) resolution of the K3-50 radio components A and C1 reveal shell-type morphologies (Turner & Matthews 1984). On a larger scale of $5''$ (0.2 pc), component A shows an ionized bipolar structure with evidence for outflow in radio recombination lines while components B and D are diffuse HII regions roughly $40''$ (1.7 pc) in diameter lying to the northeast and southeast, respectively (DePree et al. 1994). The FIR luminosity of the entire region is $10^{6.32} L_{\odot}$ (Thronson & Harper 1979). By comparing the radio continuum to the infrared Brα line flux, the visual extinction toward A, B, C1 and C2 has been measured at $A_V = 15$, 26, 97 and 32 mag, respectively, averaged over a $15''$ aperture (Roelfsema, Goss & Geballe 1988). Component D lies behind only 2 magnitudes of extinction and is visible in optical images. Component A ($V_{\rm HII} = -27.5$ km s^{-1}) is likely to be located toward the front side of the molecular cloud (Wynn-Williams et al. 1977) while components B, C1 and C2 ($V_{\rm HII} = -21$ km s-1) are situated on the far side. In a $5''$ aperture at the peak radio position, the extinction toward C1 rises to $A_V \geq 190$ mag, implying a large hydrogen column density in a compact molecular envelope surrounding the ionizing star. H92α images of K3-50C1 reveal an outflow of ionized gas from this source (DePree, Rodríguez & Goss 1995). As a whole, component C also corresponds to ON 3, an OH maser source (Wynn-Williams, Werner & Wilson 1974). A recent deep

3.6 cm image of K3-50 (see Fig. 3.30) revealed a new faint, ultracompact component called C58.75, $\sim 15''$ (0.63 pc) south of C1 and C2 (DePree 1996). This object may be coincident with a faint near-infrared source (Howard et al. 1996).

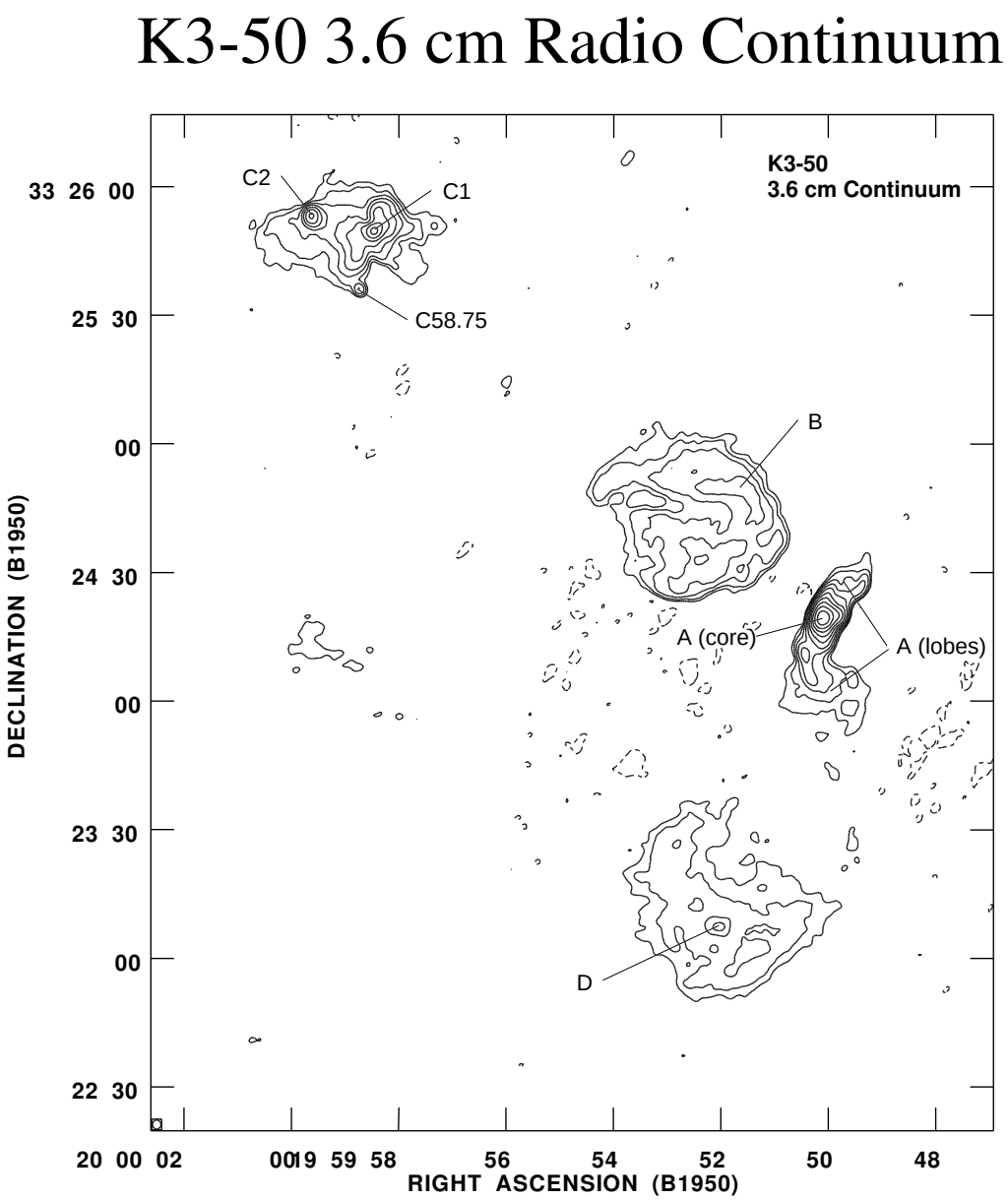

Figure 3.30: VLA 3.6 cm image of the K3-50 complex courtesy of Chris DePree.

With the exception of component D, all of the radio sources exhibit 800μm continuum emission with component A being the dominant source (see Fig. 3.31). The 350μm image of K3-50 in Fig. 3.32 provides a more detailed picture of the dust emission from the HII regions. The brightest dust source is coincident with K3-50A with a strikingly round distribution, confirming its frequent use as a submillimeter pointing source (Sandell 1994). Some faint extended emission lies to the northeast near the diffuse HII component B. Another ridge of dust is seen toward components C1 and C2 and brightening toward the south at the newly-discovered radio source C58.75. A CO J=2$\rightarrow$1 map taken at the CSO also reveals a molecular outflow emerging from the position of C58.75. These three findings indicate that C58.75 is probably the youngest massive protostar in the region. Fortunately, K3-50A and C are sufficiently separated to be resolved in the IRAS HIRES images, shown in Fig. 3.6. Separate greybody model fits to their spectral energy distribution indicate that component C is cooler than A (32 K vs. 56 K). Because the dust is heated internally, this temperature difference is consistent with the higher extinction measured toward component C and may indicate that the embedded stars there are younger than those of component A.

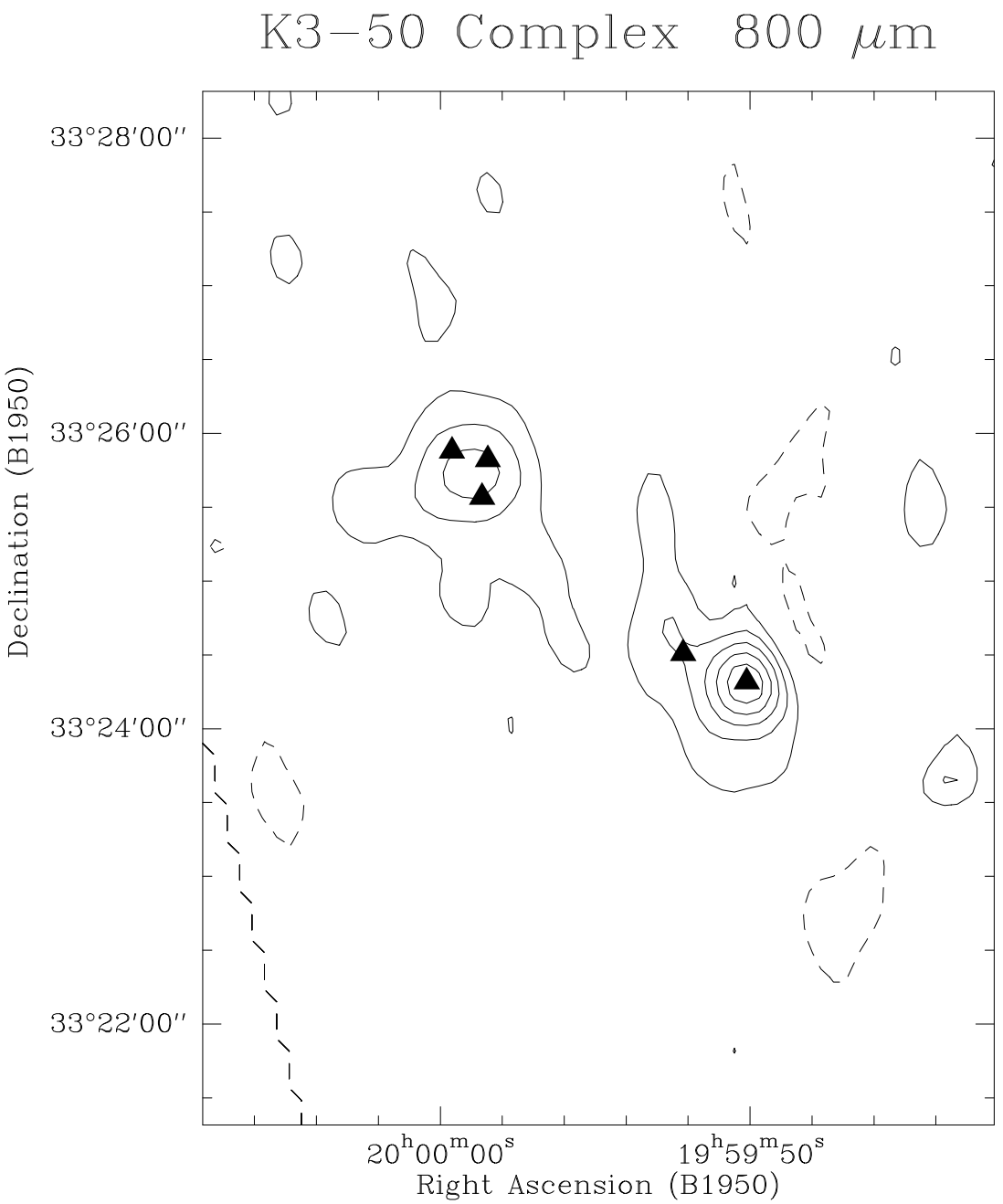

Figure 3.31: 800μm image of the K3-50 complex. Contour levels are -5, 5 to 25 by 5 Jy/beam. Triangles mark the position of the five radio components (A,B,C1,C2,C58.75) labelled in Fig. 3.32.

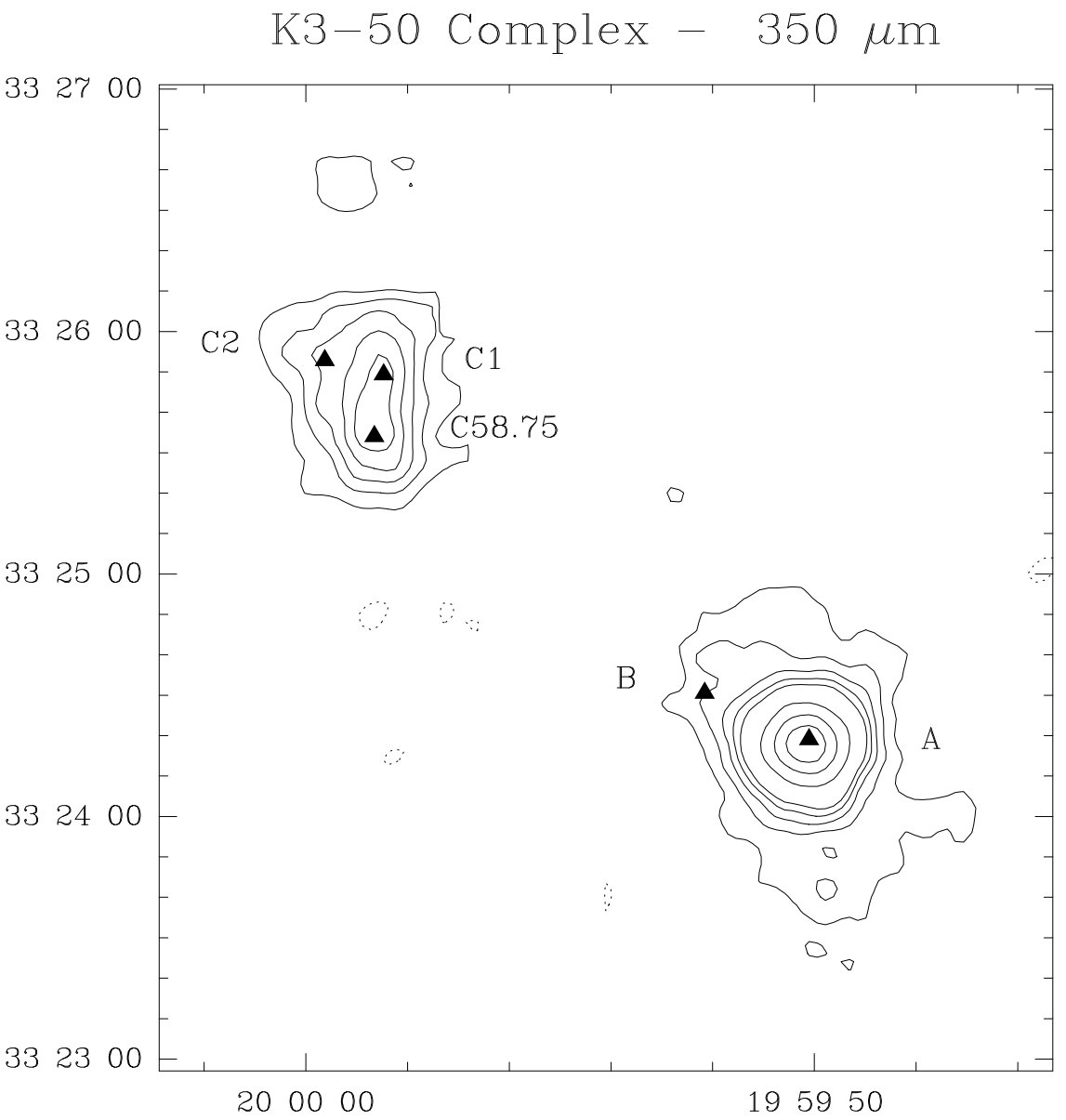

Figure 3.32: SHARC 350μm image of the K3-50 complex. Contour levels are -10, 10, 20, 30, 40, 50 to 250 by 50 Jy/beam. The radio continuum components are marked by triangles and labels (DePree et al. 1994; DePree 1996).

3.6.2 W3(OH) (G133.95+1.06, IC1795)

Discovered during the Westerhout (1958) radio survey, W3 is a complex of three HII regions (Schraml & Mezger 1969). Lying about 15′ southeast of the main radio component, W3(OH) is the prototypical shell-type UCHII region (Dreher & Welch 1981) with embedded concentrations of OH masers (Reid et al. 1980; Fouquet & Reid 1982; Norris, Booth & Diamond 1982) and CH_3OH masers (Menten 1992). Evidence for gravitational infall has been seen in the form of redshifted NH_3 absorption features (Keto 1987; Reid, Myers & Bieging 1987). Lying $\sim 7''$ (0.075 pc) east of the UCHII region is a group of 22 GHz H_2O masers (see Fig. 3.33) coincident with a faint millimeter continuum source known as the Turner-Welch (TW) object (Turner & Welch 1984). Maser emission in the 321 GHz ($10_{2,9} \rightarrow 9_{3,6}$) transition (Menten,

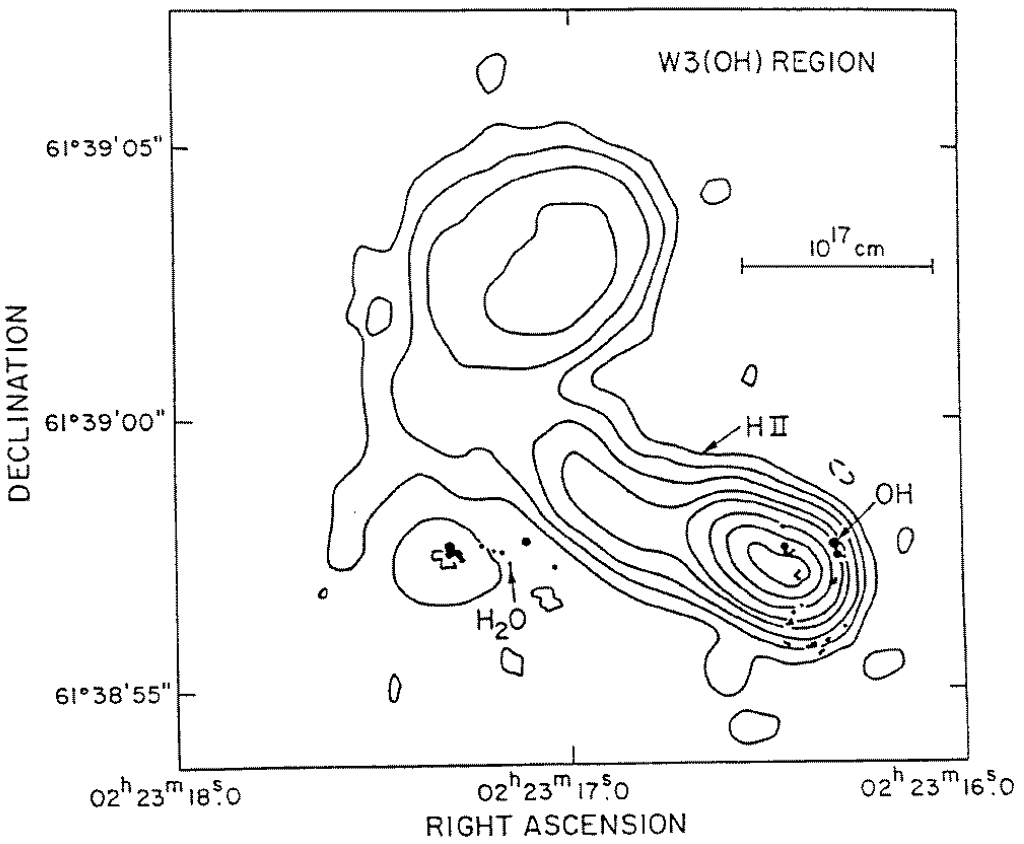

Figure 3.33: 18 cm radio continuum image of W3(OH) reproduced from Reid & Moran (1988).

Melnick & Phillips 1990) and the 183 GHz ($3_{1,3} \rightarrow 2_{2,0}$) transition (Cernicharo et

al. 1990) has also been detected from this source. Frequently dubbed as a massive protostar, this (as yet) unresolved object was recently measured to be 43 mJy and $< 0\farcs7$ (500 AU) in diameter at 87.7 GHz with the BIMA array (Wilner, Welch & Forster 1995).

At a distance of 2.2 kpc (Humphreys 1978), the FIR luminosity of W3(OH) is approximately $10^{5.0} L_\odot$ (Harper 1974; Thronson & Harper 1979). As shown in the CSO 800μm map in Fig. 3.34, the dust emission from W3(OH) peaks at the position of the UCHII region. However, some contribution of dust emission no doubt comes from the TW object. When compared with the 110 GHz IRAM flux measurement of 112 mJy (Wink et al. 1994), the 3 millimeter flux from the TW object is consistent with optically-thin dust emission with a submillimeter spectral index ~ 4, implying a dust mass in the range of 3 to $60 M_\odot$. This mass estimate is barely compatible with the $60 M_\odot$ $C^{18}O$ clump identified at the same position (Wink et al. 1994). The dust interpretation is also easily compatible with the upper limit of 1 mJy at 23 GHz (Wilson, Johnston & Mauersberger 1991).

Shown in Fig. 3.35, the SHARC image of W3(OH) gives a more sensitive picture of the region. Similar to an unpublished JCMT 450μm map (Sandell 1994), the 350μm dust emission peaks near the UCHII region with noticeable extension toward the east and northeast. The flux at the position of the TW object is 295 Jy/beam. Since the TW object is subarcsecond in size, this measurement is an upper limit to its submillimeter flux. The total angular extent of the dust emission in the region (about $80''$, 0.85 pc) matches well with the size of the molecular cloud measured from VLA H_2CO observations (Dickel et al. 1984). The FWHM of the 350μm emission is $20''$ (0.21 pc). As observed with the Kuiper Airborne Observatory (KAO), the deconvolved FWHM sizes of the FIR emission are $8''$ and $13''$ at 50 and 100μm, respectively (Campbell et al. 1989).

An interesting feature is the filament extending to the northeast which matches the shape and location of the NH_3 filament imaged by Wilson, Gaume & Johnston (1993). Although the authors offer several possible explanations for the filament, we note that the feature is analogous to the filamentary structures seen in $C^{18}O$ emission

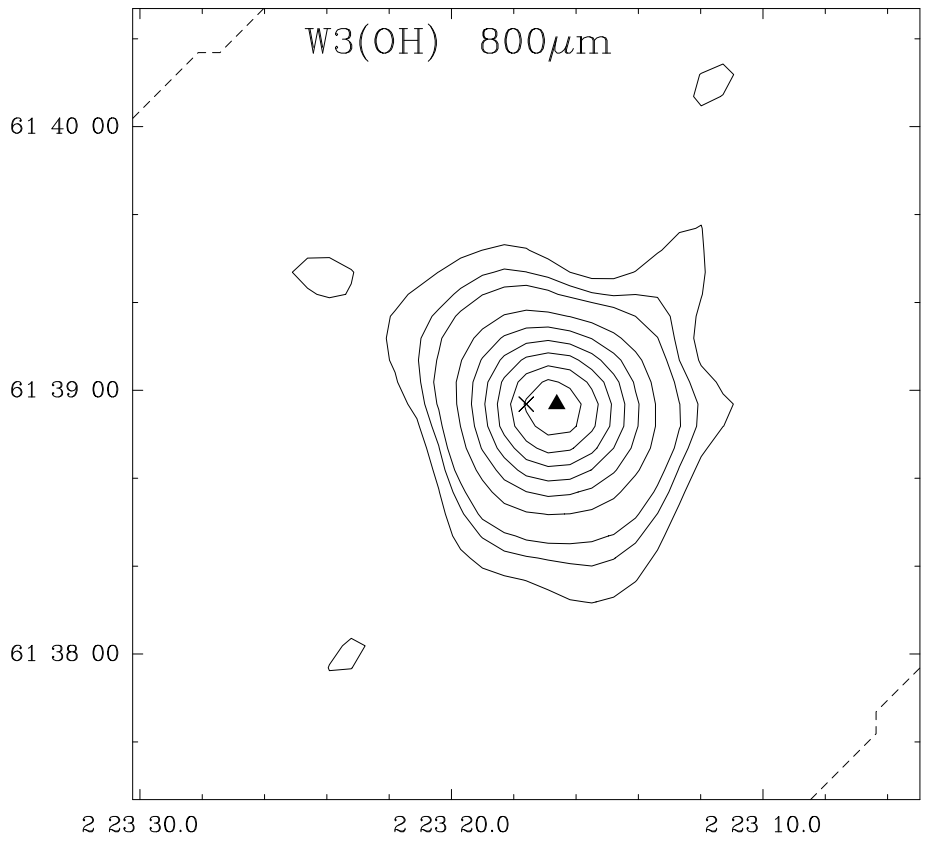

Figure 3.34: 800μm image of W3(OH). Contour levels are 6, 8, 10 to 40 by 5 Jy/beam. The position of the UCHII region is marked by the triangle (Dreher & Welch 1981) and the TW object is marked by the cross (Turner & Welch 1984).

in the Ophiuchus complex (de Geus & Burton 1991) and to the filaments emerging from the core of Orion A seen in both molecular line (Tatematsu et al. 1993) and continuum emission (Wiseman & Ho 1996; Lis et al. 1996). The nature of these filaments remains unclear though they seem to be common in molecular clouds.

3.6.3 Summary of shell-like UCHII regions

As is the case in the cometary UCHII regions, the dust surrounding the shell-like UCHII regions is concentrated about the position of the radio sources. Elongations in the dust cores match the distribution of the compact sources. Lower level dust emission also comes from the more diffuse HII regions in the vicinity of the compact sources.

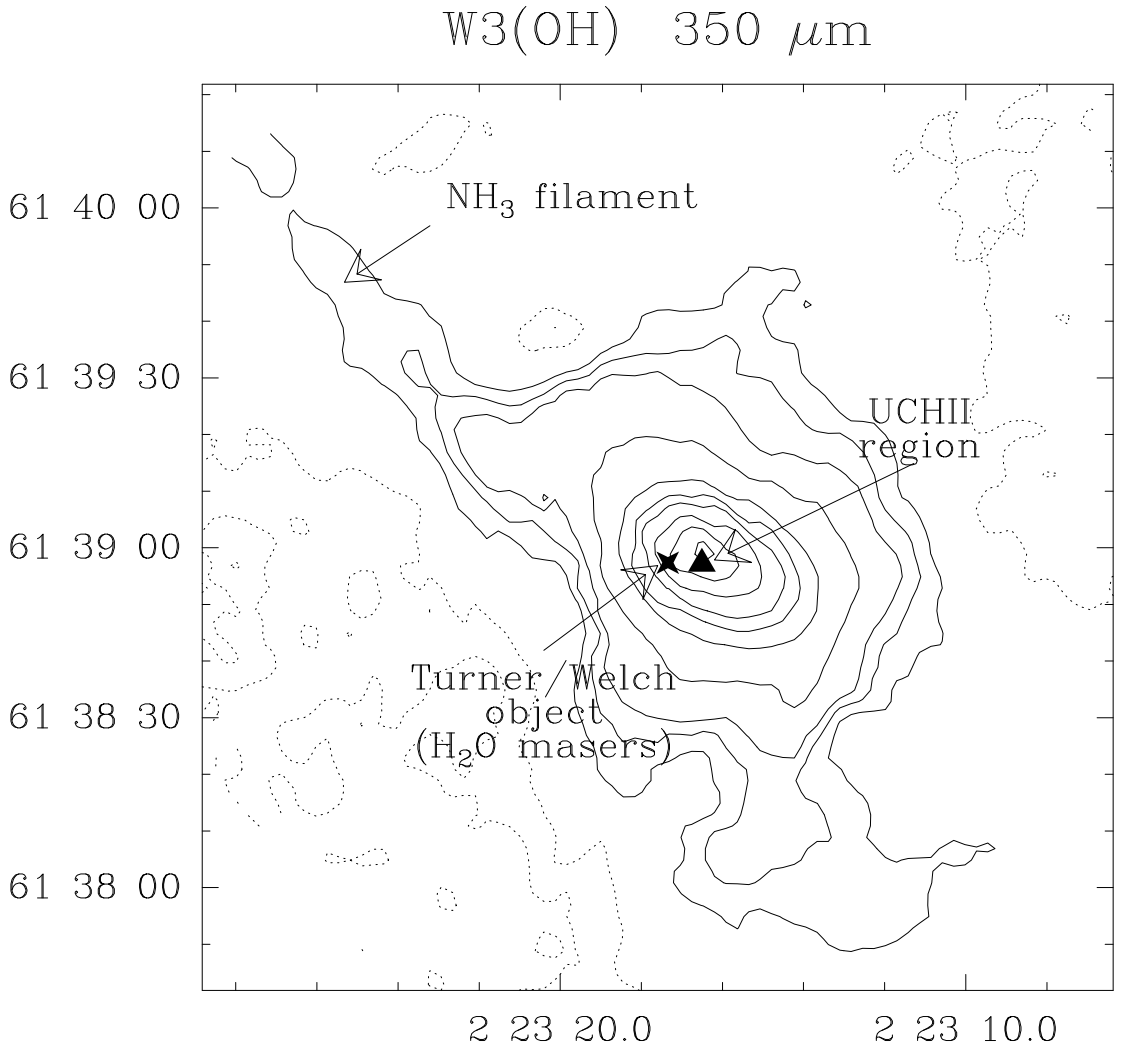

Figure 3.35: 350μm image of W3(OH) (d = 2.2 kpc). Contour levels are -15, 15, 30, 60, 120, 180, 240 to 600 by 120 Jy/beam. The position of the UCHII region and TW object are marked (Turner & Welch 1984). A filament of dust emission matches the NH_3 imaged at the VLA by Wilson, Gaume & Johnston (1993).

3.7 SHARC images of unresolved UCHII regions

3.7.1 G240.31+0.07 (I07427-2400, FIRSSE 223)

At a distance of 6.6 kpc, G240.31+0.07 was discovered to be a H_2O maser source with the Effelsberg 100-m telescope (Henning et al. 1992). Subsequently, it was found to exhibit broad CO J=1→0 line wings and a 8.4 GHz point source with a flux consistent with a B0.5 star (McCutcheon et al. 1995). The total FIR luminosity of the IRAS source is $10^{4.69} L_{\odot}$, consistent with an O9 star (Shepherd & Churchwell 1996a). A bipolar molecular outflow from the UCHII region G240.31+0.07 was resolved in a CO J=1→0 map by Shepherd & Churchwell (1996a). This discovery prompted further interest in this source. The 350μm SHARC image in Fig. 3.36 shows a compact dust core coincident with the UCHII region.

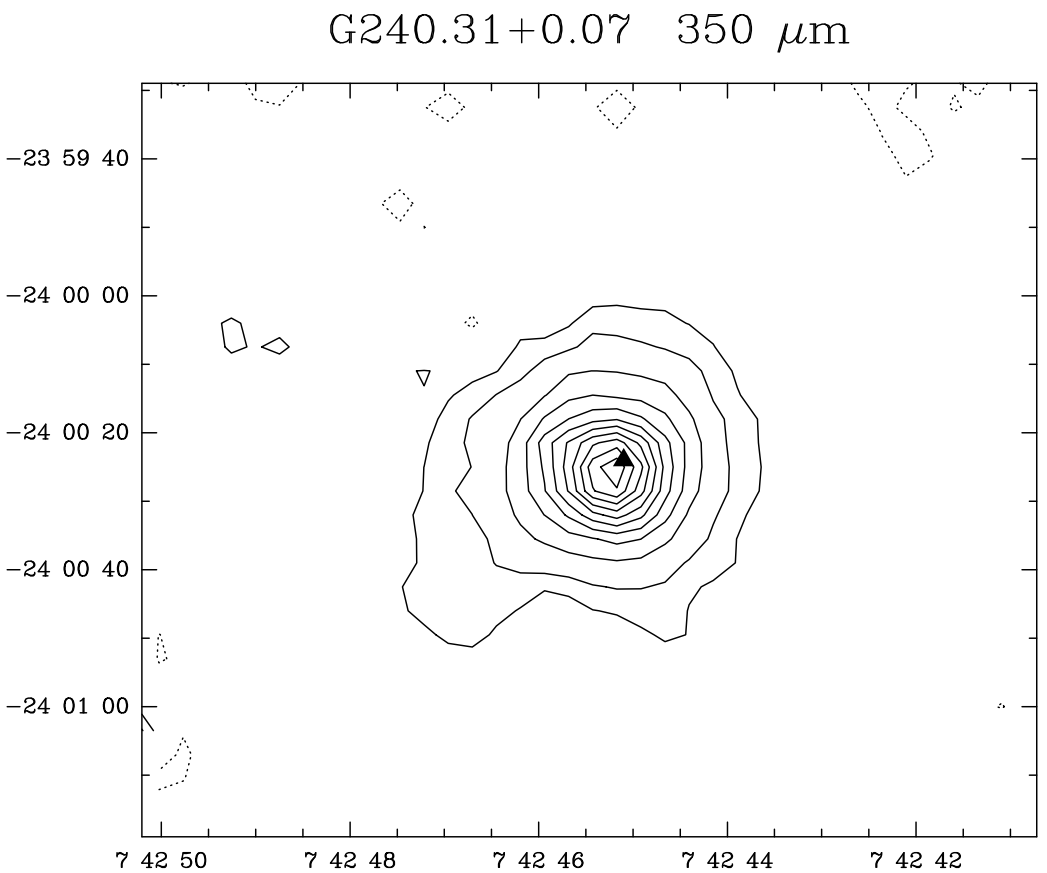

Figure 3.36: 350μm image of G240.31 (d = 6.6 kpc). Contour levels are -5, 5, 10 to 110 by 10 Jy/beam. The triangle marks the UCHII region (McCutcheon et al. 1995).

3.7.2 G138.295+1.555 & G138.300+1.558 (AFGL 4029, W5 East, I02575+6017)

The molecular cloud IC1848A lies at the border of the extended HII region S199 (W5) at a distance of 3.8 kpc. . Embedded in this cloud are the radio continuum sources G138.295+1.555 and G138.300+1.558 which have been imaged with the VLA Kurtz, Churchwell & Wood (1994). In a $40''$ beam, H_2O maser and NH_3 emission has been detected from this region (Churchwell, Walmsley & Cesaroni 1990) which is associated with the infrared cluster Air Force Geophysical Laboratory (AFGL) AFGL 4029 (Price & Murdock 1983). An optical and near-infrared study of the cluster reveals over 30 young B stars, the most massive of which ionizes the UCHII region G138.300+1.558 near the center of the cluster (Deharveng et al. 1996). The luminous ($10^4 L_\odot$) highly-reddened ($A_V = 25 - 30$ mag) object AFGL 4029-IRS1 corresponds to the radio source G138.295+1.555 which is likely to be an ionized stellar wind accompanied by a high velocity optical jet. A CO outflow is also identified with this source (Snell et al. 1988).

The 350μm SHARC image shows that the bulk of the dust emission is associated with G138.295+1.555 and lies in a short ridge that is elongated north-south. The ridge runs perpendicular to the CO outflow (see Fig. 4.5 in Chapter 4). There is no significant dust emission at the position of G138.300+1.558 and the near-infrared cluster. Apparently, the bulk of the dust lies around the younger source G138.295+1.555, which probably accounts for the H_2O maser and NH_3 emission as well.

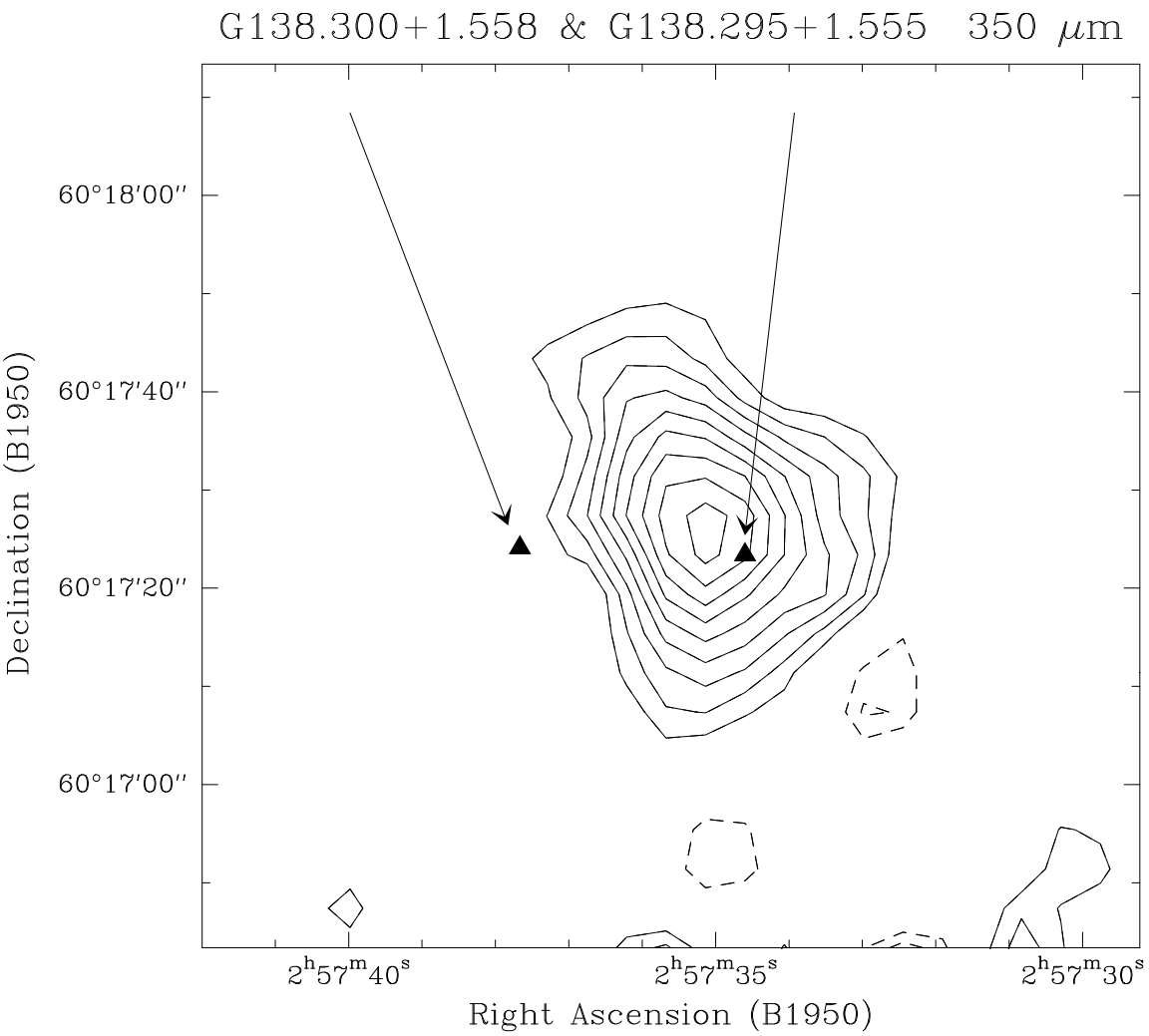

Figure 3.37: 350μm image of G138.300+1.558 and G138.295+1.555 (d = 3.8 kpc). Contour levels are 4 to 20 by 2 Jy/beam. The triangles mark the positions of the UCHII regions from Kurtz, Churchwell & Wood (1994).

3.7.3 G139.909+0.197 (AFGL 437, I03035+5819)

AFGL 437 is a compact cluster of a few dozen young stars and a reflection nebula over $30''$ (0.3 pc) in diameter in the near-infrared (Weintraub & Kastner 1996). Near the center of the cluster lie two UCHII regions imaged with the VLA (Kurtz, Churchwell & Wood 1994) and an H_2O maser (Torrelles et al. 1992). H_2O maser and NH_3 emission has been detected by Churchwell, Walmsley & Cesaroni (1990). At a distance of 2.0 ± 0.5 kpc (Arquilla & Goldsmith 1984), the total FIR (IRAS) luminosity of the cluster is $10^{4.18} L_\odot$. A wide, apparently poorly-collimated molecular outflow emerges from the center of the cluster (Gómez et al. 1992). From polarimetric imaging of the outflow cavity, Weintraub & Kastner (1996) suggest that the young stellar object WK 34 (which coincides with the H_2O maser position) illuminates the reflection nebula and drives the outflow. In Fig. 3.38, we see that the 350μm emission extends around the position of the UCHII region and the WK 34 source with an additional peak to the east near the other UCHII region. The further extent of the submillimeter emission may originate from other embedded members in the cluster (Weintraub et al. 1996).

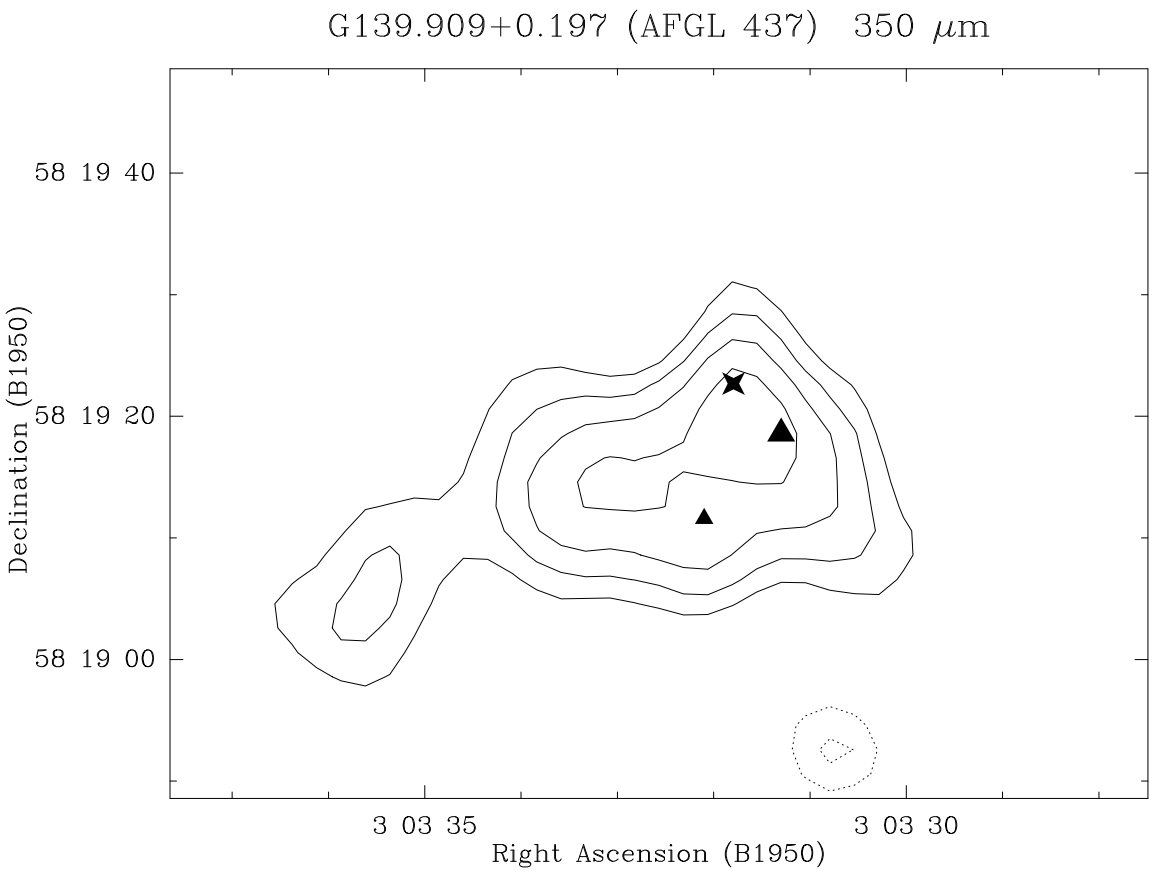

Figure 3.38: 350μm image of the G139.909+0.197 complex (d = 2.0 kpc). The large triangle marks the position of the main UCHII region while the smaller triangle marks a fainter 8.4 GHz source (Kurtz, Churchwell & Wood 1994). The cross marks the H_2O/infrared source WK 34 (Torrelles et al. 1992; Weintraub & Kastner 1996). Contour levels are -8, -6, 6 to 18 by 2 Jy/beam.

3.7.4 S255 complex (AFGL 896, I06099+1800)

Lying at a distance of 2.5 kpc (Mezger et al. 1988), the S255 molecular cloud is associated with a cluster of red nebulae S254-S257 (Sharpless 1959) with extended radio continuum emission. Also present in the cloud between two of the extended HII regions (S255 & S257) are several UCHII regions (see Fig. 3.39) labelled S255-1 = G192.584-0.041 (Israel 1976; Rengarajan & Ho 1996) and three fainter $\sim$ 1 mJy sources called S255-2a,b,c (Snell & Bally 1986).

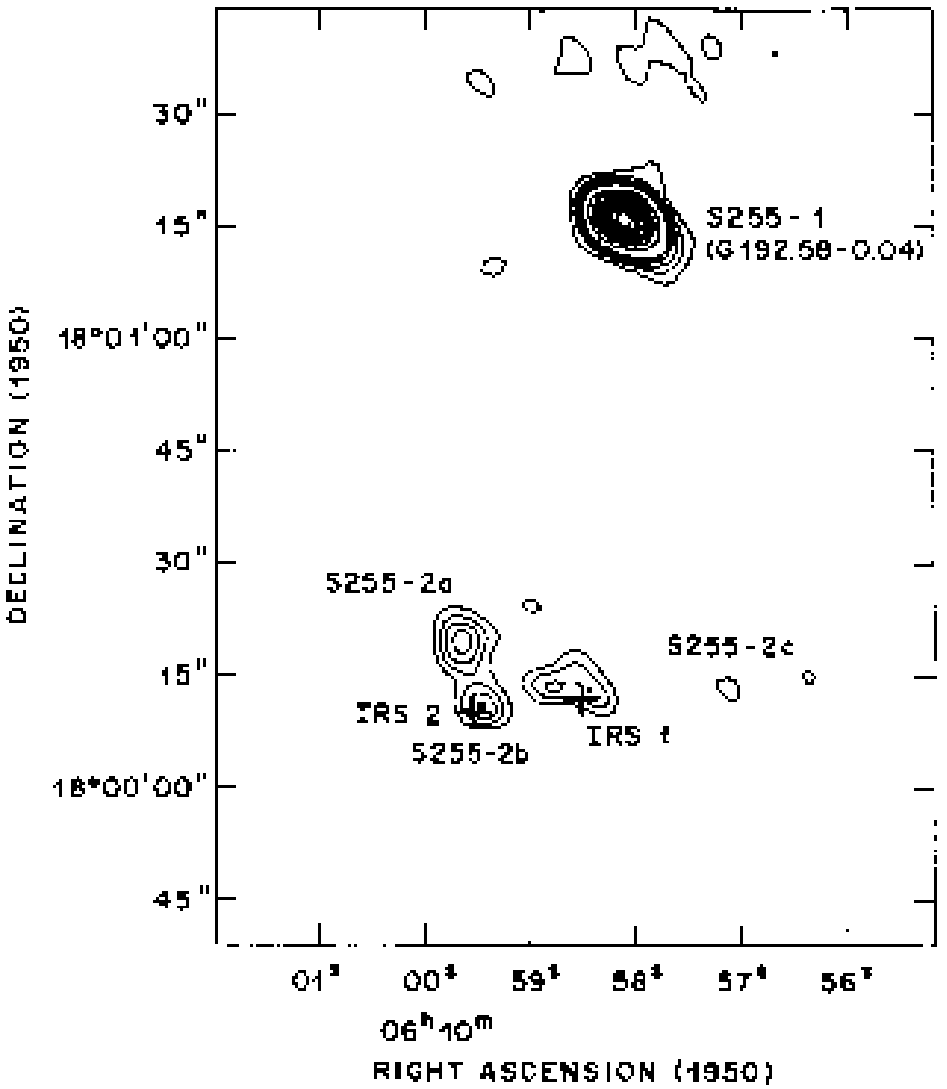

Figure 3.39: 5 GHz VLA image of the S255 molecular cloud complex reproduced from Fig. 11 of Snell & Bally (1986).

A possible tracer of shocked gas in outflows, blueshifted OH absorption appears in front of G192.584-0.041 (Ruiz et al. 1992). Components S255-2b and 2c coincide with the 20μm sources IRS 1 and IRS 2 (Beichman, Becklin & Wynn-Williams 1979). Associated with S255-2 is a cluster of 32 near-infrared sources all but 2 of which are invisible on the Palomar Observatory Sky Survey (POSS) plate (Tamura et al. 1991). Early FIR and submillimeter maps revealed two peaks separated by $\sim 1'$ in declination and coinciding with the two sources S255-1 and S255-2 (Jaffe et al. 1984; Richardson et al. 1985). Higher resolution 1.3 mm continuum maps with the IRAM 30-m telescope resolved the dust emission into distinct clumps including a third source south of the first two cores called FIR-3 (Mezger et al. 1988). All three sources are seen in the SHARC image in Fig. 3.40.

Also visible in the SHARC image, significant extended emission lies between S255-FIR1 and S255-FIR2. Four extensions of dust match with extensions in the CS J=7$\rightarrow$6 emission of the region shown as indicated by the stars in Fig. 3.41.

The S255 region has been studied in detail in the near-infrared by Howard (1996). Shown in Fig. 3.42, is an enlargement about the source S255-FIR2 with the 350μm contours overlaying a K-band image in greyscale. More than any other, this image indicates the great potential of detailed comparison of submillimeter and infrared data. The submillimeter emission locates the raw materials of star formation while the near-infrared emission identifies the embedded young stellar objects. The main structure at 350μm is a bowl-like feature extending to the northeast. In the near-infrared, the central core region of S255-FIR2 shows a limb-brightened shell of molecular hydrogen emission centered on the central core with an additional enhancement of emission along the lane of reflection nebulosity that extends from IRS1 to IRS3. The lower half of the bowl seen in 350 μm emission is also seen in H_2 as the southeastern extension of the shell (Howard 1996). The northern half of the bowl is not as clearly seen, however the northern extension of the shell lies in the direction of the northern half of 350 μm bowl-like feature.

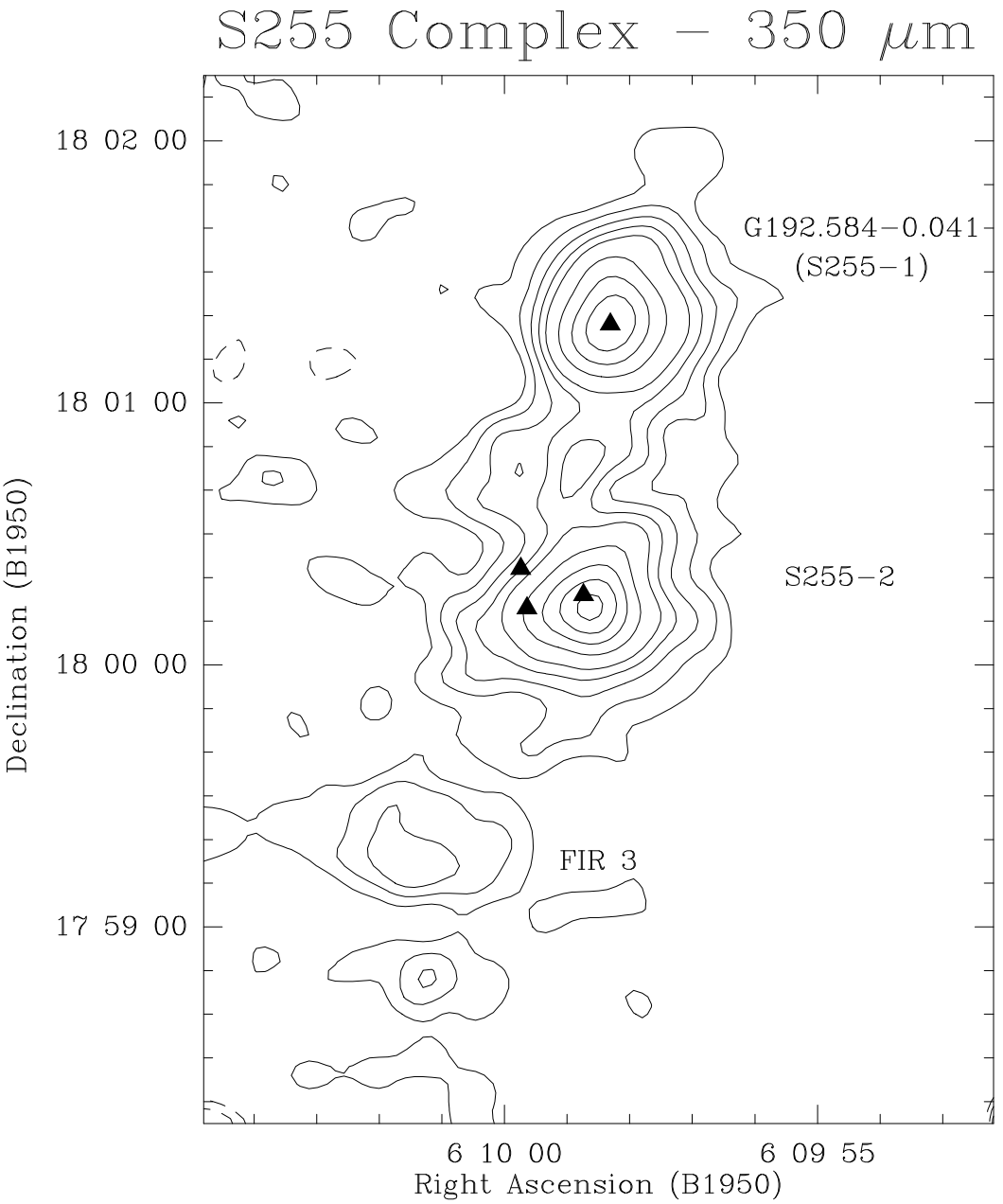

Figure 3.40: 350μm image of the S255 complex (d = 2.5 kpc). Contour levels are 4 to 12 by 4 and 16 to 28 by 4 Jy/beam. The three radio sources of S255-FIR2 are marked by triangles (Snell & Bally 1986) along with G192.584-0.041 (Israel 1976).

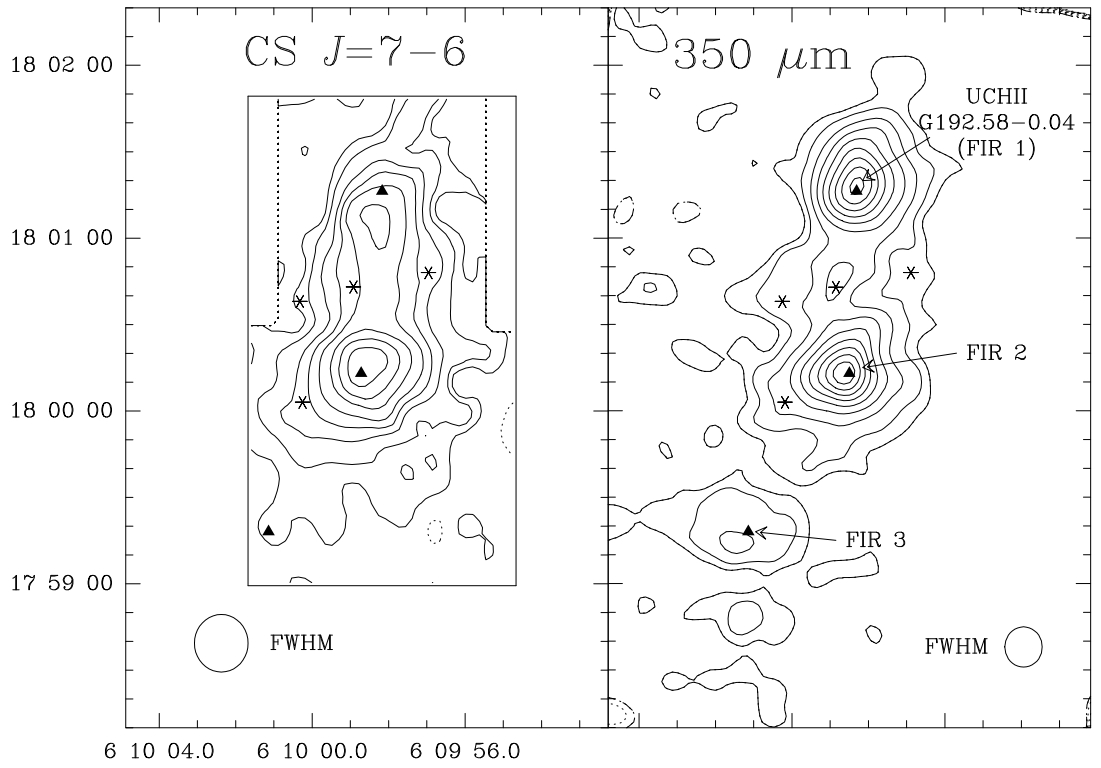

Figure 3.41: Left panel: CS J=7→6 image of the S255 complex. Four positions in the extended envelope of gas are marked by stars. Contour levels are 1.2, 2.4, 4.8, 7.2, 10 to 40 by 4 K km s^{-1}. Right panel: 350μm image of the same region with the same positions marked.

3.7.5 Summary on unresolved UCHII regions

Most of the unresolved UCHII regions presented here coincide with compact dust cores with little extended emission, except in the case of S255 where there is evidence for faint, unidentified submillimeter sources. Compared to the rest of the sample, these UCHII regions are of lower luminosity and hence lower ionizing flux which may explain why they are unresolved at radio wavelengths. Typically associated with the regions are rich clusters of young near-infrared stars mixed in and around the dust emission.

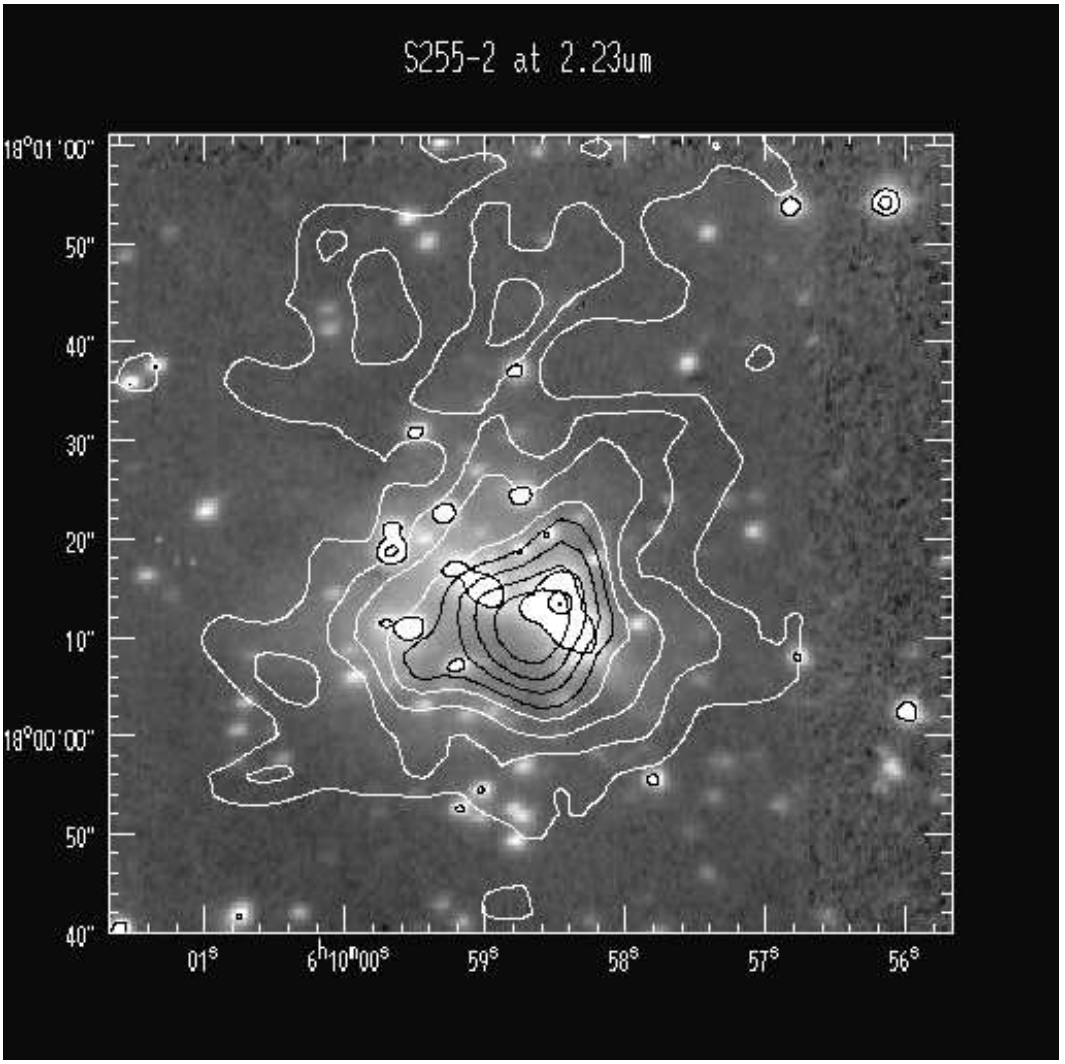

Figure 3.42: Shown in greyscale is the near-infrared K-band image (Howard 1996) centered on S255-FIR2. Overlayed are the 350μm contours with 6, 8, 10 and 12 Jy/beam shown in white contours and 14, 16, 18 and 20 Jy/beam shown in dark contours. (The dark contours surrounding white blotches are K-band contours.)

3.8 SHARC image of the G75 Complex (ON 2)

At a distance of 5.6 kpc (Wood & Churchwell 1989), the G75 complex contains several centers of compact and extended HII emission. As shown in Fig. 3.43, G75.84+0.40 is an extended double-peaked core-halo HII region lying several arcminutes to the north (Garay et al. 1993).

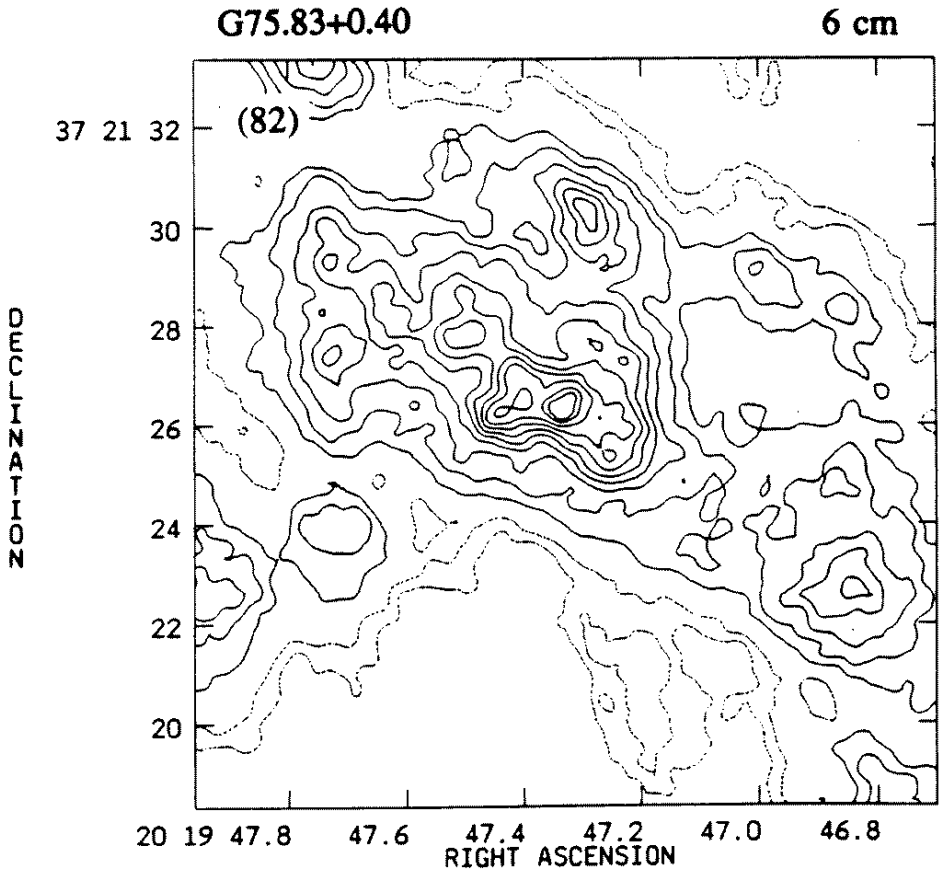

Figure 3.43: 6 cm VLA radio continuum image of G75.84+0.34 reproduced from Wood & Churchwell (1989).

As shown in Fig. 3.44, G75.78+0.34 (ON 2-N) is a cometary UCHII region lying several arcminutes to the south with associated OH maser emission and a group of H_2O maser spots (Cato et al. 1976; Walker et al. 1978; Downes et al. 1979). Dense thermal gas has also been seen in the form of NH_3 emission (Churchwell, Walmsley & Cesaroni 1990). G75.77+0.34 is a double-peaked HII region (components A and B) located about $1'$ southwest of G75.78+0.34 (Matthews et al. 1973).

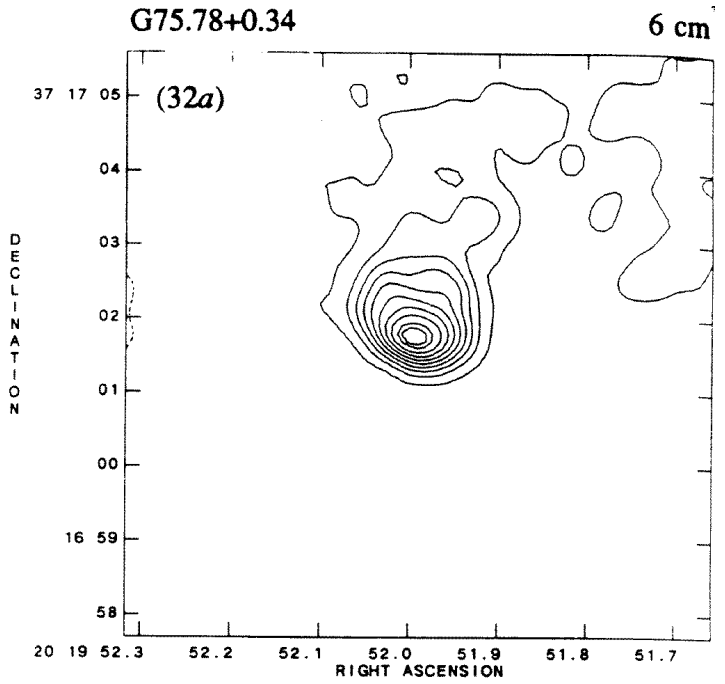

Figure 3.44: 6 cm VLA radio continuum image of G75.78+0.34 reproduced from Wood & Churchwell (1989).

Both clusters exhibit 800 and 450μm continuum emission (see Figs. 3.45 and 3.46) but G75.84+0.40 is quite diffuse, matching its radio morphology. G75.84+0.40 is also much fainter at 450μm relative to G75.78+0.34 suggesting that much of the flux is from free-free emission. Also, G75.84+0.40 was undetected in H_2O and NH_3 in the survey of Churchwell, Walmsley & Cesaroni (1990) confirming that it is a more evolved region with no dense gas nor compact sources. In contrast, the G75.78+0.34 complex contains several compact sources in the 450μm SHARC image shown in Fig. 3.46. Overlayed on the map are the positions of the UCHII regions, the millimeter CO, SiO and SO_2 peaks (Shepherd & Churchwell 1996b; Haschick & Ho 1990). Apparently, G75.78+0.34 contains a string of sources within a ridge of dust while the HII regions G75.77+0.34A and B are unassociated with prominent dust emission. Two additional submillimeter sources lie to the southwest: G75.76+0.34, recently detected as an H_2O maser (Hofner 1996b), and G75.75+0.34, unknown at other wavelengths. Like the submillimeter clumps in Mon R2 and G34.3+0.2, these sources are candidates for massive protostars which should be observed in depth at near-infrared wavelengths.

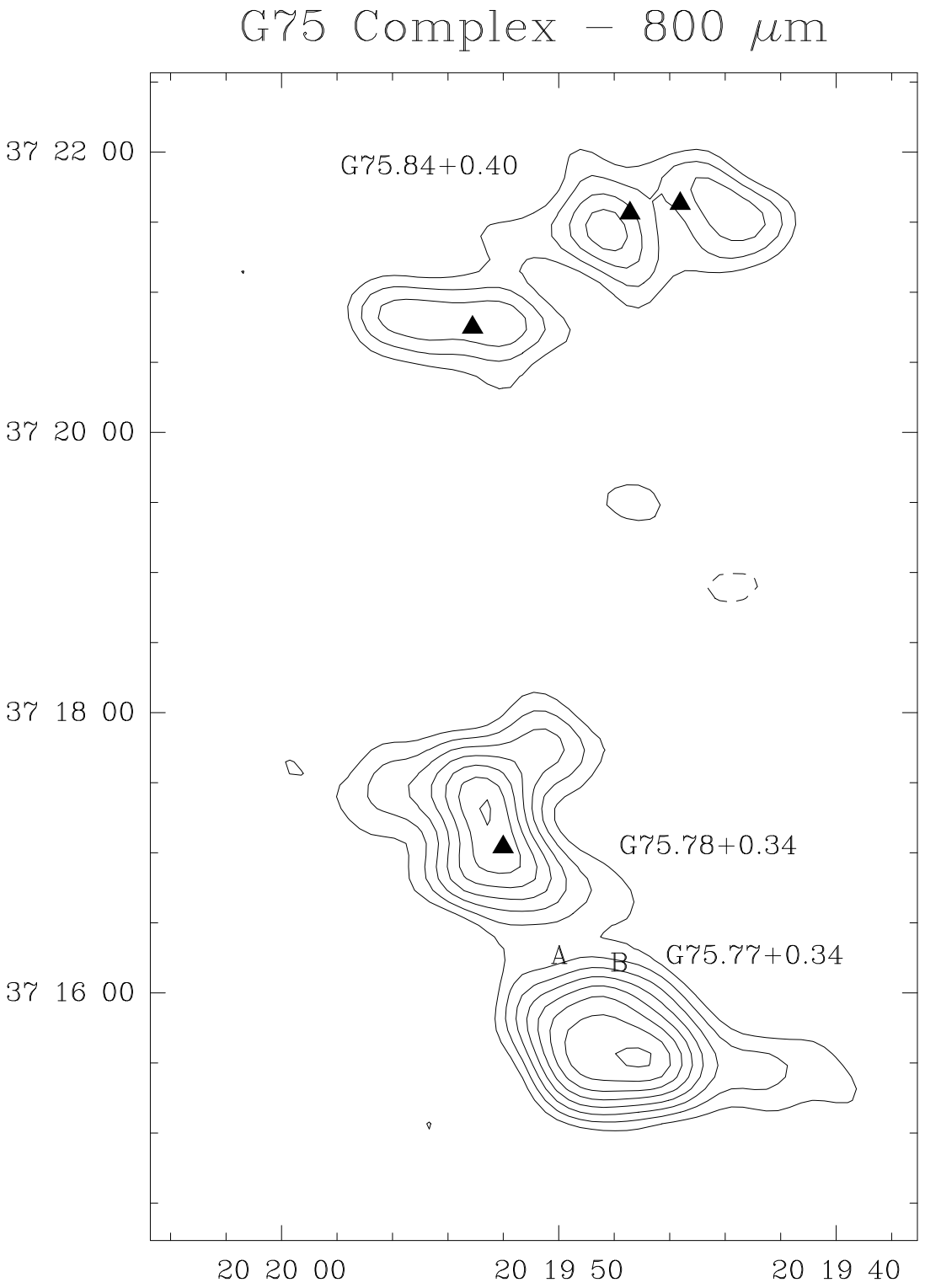

Figure 3.45: 800μm image of the G75 complex (ON 2). Contour levels are 12 to 52 by 4 Jy/beam. Triangles mark the positions of the radio continuum sources associated with the northern cluster G75.84+0.4 (Megeath et al. 1990; Pipher, Soifer & Krassner 1979) and the southern cluster G75.78+0.34 (Matthews et al. 1973).

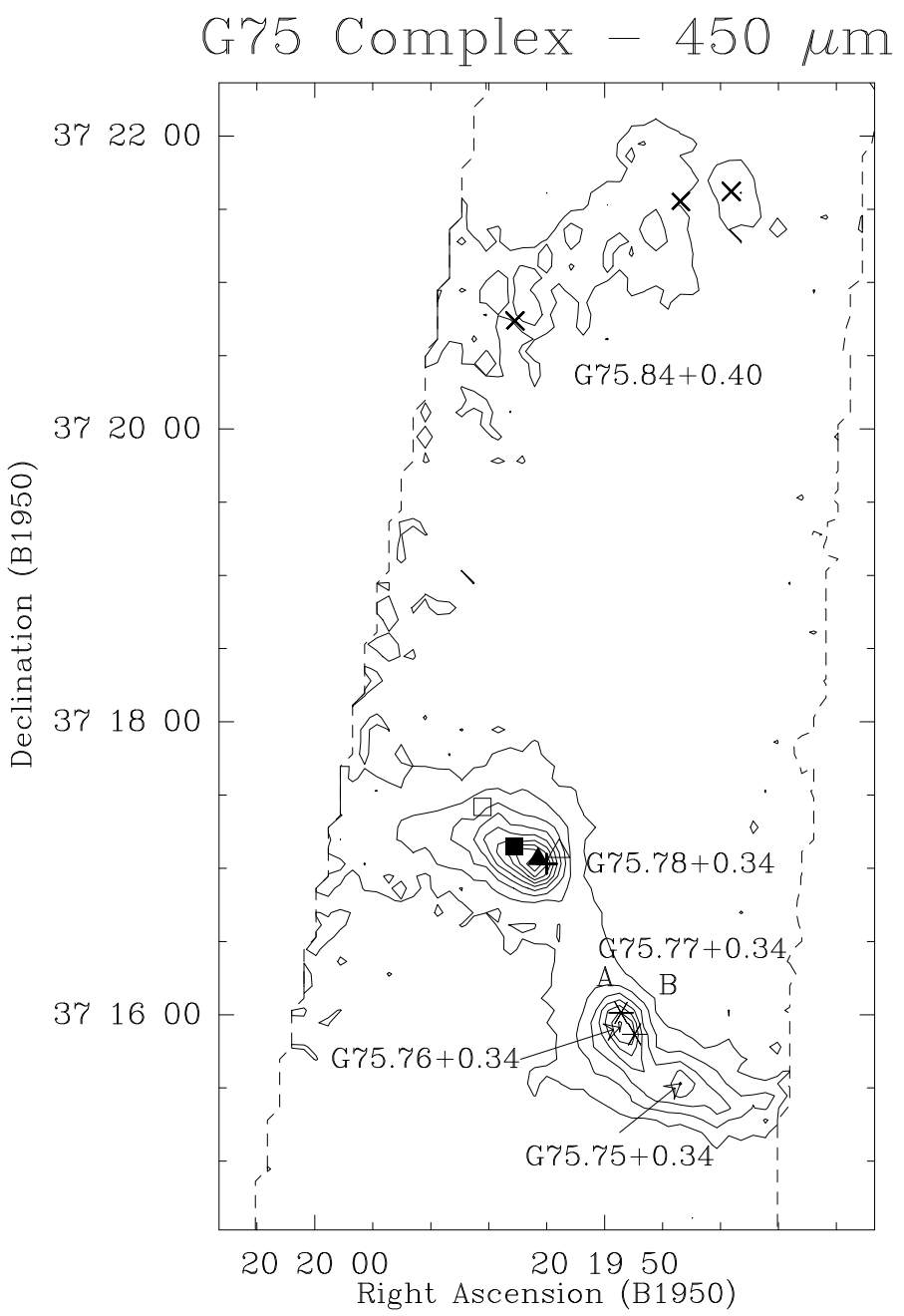

Figure 3.46: 450μm image of the G75 complex (d = 5.6 kpc) with contour levels -10, 10 to 90 by 10 Jy/beam. *Plus symbol:* G75.78+0.34 UCHII region and H_2O maser cluster (Hofner 1996b); *Filled square:* CO J=1→0 peak; *Open square:* SiO J=2→1 blob; *Filled triangle:* 115 GHz continuum peak; *Open triangle:* SO_2 blob (Shepherd & Churchwell 1996b); *Asterisk:* H_2O masers (Hofner 1996b); *Crosses:* HII region components of G75.84+0.40 (Pipher, Soifer & Krassner 1979; Garay et al. 1993). The letters A and B mark the positions of the two components of the HII region G75.77+0.34 (Matthews et al. 1973). Newly-detected submillimeter sources G75.76+0.34 and G75.75+0.34 are indicated by arrows. Dashed lines mark the edge of the map.

3.9 Greybody models

3.9.1 One-component models

In a simple first-order analysis, greybody functions have been fit to the spectral energy distribution of the 17 regions imaged with SHARC. A greybody function is simply a blackbody function multiplied by the factor $(1 - e^{-\tau_\nu})$ which accounts for the finite optical depth τ_ν of the dust cloud at all frequencies ν. The three free parameters are the dust temperature, optical depth and grain emissivity index. The source solid angle and distance is input to the program to convert to observed flux units. Using a grid search least-squares fitting routine (Bevington 1969), a single temperature greybody model was used to fit the IRAS 60 and 100μm fluxes and the SHARC 350 and/or 450μm fluxes. In most cases, 800 and 1300μm fluxes available from CSO observations or from the literature were also included in the fit. Assuming a spectral index of -0.1 from radio wavelengths, an estimate of the free-free emission contribution to the 1300μm flux was subtracted prior to the fit. Plots of the spectral energy distribution and greybody models for the 17 regions are given in Figs. 3.49 through 3.61. A summary of the model fit parameters is compiled in Table 3.4 and in Fig. 3.47. The data marked by crosses in the top 3 panels of Fig. 3.47 correspond to 3 sources which do not have flux measurements at $\lambda > 350\mu$m (G138.295+1.555, G139.909+0.197 and G240.31+0.07). The average dust temperature in the remaining 14 regions is 40 ± 10 K. This is 14 degrees cooler than the average (60μm/100μm) color temperature of all 126 UCHII regions studied in the HIRES survey (see Table 3.1). Because the model fits are less affected by the excess flux in the 60μm band contributed by warm dust, the cooler dust temperatures derived here by including the submillimeter data better portray the condition of the cool dust grains which account for the bulk of the cloud mass.

3.9.2 Two-component models

As can be seen in Figs. 3.49 through 3.64, the single component greybody models do not fit the observed 12 and 25μm fluxes. Emission at these wavelengths must come from warm dust with either low optical depth or small solid angle, i.e., primarily scattered light. In the former case, the warm dust could lie in a diffuse component more extended than the submillimeter chopper throw which would not affect the submillimeter flux measurements. However, if the warm dust is compact, escaping at only certain geometries from the core, then it could potentially affect the submillimeter measurements. The HIRES IRAS maps generally show the emission to be compact at these wavelengths. Therefore, to check whether emission from this warmer component of dust affects the submillimeter portion of the spectrum, two-component greybody models were also constructed. Five free parameters were used: the temperature, emissivity index and optical depth of the cold dust, and the temperature and optical depth of the warm dust. Because the warm dust probably consists of smaller grains without ice mantles, the emissivity index of the warm dust was held constant at $\beta = 2$. In Figs. 3.49 through 3.61, the two-component models are overlayed in dashed lines with the one-component models for the 14 sources with flux measurements at more than 5 frequencies. In nearly every source, the two-component model is indistinguishable from the one-component model at submillimeter wavelengths. Thus, the warm dust does not affect the dust properties derived from the one-component models. A comparison of the temperatures, grain emissivities and optical depths derived from the one and two-component models is given in Table 3.5.

3.9.3 Grain emissivity results

From the one-component greybody models, the average grain emissivity index (β) in the 14 regions with complete submillimeter data is 2.00 ± 0.25 with a total range of 1.35 to 2.30. These results are very consistent with those from a previous study of 12 star formation regions where $\beta = 2.0 \pm 0.4$ (Chini, Krügel & Kreysa 1986). As shown in the top right panel of Fig. 3.47, there appears to be a correlation between

the emissivity index and the dust temperature with a best fit line of $\beta = (2.89 \pm 0.30) - (0.023 \pm 0.007)T$. Because the errors are significant on both axes, the proper linear regression between two random variables was performed (Trinchieri, Fabbiano & Bandiera 1990). The data from a survey of warm clouds with larger HII regions are included as open squares in panel 3 of Fig. 3.47 (Gordon 1988). Adding these data, the correlation flattens slightly to $\beta = (2.63 \pm 0.10) - (0.015 \pm 0.002)T$. Because it includes data from 3 warmer clouds in OMC-1, this function is probably more indicative of the underlying trend of interstellar dust. One explanation for this correlation is that the dust grains in the cooler clouds are more likely to have ice mantles which steepen the grain emissivity index above $\beta = 2$. At the same time, warmer clouds have smaller grains which could flatten the grain emissivity index toward $\beta = 1$. However, the correlation may simply reflect the fact that warmer sources exhibit a broader range of dust temperatures such that their spectral energy distributions become broader via a sum of several Planck functions. Single temperature greybody models will then underestimate β in order to simulate a broader Planck function (Lis, Carlstrom & Keene 1991).

Finally, one of the definitions of a Class 0 protostar (Bachiller 1996; Barsony 1995; André 1993) is that it exhibits the ratio $L_{\rm submm}/L_{\rm bol} > 5 \times 10^{-3}$, where $L_{\rm submm}$ is the luminosity measured at $\lambda > 350\mu$m, or equivalently, $\log(L_{\rm submm}/L_{\rm bol}) > -2.30$. The average ratio over the 14 UCHII regions is -2.44, only slightly lower than the Class 0 criterion. Evidently, UCHII regions are the high mass equivalent to young low mass protostars, at least in their appearance at submillimeter wavelengths. This agreement simply reflects the fact that both classes of objects lie deeply embedded in molecular clouds.

Table 3.4: Greybody model parameters of dust around UCHII regions

Source	$D_{\rm kpc}$	T(K)	β	$\tau_{350\mu{\rm m}}$	FWHM($''$)	$d_{\rm pc}$	$\log(\frac{L}{L_\odot})$	$\log(\frac{L_{\rm submm}}{L})$	$\log(\frac{M}{M_\odot})$	$\frac{L/L_\odot}{M/M_\odot}$	$\log(\frac{N_H}{\rm cm^2})$	$\log(\frac{n_H}{\rm cm^3})$
G19.61-0.23	4.5	46	1.35	0.10	20	0.44	5.31	−2.46	3.19	130	23.97	5.84
G29.96-0.02	7.4	53	1.95	0.16	17	0.61	6.09	−2.72	3.96	130	24.46	6.18
G34.3+0.2	3.7	44	2.20	0.37	34	0.61	5.80	−2.24	4.43	23	24.93	6.65
G45.07+0.13	8.3	42	1.90	0.08	20	0.81	5.77	−2.57	3.89	76	24.15	5.75
G45.12+0.13	8.3	30	2.15	0.06	46	1.9	5.75	−2.23	4.57	25	24.10	5.34
G75.78+0.34	5.6	38	1.95	0.04	41	1.1	5.65	−2.60	3.83	66	23.80	5.26
G75.84+0.40	5.6	40	1.80	0.07	60	1.6	5.72	−2.79	3.55	150	23.19	4.49
K3-50A	8.7	56	1.95	0.14	17	0.72	6.32	−2.85	4.02	200	24.38	6.03
K3-50C	8.7	33	2.25	0.08	30	1.3	5.65	−2.30	4.41	17	24.27	5.68
G192.584-0.041	2.5	23	2.30	0.09	30	0.36	3.86	−1.79	3.42	3	24.38	6.33
S255-FIR2	2.5	41	1.80	0.03	34	0.41	4.82	−2.68	2.79	110	23.63	5.52
GGD12-15	1.0	27	2.30	0.19	39	0.19	3.79	−1.86	3.16	4	24.68	6.91
Monoceros R2	0.83	33	2.20	0.02	90	0.36	4.29	−2.55	2.74	35	23.69	5.64
W3(OH)	2.2	60	1.95	0.45	20	0.21	5.43	−2.52	3.47	91	24.89	7.08
*Average of 14		40	2.00	0.14		0.61	5.30	−2.44	3.68	76	24.28	5.90
G138.295+1.555	2.2	42	1.00	0.04	22	0.41	4.03	−2.18	2.04	98	23.36	5.50
G139.909-0.197	2.0	44	1.15	0.02	27	0.50	4.01	−2.38	1.87	140	23.10	5.19
G240.31+0.07	6.6	47	0.65	0.04	15	0.48	4.77	−2.09	2.60	150	23.31	5.13

*The last three sources lack millimeter flux measurements making the computed parameters less constrained.

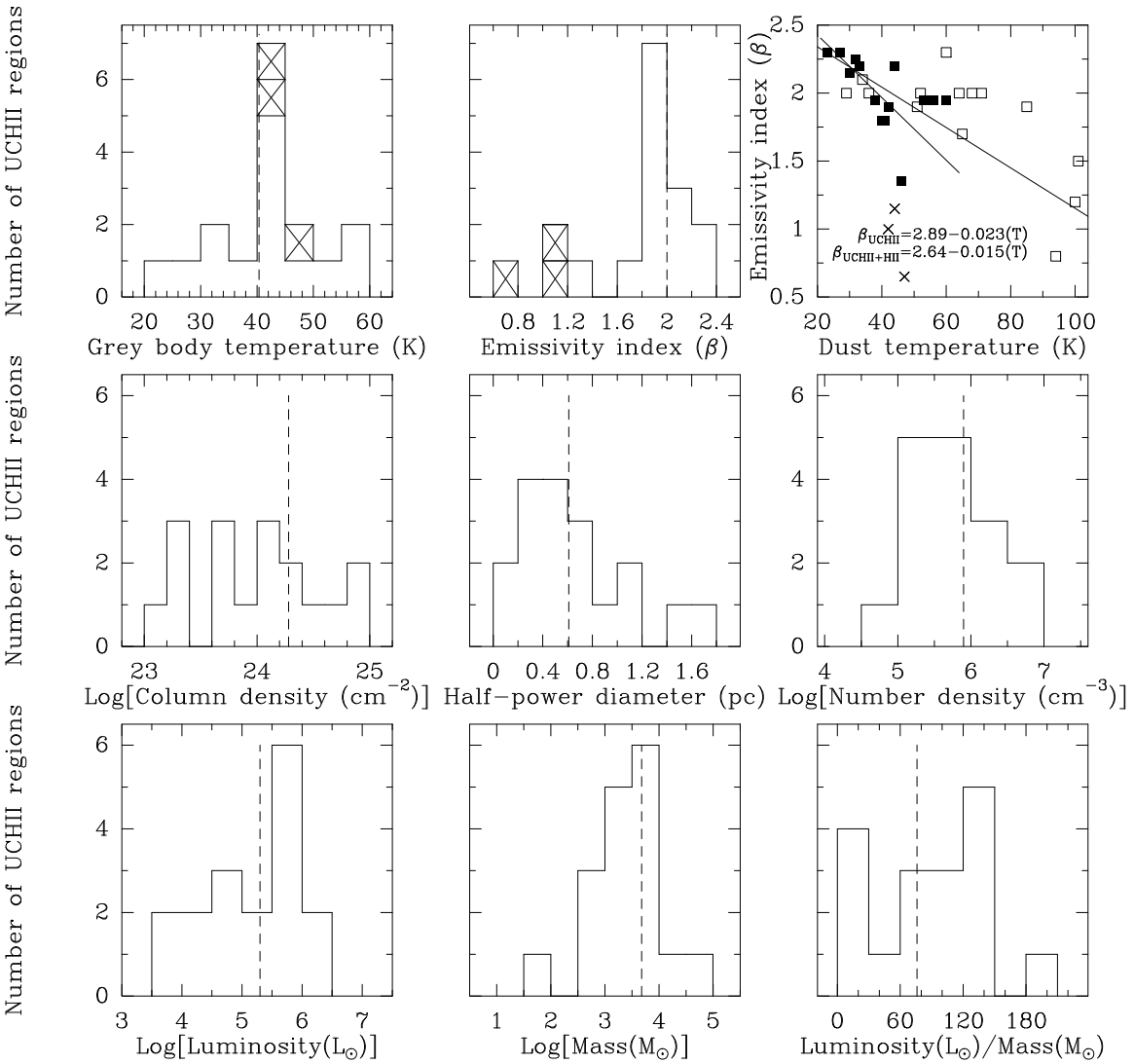

Figure 3.47: Histograms of the temperature, submillimeter grain emissivity, column density, diameter, number density, luminosity, mass and luminosity-to-mass ratio derived from greybody models of the spectral energy distribution of the 17 regions studied. 3 regions with non-existent long wavelength (1.3 mm) flux measurements are marked by crosses in the top 3 panels. Open squares in the top right panel are data from Gordon (1988). The vertical dashed line in each panel marks the average value of the 14 sources with complete submillimeter flux data.

Table 3.5: Comparison of the one- and two-component greybody models

	One component			Two components					
Source	T(K)	β	$\tau_{125\mu m}$	$T_{\rm Cold}$(K)	$\beta_{\rm Cold}$	$\tau_{\rm Cold:125\mu m}$	$T_{\rm Hot}$(K)	$\beta_{\rm Hot}$	$\tau_{\rm Hot:125\mu m}$
G19.61-0.23	46	1.35	0.40	45	1.37	0.46	110	2	1.4×10^{-4}
G29.96-0.02	53	1.95	1.22	49	1.92	1.40	111	2	8.2×10^{-4}
G34.3+0.2	44	2.20	3.63	42	2.25	4.28	110	2	1.5×10^{-4}
G45.07+0.13	42	1.90	0.60	42	1.84	0.53	107	2	2.2×10^{-4}
G45.12+0.13	30	2.15	0.54	38	1.70	0.17	116	2	8.0×10^{-5}
G75.78+0.34	38	1.95	0.27	38	1.92	0.25	114	2	3.6×10^{-5}
G75.84+0.40	40	1.80	0.10	22	3.32	1.84	54	2	1.4×10^{-2}
K3-50A	56	1.95	1.02	55	1.97	1.06	122	2	4.9×10^{-4}
K3-50C	33	2.25	0.80	29	2.75	2.03	60	2	4.3×10^{-3}
G192.584-0.041	23	2.30	1.02	21	2.40	1.36	43	2	1.1×10^{-2}
S255-FIR2	41	1.80	0.18	39	1.84	0.20	132	2	2.2×10^{-5}
GGD12-15	27	2.30	2.03	26	2.07	1.520	58	2	7.1×10^{-3}
Monoceros R2	33	2.20	0.21	33	2.19	0.20	107	2	9.3×10^{-5}
W3(OH)	60	1.95	3.35	47	1.94	2.51	56	2	1.5

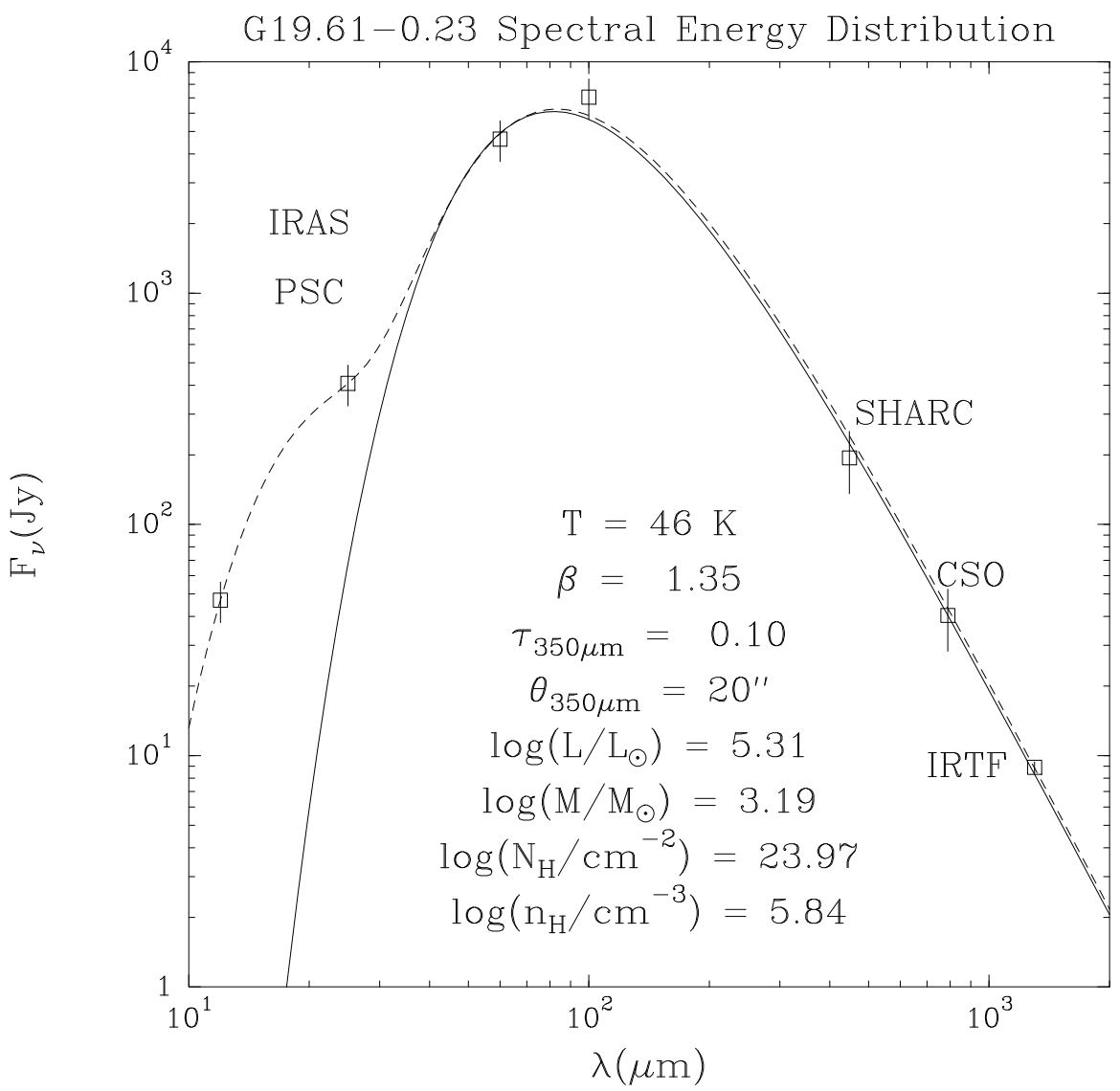

Figure 3.48: Spectral energy distribution of G19.61-0.23 with the one-component (solid line) and the two-component (dashed line) greybody models overlayed. Listed parameters correspond to the one-component model.

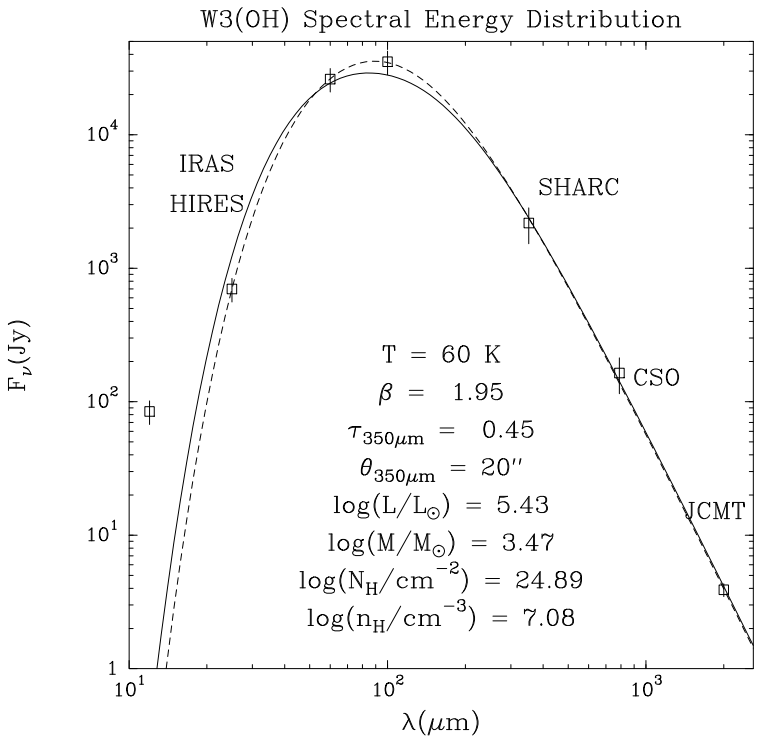

Figure 3.49: Same as Fig. 3.48 for W3(OH)

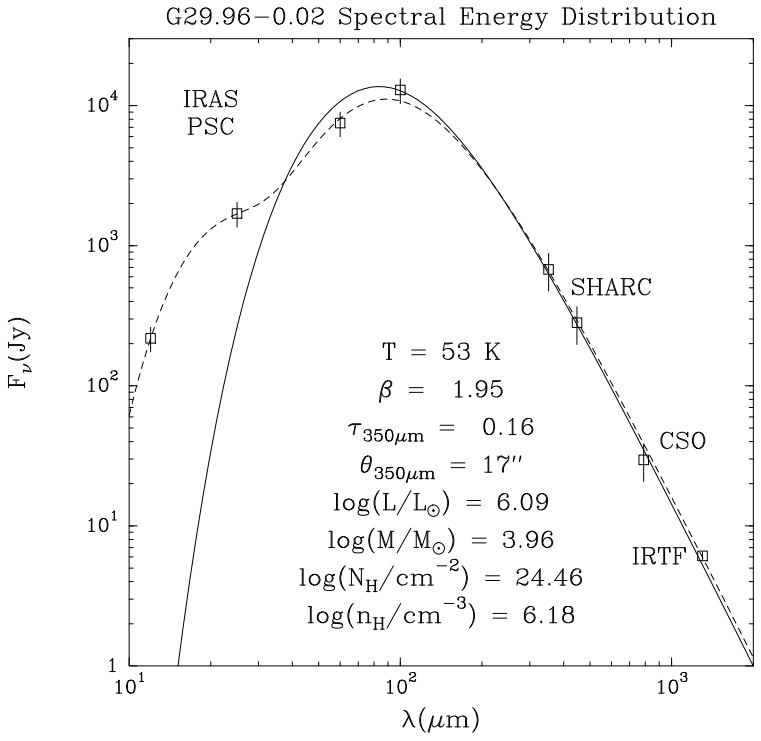

Figure 3.50: Same as Fig. 3.49 for G29.96-0.02.

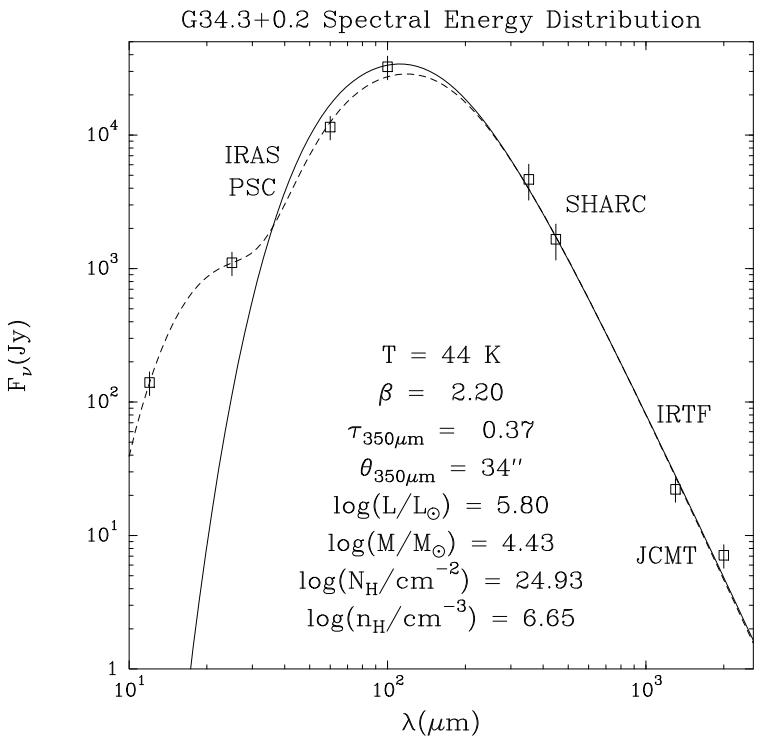

Figure 3.51: Same as Fig. 3.49 for G34.3+0.2.

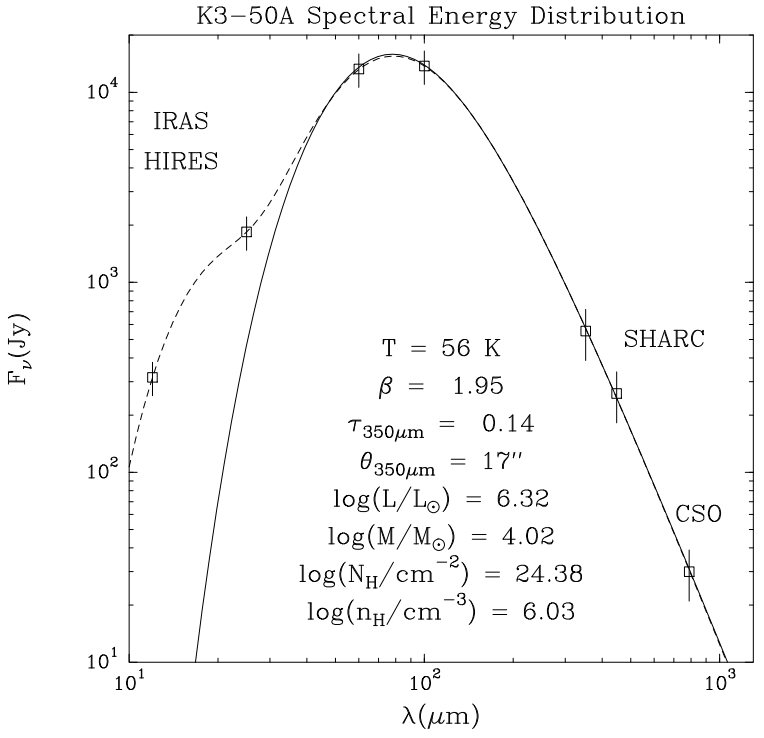

Figure 3.52: Same as Fig. 3.49 for K3-50 component A.

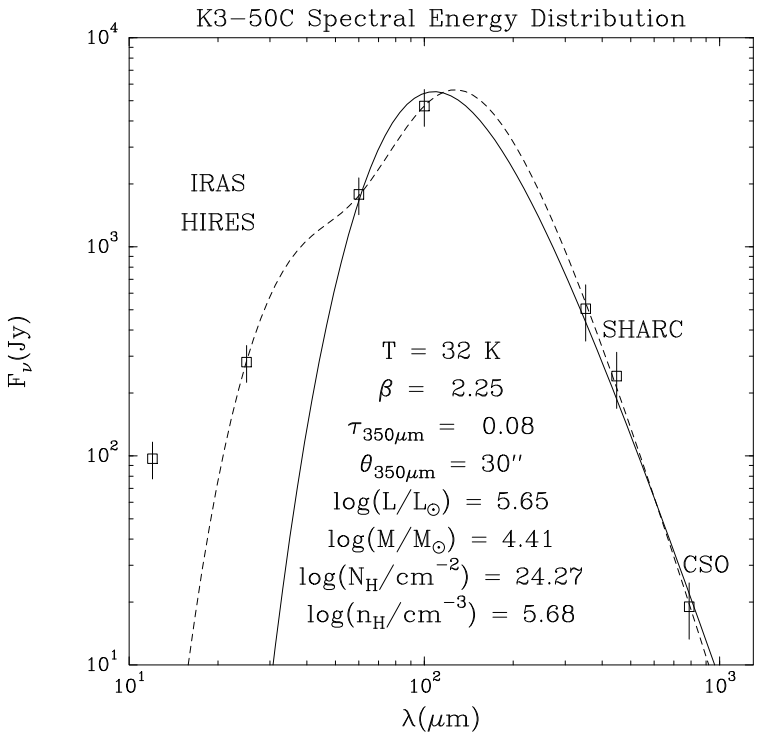

Figure 3.53: Same as Fig. 3.49 for K3-50 component C.

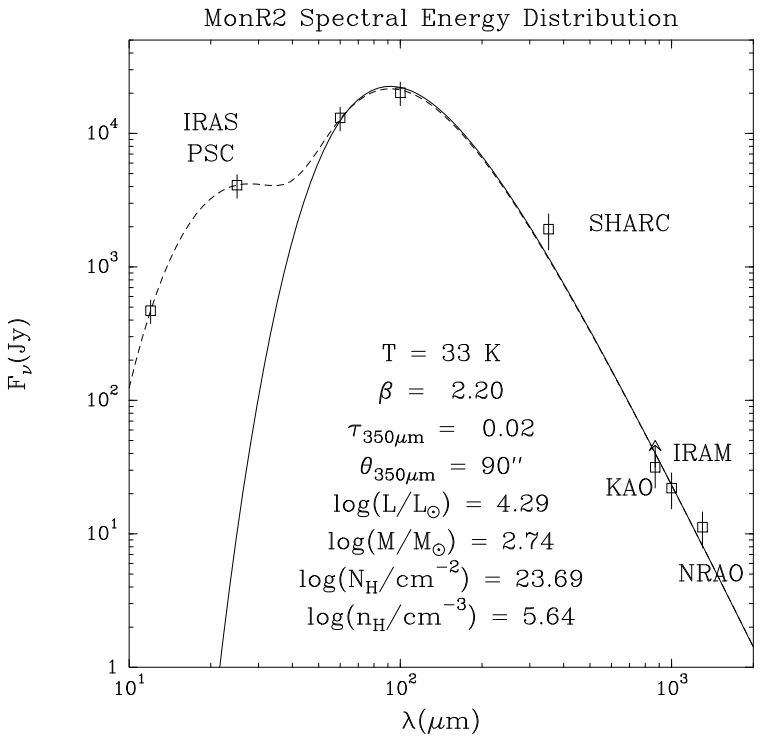

Figure 3.54: Same as Fig. 3.49 for the Monoceros R2 complex.

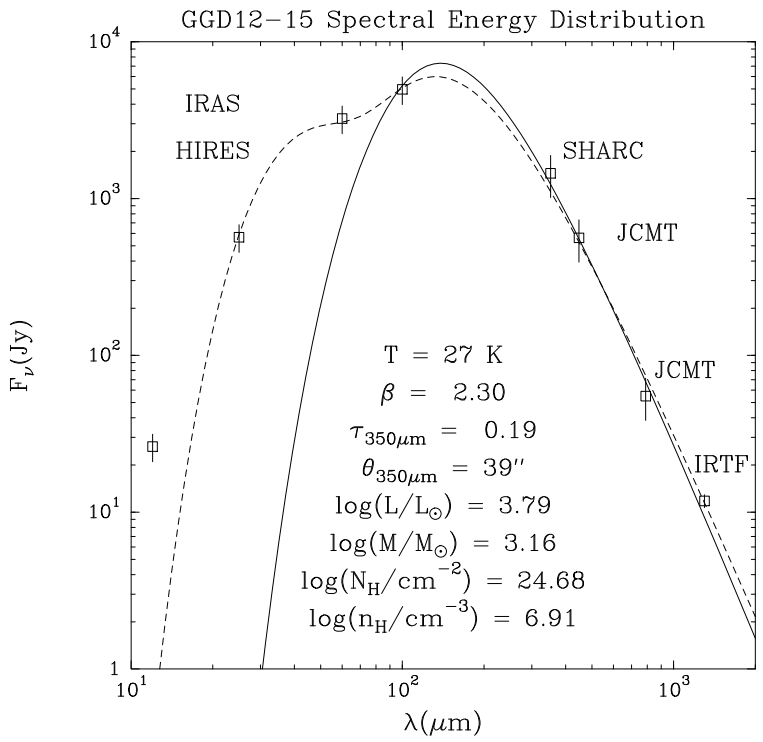

Figure 3.55: Same as Fig. 3.49 for the GGD12-15 complex

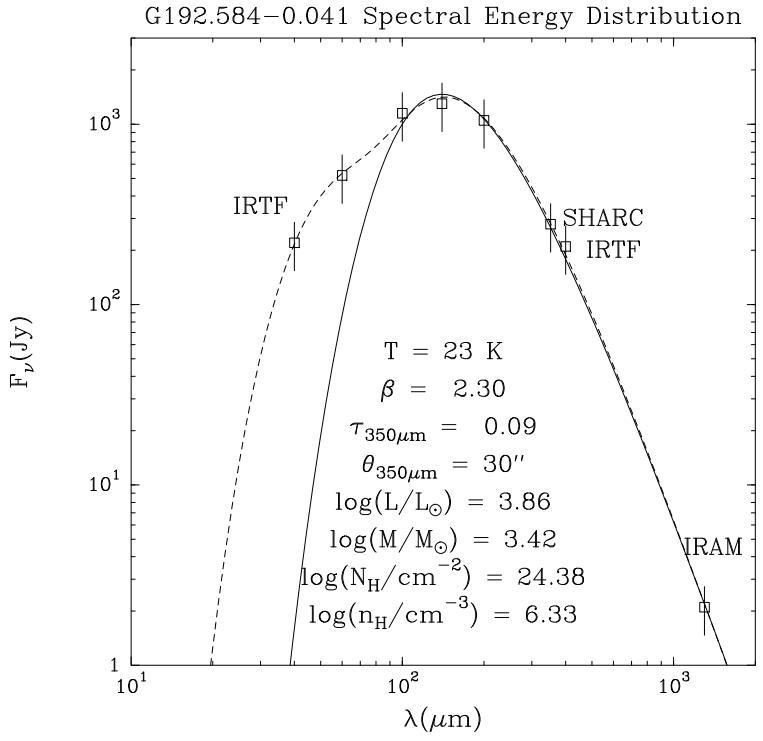

Figure 3.56: Same as Fig. 3.49 for G192.584-0.041.

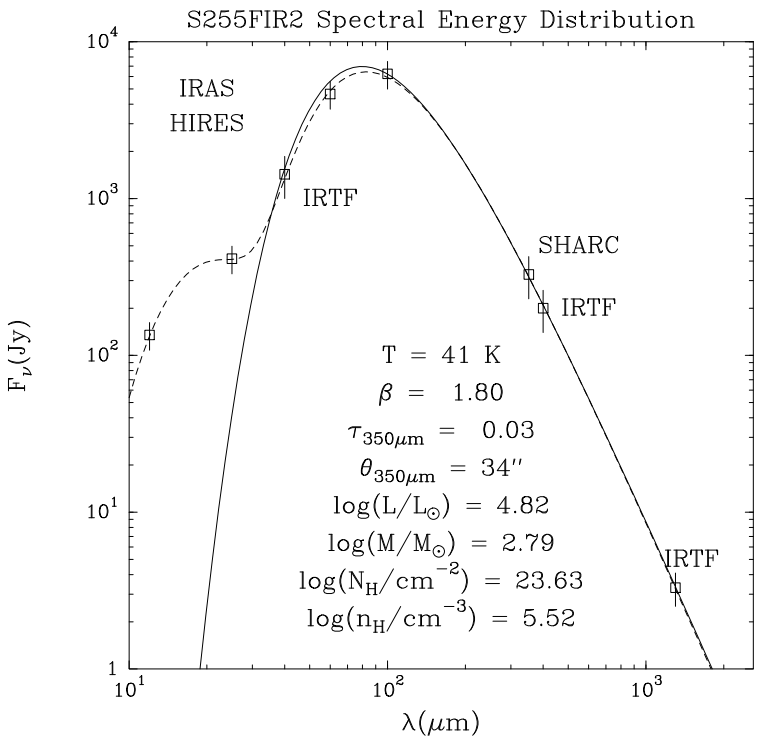

Figure 3.57: Same as Fig. 3.49 for S255-FIR2.

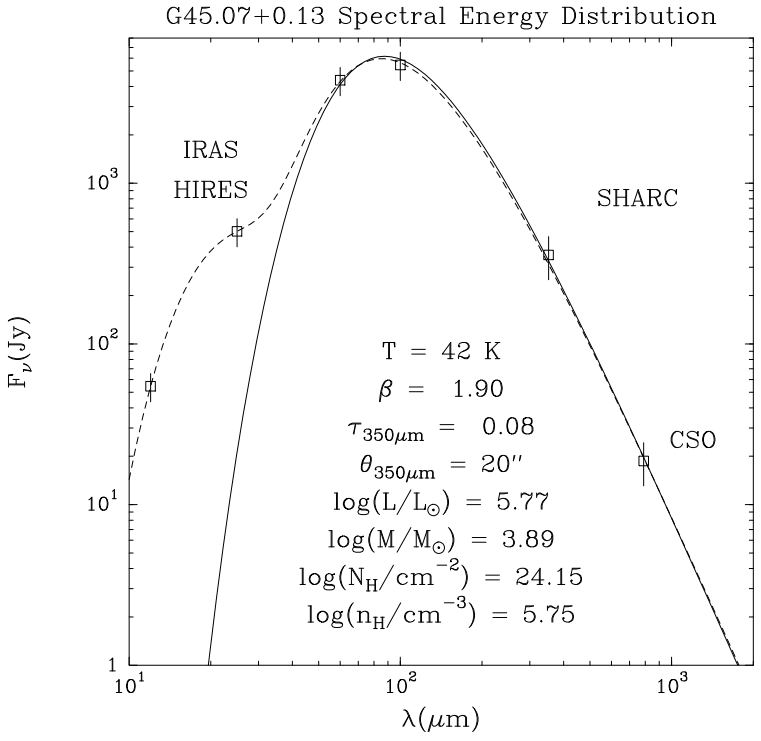

Figure 3.58: Same as Fig. 3.49 for G45.07+0.13.

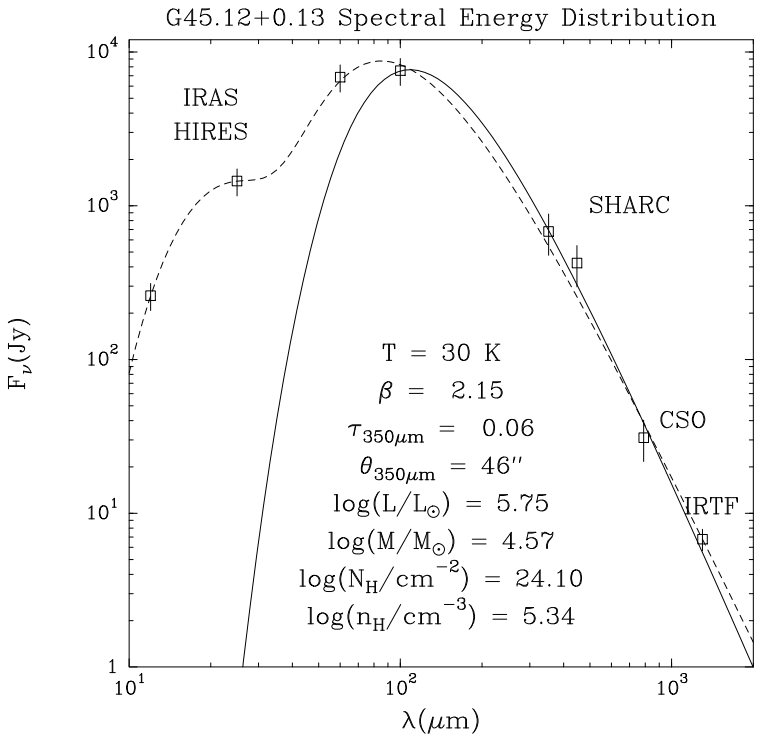

Figure 3.59: Same as Fig. 3.49 for G45.12+0.13.

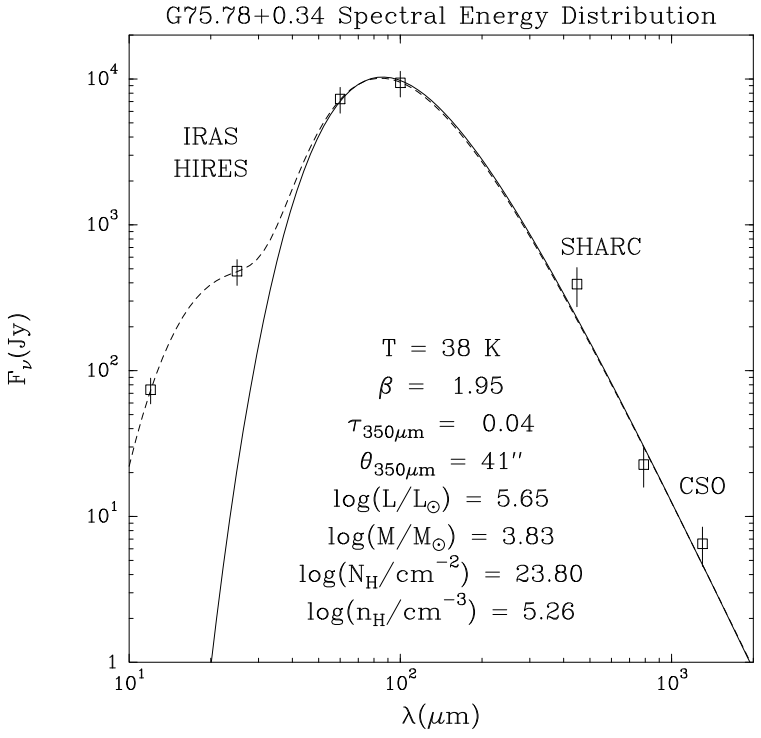

Figure 3.60: Same as Fig. 3.49 for G75.78+0.34.

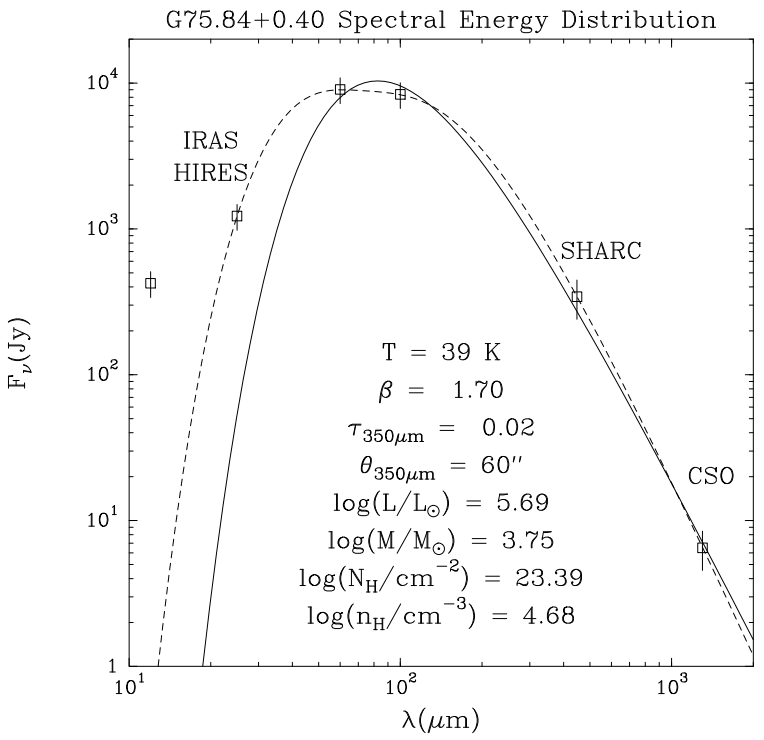

Figure 3.61: Same as Fig. 3.49 for G75.84+0.40.

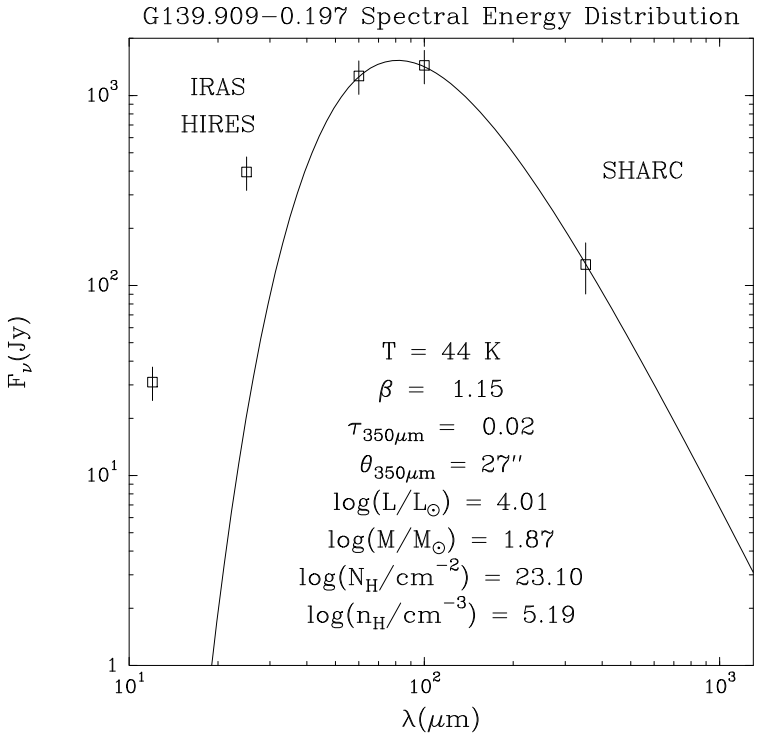

Figure 3.62: Spectral energy distribution of G139.909+0.197. With only 5 flux measurements, a two-component greybody fit was not possible.

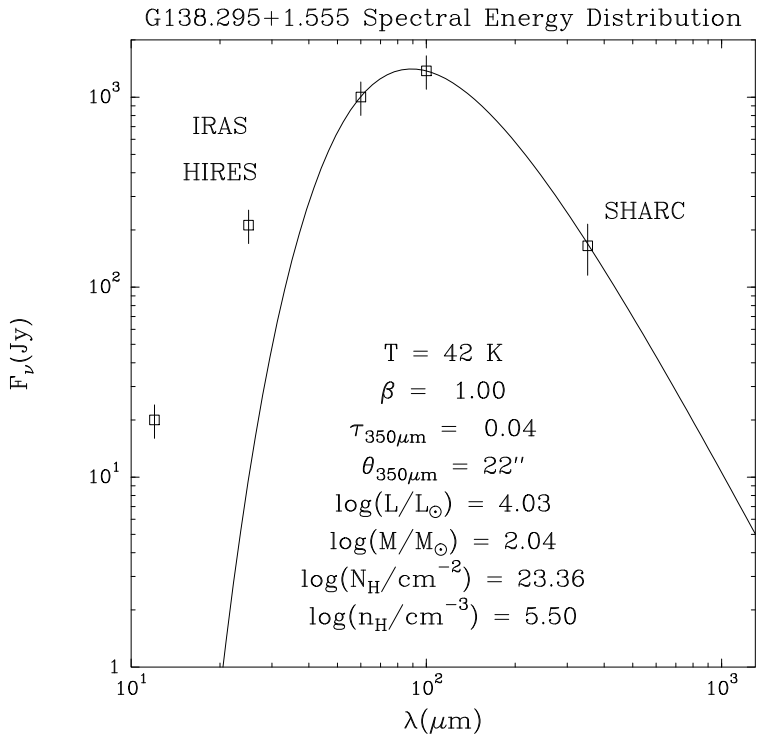

Figure 3.63: Spectral energy distribution of G138.295+1.555. With only 5 flux measurements, a two-component greybody fit was not possible.

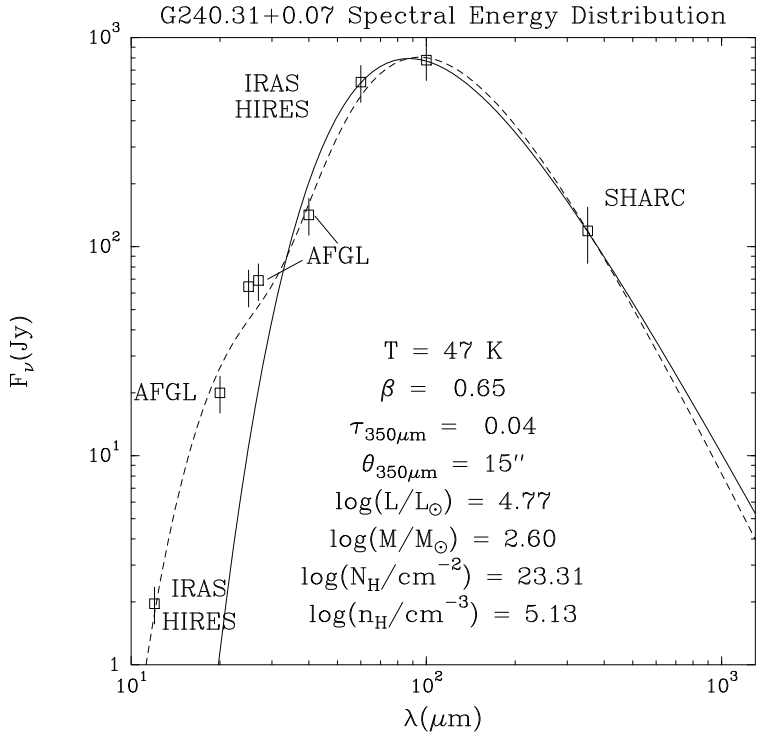

Figure 3.64: Spectral energy distribution of G240.31+0.07. The flux measurements at 20, 27 and 40μm reported by Gezari et al. (1993) are from the AFGL survey.

3.10 Density profiles

3.10.1 Signature of collapse

Numerical analysis of the gravitational collapse of an initially-uniform density, spherical gas cloud reveals that the cloud quickly acquires a density profile

$$n(r) \propto r^{-2} \tag{3.19}$$

which resembles an isothermal sphere (Bodenheimer & Sweigart 1968; Larson 1969; Penston 1971; Hunter 1977). This profile allows the cloud to approach hydrostatic equilibrium between the outward force of gas pressure and the inward force of self-gravitation. However, there exists an upper limit to the cloud mass above which equilibrium is impossible in the presence of external pressure from the interstellar medium (Bonnor 1956),

$$M_{\rm crit} = 1.18 c_s^4 (G^3 P_{\rm ext})^{-1/2}, \tag{3.20}$$

where the sound speed c_s is given by

$$c_s \approx \sqrt{\frac{kT}{m_{\rm H_2}}} = 0.35 \text{ km s}^{-1} \text{ for 30 K gas}, \tag{3.21}$$

and the external pressure of neutral interstellar gas is given by

$$P_{\rm ext} = nkT = 4 \times 10^{-12} \text{ dyn cm}^{-2} \text{ for gas with } n = 10^3 \text{ cm}^{-3}. \tag{3.22}$$

With these particular parameters, $M_{\rm crit} = 25 M_\odot$. If the mass exceeds this critical value, dynamical collapse will follow, proceeding most rapidly in the central regions where the density is largest and the free-fall timescale is shortest (Mestel 1965):

$$\tau_{\rm free-fall} \approx \sqrt{\frac{3\pi}{32 G \rho}} \propto r. \tag{3.23}$$

In the outer parts of the cloud, the sound travel timescale is less than the gravitational timescale and subsonic motions can produce pressure gradients that oppose and slow the free-fall. For example, in an isothermal cloud of mass $M_0 = 10000 M_\odot$ and radius r_0=1.0 pc, ($\bar{n} = 10^5$ cm^{-3}), the initial gravitational acceleration at large radius is

$$a = \frac{GM(< r)}{r^2} \approx \frac{GM_0}{r_0^2} = 0.44 \times 10^{-4} \text{ km s}^{-1} \text{ yr}^{-1}. \tag{3.24}$$

Thus, subsonic motions can redistribute material within the outer radii of the cloud for at least $\sim 10^4$ yr and thereby slow the collapse before the gravitational velocity approaches the sound speed. Because the cloud is already centrally concentrated,

$$M(< r) = \int_0^r \rho(r') 4\pi r'^2 dr' \propto r, \tag{3.25}$$

$$a \propto r^{-1}, \tag{3.26}$$

and hence the gravitational collapse acts more quickly on the inner parts of the cloud, leading to an inside-out collapse. This simple prediction is vindicated by more detailed solutions to the self-gravitating isothermal flow problem. In particular, Shu (1977) showed analytically and numerically that in the course of self-similar dynamical collapse, the r^{-2} density profile breaks down at small r such that

$$n(r) \propto r^{-3/2}, \tag{3.27}$$

and the infall velocity is given by

$$v(r) \propto r^{-1/2}. \tag{3.28}$$

This configuration is consistent with a steady mass accretion rate onto the core:

$$\dot{M}(r) = 4\pi r^2 n(r) v(r) \propto r^0. \tag{3.29}$$

Some observational results match these collapse predictions. The earliest measurements of the density profile of molecular cores were determined from extensive maps of two H_2CO transitions. Focusing on the nearby low-mass star-forming clouds ρ Oph A & B and R CrA to get the best spatial resolution, Loren, Sandqvist & Wootten (1983) found that the maps were consistent with radiative transfer models in which the density profiles ranged from r^{-2} to $r^{-3/2}$. More recently, radio and millimeter spectroscopy has been used to search for kinematic evidence for collapse. For example, redshifted NH_3 absorption has been reported toward the UCHII regions W3(OH) (Keto 1987; Reid, Myers & Bieging 1987), G34.3+0.2 (Keto 1987), and G10.6-0.4 where the infall velocity scales as $v \propto r^{-0.2}$ (Keto 1990; Ho & Haschick 1986). Similarly, redshifted HCO^+ absorption and blueshifted emission from W51IRS2 and W51e2 are consistent with large-scale dynamical collapse (Rudolph et al. 1990). By modeling line profiles, Zhou & Evans (1994) show that infall will create an asymmetry between the strength of the blueshifted and redshifted emission as a function of the optical depth of the molecular transition. This effect has been observed toward B335 and IRAS16293-2422. Similar results have also been found in the dark clouds (Lynds 1962) L1527 and L483 (Myers, Bachiller & Caselli 1995).

In addition to spectroscopy, continuum observations of dust provide evidence for collapsing structures. For example, the 50 and 100μm continuum profile of the massive star-forming region Cepheus A is consistent with the $r^{-3/2}$ density profile (Colomé & Harvey 1995). An IRAS study of 12 Bok globules yielded density profiles in the range from r^{-1} to $r^{-5/2}$ (Yun & Clemens 1991). In a higher resolution study, the millimeter and submillimeter dust emission profile from the Bok globule B335 was consistent with an $r^{-3/2}$ density profile (Chandler, Carlstrom & Terebey 1994). Similar results are found in L1527 (Motte, André & Neri 1996), L1489 and L1587 (Ladd et al. 1991) and in L1551IRS5 (Butner et al. 1991). In L1689B, the density profile approaches r^{-2} in the outer regions of the cloud and becomes at least as flat as $r^{-1.2}$ within 0.02 pc (André, Ward-Thompson & Motte 1996). 100μm observations of NGC2071 match an r^{-1} density profile (Evans 1989). Observations of the low-mass protostellar source VLA1623 in the ρ Oph A cloud indicate an even shallower density profile of

$r^{-1/2}$ (Barsony 1995). Clearly, further high-resolution observations of dust continuum emission from a larger sample of sources are needed to measure how common each type of density profile is.

3.10.2 The case of massive stars

Current evolutionary models of massive stars ($M > 8M_{\odot}$) predict that hydrogen burning begins before protostellar accretion has ended, precluding a pre-main sequence phase (Palla & Stahler 1993; Beech & Mitalas 1994). Thus, it is likely that the protostellar cloud is still collapsing on a large scale even after the appearance of the first stars (Larson 1972). In attempts to model the dust distribution around UCHII regions, Churchwell, Wolfire & Wood (1990) found that constant or very shallow density profiles ($r^{\pm 1/2}$) provide the best fit to the near-infrared to 100μm spectral energy distributions of these objects. However, emission at these wavelengths is most sensitive to warm dust near the central star which accounts for a small fraction of the total dust mass. By spatially resolving the dust clouds, the maps presented in this chapter allow a more direct measure of the density profile. In the following subsections, I model the density profile of the dust clouds surrounding the UCHII regions via radiative transfer simulations in an attempt to match the observed dust continuum flux profile from the submillimeter maps.

3.10.3 Flux density profiles of UCHII regions

Although the greybody models characterize the global properties of the dust, they do not immediately indicate the distribution. As seen in Table 3.4, the 350μm optical depth of the dust cores is typically much smaller than 1. This means that the flux density in a given aperture is proportional to the temperature-weighted mass in the beam. Because the dust emission is resolved in many of the SHARC images, there is more information to be gleaned. Aperture photometry was performed on each of the UCHII regions, recording the flux density in apertures of logarithmically increasing radii about the centroid of the source. The average flux density per pixel in the

outermost ring inscribed in the map was subtracted as a background value from all pixels in the inner apertures; but typically there was no significant offset present.

3.10.4 Radiative transfer models

One can compare the submillimeter flux density profile to predicted profiles from radiative transfer models. (To avoid confusion with the particle density profiles, flux density profiles are hereafter referred to as "flux profiles.") For this purpose, I have modeled the appearance of dust cocoons around UCHII regions with the radiative transfer program CSDUST which solves for the dust temperature at all radii within the cocoon (Egan, Leung & Spagna 1988).

3.10.4.1 Input parameters

Even with the assumption of spherical symmetry, a complete model requires many input parameters: the dust emissivity index (β), the normalized mass opacity of the dust (κ_0) at some specified frequency ν_0, an initial dust temperature distribution ($T(r)$) the outer boundary of the cloud (r_o), the inner core radius of the cloud where the power-law density profile levels off (r_i), the power-law index of density profile (p), the optical depth at ν_0 from the center to the surface, the luminosity $L_{\rm bol}$ and effective temperature $T_{\rm eff}$ of the internal heat source, and the external radiation field intensity. In the following simulations, β, $\tau_{120\mu{\rm m}}$, and $L_{\rm bol}$ are taken from the greybody models for each source and a normalized dust emissivity of 7.5×10^{-4} at 120μm is assumed (Hildebrand 1983). At wavelengths shorter than 100μm the dust emissivity index is set to 1.0 to match the typical observed values in the mid-infrared (Hildebrand 1983):

$$Q_\lambda = Q_{125\mu{\rm m}} \left(\frac{125\mu{\rm m}}{\lambda} \right)^\beta, \text{ for } \lambda > 100\mu{\rm m}, \tag{3.30}$$

$$= Q_{125\mu{\rm m}} \left(\frac{125\mu{\rm m}}{100\mu{\rm m}} \right)^\beta \left(\frac{125\mu{\rm m}}{\lambda} \right)^{1.0}, \text{ for } \lambda \leq 100\mu{\rm m}, \tag{3.31}$$

$$\text{where } Q_{125\mu{\rm m}} = 7.5 \times 10^{-4}. \tag{3.32}$$

A final constraint is placed such that $Q_\lambda \leq 1.0$ at short wavelengths. $T_{\rm eff}$ is taken from the zero age main sequence values for a star with the appropriate value of $L_{\rm bol}$ (Thompson 1984; Panagia 1973). An external radiation field of one standard ISRF is also assumed.

3.10.4.2 Model procedure

Because of sensitivity limitations in the maps, especially to emission structures larger than the chopper throw, the true outer boundary of the cloud r_o is uncertain and should be varied to obtain the most accurate model (e.g., Mundy et al. 1996). However, as a simplification to the model procedure owing to time constraints on this research, the value of r_o has been fixed at the radius where the intensity of the submillimeter emission vanishes (usually equal to or close to the size of the map). Models were then run for 3 different power-law density profile indices, $p = 1, 1.5$, and 2. The results are compared to the observations and the value of p most consistent with the data is assigned to the source. As a self-consistency check, the predicted spectral energy distributions of the 3 models are compared to the measured FIR and submillimeter flux densities to confirm that the assigned value of p provides the best fit.

Regarding the starting point for $T(r)$, radiative transfer models of infrared sources in molecular clouds have previously revealed that $T(r) \propto r^{-q}$ (Goldreich & Kwan 1974; Scoville & Kwan 1976) where $q = 2/(4+\beta)$ (Harvey et al. 1991; Adams 1991). Thus the input temperature distribution was computed for each source using the value of β from the greybody model and normalizing the temperature at the half-power radius to the greybody temperature. The program CSDUST modifies this distribution slightly after each iteration while converging toward equilibrium. Because power-law density profiles become singular at the origin, it is necessary to cap them at small radii. The program achieves this requirement by smoothly matching the input power-law density profile to a Gaussian density profile. The match point (r_i) is set to the radius inside of which 80% of the optical depth lies. Typically this occurs at a fractional radius of 0.05. Repeated models with the match point set to 90% revealed

that the model flux profiles are fairly insensitive to the match point over the range of fractional radii probed by the observations.

3.10.5 Convolution with the instrumental beam pattern

Once the radiative transfer model has converged, the result must be convolved with the telescope beam to obtain a prediction of the observed flux profile at a specific wavelength. To do this properly, I have modeled the instrumental beam response to a point source from images of Uranus. Because its angular diameter ($\approx 3\farcs5$) is much smaller than the beamsize, it can be taken as a good approximation to a point source. Shown in Fig. 3.65 is the integrated flux profile extracted from the 350μm image of Uranus obtained with a chopper throw of 87″ (Fig. 3.66). Overlayed on the observations is the flux density profile of a 14″ Gaussian beam which matches the full-width half-power diameter in the Uranus image but fails to match the broad wings of the response. As discussed in Chapter 2, the SHARC/CSO beam response can be described by a sum of two functions: a diffraction-limited component (convolved with the pixel size) and a larger sidelobe component. In Fig. 3.65 I have also overlayed the flux profile predicted by the sum of two Gaussian beams: a 12″ beam with 75% of the power and a 30″ beam with 25% of the power. Although the main beam efficiency of the CSO is known to be only $\sim 30\%$ at 350μm, much of the sidelobe power evidently lies in an even more extended error pattern which is either chopped out or too faint to be seen in the beam map. Thus, the emergent intensity at each impact parameter of the radiative transfer model has been convolved with the sum of these two beams in order to derive the predicted flux profile.

In Figs. 3.67 through 3.79, I compare the observed flux profile with predicted flux profiles from the CSDUST radiative transfer models with particle density profiles of $n(r) \propto r^{-2}$, $n(r) \propto r^{-3/2}$ and in some cases $n(r) \propto r^{-1}$. Mon R2 is excluded from this analysis as it is clearly a non-spherical cluster of individual sources (primarily because it is the nearest source in the survey). The rest of the sources can be characterized into four categories: isothermal, central collapse, bulk collapse, and logatropic.

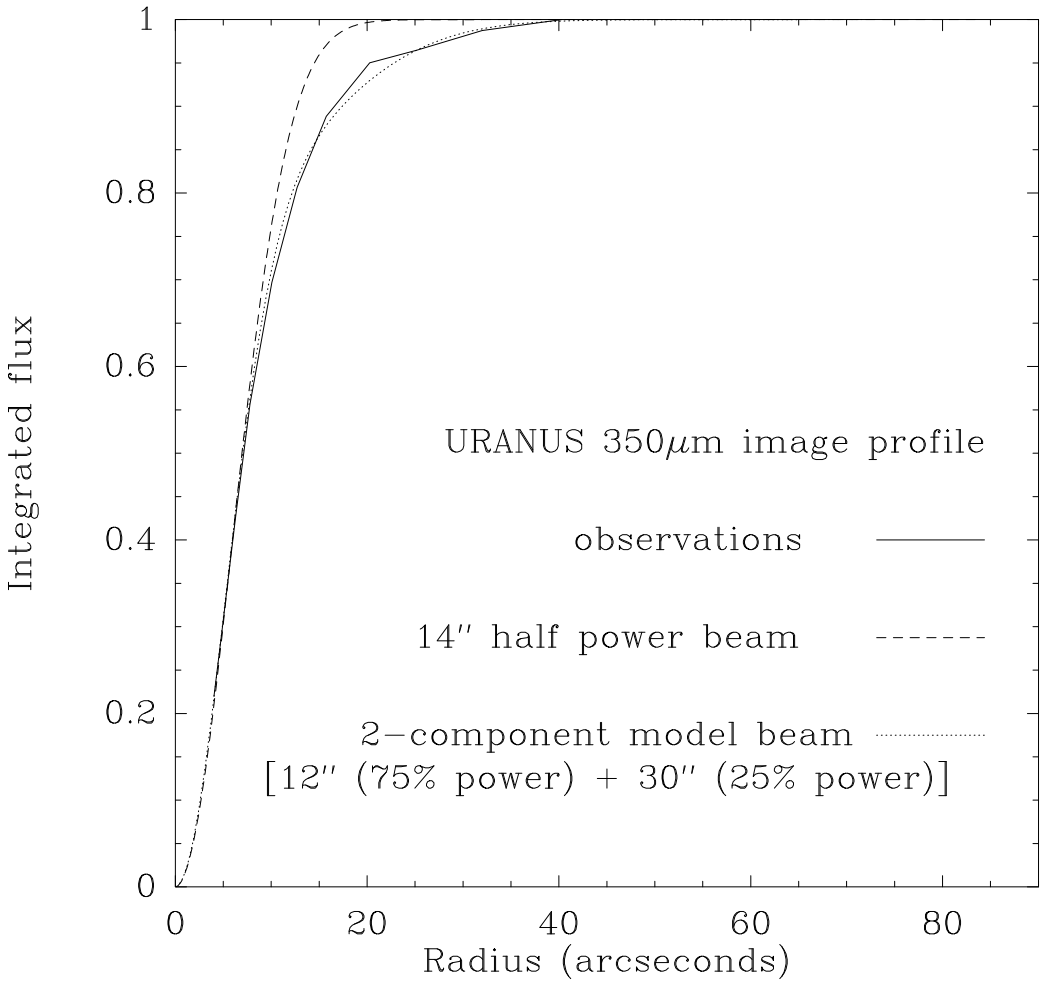

Figure 3.65: Observed flux profile of Uranus measured from the 350μm image and compared to predictions from a 14″ Gaussian beam which matches the half-power diameter, and the sum of a 12″ Gaussian main beam and a 30″ Gaussian sidelobe beam which provide a better match to the response pattern.

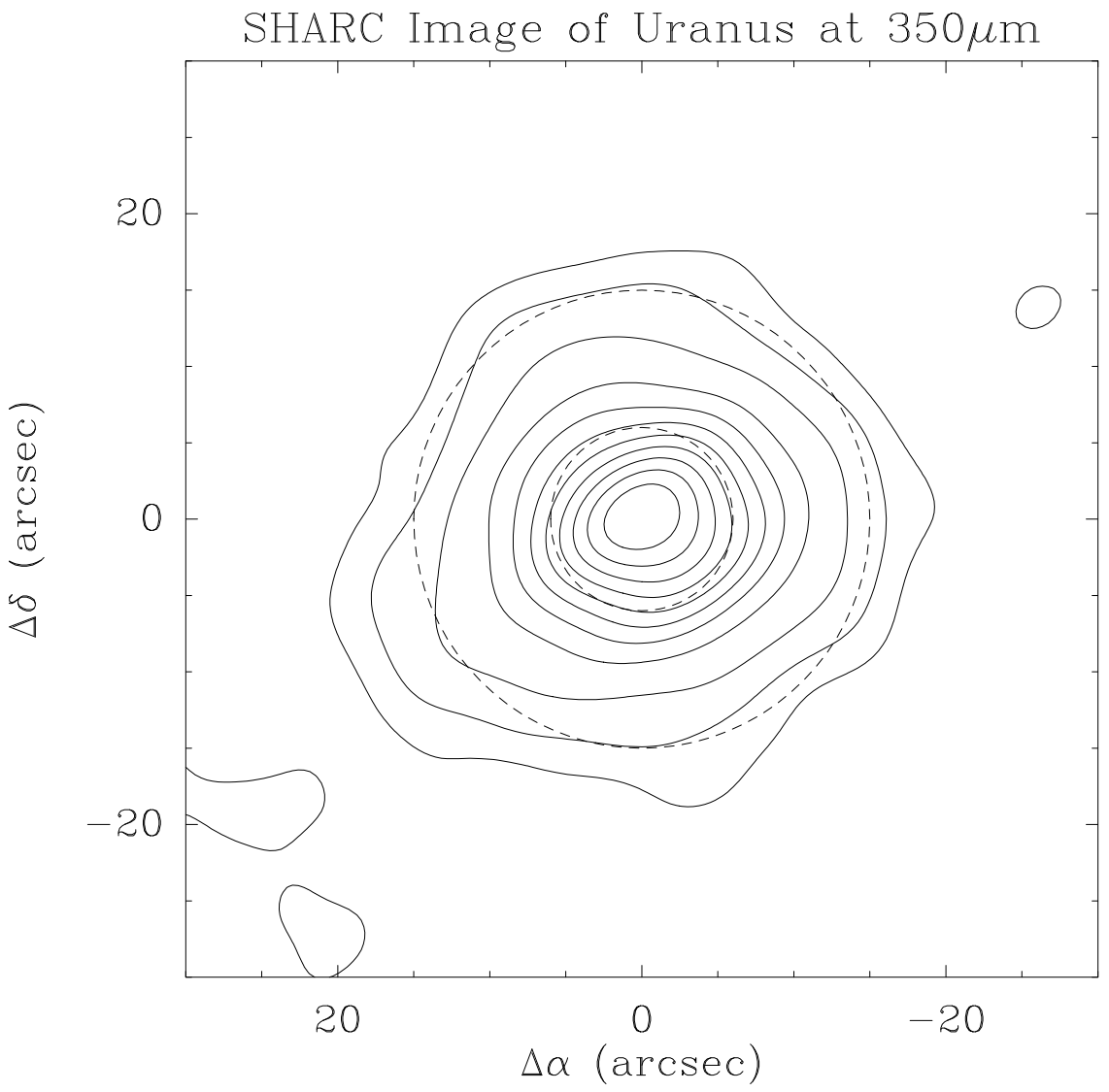

Figure 3.66: 350μm SHARC image of Uranus in celestial coordinates from which the flux profile of Fig. 3.65 was measured. Contour levels are 2.5%, 5%, 10% to 90% by 10%. The dashed contours represent the half-power levels of the 12″ and 30″ Gaussian beams that comprise the model of the response pattern.

3.10.6 Sources resembling an isothermal sphere

At all scales, the flux profile of G240.31+0.07 closely matches the $n \propto r^{-2}$ density profile of the isothermal sphere, suggesting that it is in an early stage of star formation development before substantial collapse has occurred. As discussed in section 3.7.1, so far there is evidence for only a single object forming in this core.

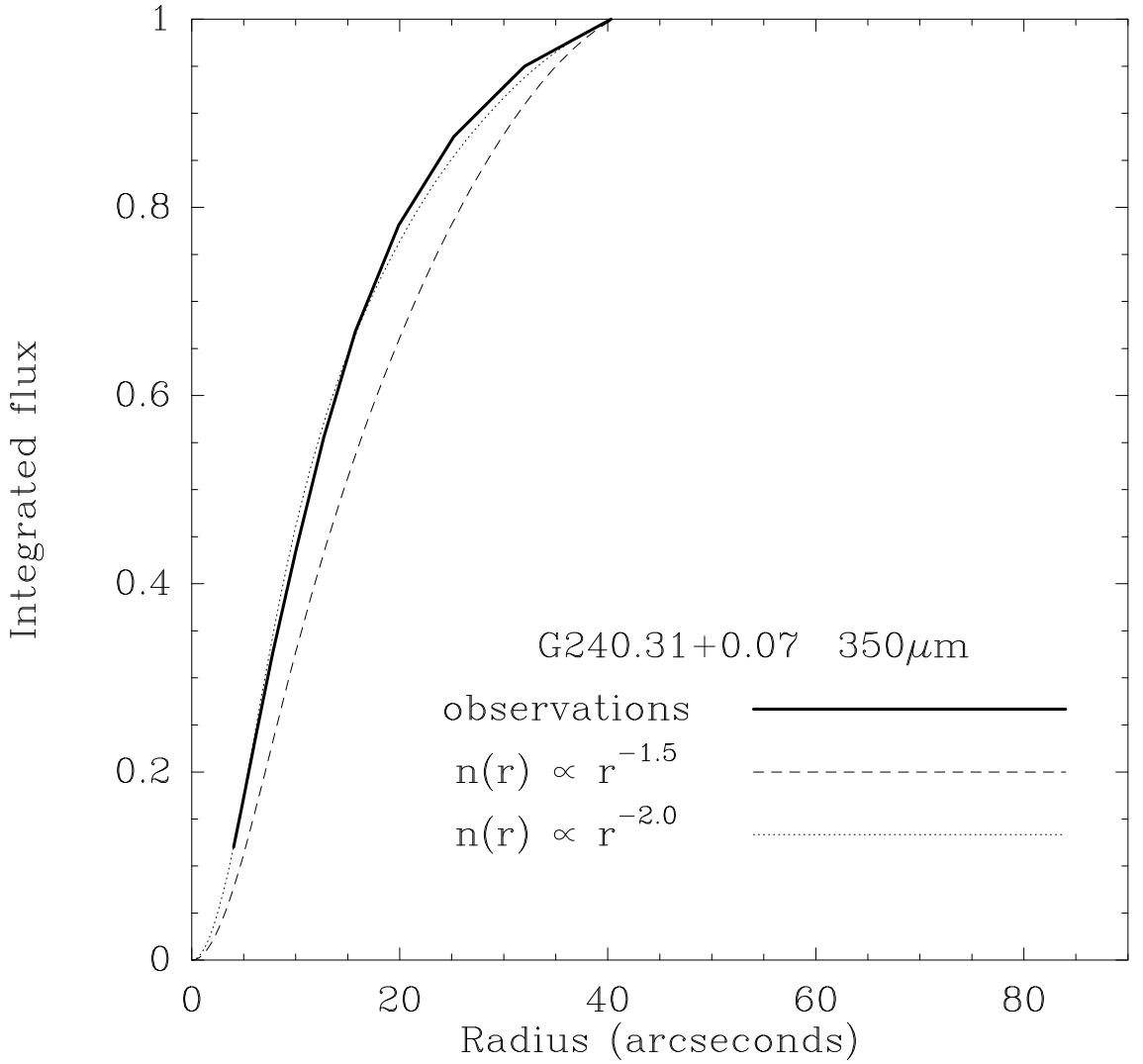

Figure 3.67: Observed flux profile of G240.31+0.07 measured from the 350μm image and compared to predictions of radiative transfer models.

Like G240.31+0.07, G19.61-0.23 resembles the isothermal sphere throughout most of the cloud, although the slope appears to become shallower in the outermost regions. This broadening may be due to fainter subclumps in the halo, especially since a cluster of 5 UCHII regions is seen in this source (see Fig. 3.25 in Section 3.5.3).

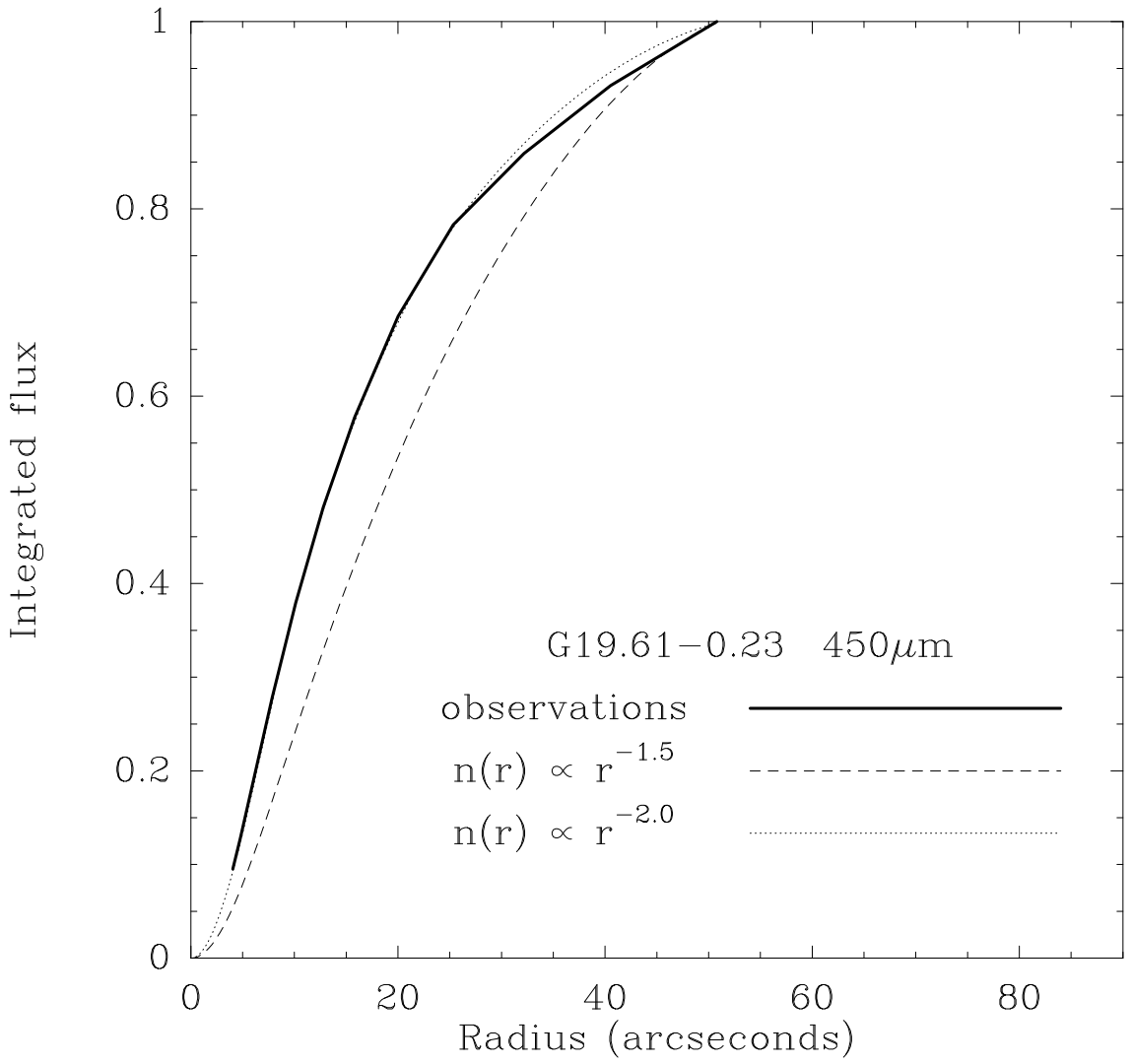

Figure 3.68: Observed flux profile of G19.61-0.23 measured from the 450μm image and compared to predictions of radiative transfer models.

The flux profile of G29.96-0.02 matches the isothermal sphere through most of the cloud though it appears to deviate slightly in the inner regions. However, small pointing and tracking errors between subsequent scans of the map may broaden the profile up to $\sim 2''$. This effect will be especially noticeable at small radii. Thus within the estimated error, the observed profile is consistent with the isothermal sphere at all scales. The presence of the UCHII region, a separate concentration of H_2O masers, and a small near-infrared cluster indicates several sites of star formation already exist at the core.

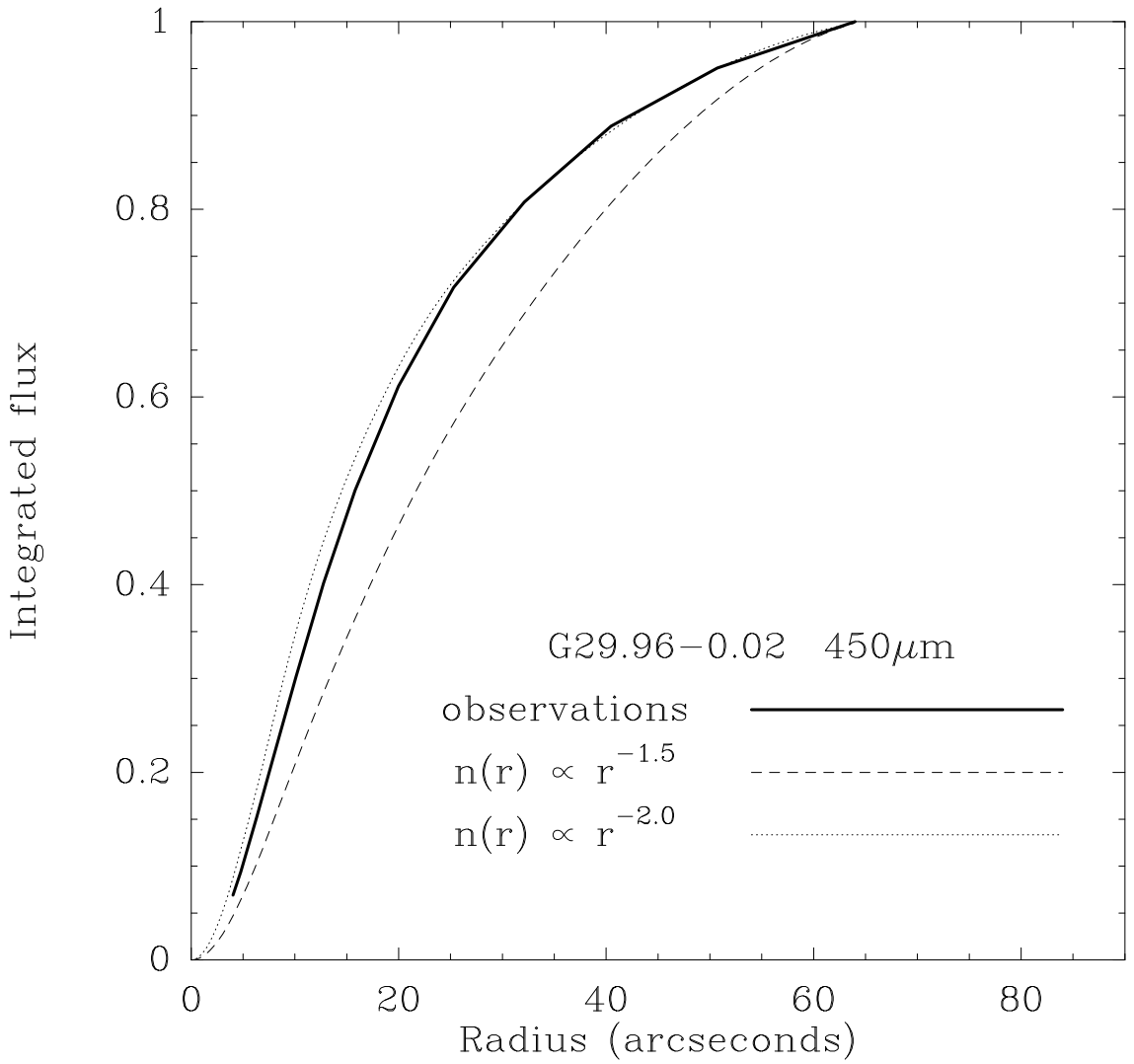

Figure 3.69: Observed flux profile of G29.96-0.02 measured from the 450μm image and compared to predictions of radiative transfer models.

3.10.7 Sources resembling the collapse profile at the center

The flux profile of W3(OH) matches the isothermal sphere in the outer parts of the cloud but rapidly approaches the $n(r) \propto r^{-3/2}$ law at the innermost radii. This profile is consistent with collapse in the central core ($r \lesssim 10''$ or 0.1 pc), while the outer regions ($r \gtrsim 40''$ or 0.4 pc) remain isothermal and have not yet felt the collapse. To estimate the time since the collapse began, I assume uniform gravitational acceleration and set the collapse velocity at $r = 0.4$ pc equal to the sound speed (Eq. 3.24). Using the mass and temperature from Table 3.4, this yields a timescale of 5×10^3 yr, virtually identical to the typical dynamical timescale of UCHII regions derived in Chapter 1. Note that there are at least two young objects already formed in this core: the UCHII region and the Turner-Welch object.

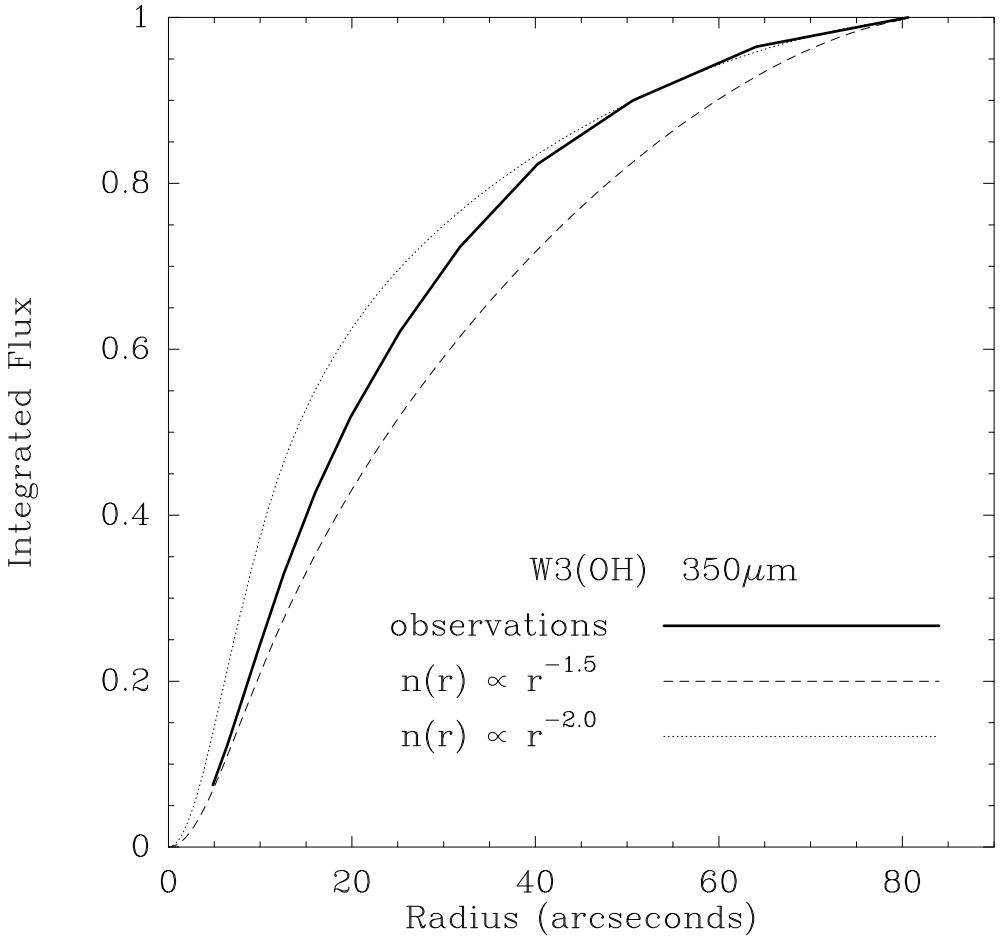

Figure 3.70: Observed flux profile of W3(OH) measured from the 350μm image and compared to predictions of radiative transfer models.

Like W3(OH), the flux profile of K3-50A matches the prediction of the isothermal density profile in the outer regions of the cloud and approaches the collapse profile in the inner regions. Like W3(OH) there is evidence for several young objects in this core, the UCHII region, an outflow source lying to the east (identified in Chapter 4) and a possible near-infrared cluster (Howard et al. 1996).

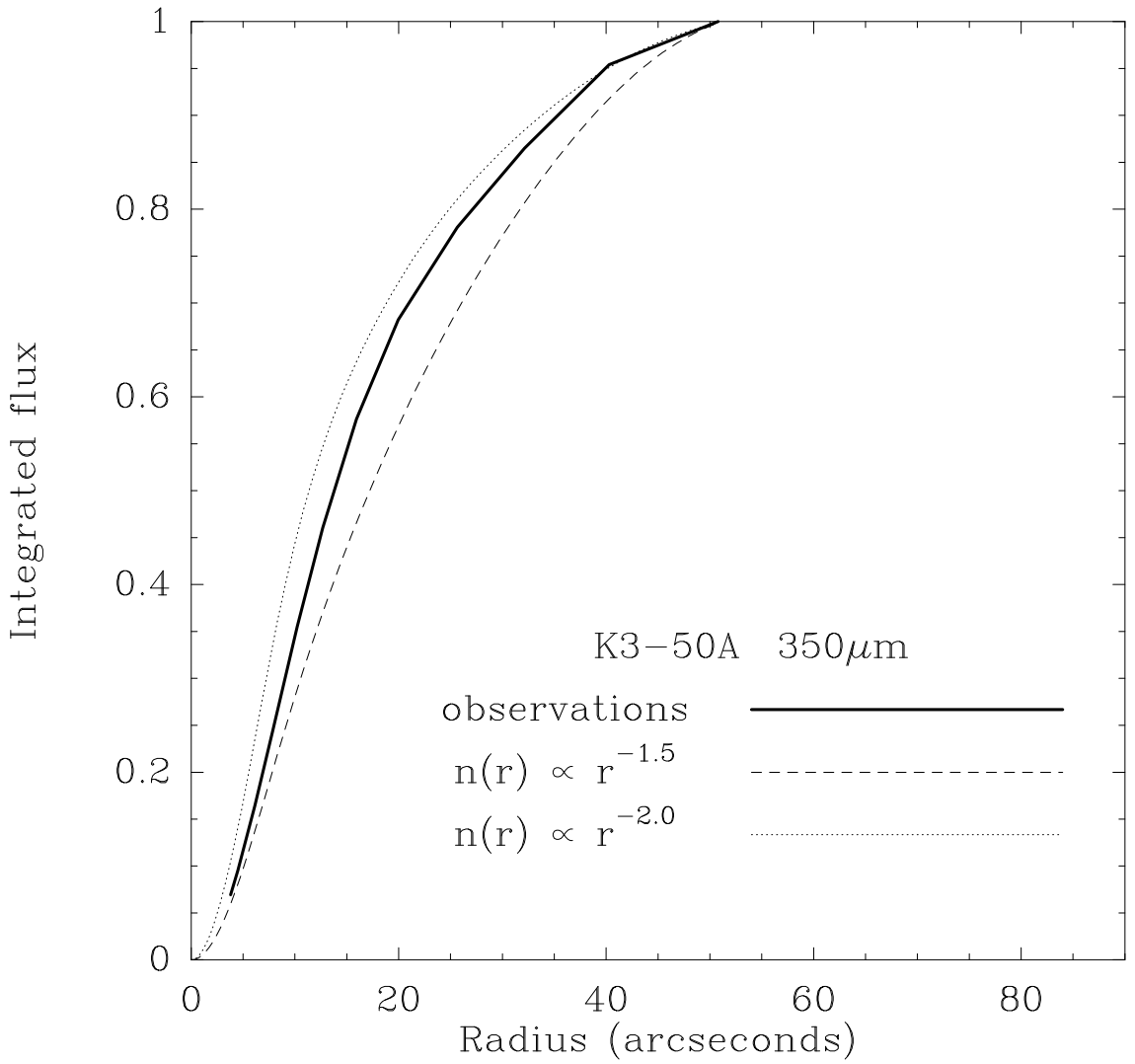

Figure 3.71: Observed flux profile of K3-50A measured from the 350μm image and compared to predictions of radiative transfer models.

3.10.8 Sources resembling the collapse profile

Throughout the cloud, the flux profile of S255 FIR2 matches the prediction from the collapse model density profile suggesting that the bulk of the cloud is currently undergoing collapse. Several radio sources and a near-infrared cluster show that substantial star formation has already occurred at the core.

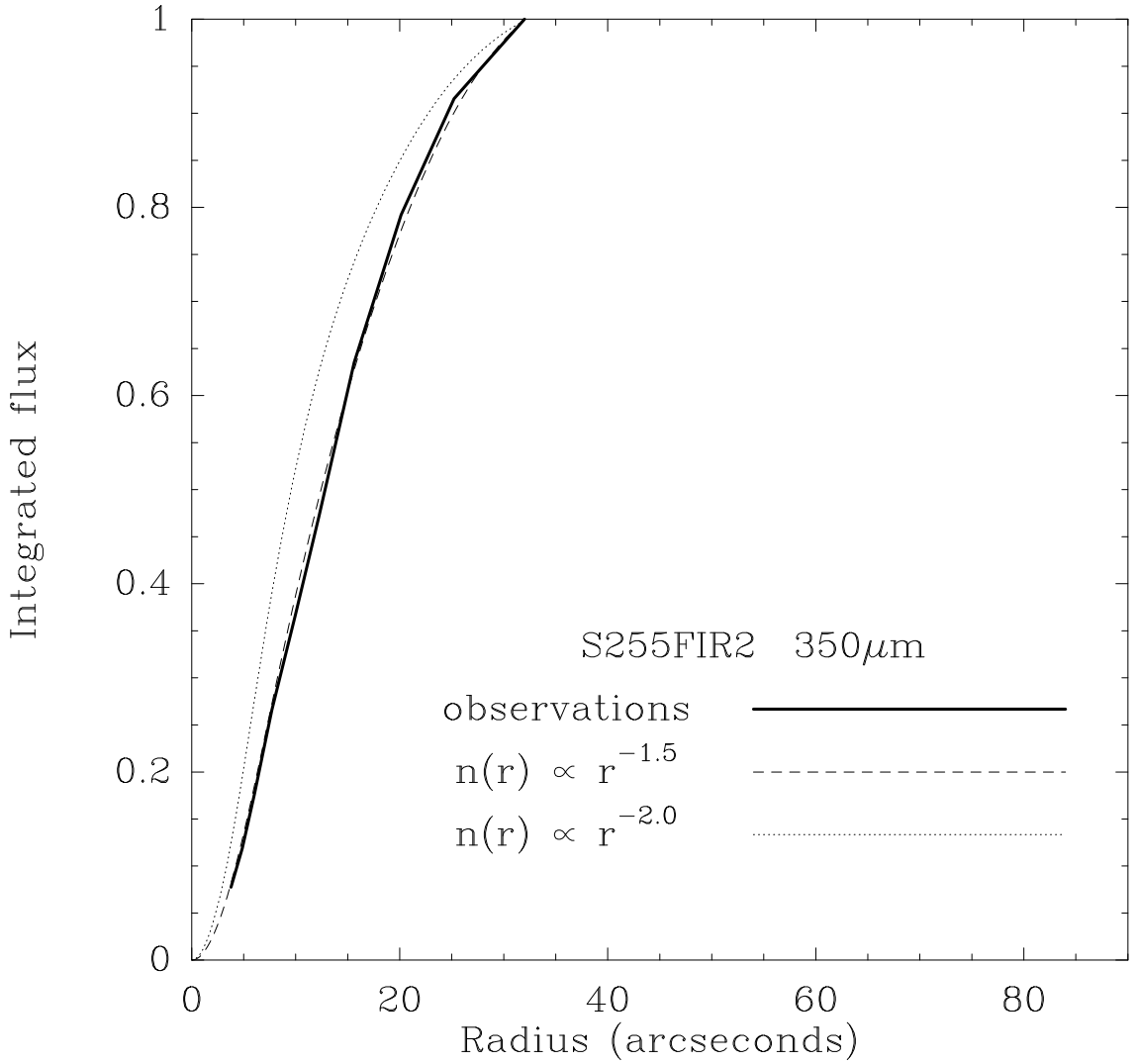

Figure 3.72: Observed flux profile of S255 FIR2 measured from the 350μm image and compared to predictions of radiative transfer models.

On all scales, the flux profile of G75.78+0.34 lies between the predictions from the isothermal and collapse model density profiles. It appears to be consistent with a profile of $r^{-1.75}$; however, the models are not easily distinguishable due to the limited spatial resolution achieved on this source. Nevertheless, it will be classified here as a collapse profile. Like W3(OH) and K3-50A, there is evidence for more than one young object forming in this core (Shepherd & Churchwell 1996b).

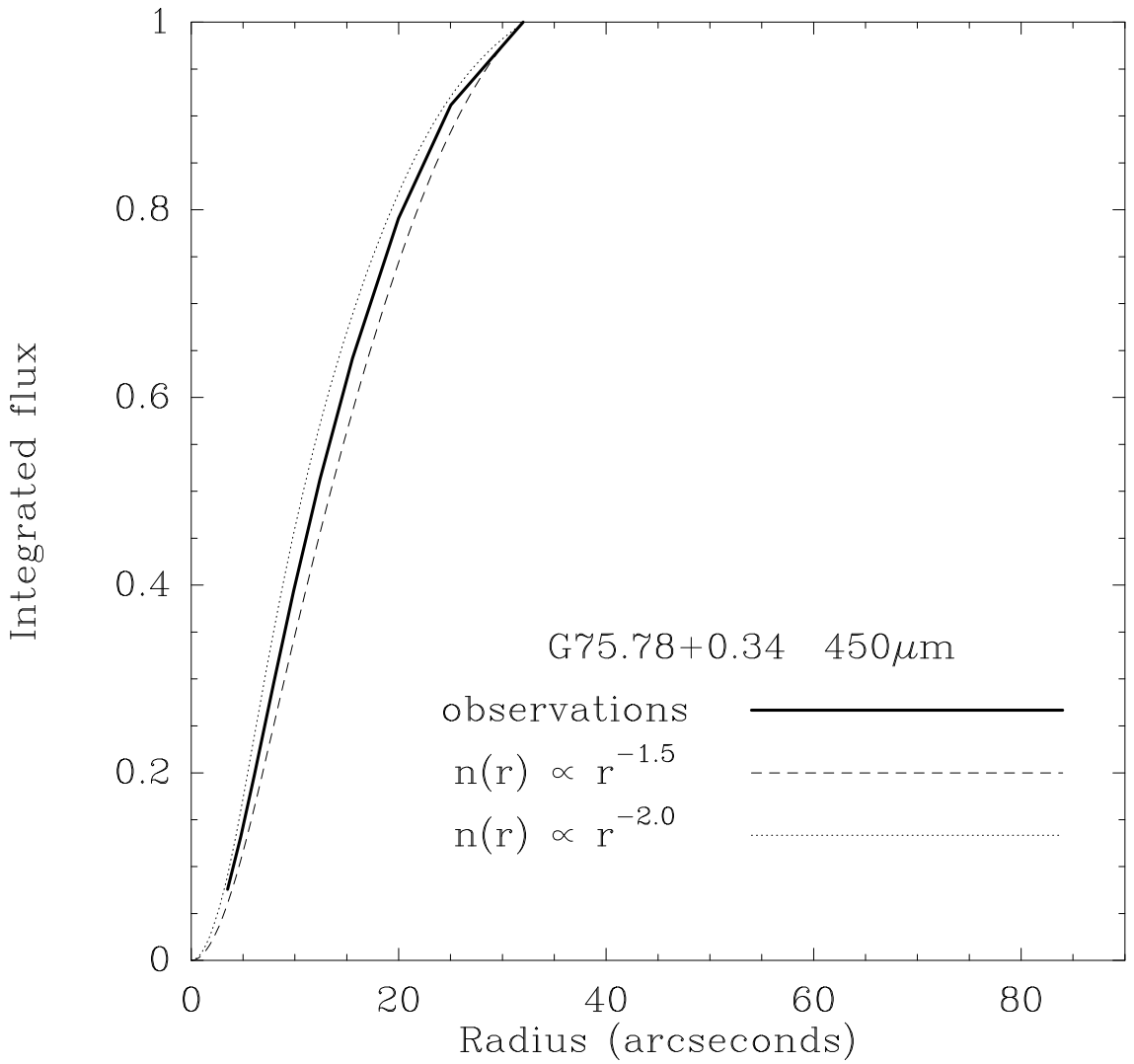

Figure 3.73: Observed flux profile of G75.78+0.34 measured from the 450μm image and compared to predictions of radiative transfer models.

In the outer half of the cloud, the flux profile of G45.07+0.13 matches the prediction from the collapse model density profile suggesting that the entire cloud is currently undergoing collapse. As in G29.96-0.02, the slight broadening of the profile at small radii is consistent with a 2″ tracking error. To date, only the UCHII region/H_2O maser source has been identified in this distant source.

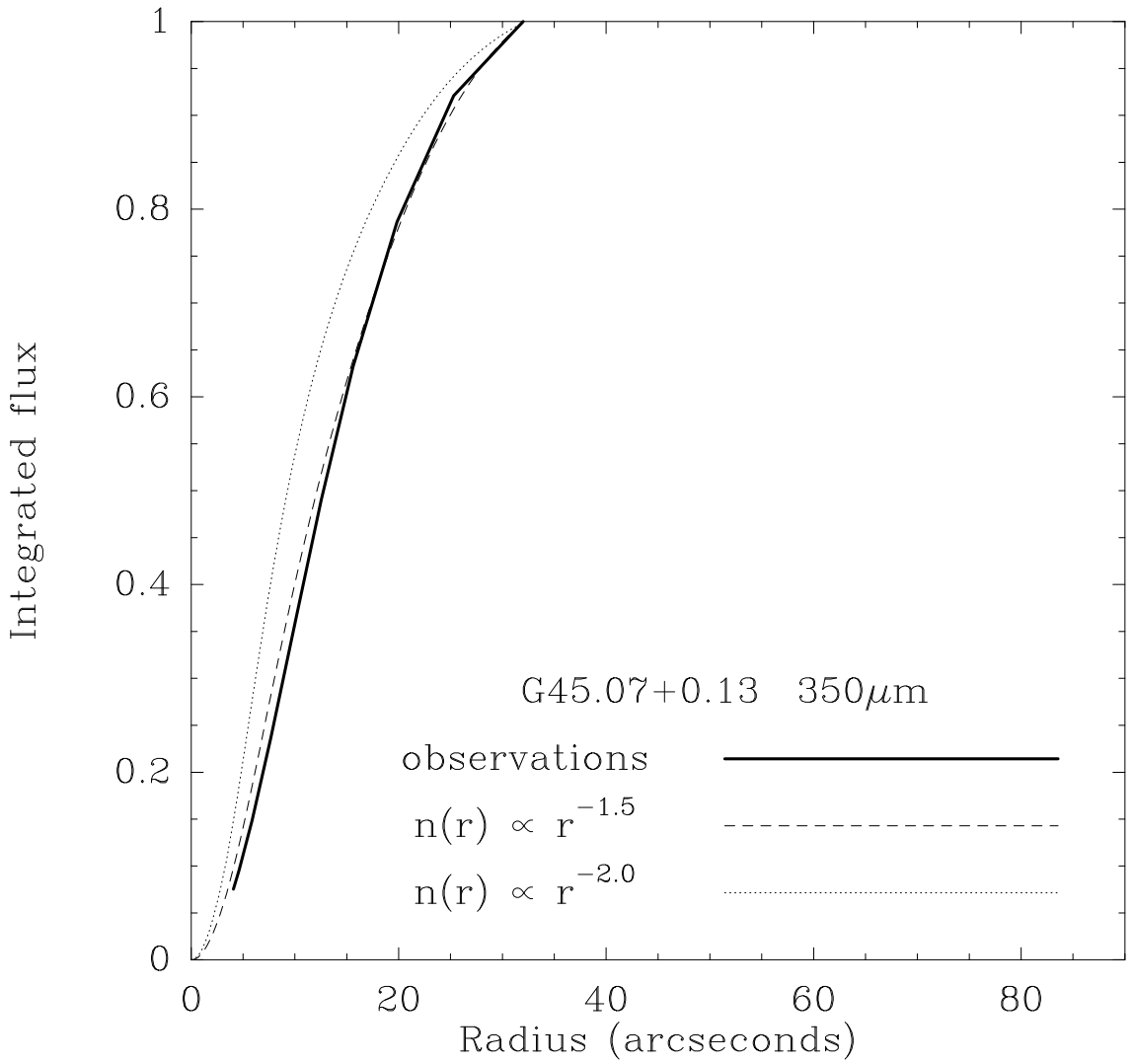

Figure 3.74: Observed flux profile of G45.07+0.13 measured from the 350μm image and compared to predictions of radiative transfer models.

Based on the image in Fig. 3.17, the outer parts of the flux profile of G34.3+0.2 is obviously widened due to contamination from of additional point sources in the extended halo. Without this confusion, the profile would likely exhibit the collapse profile throughout the cloud, as it does in the inner regions. The UCHII region, H_2O maser sites, and submillimeter sources reveal multiple cores of star formation in this cloud.

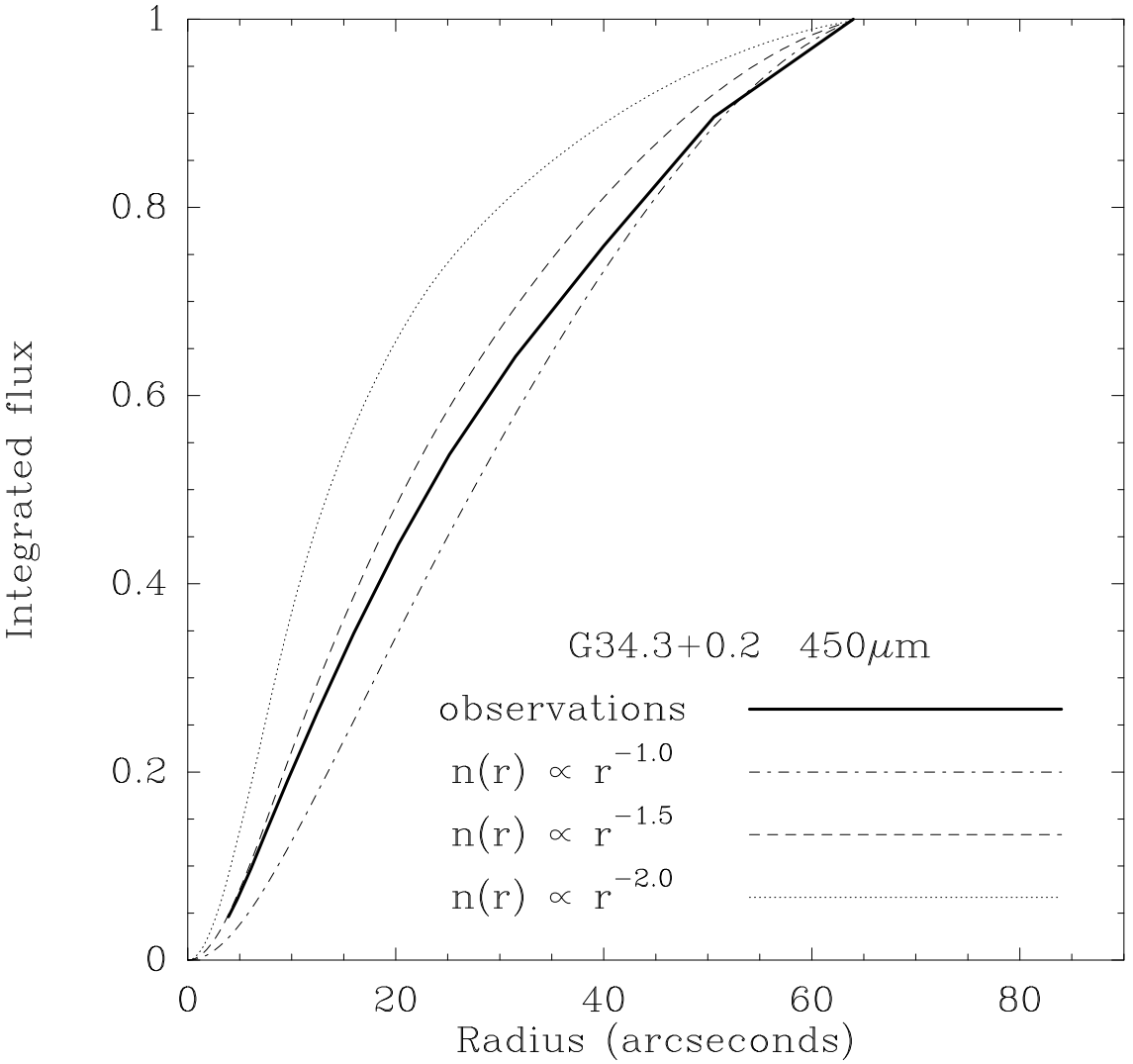

Figure 3.75: Observed flux profile of G34.3+0.2 measured from the 450μm image and compared to predictions of radiative transfer models.

3.10.9 Sources resembling logatropic spheres

The profile of K3-50C, a ridge-like source containing 3 UCHII regions, is consistent with a shallower density profile of $n(r) \propto r^{-1}$. This type of profile is known as a logatropic sphere (Lizano & Shu 1989) and implies equal column density on all scales. The structural analysis of dark clouds by automatic starcounts yields an internal density structure of $n(r) \propto r^{-1.0\pm0.4}$ (Stüwe 1990), and in particular for the Taurus-Auriga complex, $n(r) \propto r^{-1.3}$ (Cernicharo, Bachiller & Duvert 1985). Similarly, the distribution of the average densities of molecular clouds of varying radius follows the relation $n \propto r^{-1.1}$ (Larson 1981). Therefore, this density profile may be the signature of either a cluster of dust cores (consistent with the 3 UCHII regions found here).

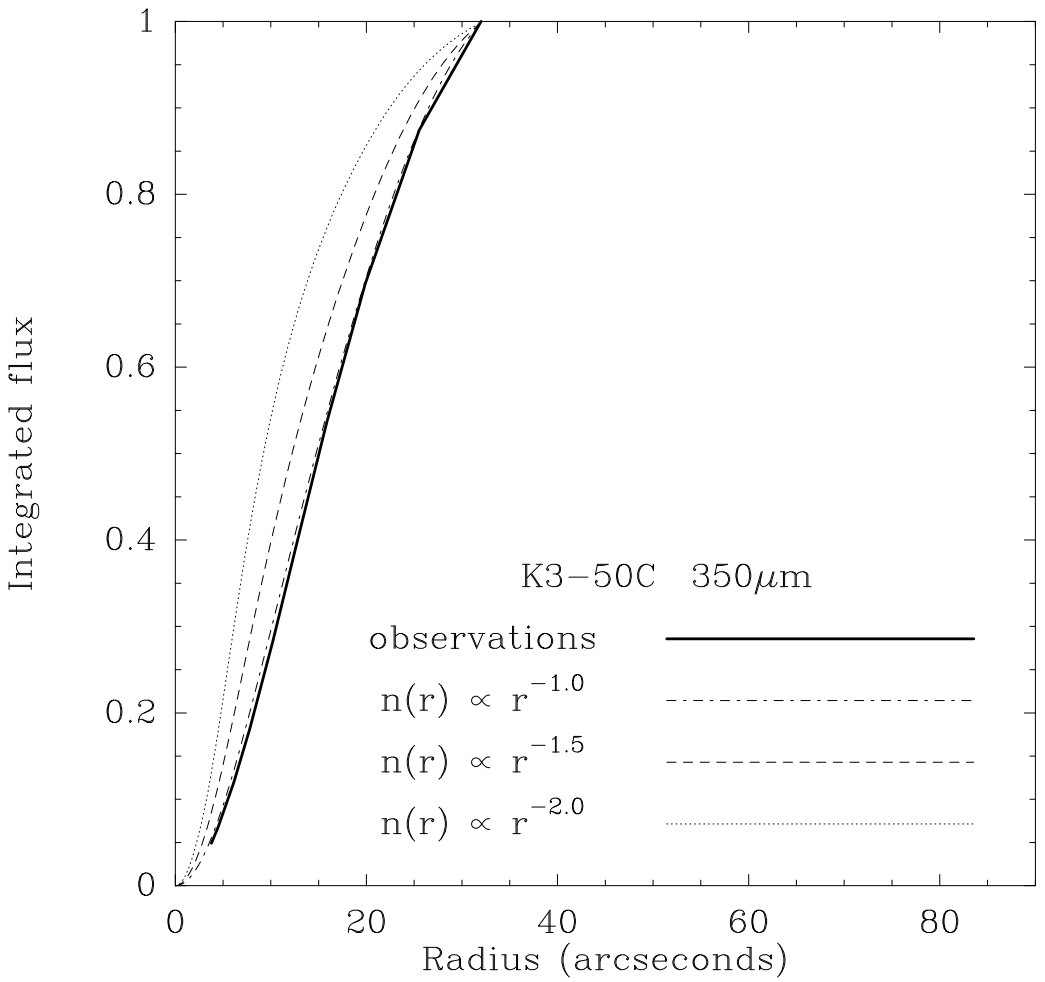

Figure 3.76: Observed flux profile of K3-50C measured from the 350μm image and compared to predictions of radiative transfer models.

The profile of G45.12+0.13 exhibits a similar shallow profile to that seen in K3-50C. Including the UCHII region, this source contains at least 2 young objects with outflows (see Chapter 5).

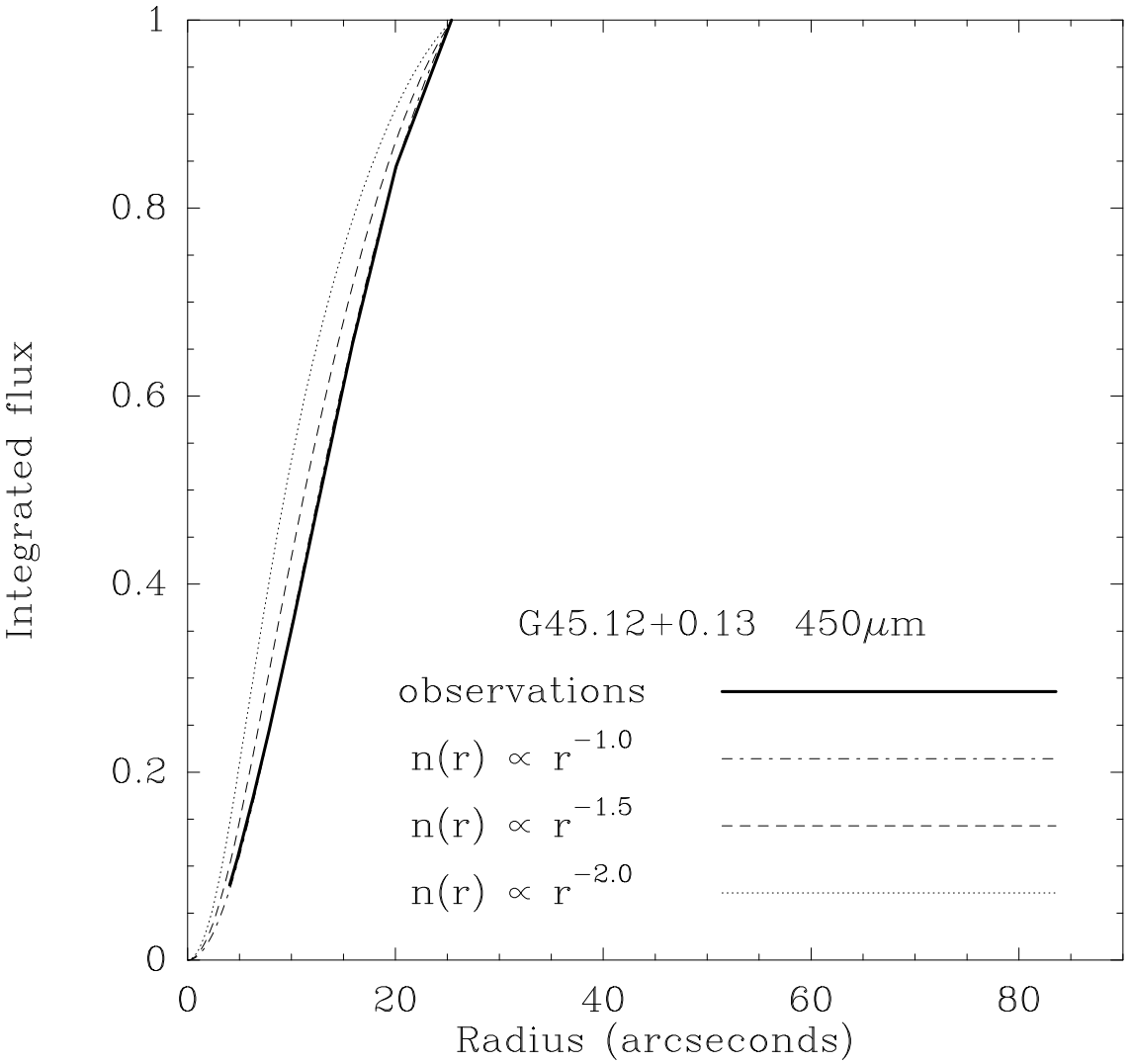

Figure 3.77: Observed flux profile of G45.12+0.13 measured from the 450μm image and compared to predictions of radiative transfer models.

Like G45.12+0.13 and K3-50C, GGD12-15 matches the $n(r) \propto r^{-1}$ power-law. At least two sources, the UCHII region and H_2O maser, have formed in this relatively lower luminosity object ($L < 10^4 L_\odot$).

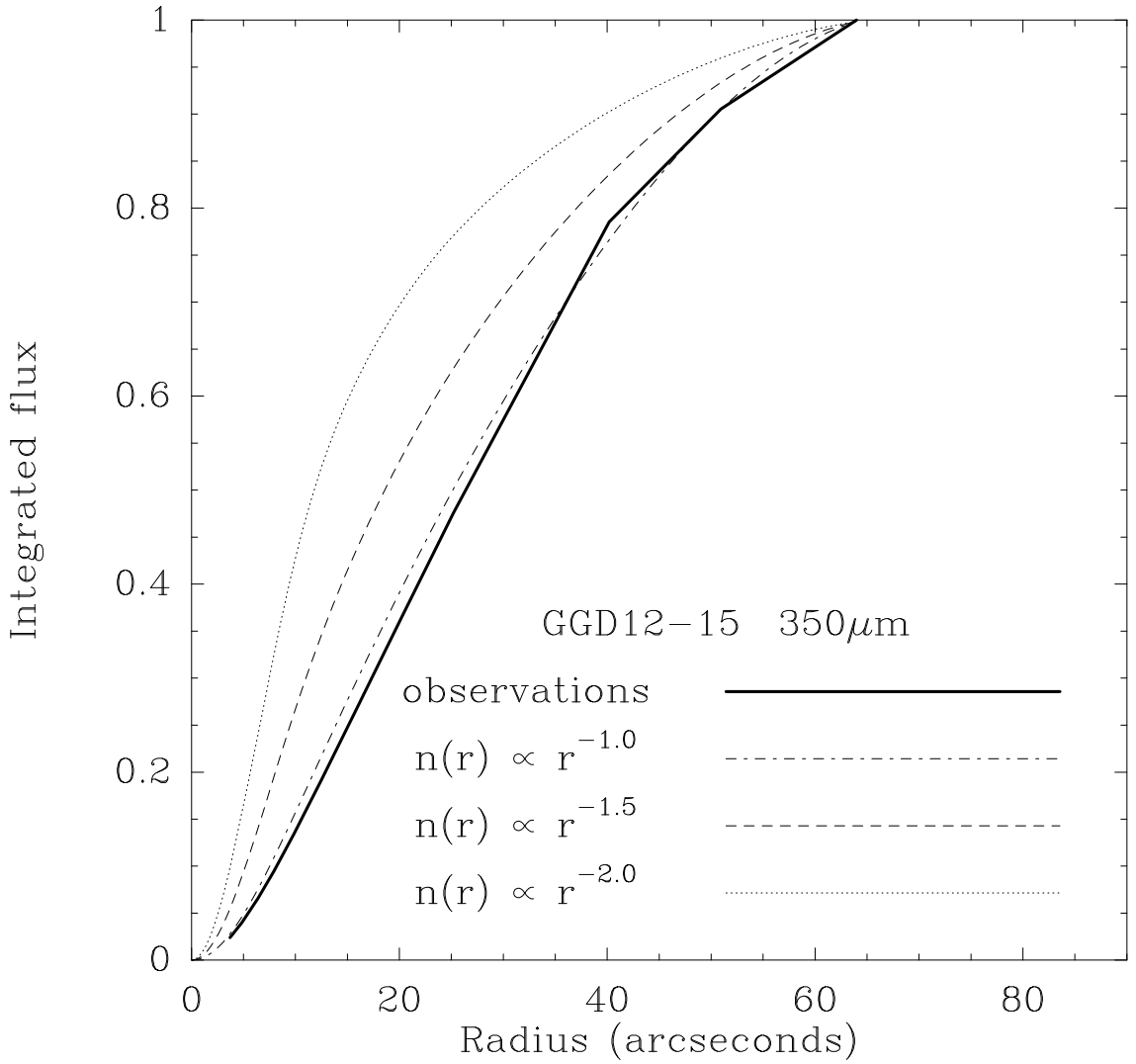

Figure 3.78: Observed flux profile of GGD12-15 measured from the 350μm image and compared to predictions of radiative transfer models.

G192.584-0.041 also matches the $n(r) \propto r^{-1}$ law throughout the cloud. Although only a single dominant radio source has been detected, there is an infrared cluster as well as faint radio and submillimeter emission to the north. Like GGD12-15, it is one of the lowest luminosity sources in the sample.

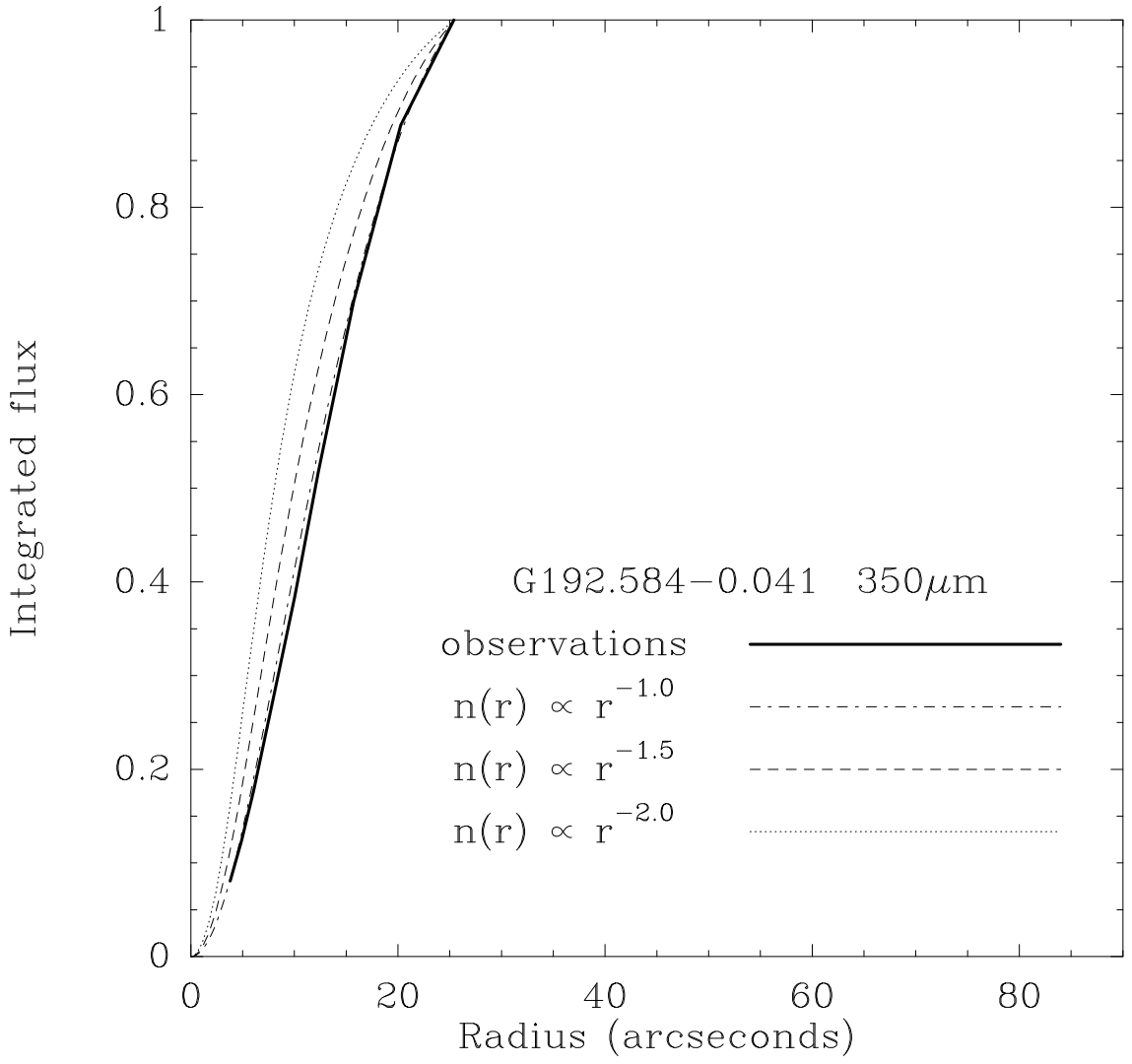

Figure 3.79: Observed flux profile of G192.584-0.041 measured from the 350μm image and compared to predictions of radiative transfer models.

G138.295+1.555 also matches the $n(r) \propto r^{-1}$ law throughout the cloud. As discussed in section 3.7.2, this cloud contains two radio sources and an infrared cluster of at least 30 stars. Like GGD12-15 and G192.584-0.041, it is one of the lowest luminosity sources in the sample.

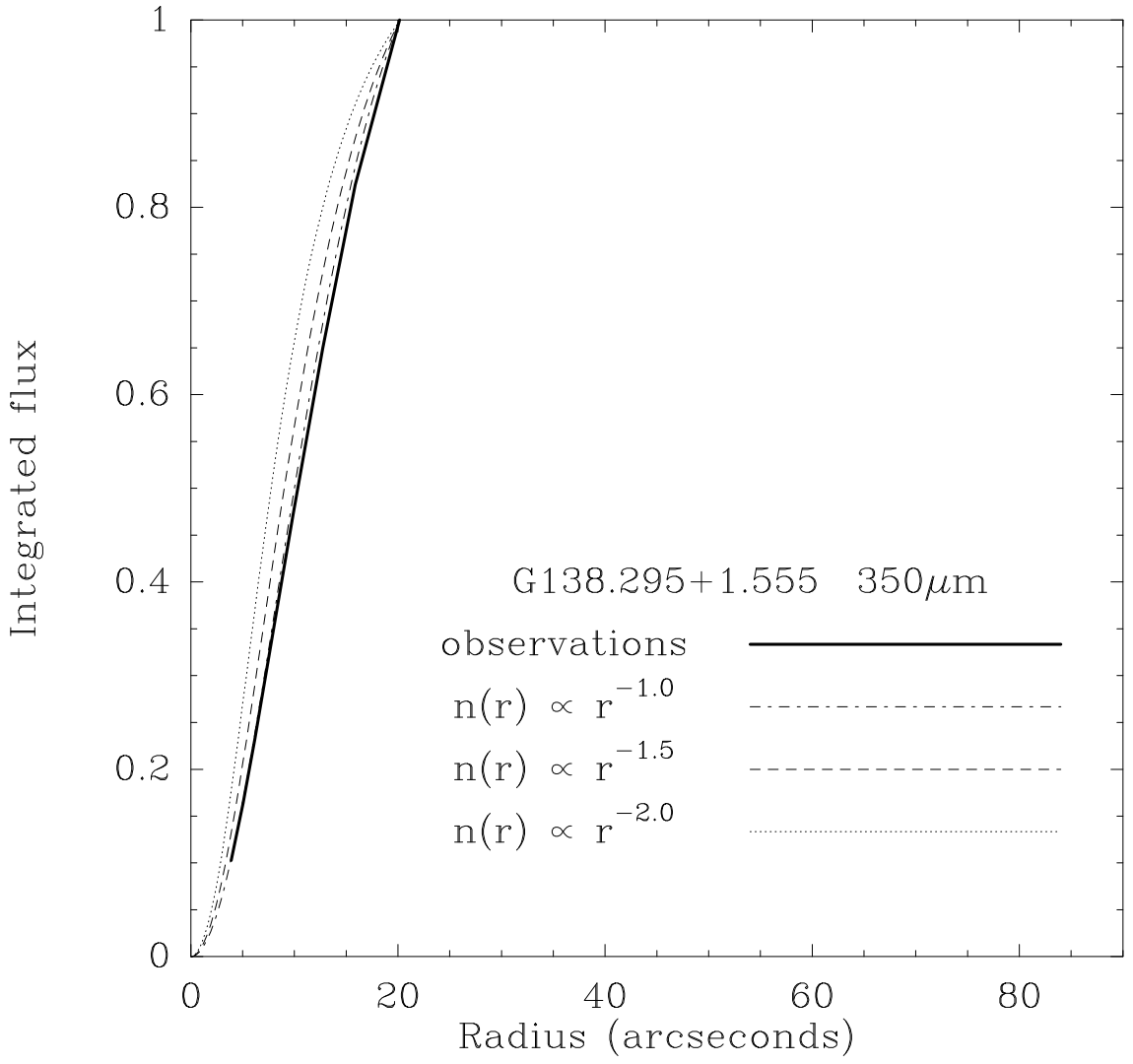

Figure 3.80: Observed flux profile of G138.295+1.555 measured from the 350μm image and compared to predictions of radiative transfer models.

Finally, G139.909-0.197 also matches the $n(r) \propto r^{-1}$ law. Like G138.295+1.555, this lower luminosity cloud contains more than two dozen young stars and possibly as many as five dozen (Weintraub & Kastner 1996; Weintraub et al. 1996).

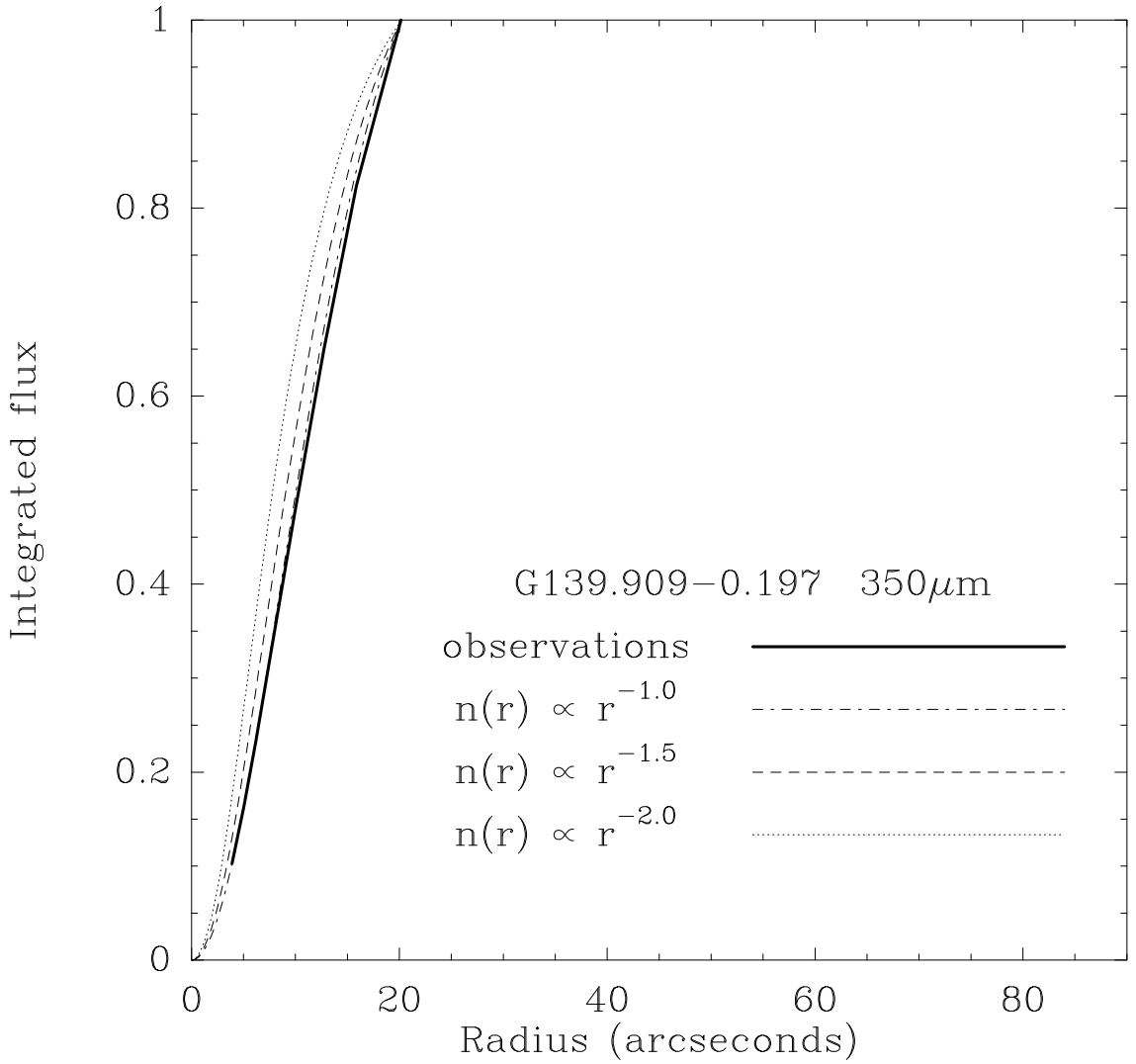

Figure 3.81: Observed flux profile of G139.909-0.197 measured from the 350μm image and compared to predictions of radiative transfer models.

3.10.10 Confirmation of the spectral energy distributions

Besides predicting the flux profiles discussed in the preceding section, the radiative transfer models also predict the total source flux as a function of wavelength. For a self-consistency check, these predictions can be compared to the measured fluxes that were used to fit the greybody models in section 3.9. Plotted in Fig. 3.82 are the predicted spectral energy distributions (SEDs) from the radiative transfer model for each source. Separate curves are plotted for the r^{-2}, $r^{-3/2}$ and the r^{-1} density profiles. In nearly every case, the measured far-infrared and submillimeter fluxes lie (within the error bars) on the appropriate curve that matches the flux profile. Like the one-component greybody models, the curves tend not to match well with the mid-infrared (12 and 25μm) fluxes. Apparently the dust model is not detailed enough to treat these wavelengths properly. Since only a single dust grain size was used, this shortcoming is not surprising. A more complex model would be necessary to treat features such as the mid-infrared silicate bands. However the simple model presented here does serve well at the wavelengths of interest.

3.10.11 Temperature distributions

Plotted in Fig. 3.83 are the equilibrium temperature distributions from the radiative transfer models. As can be seen by the thin straight lines overlayed, the simple scaling laws of $T(r) \propto r^{-2/5}$ or $r^{-1/3}$ (corresponding to $\beta = 1$ or 2) are good approximations to the model temperature distributions in the outer parts of the cloud. The general upturn in the model temperature occurs about the radius at which the model power-law density profile is matched to a Gaussian profile.

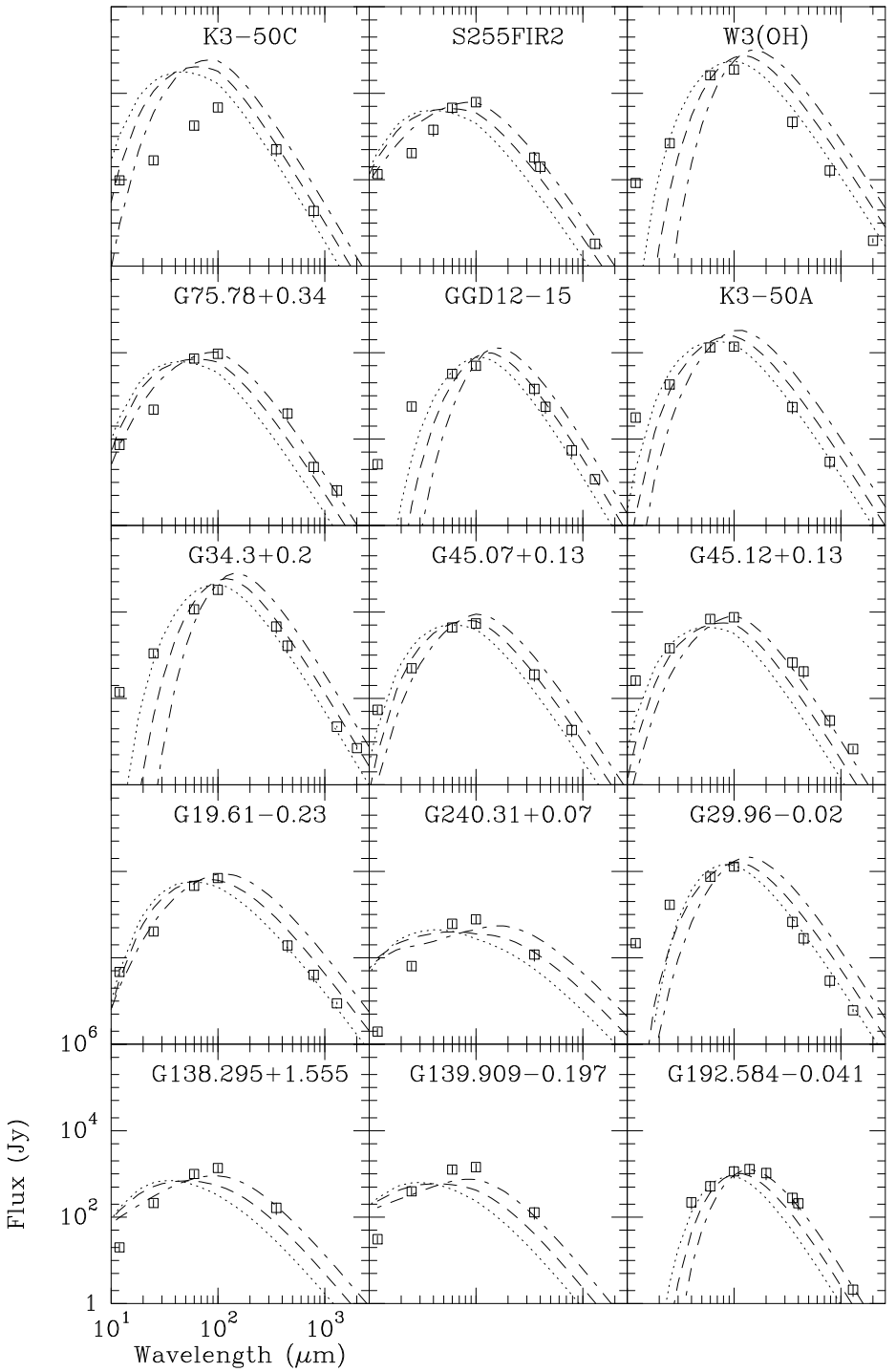

Figure 3.82: The predicted spectral energy distributions from the radiative transfer models are plotted as curves; *dotted:* $\rho \propto r^{-2}$, *dashed:* $r^{-3/2}$, *dash-dot:* r^{-1}. The boxes mark the observed fluxes from each source corresponding to IRAS, submillimeter, and millimeter measurements.

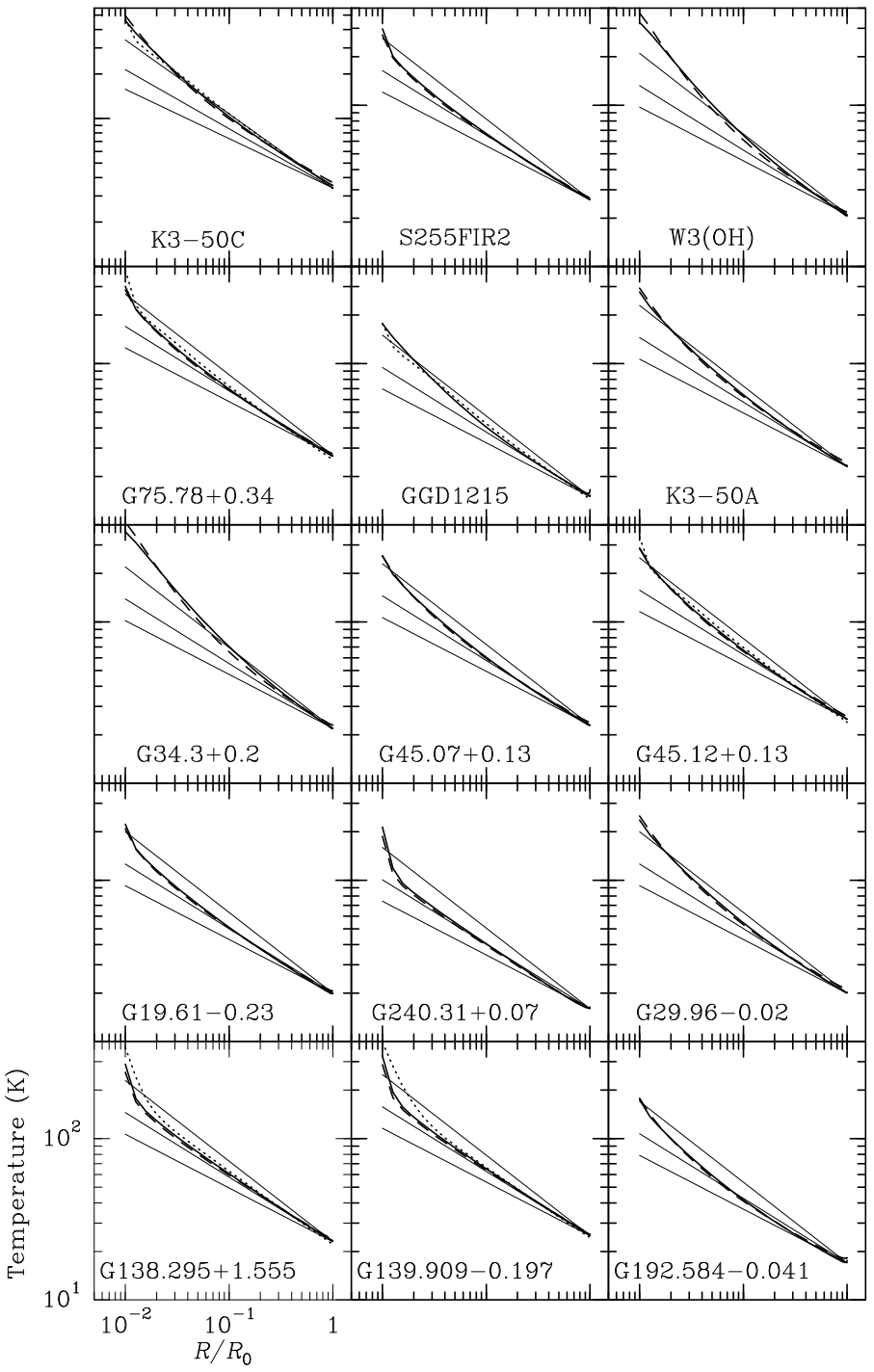

Figure 3.83: The predicted temperature distributions from the radiative transfer models are plotted as curves; *dotted:* $\rho \propto r^{-2}$, *dashed:* $r^{-3/2}$, *dash-dot:* r^{-1}. The straight lines mark the simple scaling laws of $T(r) \propto r^{-1/2}, r^{-2/5}$ and $r^{-1/3}$ (from top to bottom). The upturns in the model temperature at small radii correspond to the core radius where the power-law density profile is matched to a Gaussian profile.

3.11 Luminosity to mass ratios

With the density profile analysis complete, a final relation to explore in these UCHII regions is their FIR luminosity to dust mass ratio ($L_{\rm FIR}/M_{\rm dust}$) versus dust temperature. As evident in Table 3.4, a large range exists in the $L_{\rm FIR}/M_{\rm dust}$ ratio (3 to 200). Because the FIR dust emission derives from re-processed starlight originating at the core of molecular clouds, the $L_{\rm FIR}/M_{\rm CO}$ ratio has been quoted as a measure of the star formation rate of whole galaxies and individual giant molecular clouds (Young et al. 1986; Mooney & Solomon 1988; Scoville & Good 1989; Carpenter, Snell & Schloerb 1990). Typically, the mass has been determined from CO observations; but in this case, we can measure the dust mass directly from the greybody models. Because the FIR dust luminosity is proportional to dust mass and the frequency integral of the modified Planck function, the $L_{\rm FIR}/M_{\rm dust}$ should be proportional to the latter quantity (Cox & Mezger 1989):

$$\frac{L_{\rm FIR}}{M_{\rm dust}} \propto \int_0^\infty B_\nu(T_{\rm dust}) Q_\nu d\nu \propto \int_0^\infty B_\nu(T_{\rm dust}) \nu^\beta d\nu \propto T_{\rm dust}^{4+\beta}. \tag{3.33}$$

As expected, Fig. 3.84 indicates a strong correlation between the $L_{\rm FIR}/M_{\rm dust}$ ratio and the dust temperature of UCHII regions. No correlation is seen in the $L_{\rm FIR}$ versus $T_{\rm dust}$ diagram due to the range of masses present in the source sample. A simple explanation for the observed $L_{\rm FIR}/M_{\rm dust}$ vs. $T_{\rm dust}$ relation is that it represents an evolutionary track. That is, the more evolved sources lie to the upper right because they have formed a greater number of hot stars that have boosted the luminosity and heated the dust to a higher temperature over a longer period. However, the sources tend to group together on the $L_{\rm FIR}/M_{\rm dust}$ vs. $T_{\rm dust}$ diagram as a function of their density profile, with isothermal cores showing the largest $L_{\rm FIR}/M_{\rm dust}$ ratios and temperatures and logatropic cores showing the smallest. In other words, the more centrally-condensed cores contain warmer dust. A similar correlation is seen in extragalactic studies in which merging and interacting galaxies lie to the upper right and isolated galaxies lie to the lower left of the $L_{\rm FIR}/M_{\rm CO}$ vs. ($F_{60\mu{\rm m}}/F_{100\mu{\rm m}}$) diagram

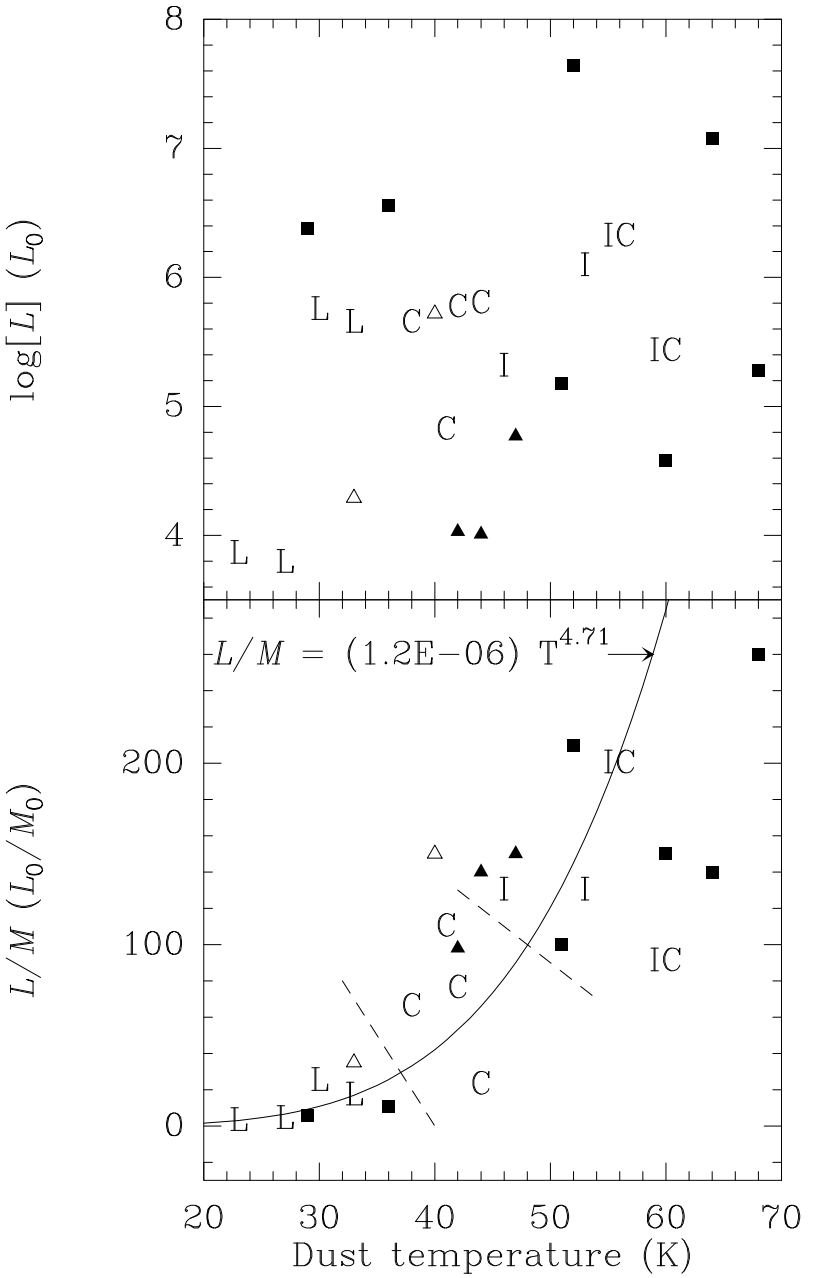

Figure 3.84: *Upper panel:* The luminosity plotted against the dust temperature from the one-component greybody model. Letters denote the UCHII regions whose density profiles indicate the isothermal (I), collapse (C), isothermal/collapse (IC) and logatropic (L) profiles. Filled triangles mark the UCHII regions with no long wavelength flux measurements and open triangles mark Mon R2 and G75.84+0.40 for which density profiles could not be reliably measured. Squares mark HII regions from Gordon (1988). There is little correlation due to the range of masses in the sample. *Lower panel:* Same as the upper panel for the luminosity to dust mass ratio, a measure of star formation efficiency which correlates with dust temperature. Overlayed is a power law fit consistent with a modified Stefan-Boltzmann law with $\beta = 0.71$.

(Young 1990). Thus, perhaps the range of values is not established *directly* by the time evolution in the star formation rate from lower to higher values of $L_{\rm FIR}/M_{\rm dust}$. Instead, a range of initial conditions may determine the collapse density profile, which in turn sets the star formation rate and the dust temperature. Specifically, clouds with steeper radial density profiles yield higher star formation rates and warmer dust. A further argument against simple time evolution is that because all of the sources contain UCHII regions, they may all be of similar age and in a similar evolutionary stage.

3.12 Summary

The dust cores surrounding a sample of 17 UCHII regions are resolved for the first time in the high-resolution submillimeter continuum images presented in this chapter. The first impression left by the images is the presence of clusters of dust emission. Undoubtedly the UCHII regions dominate the peak emission due to the warm dust surrounding them. However, in many cases, cores of lower level emission lie in their vicinity. H_2O masers are often found in these sub-cores, although many are not associated with any known maser or radio continuum source. These newly-identified sources should be followed up with deep near-infrared surveys to search for the counterparts of these massive, possibly protostellar sources.

As a sample, the sources cover a fairly wide range of bolometric luminosity (10^4 to $10^6 L_\odot$) and temperature (23 to 60 K). One-component and two-component greybody models show that the submillimeter emission can be characterized accurately by a single temperature and grain emissivity index. The average temperature is 40 ± 10 K and the average grain emissivity index (β) is 2.00 ± 0.25, consistent with results from prior 1.3 mm surveys. Using power-law density profiles of the form $n(r) \propto r^{-n}$, radiative transfer models successfully predict the flux profile of the dust. Three of the sources are consistent with r^{-2} resembling an isothermal cloud. In two sources, the outer parts of the cloud are consistent with the r^{-2} profile while the inner parts approach the shallower $r^{-1.5}$ profile indicative of dynamical collapse.

The appearance of these two sources is likely to be short-lived as the collapse has been occurring for only ~ 5000 yr. Four sources are consistent with the $r^{-1.5}$ profile throughout the cloud, possibly indicating a more advanced state of collapse. The final six regions are shown to exhibit a density profile approaching the r^{-1} law, similar to that seen in nearby extended dark clouds.

It should be noted that of the six logatropic sources, four are the least distant ($d < 2.5$ kpc) regions in the sample. These four are also the lowest luminosity sources in the sample ($L < 10^{4.3} L_{\odot}$) corresponding to stellar types later than B0.5. In most cases, these regions show evidence for a cluster of young embedded stars on scales larger than the beamsize. Hence it is no surprise that they appear more like local low-mass star-forming dark clouds than the rest of sample. When these four sources are discarded from the statistics, over half (6 out of 11) UCHII regions exhibit the collapse density profile to some degree. These results are summarized in Table 3.6.

Table 3.6: Summary of dust density profiles

Density profile	power-law index	# sources	# sources with $L > 10^{4.3} L_{\odot}$	% of sources with $L > 10^{4.3} L_{\odot}$	
isothermal	r^{-2}	3	3	27%	
isothermal/collapse	$r^{-2}/r^{-3/2}$	2	2	18%	} 55%
collapse	$r^{-3/2}$	4	4	36%	
logatropic	r^{-1}	6	2	18%	

Finally, an interesting discovery is that sources with similar density profiles lie in similar areas of the $L_{\rm FIR}/M_{\rm dust}$ (star formation rate) vs. $T_{\rm dust}$ diagram. Isothermal clouds lie to the upper right where the star formation rate is high, while logatropic clouds lie to the lower left where the rate is low. Apparently, clouds with more highly concentrated density profiles develop star formation more rapidly than other configurations. Because all the clouds contain UCHII regions with typical lifetimes of $\sim 5 \times 10^4$ yr, it is possible that this difference arises from different physical conditions (such as the relative importance of magnetic field support) rather than being different evolutionary states of a general track.

As expected from the relative timescales, the inner region and in many cases the bulk of the dust cloud is still collapsing even after the first OB star(s) have formed near

the core. Opposing the collapse motion are bipolar molecular outflows from young embedded objects in the core. It has been proposed that outflows may ultimately limit the mass of an accreting star (Silk 1995). Measuring the strength of outflows from these clouds and determining whether the UCHII regions or associated sources drive the outflows is the subject of the next chapter.

Chapter 4 Molecular Outflows from UCHII Regions

4.1 Characteristics of molecular outflows

At some point during the formation process of a new star, an outflow phase begins which can manifest itself in various observational forms including the bipolar molecular outflow (Lada 1985; Bachiller & Gómez-González 1992; Bachiller 1996). Molecular outflows are most commonly observed as high velocity wings in the rotational transitions of CO, the most abundant interstellar molecule after H_2. These line wings usually extend to velocities of 5-30 km s^{-1} away from the systemic velocity but can reach to velocities > 100 km s^{-1} in the case of extremely high velocity (EHV) bullets (such as in HH7-11, Lizano et al. 1988; Masson et al. 1990; Bachiller & Cernicharo 1990). Although not yet fully understood, the acceleration mechanism of the molecular gas must be intimately related to the star formation process (Shu et al. 1994). When the high velocity CO emission can be resolved spatially, it usually exhibits a collimated bipolar morphology, analogous to the ionized jets sometimes seen at visible and radio wavelengths from young stellar objects (e.g., Reipurth & Heathcote 1993; Staude & Elsässer 1993). In many cases, the CO outflows align with bright knots of emission nebulae known as Herbig-Haro (HH) objects which often exhibit large proper motions implying velocities of ~ 200 km s^{-1} away from the driving source (see references in Schwartz 1983). The similar morphology of these phenomena suggests a common driving mechanism and invites a comparison of their physical attributes.

4.1.1 Momentum comparison between jets and outflows

An important physical measure of a jet or outflow is the force, or the rate at which momentum is deposited into the flow. Usually the force F is expressed as the product

of the mass loss rate $\dot{m}$ and the flow velocity v. In the case of optical jets, v can be determined from high resolution spectroscopy of the Hα line. With Hα imaging, one can measure the length of the jet and compute a kinematic age t, the dynamical crossing timescale. The electron density $n_{\rm e}$ can be estimated from the intensity ratio of forbidden lines such as the 6717 and 6731 Å lines of ionized sulfur (Hartmann & Raymond 1984). Combining $n_{\rm e}$ with the linear dimensions of the jet leads to an estimate of the mass m of ionized gas in the flow. Combining these parameters yields the outflow force:

$$F = \dot{m}v = \frac{mv}{t} = \frac{mv}{r/v} = \frac{mv^2}{r}. \tag{4.1}$$

In the case of molecular outflows, v can be determined from CO spectra, r from the CO maps, and m from the integrated CO emission (Lada 1985). In the case of L1551 IRS5, the force observed in the optical jet (Sarcander, Neckel & Elsässer 1985) is 2 to 3 orders of magnitude less than the force required to drive the molecular outflow (Moriarty-Schieven & Snell 1988). This result has been typical of young stellar objects; the force exerted by the ionized gas of optical jets is about 2 orders of magnitude too small to drive the molecular outflows (Mundt, Brugel & Bührke 1987). Consequently, it was widely speculated that the two phenomena had separate origins, with the optical jet being driven by a collimated stellar wind while the larger molecular outflow was driven by a wide-angle wind from the accretion disk (Pudritz 1988; Pudritz & Norman 1983).

However, the discrepancy in momenta of jets and outflows has been eased by the discovery of two key facts. First, it was realized that the outflows may be much older than previously assumed. The typical kinematic age of molecular outflows is $\sim 10^4$ yr (Masson & Chernin 1993). However, in a survey of a well-defined sample of IRAS sources from the Class I or Class II-D phase of low-mass young stellar objects (as defined by Adams, Lada & Shu (1987)), 9 out of 12 embedded IRAS point sources contained outflows (Parker, Padman & Scott 1991). The combined duration of the Class I and II-D phases is believed to be 2.5×10^5 yr (Beichman et al. 1986; Myers

et al. 1987). Therefore, the statistical lifetime τ of the outflows is

$$\tau = \left(\frac{\text{number of sources with outflows}}{\text{number of sources}}\right) = \left(\frac{9}{12}\right) 2.5 \times 10^5 \text{ yr} = 1.9 \times 10^5 \text{ yr}. \tag{4.2}$$

A similar lifetime has been derived by comparing the number of outflow sources with the number of optically-identified T Tauri stars in the nearby dark cloud L1641 (Fukui 1993).

Second, calculations suggest that much of the optical jet material ($\sim$ 98%) is neutral gas (Hartigan, Morse & Raymond 1994; Raga, Binette & Cantó 1990). The presence of neutral gas in jets has been confirmed by the detection high-velocity HI emission in the 21 cm line from HH7-11 (170 km s^{-1}) (Lizano et al. 1988) and L1551 (260 km s^{-1}) (Giovanardi et al. 1992). The combination of these two facts can close the gap in momentum between the two different phenomena (Raga 1991; Padman & Richer 1994). For example, it has been observed that the HH111 jet may provide sufficient momentum to drive the surrounding CO outflow in L1617 (Cernicharo & Reipurth 1996). Similar results are found in the red nebulous object RNO43 (Bence, Richer & Padman 1996). Finally, the fact that both jets and outflows are high-velocity and highly-collimated structures points to a common driving and collimation mechanism near the central source (Masson & Chernin 1994). They could well be different manifestations of the same phenomenon.

4.1.2 Conservation of momentum in outflows

One of the observational constraints on molecular outflow models is that they appear to be driven by a process that conserves linear momentum. Because outflows generally exhibit strong bipolarity in both velocity and space, the transverse velocity of material must be small compared to the radial velocity along the axis of the flow. This feature is a natural characteristic of a momentum-driven flow. In contrast, a pressure-driven flow that conserves energy would tend to inflate bubbles of ambient gas, leading to larger transverse velocities than are observed (Meyers-Rice & Lada 1991). Such a flow

would also exhibit backward moving material in each lobe which is generally not seen. Furthermore, such a flow cannot be collimated by the ambient cloud without inducing substantial transverse motion in the collimating mass (Takano et al. 1984). Thus, outflows must be driven in a momentum-conserving manner by a bipolar collimated wind at the central source (Masson & Chernin 1993).

4.1.3 Momentum transfer in jet-driven outflows

In parallel with these new conclusions, unified models of jet-driven molecular outflows have been developed (Raga et al. 1993; Raga & Cabrit 1993; Masson & Chernin 1993; Chernin et al. 1994). In general, the models must transfer momentum (P) from a supersonic jet to the dense ambient gas that will comprise the molecular outflow. The rate of momentum transfer can be written:

$$\frac{dP}{dt} = \dot{P} = (\dot{m}v)_{\rm outflow} = \epsilon(\dot{m}v)_{\rm jet}, \tag{4.3}$$

where ϵ is the entrainment efficiency, which equals 1 if the jet is completely stopped by the ambient material. The physical device used in the models to accomplish the momentum transfer from the jet to the outflow is a bow shock. When a supersonic jet impacts stationary gas, the jet rapidly decelerates in a jet shock while the ambient gas is accelerated by a forward bow shock (Blandford & Rees 1974). Following Chernin et al. (1994), the rate of momentum transfer ($\dot{P}$) at the working surface (ws) of a bow shock is:

$$\dot{P} = \rho_{\rm jet} A_{\rm ws} (v_{\rm jet} - v_{\rm ws})^2 = \epsilon_{\rm BS} \rho_{\rm jet} A_{\rm jet} v_{\rm jet}^2, \tag{4.4}$$

where $\epsilon_{\rm BS}$ is the entrainment efficiency of the bow shock, $A_{\rm jet}$ is the geometrical area of the jet, $A_{\rm WS}$ is the geometrical area of the working surface of the bow shock, and $\rho_{\rm jet}$ is the gas density in the jet. One can solve this equation for $\epsilon_{\rm BS}$ in terms of the

observable parameters:

$$\epsilon_{\rm BS} = \frac{A_{\rm ws}}{A_{\rm jet}}\left(1 - \frac{v_{\rm ws}}{v_{\rm jet}}\right)^2. \tag{4.5}$$

In the limit that all of the energy released in the bow shock is immediately radiated away, there is no additional thermal pressure and the ram pressure in the jet equals the ram pressure of the swept-up medium at the working surface of the bow shock:

$$\dot{m}_{\rm jet} v_{\rm jet} = \dot{m}_{\rm ambient} v_{\rm ws} \tag{4.6}$$

$$\rho_{\rm jet} A_{\rm jet} (v_{\rm jet} - v_{\rm ws})^2 = \rho_{\rm ambient} A_{\rm ws} v_{\rm ws}^2. \tag{4.7}$$

Using the quadratic formula, one can solve for the velocity of the working surface:

$$v_{\rm ws} = v_{\rm jet}\left(\frac{\sqrt{\eta\alpha}}{1+\sqrt{\eta\alpha}}\right) \tag{4.8}$$

$$\text{where } \eta \equiv \frac{\rho_{\rm jet}}{\rho_{\rm ambient}} \tag{4.9}$$

$$\text{and } \alpha \equiv \frac{A_{\rm jet}}{A_{\rm ws}}. \tag{4.10}$$

In this case, the bow shock entrainment efficiency then becomes:

$$\epsilon_{\rm BS} = \frac{1}{\alpha}\left(\frac{1}{1+\sqrt{\alpha\eta}}\right). \tag{4.11}$$

Chernin et al. (1994) have computed three-dimensional smoothed particle hydrodynamic simulations of jets in which the jet area and bow shock areas are equal ($\alpha = 1$) and with several different values of density contrast (η) and jet Mach number (M). The jet radius was $r_{\rm jet} = 2 \times 10^{16}$ cm and the sound speed in the jet was 12 km s^{-1}, appropriate for ionized gas with $T \sim 10^4$ K from Eq. 3.21. These simulations show that in the case of a high Mach number jet ($M = 30$, $v = 350$ km s^{-1}), $\epsilon \approx \epsilon_{\rm BS}$ and the jet is not decelerated significantly until it reaches a radius of $\sim 20 r_{\rm jet}$, or 0.13 pc (corresponding to $27''$ at a distance of 1 kpc). Ambient gas is entrained only at the end of the jet, a process called prompt entrainment (DeYoung 1986). This process leads to a parabolic-shaped nebula with the vertex at the bow shock and the curve

opening toward the driving source. However, in a low Mach number jet ($M = 3$, $v = 39$ km s^{-1}) $\epsilon_{\rm BS}$ is a factor of a few smaller than ϵ and the jet is decelerated by $\sim 25\%$ by the time it flows a distance $= 3r_{\rm jet}$. In this case, called steady-state (or turbulent) entrainment, the ambient gas is entrained essentially along the entire jet. Because the transverse motion of gas remains roughly constant, this process creates a conical outflow of increasing radius with distance.

4.1.4 Comparison to observations

The detection of EHV features in outflows is the most important piece of evidence for jet-driven outflows. EHV gas requires that protostellar jets have high Mach numbers, suggesting that prompt entrainment dominates the flow. This process can explain the common observational finding that the highest velocity gas shows the highest degree of collimation as in the outflows of NGC2024 FIR5 (Richer, Hills & Padman 1992) and NGC2264G (Lada & Fich 1996). A specific numerical model of Chernin et al. (1994) with high Mach number and $\eta = \alpha = 1$ actually predicts the existence of a small clump of gas ($10^{-3} M_{\odot}$) moving at 100 km s^{-1} in the post-shock region. In this case, $\epsilon \approx \epsilon_{\rm BS} = 0.25$, implying that the momentum transfer is 25% efficient. Another observational finding that may support the bow shock model is the frequent presence of infrared reflection nebulae near the origin of molecular outflows (Hodapp 1994; Hunter et al. 1995). Although they may be illuminated by radiation from young stellar clusters, these nebulae could also be powered in part by the cooling radiation from bow shocks (Testi et al. 1994).

Even though the jet-driven outflow model of Chernin et al. (1994) is promising, it does possess a few shortcomings. First, the model does not treat the evolution of the cavity region left behind by the outwardly-moving bowshock; thus, alone, it may not properly predict the appearance of older outflows. Raga et al. (1993) propose a similar jet model but with a large number of internal working surfaces along the length of the jet that eject mass sideways to form a turbulent, isothermal envelope of jet material mixed with entrained ambient gas. This envelope can then refill the

trailing cavity left by the bowshocks and preserve the continuous appearance of the molecular outflow. Evidence for this scenario comes from the morphology of the near-infrared vibrationally-excited H_2 line emission which traces hot gas ($T \gtrsim$ 2000 K). Frequently, as in NGC2071 (Garden, Russell & Burton 1990) and IRAS 03282+3035 (Bachiller et al. 1994), the hot H_2 gas lies in a collimated structure along the axis of the flow, tracing the turbulent interface where kinetic energy from the jet heats the molecular cloud.

A shortcoming ascribed to jet-driven outflow models in general is that they cannot explain the existence of poorly-collimated HH flows. Numerical simulations show that supersonic jets develop a radiatively-cooling dense shell of gas between the jet shock and the leading bow shock which may be the source of the optical emission from HH objects (Blondin, Königl & Fryxell 1989; Wolfire & Königl 1991). But in L1551, the objects HH28 and HH29 lie far from the outflow axis emanating from IRS5 yet they both have high proper motions and radial velocities (Davis et al. 1995). Also, rather than tracing the jet, the H_2 emission extends over most of the Hα cavity which coincides with the blue CO outflow lobe. These phenomena suggest a wide-angle wind from the central source (Snell, Loren & Plambeck 1980); however, they could conceivably be explained by wandering of the central jet. Recent observations of RNO43 show unambiguous evidence for jet wandering in the form of pairs of symmetric HH objects lying at various position angles within the total opening angle of the outflow (Bence, Richer & Padman 1996). This evidence supports an appealing idea that the various morphologies of molecular outflows simply represent the integrated effect of a wandering central jet over a long timescale.

4.2 Possible mechanisms of jet-driven outflows

4.2.1 Radiation pressure

If molecular outflows are driven by stellar jets, then what is the ultimate driving mechanism of the jet? Assuming a central star has already formed, one obvious mechanism

for a momentum-conserving outflow is radiation pressure on the surrounding dust envelope. The radiation pressure from a star of luminosity L has the potential of driving a mass outflow $\dot{M}$ at velocity $V(r)$:

$$\dot{M}V(r) = 4\pi r^2 \beta P_{\rm rad} = \frac{\beta L}{c} = 2.0 \times 10^{-8} \beta \left(\frac{L}{L_\odot}\right) M_\odot \text{ km s}^{-1} \text{ yr}^{-1} \tag{4.12}$$

where β is an efficiency factor amounting to some measure of the optical depth of dust in the envelope with $\beta = 1$ corresponding to the optically-thick case (Knapp et al. 1982). Radiation pressure acts primarily on the dust component rather than the gas because the mass absorption coefficient of the dust ($\kappa_{\rm dust}$) is much higher than that of the gas ($\kappa_{\rm gas}$). For example, in ionized gas, a major component of the continuum opacity comes from Thomson scattering off the free electrons giving a mass absorption coefficient

$$\kappa_{\rm gas} = \frac{\sigma_{\rm T}}{m_{\rm H}} \approx 0.4 \text{ cm}^2 \text{ g}^{-1}, \tag{4.13}$$

where $\sigma_{\rm T}$ is the Thomson cross section (Rybicki & Lightman 1979). For dust, the mass absorption coefficient from the geometric cross section is

$$\kappa_{\rm dust} = \frac{\sigma_{\rm gr}}{m_{\rm gr}} = \frac{\pi r_{\rm gr}^2}{\frac{4}{3}\pi r_{\rm gr}^3 \rho_{\rm gr}} \approx \frac{1}{4 r_{\rm gr}} = 2.5 \times 10^3 \left(\frac{r_{\rm gr}}{0.1 \mu\text{m}}\right)^{-1} \text{ cm}^2 \text{ g}^{-1} \tag{4.14}$$

$$>> (R\kappa_{\rm gas} \approx 40), \tag{4.15}$$

assuming spherical grains with density $\rho_{\rm gr} = 3$ g cm^{-3} and a gas to dust mass ratio $R = 100$. However, the gas mixed with the dust will presumably acquire a similar outflow motion through collisions with grains (Shull 1977). The timescale for collision $t_{\rm coll}$ of a gas particle with a grain (Goldreich & Kwan 1974) in the high density

($\sim 10^5$ cm^{-3}) ionized gas near the star is:

$$t_{\rm coll} = (n_{\rm dust}\sigma_{\rm gr}c_s)^{-1} = (\rho_{\rm dust}\kappa_{\rm dust}c_s)^{-1} = \left(\frac{n_{\rm H}m_{\rm H}\kappa_{\rm dust}c_s}{R}\right)^{-1} \tag{4.16}$$

$$= 3.8\times10^2\left(\frac{n_{\rm H_2}}{10^5\ {\rm cm^{-3}}}\right)^{-1}\left(\frac{c_s}{10\ {\rm km\ s^{-1}}}\right)^{-1}\left(\frac{r_{\rm gr}}{0.1\mu{\rm m}}\right)\left(\frac{R}{100}\right)\ {\rm yr} \tag{4.17}$$

$$<< t_{\rm outflow}. \tag{4.18}$$

Higher densities, smaller grains and a smaller gas to dust mass ratio (R) will all lead to a shorter collision timescale.

Using Eq. 4.12, one can compare the observed values of the outflow momentum supply rate with the maximum amount available from radiation pressure. In the case of RNO43, the central source has a bolometric luminosity of $6L_\odot$ and the momentum flux in the outflow is $4\times10^{-4}M_\odot$ km s^{-1} yr^{-1} (Bence, Richer & Padman 1996). This value is 3 orders of magnitude larger than radiation pressure can supply! This discrepancy is typical of outflows from low-mass stars (Lada 1985; Mozurkewich, Schwartz & Smith 1986) and remains significant even with a factor of 10 correction for the outflow age (as discussed in section 4.1.1). Empirically, the mass loss rate of outflows scales as $\dot{M} \propto L^{0.6\pm0.1}$ over the range of 1 to $10^5L_\odot$ (Levreault 1988). Thus, the large discrepancy between radiation pressure and outflow momentum flux may disappear in sufficiently massive stars if the driving mechanism remains the same. This possibility must be checked with observations of outflows from high-mass stars. In either case, a different source of outflow momentum must be considered for low-mass stellar outflows.

4.2.2 Disk winds

In order to explain the large observed values of momentum flux in outflows, theories of particle winds from accretion disks have been developed. The formation of disks around protostars has been shown to be inevitable because the excess of angular momentum in a typical molecular core over that of a pre-main sequence star leads to

a non-radial collapse (Terebey, Shu & Cassen 1984; Boss 1987). Recently, elongated disks of radius ~ 70 AU perpendicular to the outflow axes in L1551 IRS5 and HL Tau have been resolved in submillimeter continuum with the CSO-JCMT interferometer (Lay et al. 1994). Presumably, accretion processes in the disk allow mass to move inward and angular momentum to move outward (Pringle 1981). Ejection of this angular momentum is a possible source of jets and molecular outflows, however a plausible mechanism requires both strong magnetic fields and rapid rotation (Shu et al. 1988; Shu et al. 1994). The basic model of a magnetocentrifugally driven flow provides for a wind of magnitude $\dot{M}_w$:

$$\dot{M}_w = f\dot{M}_d, \tag{4.19}$$

where $\dot{M}_d$ is the accretion rate and f is an efficiency factor related to the angular momentum of the inflowing and outflowing matter (Najita & Shu 1994). The wind presumably emerges at the radius where the gravitational and centrifugal accelerations balance, the so-called X-point. For this reason, the wind is referred to as an X-wind with a linear velocity V_X of the same order of magnitude as the angular velocity Ω_X in the plane of the disk:

$$\frac{V_X^2}{R_X} = \frac{GM_*}{R_X^2} \tag{4.20}$$

$$\Omega_X = \sqrt{\frac{GM_*}{R_X^3}} \tag{4.21}$$

$$V_X \approx R_X\Omega_X = \sqrt{\frac{GM_*}{R_X}}. \tag{4.22}$$

For a $1M_\odot$ protostar, if $R_X \sim 10R_\odot$ then $V_X \sim 140$ km s^{-1}, typical of HH jet velocities. The resulting momentum supply rate to the wind can be estimated by

assuming the accretion process takes place during the typical outflow timescale:

$$\frac{dP}{dt} = \dot{M}_w V_X = f\dot{M}_d V_X \tag{4.23}$$

$$= 7 \times 10^{-4}(f)\left(\frac{M_*}{M_\odot}\right)^{\frac{3}{2}}\left(\frac{t_{\rm acc}}{2\times10^5\ {\rm yr}}\right)^{-1}\left(\frac{R_X}{10\ R_\odot}\right)^{-\frac{1}{2}} M_\odot\ {\rm yr}^{-1}\ {\rm km\ s}^{-1}. \tag{4.24}$$

This value is sufficient to drive the observed outflow in RNO43 with values of $f \sim 0.5$. The luminosity carried by the wind will consist of two parts, one component carried by the gas and the other carried by the magnetic field. The upper limit to the wind luminosity can be expressed simply as the energy released during accretion:

$$L_w \lesssim \frac{GM_*\dot{M}_d}{R_X} \approx 3\times10^2\left(\frac{M_*}{M_\odot}\right)\left(\frac{\dot{M}_d}{10^{-4}M_\odot\ {\rm yr}}\right)\left(\frac{R_X}{10R_\odot}\right)^{-1} L_\odot. \tag{4.25}$$

Clearly, in the case of low-mass stars, the wind luminosity has the potential to greatly exceed the radiative luminosity of the central star. However, in the case of a $30M_\odot$ O-star accreting at a rate of $3\times10^{-4}M_\odot$ yr^{-1}, the limiting wind luminosity is $10^{4.5}L_\odot$ which is only comparable to or less than the stellar luminosity. Because the wind will proceed into a jet-driven outflow in a momentum-conserving fashion, much of this luminosity will be re-radiated at shocks (Draine & McKee 1993). Nevertheless, this calculation parallels the prediction given in the previous section: that radiation pressure will eventually dominate over an accretion disk wind in the most luminous stars.

4.3 Outflows from high-mass star-forming regions

All of the specific outflow sources discussed in the previous section are examples from low-mass star-forming regions. Outflows are known to exist in high-mass star-forming regions and generally have significantly larger mass flow rates and momenta. However, there is insufficient evidence to conclude that the nature of the outflow driving mechanism is the same as in low-mass outflows. One reason for this uncertainty is

that far fewer massive outflows have been studied at comparable spatial resolution due to their larger distance. Also, the coeval formation of low-mass stars with high-mass stars will likely lead to a confusing cluster of outflows present simultaneously in the host molecular cloud. The typical result that high-mass outflows appear less collimated than their low-mass counterparts may be due to a simple superposition of flows. A dedicated single-dish search for high-velocity CO emission from UCHII regions has recently been completed with a 90% success rate (Shepherd & Churchwell 1996a). Further single-dish mapping and interferometric imaging is needed to determine if this CO emission is bipolar and if it corresponds to outflows from the UCHII regions or from younger, nearby sources. Analogous to the prior studies of low-mass outflows, a comparison of the dynamical and statistical ages of these outflows should also be made. In the following sections, results derived from the observation of outflows toward 17 UCHII regions are presented, followed by a discussion of their implications.

4.4 CO spectra

Prior to the installation of SHARC at CSO, I performed a search for molecular outflows from 17 UCHII regions in transitions of ^{12}CO. Most of the sources mapped were also imaged with SHARC, including K3-50A&C, W3(OH), G138.295+1.555, G139.909+0.197, G240.31+0.07, G19.61-0.23, G29.96-0.02, G75.78+0.34, G75.84+0.40 and the S255 complex. The outflow maps of G45.07+0.13 and G45.12+0.13 are presented separately in Chapter 5. Outflow maps already exist in the literature for GGD12-15 (Little, Heaton & Dent 1990) and Monoceros R2 (Wolf, Lada & Bally 1990). Other sources not imaged with SHARC were mapped in CO including G45.45+0.06, G45.47+0.05, G5.97-1.18 and the Cepheus A complex. All of the sources studied in this survey were found to exhibit moderate to high velocity CO emission. A mosaic of the CO spectra recorded at the central position of each source (defined by the UCHII region) are shown in Fig. 4.1. In all cases, a designated reference position was used (typically about 1° away) to avoid contamination of the profile

from the host giant molecular cloud (GMC). Constant or linear baselines have been subtracted to set the continuum level to zero. Many of the spectra contain dips near the LSR velocity of the molecular cloud which can be attributed to self-absorption of the line radiation by cool molecules on the front side of the GMC. Another common feature is a shoulder of emission adjacent to the line peak on either the redshifted or blueshifted side.

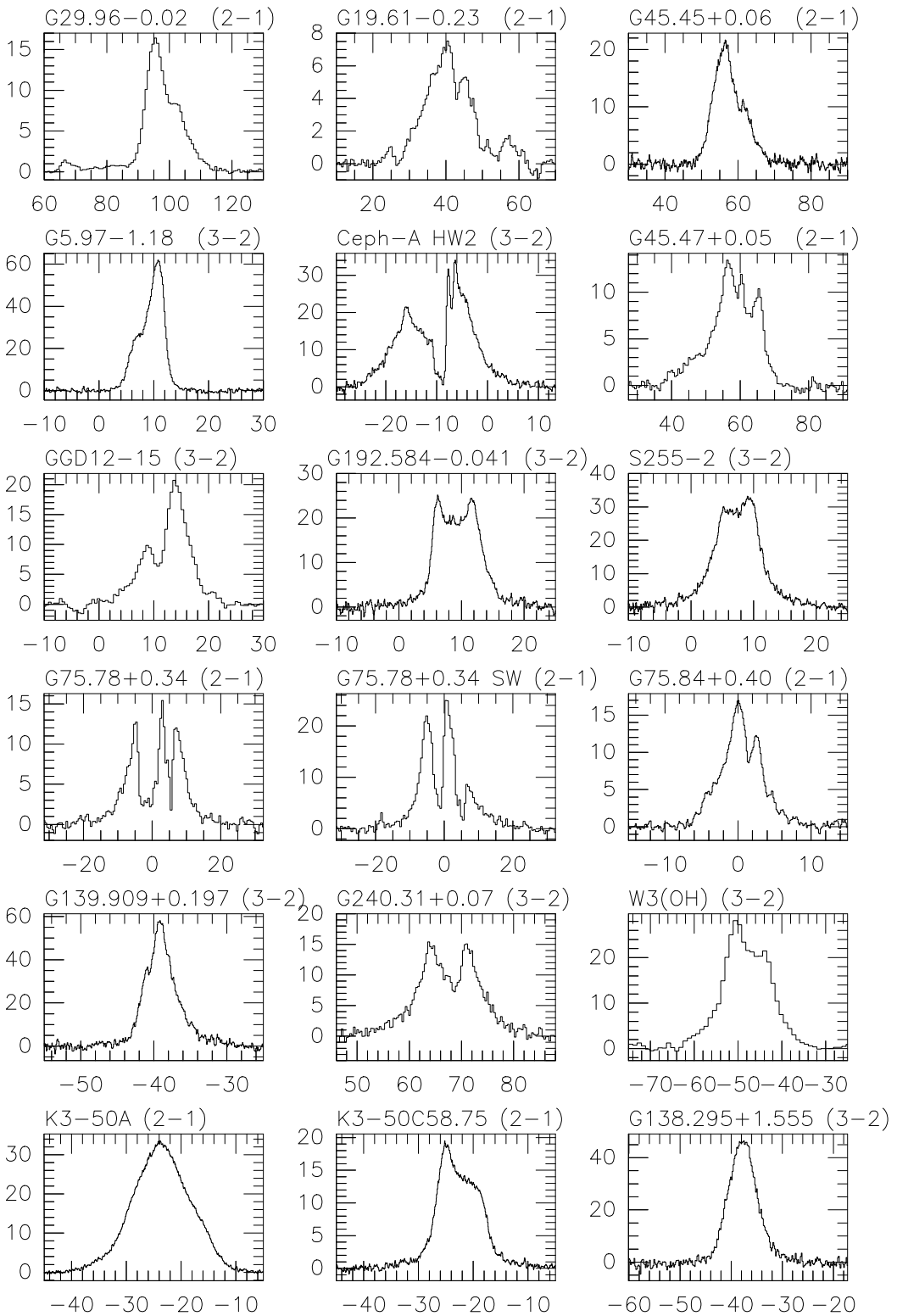

Figure 4.1: CO spectra of the outflows mapped at the CSO. The horizontal scale is LSR velocity in units of km s^{-1} and the vertical scale is main beam brightness temperature in Kelvins.

4.5 CO outflow maps

The procedure of spectral line On-the-Fly (OTF) mapping employed at CSO is similar to continuum OTF mapping discussed in section 2.4.4.1. The three main differences are: 1) the secondary mirror does not chop during the scanning of the rows, 2) reference position integrations are acquired between row scans, and 3) scans are made in celestial coordinates. The absolute pointing accuracy is generally $\pm 5''$. The CSO beamsize in the $2 \rightarrow 1$ transition is $30''$ and in the $3 \rightarrow 2$ transition is $20''$. Contour maps of the redshifted and blueshifted CO wings are presented in this section along with a brief description of the results on each source. All maps are given in B1950 celestial coordinates.

4.5.1 K3-50

Two compact outflows have been detected in the K3-50 region (Fig. 4.2). A faint outflow appears to originate from the UCHII region C58.75. The outflow is barely resolved into an east-west direction which is perpendicular to the direction of the dust ridge (Fig. 3.32). A second, more luminous outflow lies near the UCHII region A. Although only marginally resolved, the bipolarity in the CO matches that of the radio recombination line outflow (DePree et al. 1994). However the origin of the outflow is displaced about $5''$ to the east of the UCHII region, and the bipolarity of the high-velocity molecular gas disagrees with older Kitt Peak 12m CO maps (Phillips & Mampaso 1991). These facts prompted a follow-up map at higher frequency to obtain higher angular resolution.

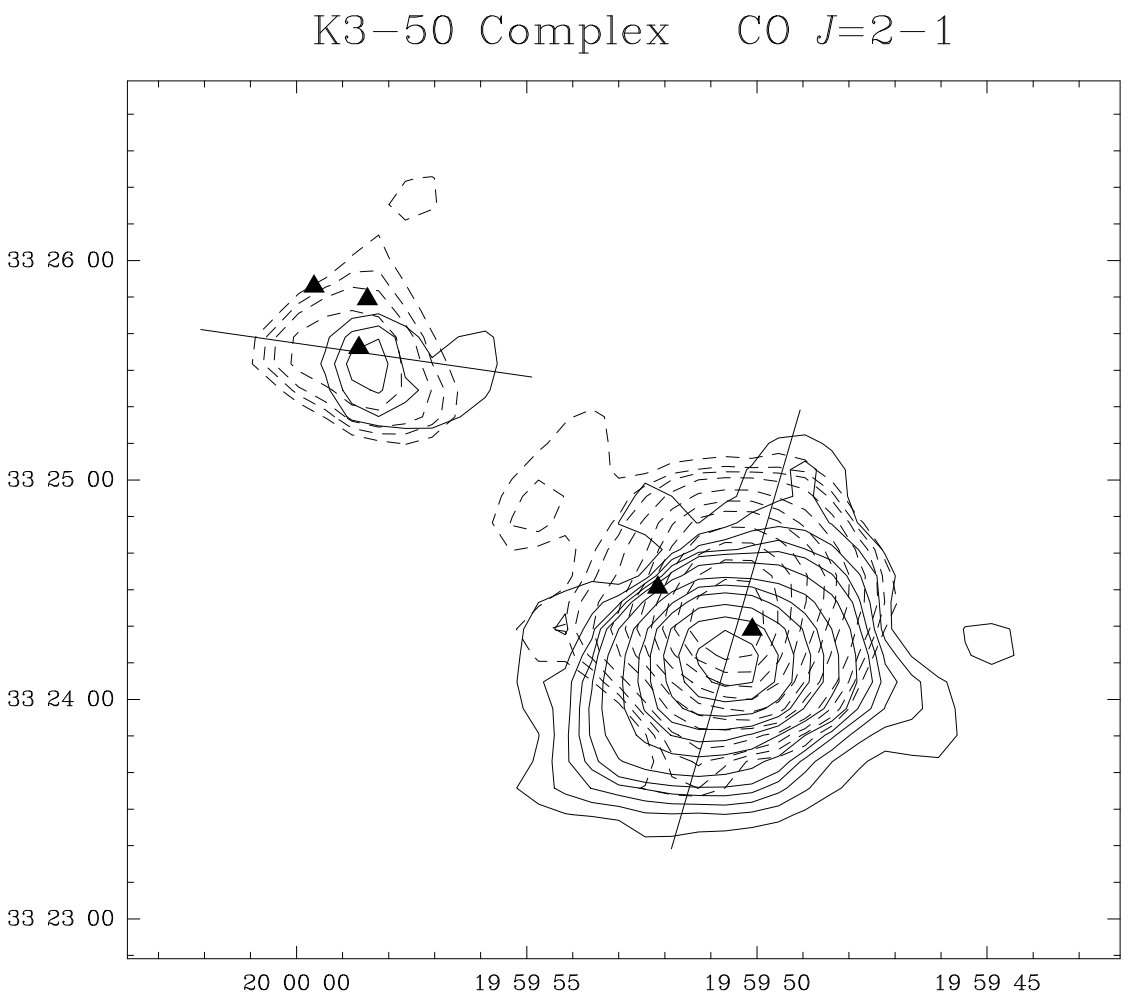

Figure 4.2: CO J=2→1 map of the K3-50 complex. Blueshifted emission (-40 to -32 km s^{-1}) is shown in solid contours and redshifted emission (-16 to -8 km s^{-1}) is shown in dashed contours. Levels are 1, 1.5, 2, 2.5, 3, 4, 6, 8, 10, 13, 16, 19 and 22 K km s^{-1}. Triangles mark the positions of the UCHII regions (DePree et al. 1994) and straight lines indicate the suggested outflow axes.

In this 20″ resolution map of K3-50A (Fig. 4.3), the north-south bipolarity is confirmed as well as the offset of the flow axis from the position of the UCHII region A. The magnitude of the offset is about 5″ (0.2 pc), which equals the absolute pointing accuracy. From this map, the driving source of the outflow is consistent with K3-50A; but the fact that both maps show a consistent offset suggests that the outflow may originate from a separate embedded source. The redshifted lobe seems to indicate a broad conical opening angle.

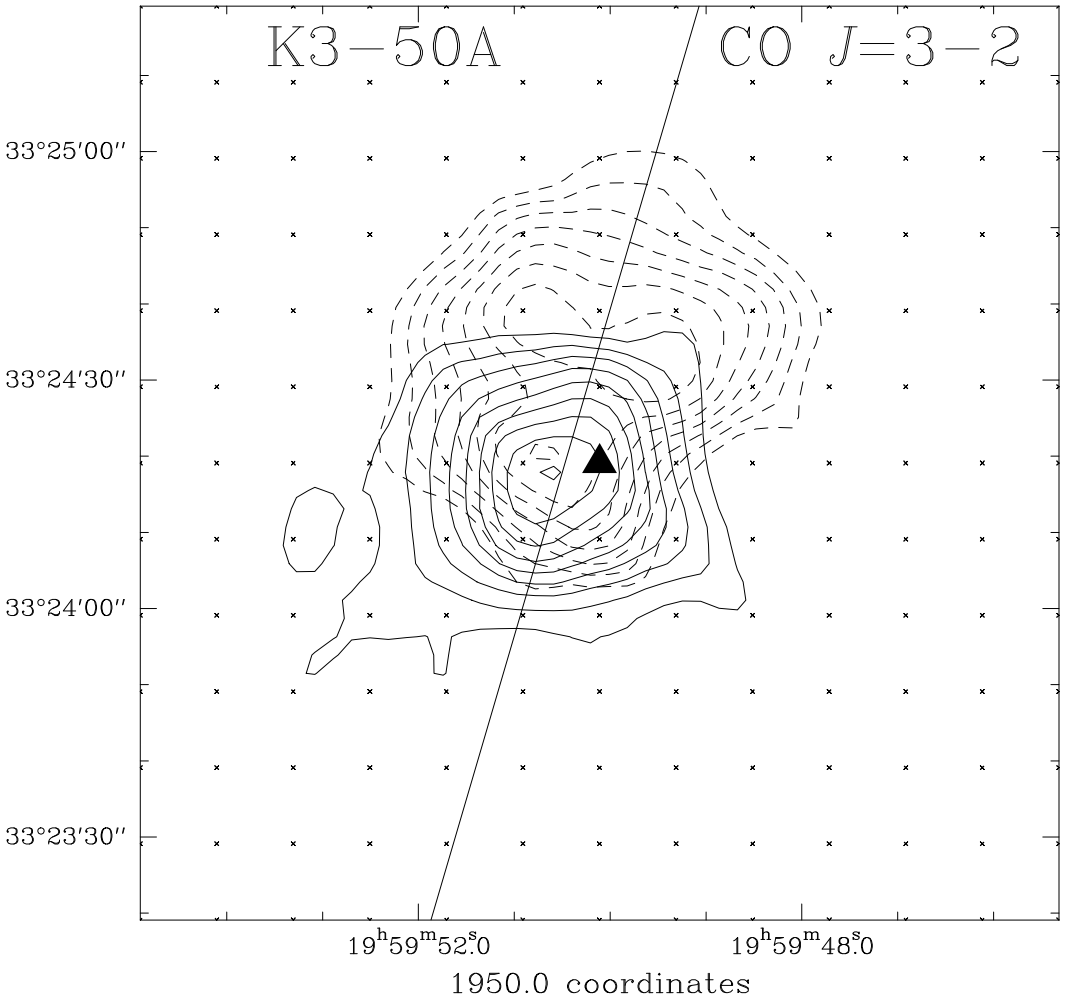

Figure 4.3: CO J=3→2 map of K3-50A. Blueshifted emission (-40 to -34 km s^{-1}) is shown in solid contours and redshifted emission (-14 to -8 km s^{-1}) is shown in dashed contours. Levels are 3 to 15 by 1.5 K km s^{-1}. The triangle marks the position of the UCHII region (DePree et al. 1994) and the straight line indicates the estimated outflow axis, identical to the line in Fig. 4.2.

4.5.2 W3(OH)

As shown in Fig. 4.4, the high velocity CO emission toward W3(OH) is complex. There are two directions of bipolarity evident in the map: a northeast-southwest outflow that lies parallel to the NH_3 and 350μm filament (Fig. 3.35), and a possible east-west outflow north of the core. With the 5″ pointing uncertainty, the northeast-southwest outflow could originate from either UCHII region or the TW object.

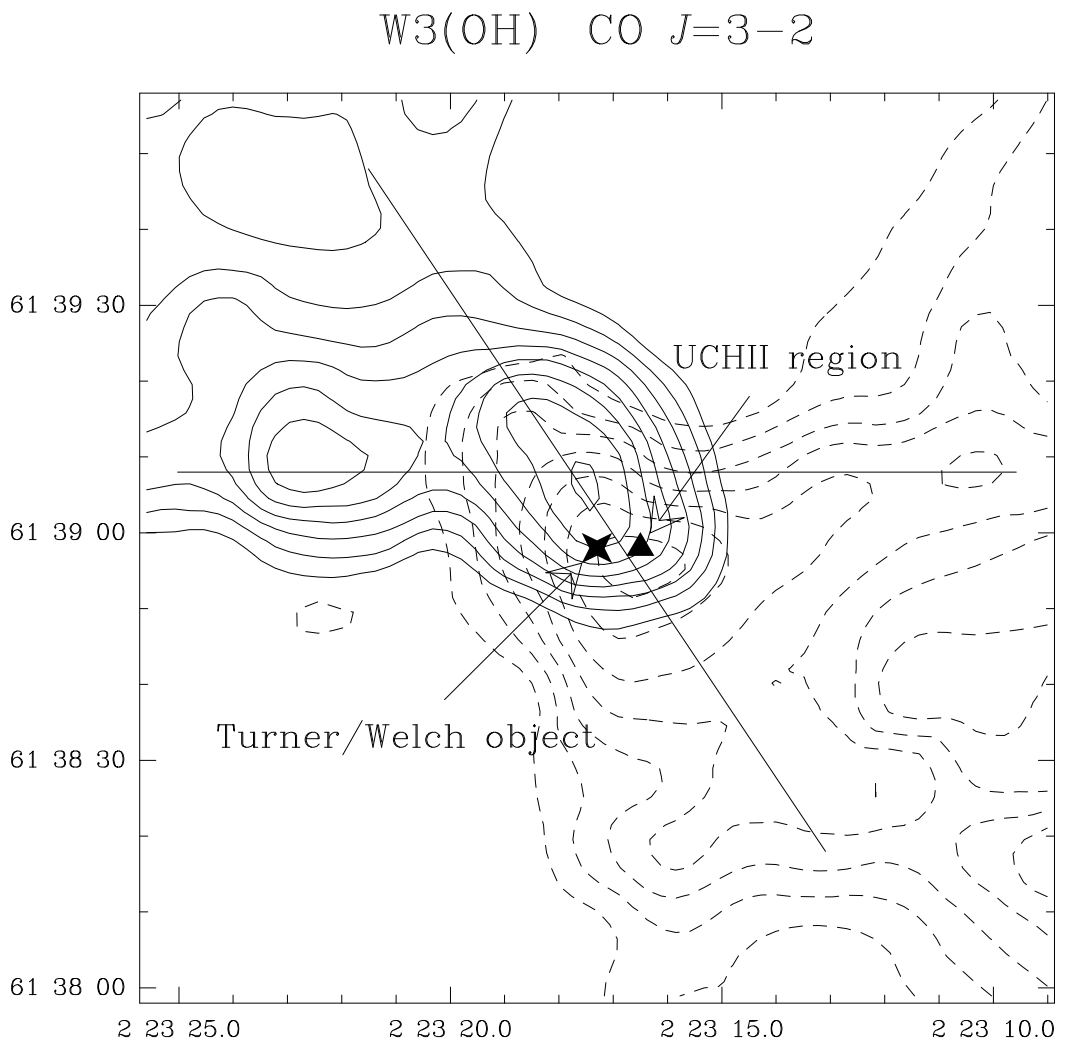

Figure 4.4: CO J=3→2 map of W3(OH). Blueshifted emission (-60 to -52 km s^{-1}) is shown in solid contours and redshifted emission (-44 to -36 km s^{-1}) is shown in dashed contours. Levels are 9 to 30 by 3 K km s^{-1}. Two suggested axis of outflow are indicated by straight lines.

4.5.3 G138.295+1.555

As seen in Fig. 4.5, a prominent east-west outflow originates from within 2″ of the UCHII region G138.295+1.555. Also, a fainter, more extended north-south outflow appears to originate from the adjacent radio source G138.300+1.558. As shown in Fig. 3.37, a dust core envelopes G138.295+1.555. It is interesting that the bright source with the more compact outflow is associated with the strong dust emission while the extended outflow source is not, suggesting that the dust source is younger.

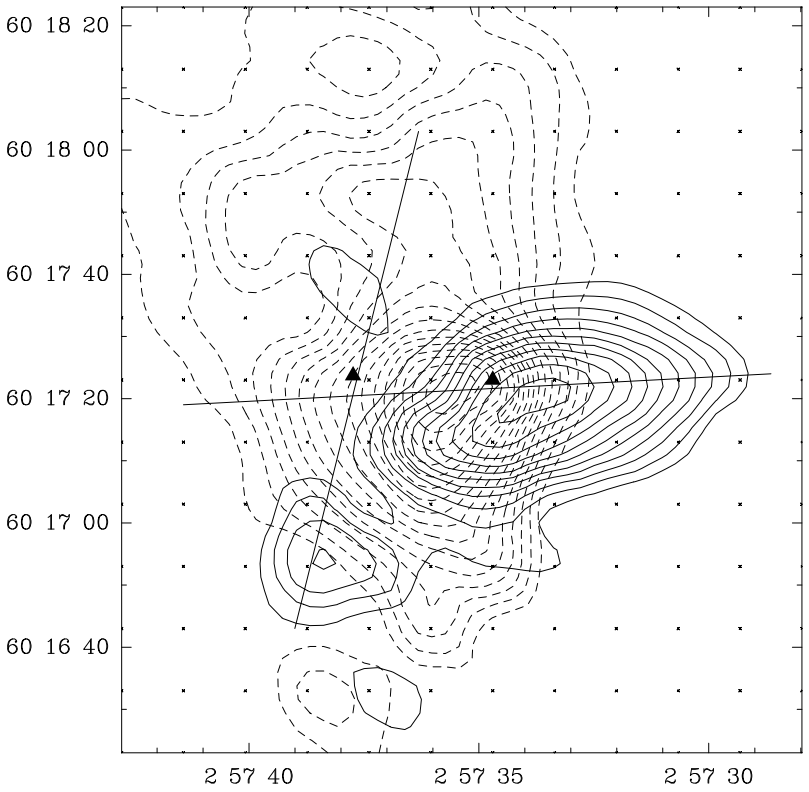

Figure 4.5: CO J=3→2 map of the G138.295+1.555. Blueshifted emission (-81 to -75 km s^{-1}) is shown in solid contours and redshifted emission (-69 to -63 km s^{-1}) is shown in dashed contours. Levels are 12 to 57 by 3 K km s^{-1}. Triangles mark the positions of the radio sources G138.300+1.558 to the east G138.295+1.555 at the center (Kurtz, Churchwell & Wood 1994). The lines suggest outflow axes from each source.

4.5.4 G139.909+0.197

In the CO J=3→2 map of G139.909+0.197 (Fig. 4.6), we see why the outflow was originally classified as a wide, low-collimated outflow (Gómez et al. 1992). However, in this map, the multiple peaks in the lobes suggest overlapping outflows from a cluster of young stars as is seen in IRAS 20050+2720 (Bachiller, Fuente & Tafalla 1995). One outflow appears to originate from the main UCHII region while another outflow may emerge from an unknown source about 40″ (0.4 pc) to the east. Higher resolution imaging is necessary to disentangle the emission.

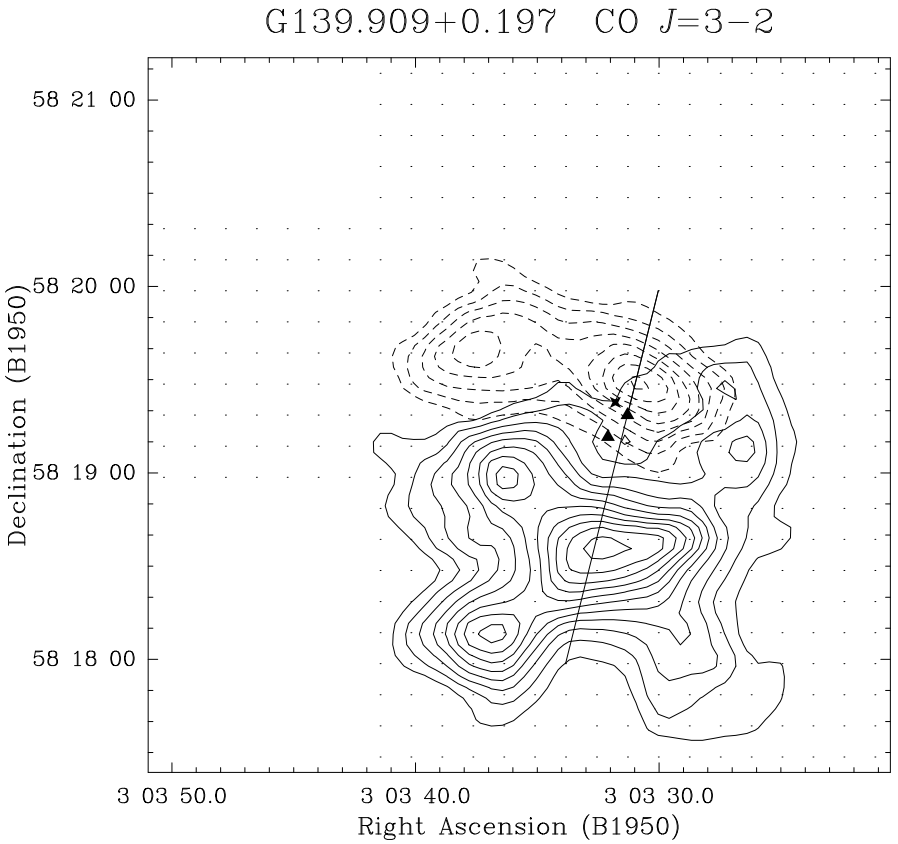

Figure 4.6: CO J=3→2 map of G139.909+0.197. Blueshifted emission (-48 to -43 km s^{-1}) is shown in solid contours and redshifted emission (-35 to -30 km s^{-1}) is shown in dashed contours. Contour levels are 8 to 48 by 4 K km s^{-1}. The triangles mark the position of the two UCHII regions (Kurtz, Churchwell & Wood 1994). The cross marks the H_2O maser (Torrelles et al. 1992) associated with the infrared source WK 34 (Weintraub & Kastner 1996).

4.5.5 G240.31+0.07

In Fig. 4.7, a prominent outflow is resolved toward G240.31+0.07. In the lowest contours there is marginal evidence for a second outflow axis. The UCHII region lies within 5″ (0.16 pc) of the central point of both axes. Interferometric observations will be necessary to confirm the UCHII region as the driving source of one or both outflows.

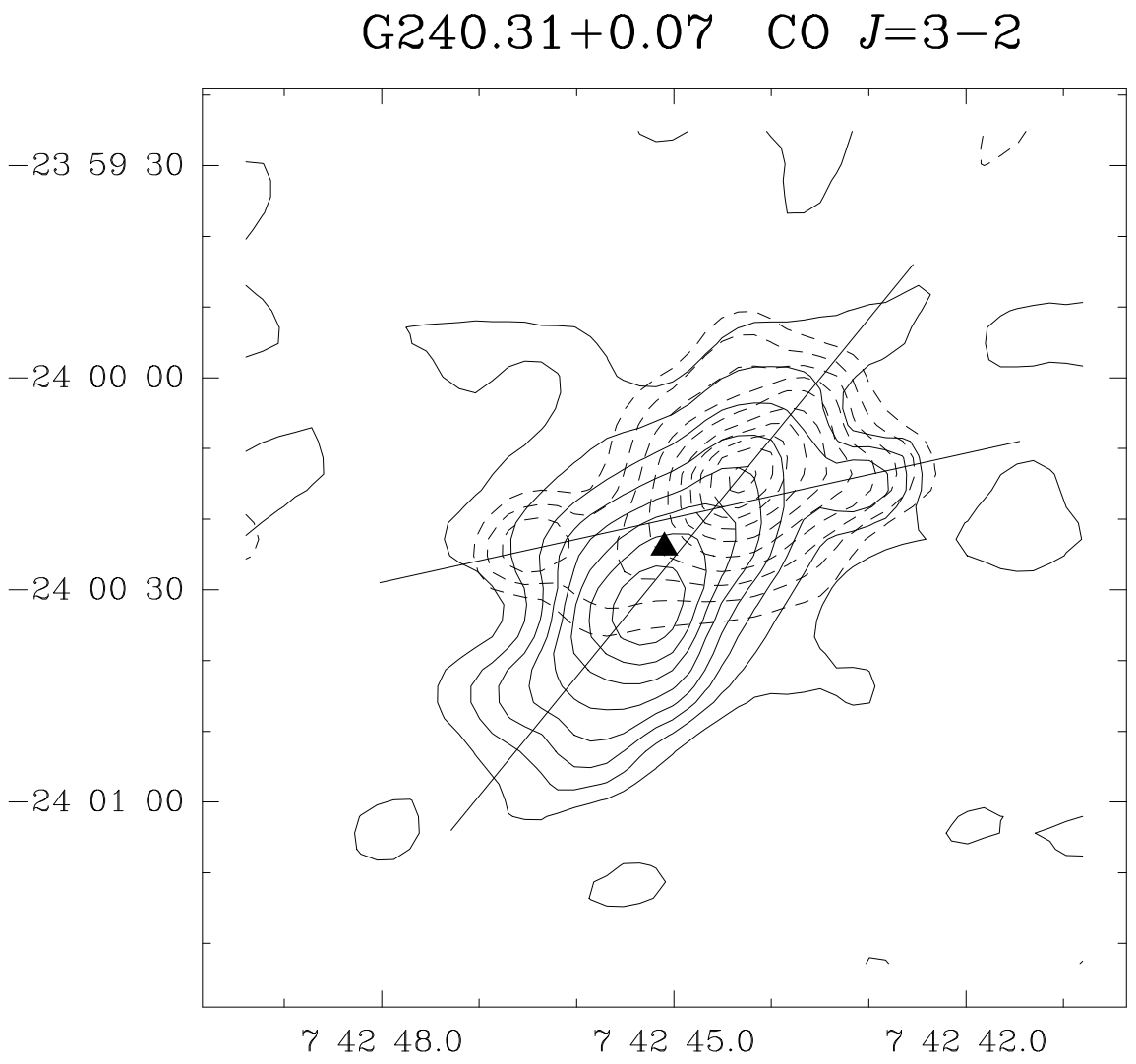

Figure 4.7: CO J=3→2 map of UCHII region G240.31+0.07, indicated by the triangle (McCutcheon et al. 1995). Blueshifted emission (52 to 62 km s^{-1}) is shown in solid contours and redshifted emission (75 to 85 km s^{-1}) is shown in dashed contours. Contour levels are 4 to 40 by 4 K km s^{-1}. Straight lines suggest the axes of the main outflow and a possible second outflow.

4.5.6 G75 Complex (ON 2)

As shown in Fig. 4.8, two strong, compact outflows are detected in the ON 2 region. One outflow is located 10″ (0.27 pc) northeast of the UCHII region G75.78+0.34. Higher resolution BIMA observations show this region to be composed of multiple outflows (Shepherd & Churchwell 1996b). A second outflow is associated with the H_2O maser/submillimeter continuum source G75.76+0.34 (see Fig. 3.46) and shows an extended tail of blueshifted emission to the southwest.

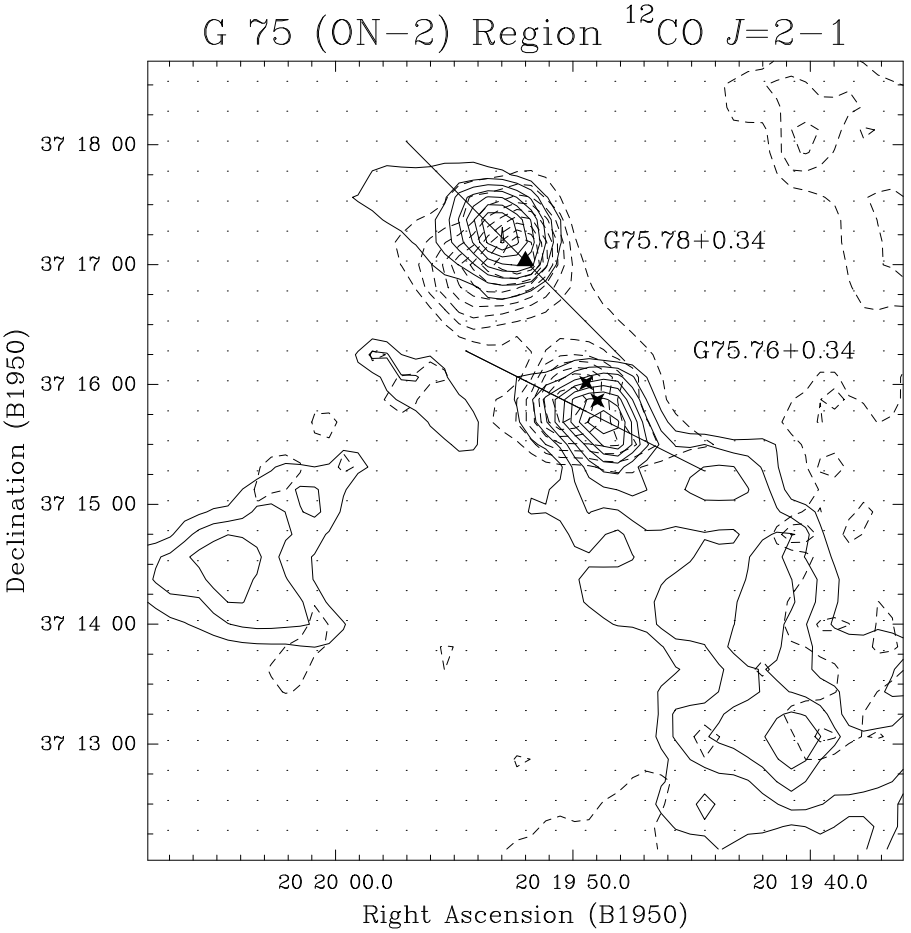

Figure 4.8: CO J=2→1 map of the G75.77+0.34 complex. Blueshifted emission (-6 to -12 km s^{-1}) is shown in solid contours and redshifted emission (4 to 10 km s^{-1}) is shown in dashed contours. Levels are 12 to 44 by 4 K km s^{-1}. The triangle marks the UCHII region G75.78+0.34 (Wood & Churchwell 1989) and the crosses mark H_2O maser positions (Hofner 1996a).

Lying about $4'$ (6.5 pc) north of G75.78+0.34, the extended HII region G75.84+0.40 also exhibits an outflow consistent with being centered on the peak radio position. An additional redshifted lobe crosses the region with a faint blueshifted counterpart suggesting a second outflow originating from a source $\sim 75''$ (2.0 pc) east of the UCHII region.

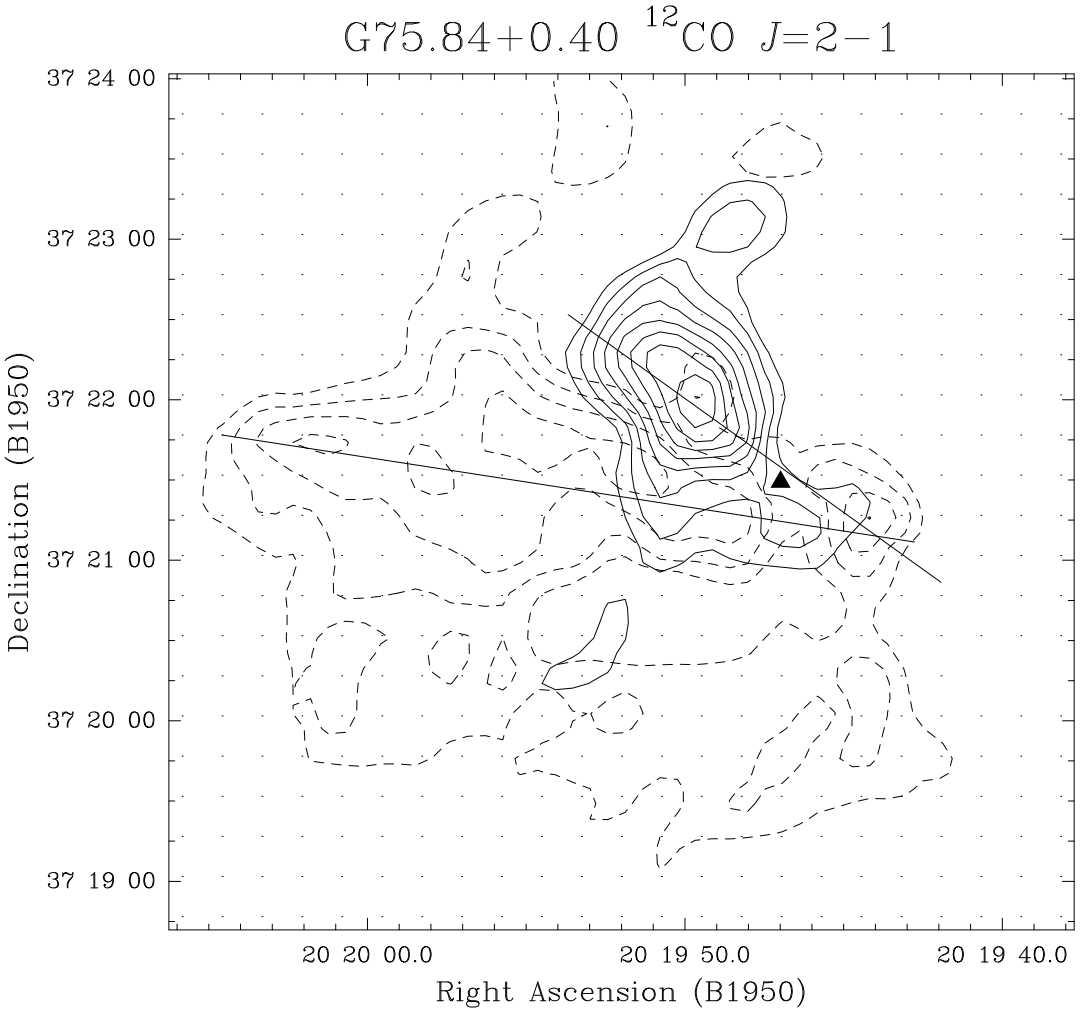

Figure 4.9: CO J=2→1 map of G75.84+0.40. Blueshifted emission is shown in solid contours and redshifted emission is shown in dashed contours. Levels are 24 to 60 by 4 K km s^{-1}. The triangle marks the peak position of the HII region (Wood & Churchwell 1989).

4.5.7 S255 Complex

As shown in Fig. 4.10, the high velocity CO emission is complex in the S255 region. Though displaced about 10″ (0.12 pc) southwest from the origin, the westernmost UCHII region of S255-FIR2 triplet lies on the outflow axis generated by connecting the peak position of the redshifted lobe with the lower contour ridge of the blueshifted lobe. Another outflow lies between S255-FIR2 and G192.584-0.041 and may be driven by the faint submillimeter continuum source detected there in the SHARC image (see Fig. 3.41).

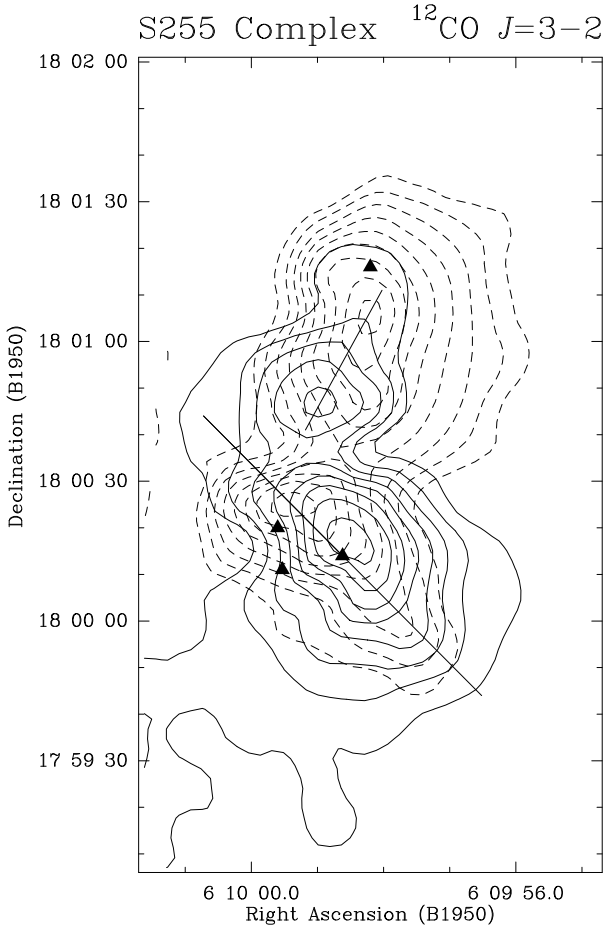

Figure 4.10: CO J=3→2 map of the S255 complex. Blueshifted emission (-6 to 6 km s^{-1}) is shown in solid contours and redshifted emission (10 to 22 km s^{-1}) is shown in dashed contours. Contour levels are 30 to 110 by 10 K km s^{-1}. Triangles mark UCHII regions (Snell & Bally 1986) and lines mark two suggested outflow axes.

4.5.8 G19.61-0.23

In Fig. 4.11, the high velocity CO emission shows compact local maxima at the position of the cometary UCHII region G19.61-0.23 component A. The blueshifted lobe shows an extended tail in the general direction of the radio tail. Diffuse emission contaminates the redshifted lobe to the north and east.

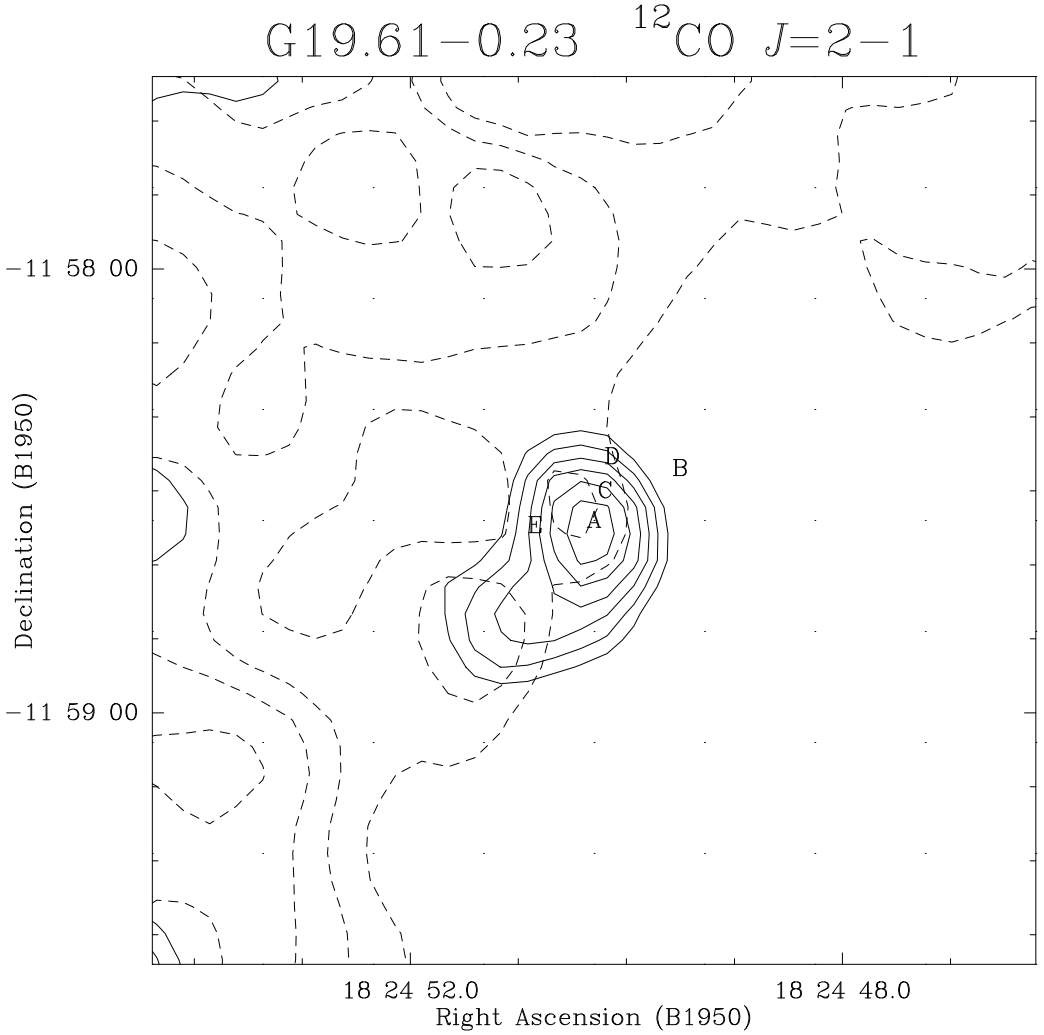

Figure 4.11: CO J=2→1 map of G19.61-0.23. Blueshifted emission (24 to 34 km s^{-1}) is shown in solid contours and redshifted emission (53 to 63 km s^{-1}) is shown in dashed contours. Levels are 5 to 10 by 1 K km s^{-1}. The letters mark the position of the 5 UCHII regions from Wood & Churchwell (1989).

4.5.9 G29.96-0.02

As seen in Fig. 4.12, extended emission dominates the high velocity channels toward G29.96-0.02. The peak in the blueshifted wing occurs within 10″ of the UCHII region but there is no clear evidence for a bipolar outflow.

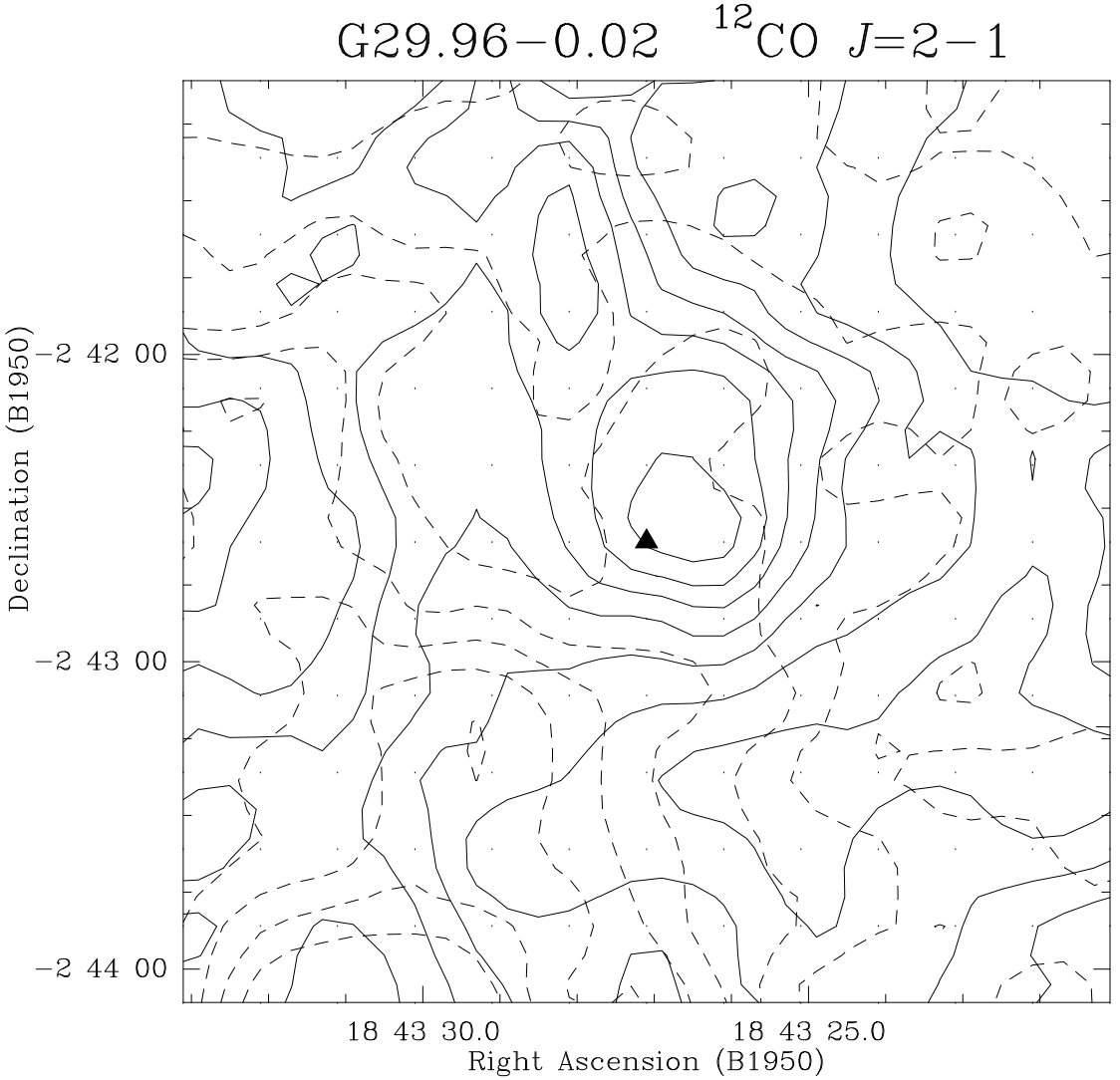

Figure 4.12: CO J=2→1 map of G29.96-0.02. Blueshifted emission is shown in solid contours and redshifted emission is shown in dashed contours. Contour levels are 9 to 27 by 3 K km s^{-1}.

4.5.10 G5.97-1.18

Although not imaged with SHARC, G5.97-1.18 is an interesting UCHII region near the O7 V star Herschel 36 (Her 36) located west of the Hourglass Nebula in M8. At a distance of 1.5 kpc (Georgelin & Georgelin 1976), a 0.″5 (750 AU) jet from Her 36 has been detected in K-band with a ground-based adaptive optics camera and in Hα with the Hubble Space Telescope Planetary Camera (Steckum et al. 1995). The jet points toward the UCHII region located about 3″ (0.02 pc) to the southeast (Wood & Churchwell 1989). Evidence for a corresponding molecular outflow is shown in Fig. 4.13. However, although the blueshifted CO lobe extends along the extrapolated direction of the jet, it is offset from Her 36 and the UCHII region while the redshifted lobe bends northeast. Thus, this outflow is probably driven by a different source in the core about 20″ (0.15 pc) northeast of the UCHII region and Her 36.

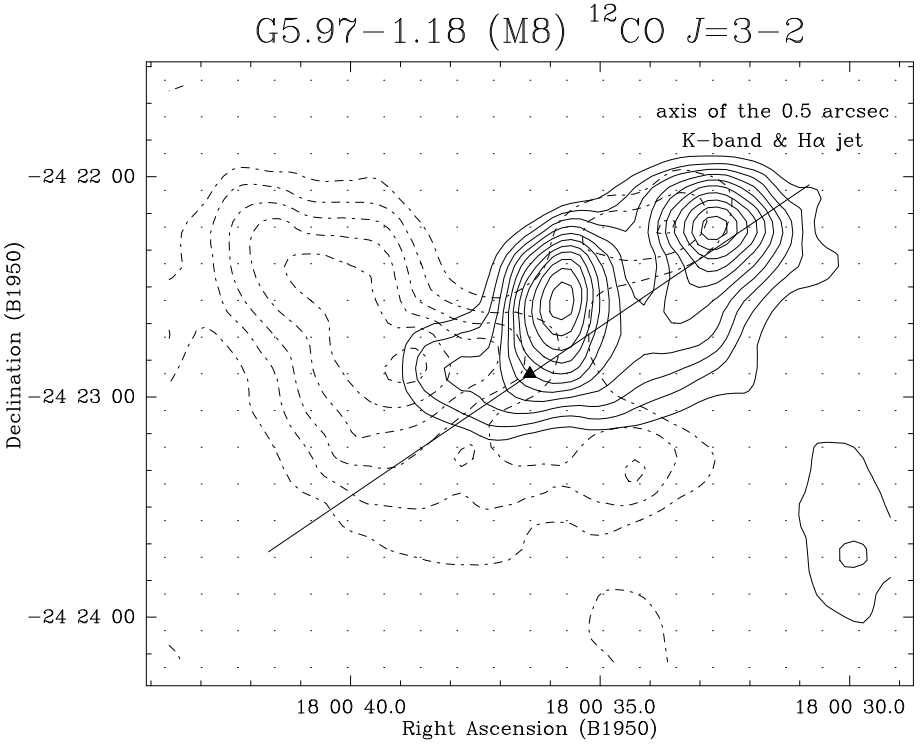

Figure 4.13: CO J=3→2 map of G5.97-1.18, indicated by the triangle (Wood & Churchwell 1989). Blueshifted emission (2 to 7 km s^{-1}) is shown in solid contours and redshifted emission (12 to 17 km s^{-1}) is shown in dashed contours. Levels are 18 to 90 by 6 K km s^{-1}.

4.5.11 Cepheus A (G109.87+2.11, I22543+6145)

The Cepheus A complex was not imaged with SHARC as it has been mapped in the past at wavelengths of 450 and 800μm at JCMT (Moriarty-Schieven, Snell & Hughes 1991). Embedded in the dust core lie 14 discrete radio continuum sources (Hughes & Wouterloot 1984; Hughes, Cohen & Garrington 1995), one of which (HW2) is a powerful thermal radio jet (Rodríguez et al. 1994). Surrounding the jet origin, 39 H_2O maser spots have been resolved, spatially and kinematically, into a disk-like structure (Torrelles et al. 1996). Clusters of H_2O and OH masers also coincide with several of the other UCHII regions (Cohen, Rowland & Blair 1984; Lada et al. 1981) and the H_2O masers show rapid variability (Mattila et al. 1985). Maser emission in the 183 GHz transition of H_2O has also been detected (Cernicharo et al. 1990). Lying adjacent to the Cep OB3 association at a distance of 0.73 kpc (Blauuw 1964), Cepheus A was the first source after Orion to exhibit high velocity CO emission (Ho, Moran & Rodríguez 1982). Further observations led to the suggestion that the outflow was quadrupolar (Torrelles et al. 1993). Shown in Fig. 4.14 is a CSO map of the region, clearly showing two distinct outflows: an extended north-south outflow and a compact east-west outflow with different origins. The submillimeter dust emission is closely associated with the origin of the compact outflow. However, neither outflow origin cannot be uniquely identified with any particular compact radio component. Rather, the radio sources seem to lie along ridges of the CO gas. For example, the four radio sources (7a,b,c,d) lying in a line to the southeast align with a faint arm of redshifted CO J=6$\rightarrow$5 emission. This arm also passes through the central cluster of radio sources 2, 3, 8 and 9. With 2 VLA maps separated by a 10 year baseline, a tentative outward (east-southeasterly) proper motion of 300 km s^{-1} has been reported in component 7c, consistent with the typical velocities of HH jets (Hughes 1993). The bipolar CO 6$\rightarrow$5 emission coincides with an H_2 1-0 S(1) emission nebula (Hoare & Garrington 1995) and a bipolar NH_3 structure (Torrelles et al. 1986; Güsten, Chini & Neckel 1984). These findings support the jet-driven outflow model, as the CO 6$\rightarrow$5 emission is likely tracing the warm entrained gas surrounding the jet

bow shocks, much like vibrationally-excited H_2 line emission is believed to do.

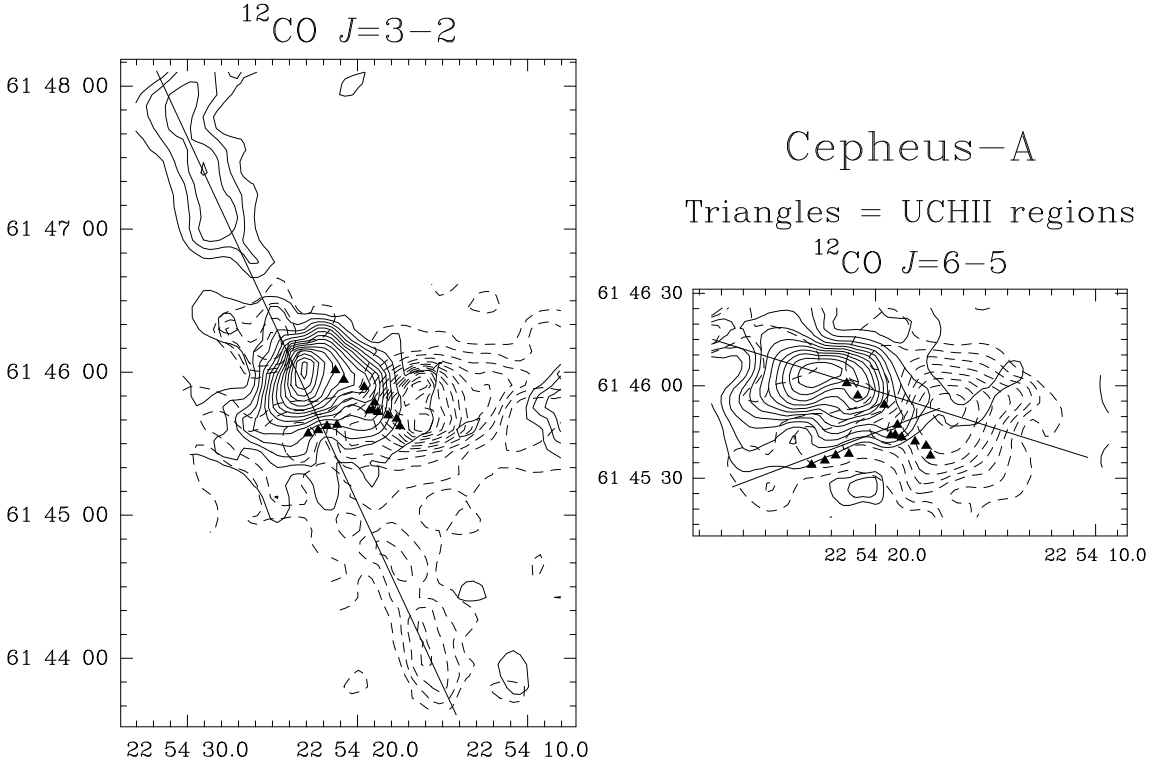

Figure 4.14: *Left panel:* CO J=3→2 map of the Cepheus-A complex. Blueshifted emission (-16 to -8 km s^{-1}) is shown in solid contours and redshifted emission (-1 to 6 km s^{-1}) is shown in dashed contours. Contour levels are 3 to 45 by 3 K km s^{-1}. Triangles mark the position of compact radio continuum components (Hughes & Wouterloot 1984; Hughes, Cohen & Garrington 1995). *Right panel:* CO J=6→5 map of the central region. Blueshifted emission (-26 to -19 km s^{-1}) and redshifted emission (-1 to 6 km s^{-1}) contour levels are 20 to 130 by 10 K km s^{-1}.

4.5.12 G45.45+0.06, G45.47+0.05 & G45.48+0.13A&B

Shown in Fig. 4.15 is a map that covers the two UCHII regions of G45.47+0.05 and G45.45+0.06, which lie at a distance of 8.3 kpc (Kuchar & Bania 1994). Unresolved at radio wavelengths, the UCHII region G45.47+0.05 lies about 15″ southwest of the center of what appears to be a compact outflow. The origin of this outflow coincides with a faint clump of SiO emission imaged by Wilner, Ho & Zhang (1996), so perhaps it traces a young embedded source. From interferometric imaging of the HCO^+ J=1→0 and SiO J=2→1 transitions, these authors found no evidence of spherical collapse in the UCHII region. The spectral index of the centimeter radio emission (1.1) suggests that it may be a partially ionized stellar wind. The cometary UCHII region G45.45+0.06 coincides with the peak blueshifted CO emission. However, it is difficult to discern additional bipolar outflows in this complex.

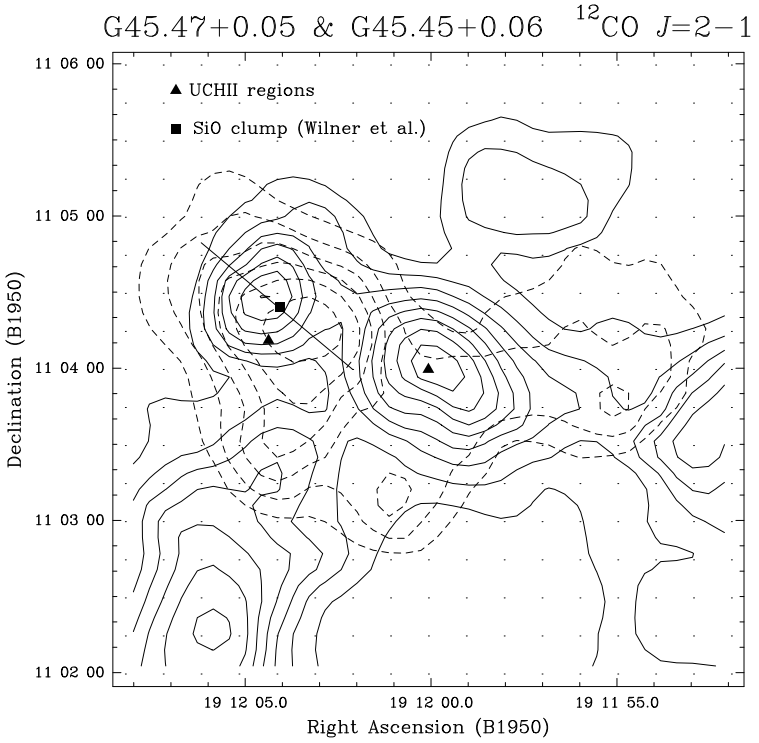

Figure 4.15: CO J=2→1 map of the UCHII regions G45.47+0.05 and G45.45+0.06, marked by triangles from left to right (Wood & Churchwell 1989). Blueshifted emission (50 to 55 km s^{-1}) is shown in solid contours and redshifted emission (63 to 68 km s^{-1}) is shown in dashed contours. Contour levels are 6 to 27 by 3 K km s^{-1}.

4.6 Calculation of outflow energetics

From maps presented in the previous section, the energetics of the outflows can be calculated. The outflow radius projected on the sky, $r_{\rm o} = D\theta_{\rm o}$, combined with the observed velocity $b_{\rm o}$ can be used to compute the observed dynamical timescale $t_{\rm o}$:

$$t_{\rm o} = \frac{r_{\rm o}}{v_{\rm o}} = \frac{D\theta_{\rm o}}{v_{\rm o}}. \tag{4.26}$$

The intrinsic dynamical timescale of the outflow is related to the observed value via the inclination angle, i, of the flow via the trigonometric relation:

$$t = t_{\rm o} \cot{(i)} = \frac{D\theta_{\rm o}}{v_{\rm o}} \cot{(i)}. \tag{4.27}$$

Unfortunately, since proper motions of molecular outflows are too small to detect, i is a difficult parameter to measure. For an outflow with $i = 45^{\circ}$, the observed timescale equals the intrinsic timescale, so this value is conveniently assumed when no other information is available.

With some basic assumptions, including local thermodynamic equilibrium, the integrated flux of the line emission from a linear, rigid rotor molecule can be converted into a column density of molecules within the solid angle of the telescope beam. Following Appendix A of Garden et al. (1991), the column density can be expressed as follows

$$N = \frac{3kf}{8\pi^3 B\mu^2} \frac{\exp{[hBJ_l(J_l+1)/kT_{\rm ex}]}}{(J_l+1)} \frac{(T_{\rm ex} + hB/3k)}{[1-\exp{(-h\nu/kT_{\rm ex})}]} \int \tau_v dv, \tag{4.28}$$

where B and μ are the rotational constant and permanent dipole moment of the molecule, J_l is the rotational quantum number of the lower state of the observed transition, $T_{\rm ex}$ is the excitation temperature of the molecule, and f is the beam filling factor of the source. For ^{12}CO, $\mu = 0.11$ Debye $= 0.11 \times 10^{-18}$ esu cm and $B = 57.898$ GHz (Townes & Schawlow 1975). The antenna temperature T_a^* recorded

on the source is related to f and the microwave background temperature $T_{\rm bg}$ by the following formula

$$\frac{T_a^*}{\eta_{\rm MB}} = \frac{f h\nu}{k}\left[\frac{1}{\exp\left(h\nu/kT_{\rm ex}\right)} - \frac{1}{\exp\left(h\nu/kT_{\rm bg}\right)}\right][1-\exp\left(-\tau_v\right)], \tag{4.29}$$

where $\eta_{\rm MB}$ is the main beam efficiency of the telescope. Combining these two equations, reduced formulas for the lowest four rotational transitions of CO are listed below:

$$N_{\rm CO} = 4.34\times10^{13}\left[\frac{T_{\rm ex}+0.92}{\exp(-\frac{5.52}{T_{\rm ex}})}\right]\int\frac{T_a^*(1\rightarrow0)}{\eta_{MB}}\frac{\tau_v}{1-e^{-\tau_v}}dv\ {\rm cm}^{-2}, \tag{4.30}$$

$$N_{\rm CO} = 4.32\times10^{13}\left[\frac{T_{\rm ex}+0.92}{\exp(-\frac{16.56}{T_{\rm ex}})}\right]\int\frac{T_a^*(2\rightarrow1)}{\eta_{MB}}\frac{\tau_v}{1-e^{-\tau_v}}dv\ {\rm cm}^{-2}, \tag{4.31}$$

$$N_{\rm CO} = 4.81\times10^{12}\left[\frac{T_{\rm ex}+0.92}{\exp(-\frac{33.12}{T_{\rm ex}})}\right]\int\frac{T_a^*(3\rightarrow2)}{\eta_{MB}}\frac{\tau_v}{1-e^{-\tau_v}}dv\ {\rm cm}^{-2}, \tag{4.32}$$

$$N_{\rm CO} = 2.70\times10^{12}\left[\frac{T_{\rm ex}+0.92}{\exp(-\frac{88.50}{T_{\rm ex}})}\right]\int\frac{T_a^*(4\rightarrow3)}{\eta_{MB}}\frac{\tau_v}{1-e^{-\tau_v}}dv\ {\rm cm}^{-2}, \tag{4.33}$$

where v is in units of km s^{-1}. From the column density of CO, the mass of H_2 gas in a cloud of angular size Ω at distance D is simply

$$M_{\rm H_2} = M_{\rm CO}\left[\frac{\rm H_2}{\rm CO}\right] = D^2\left[\frac{\rm H_2}{\rm CO}\right]\int_\Omega N_{\rm CO}(\Omega')d\Omega', \tag{4.34}$$

where $d\Omega'$ is the telescope beamsize and the factor [H_2/CO] is an empirical abundance ratio $\sim 10^4$ (Blake et al. 1987). With a measurement of the gas mass, one can compute the momentum (P) and the energy (E) of the outflow.

$$P = mv = \frac{mv_0}{\cos i} \tag{4.35}$$

$$E = \frac{mv^2}{2} = \frac{m}{2}\left(\frac{v_0}{\cos i}\right)^2. \tag{4.36}$$

Knowing the age of the outflow, the mass outflow rate ($\dot{m}$), the momentum supply rate (or force) required to drive the flow ($\dot{P}$), and the mechanical luminosity ($L_{\rm mech}$) can also be computed. If the age of the outflow (t) is taken as the dynamical timescale, then

$$\dot{m} = \frac{m}{t} = \frac{m v_0 \tan i}{r_0} \tag{4.37}$$

$$\dot{P} = \dot{m} v = \frac{mv}{t} = \left(\frac{v_0}{\cos i}\right)^2 \frac{m \sin i}{r_0} \tag{4.38}$$

$$L_{\rm mech} = \dot{E} = \frac{E}{t} = \frac{m \sin i}{2 r_0} \left(\frac{v_0}{\cos i}\right)^3 . \tag{4.39}$$

In reality, gas molecules with a range of v_0 contribute to the spectral line profile. For this reason, the integrals over velocity and solid angle must be shifted from the column density equations to the momentum and energy equations 4.37-4.39. These equations are numerically integrated over a specified velocity range to compute the total value of each parameter. Selecting the velocity range is inevitably an arbitrary procedure in which one tries to avoid including emission from the line center because it primarily traces the large mass of ambient gas unassociated with the outflow. This selection can be a significant source of error in the outflow mass (Masson & Chernin 1994). Fortunately, it is less of a concern to the velocity-weighted parameters in which the high-velocity emission contributes more heavily to the integral. As another source of potential error, the fact that statistical lifetimes of molecular outflows may be up to a factor of 10 longer than the dynamical timescales (Parker, Padman & Scott 1991) will cause all of the computed parameters that include the age ($\dot{m}, \dot{P}, L_{\rm mech}$) to be overestimates. Fortunately, the momentum and energy values are unaffected by this uncertainty as they simply reflect the observed state of the gas.

A computer program was written to perform the proper numerical integration of these equations over a given velocity range from a CO data cube input as a set of files in tabular format. To be flexible, the program accepts a set of inputs including the specific CO transition and isotopomer observed. Other required inputs are the source distance, gas excitation temperature (generally taken from the peak ^{12}CO

brightness temperature), the velocity limits of the outflow and estimates of the optical depth and inclination angle of the flow. The format of the input file is specified in Appendix C. The results of the program for the observed outflows are presented in Table 4.1. In order to ensure consistent measurements, the outflow angular size is defined as half the angle along the outflow axis between the outer half-power CO contours in the red and blueshifted lobes. In all cases, an intermediate inclination angle of 45° has been assumed. Thus, the length $l_{1/2}$ reported in column 11 of Table 4.1 is the source distance times the computed half-length deprojected to this inclination angle. Because high-sensitivity maps of the less abundant species ^{13}CO are not available to estimate the optical depth, the high-velocity gas is assumed to be optically thin.

The average dynamical timescale of these outflows is $\sim 1 \times 10^5$ yr, which roughly matches the statistical age of outflows from low-mass stars (Parker, Padman & Scott 1991). Also, this timescale is a factor of 2 greater than the statistical lifetime of UCHII regions (Comerón & Torra 1996). Apparently, the typical outflow begins before the star develops a significant ionized region. This finding supports an accretion-disk wind-driven outflow rather than an outflow driven purely by radiation pressure, at least in the early stages of accretion.

Table 4.1: Observed and computed parameters of bipolar outflows

Outflow source	D kpc	$v_{\rm lsr}$	$v_{\rm blue}$ $\frac{\rm km}{\rm s}$	$v_{\rm red}$	m $M_\odot$	$\bar{v}$ $\frac{\rm km}{\rm s}$	P $M_\odot \frac{\rm km}{\rm s}$	$\log(E)$ $L_\odot$ yr	$\log(\dot{P})$ $M_\odot \frac{\rm km/s}{\rm yr}$	$l_{1/2}$ pc	$\log(t)$ yr	$\log(L_{\rm mech})$ $L_\odot$	$\log(\dot{m})$ $\frac{M_\odot}{\rm yr}$
G45.12+0.13	8.3	59	[45,56]	[62,73]	435	6.3	3900	6.54	−1.71	1.3	5.30	0.93	−2.66
G45.47+0.05	8.3	58	[35,52]	[64,80]	260	13	3500	6.64	−1.57	1.7	5.11	1.54	−2.68
G75.78+0.34	5.6	0	[-25,-5]	[5,25]	54	13	710	5.99	−2.13	1.3	4.98	1.00	−3.25
G75.76+0.34	5.6	0	[-25,-5]	[5,25]	49	14	660	5.96	−2.15	1.3	4.97	0.99	−3.28
G75.84+0.40	5.6	0	[-10,-2]	[5,13]	68	7.1	440	5.45	−2.89	2.7	5.57	−0.19	−3.74
K3-50A	8.7	-24	[-42,-28]	[-20,-8]	69	9.2	630	5.73	−2.50	1.8	5.30	0.44	−3.46
K3-50C	8.7	-24	[-42,-28]	[-20,-8]	15	8.4	130	4.98	−3.11	1.4	5.22	−0.25	−4.03
G19.61-0.23	4.5	-40	[20,35]	[45,60]	17	12	230	5.47	−2.21	0.40	4.52	0.95	−3.28
G5.97-1.18	1.8	10	[0,8]	[12,20]	12	4.5	52	4.33	−3.63	1.0	5.34	−1.00	−4.28
Cepheus-A EW	0.73	-10	[-28,-12]	[-8,12]	2.4	8.3	20	4.24	−3.08	0.20	4.37	−0.13	−4.00
Cepheus-A NS	0.73	-10	[-28,-12]	[-8,12]	2.3	6.6	16	4.06	−3.85	0.75	5.04	−1.00	−4.68
G138.295+1.555	2.2	-38	[-51,-41]	[-35,-25]	4.2	6.2	25	4.14	−3.46	0.47	4.87	−0.73	−4.25
G139.909+0.197	2.0	-39	[-53,-43]	[-35,-25]	3.8	6.2	26	4.16	−3.61	0.60	4.98	−0.82	−4.40
G192.584-0.041S	2.5	9	[-2,6]	[12,20]	3.6	5.9	20	4.00	−3.45	0.34	4.76	−0.74	−4.20
S255-FIR2	2.5	8	[-4,6]	[10,20]	8.7	4.9	42	4.28	−3.34	0.46	4.97	−0.69	−4.03
G240.31+0.08	6.6	67	[50,63]	[73,84]	57	9.5	570	5.70	−2.52	1.9	5.28	0.41	−4.20
W3(OH)	2.2	-48	[-67,-54]	[-45,-32]	13	8.8	95	4.84	−2.67	0.39	4.64	0.20	−3.52
G45.07+0.13	8.3	59	[35,55]	[65,85]	45	4.9	480	5.92	−2.79	0.60	4.83	0.01	−3.73

4.7 Scaling relations

From the data in Table 4.1, one can search for correlations in the outflow parameters that scale with the luminosity of the driving source. Fig. 4.16 shows that the outflow mechanical luminosity scales with the 1.02 ± 0.12 power of the bolometric luminosity, where the quoted uncertainty is 1σ computed assuming that the data on both axes are random variables with 50% error. Clearly, only a small fraction ($\sim 10^{-4}$) of the total luminosity is ultimately converted into mechanical motion of the molecular gas. Both of these results are consistent with the outflows measured from lower luminosity pre-main sequence stars also plotted (Levreault 1988).

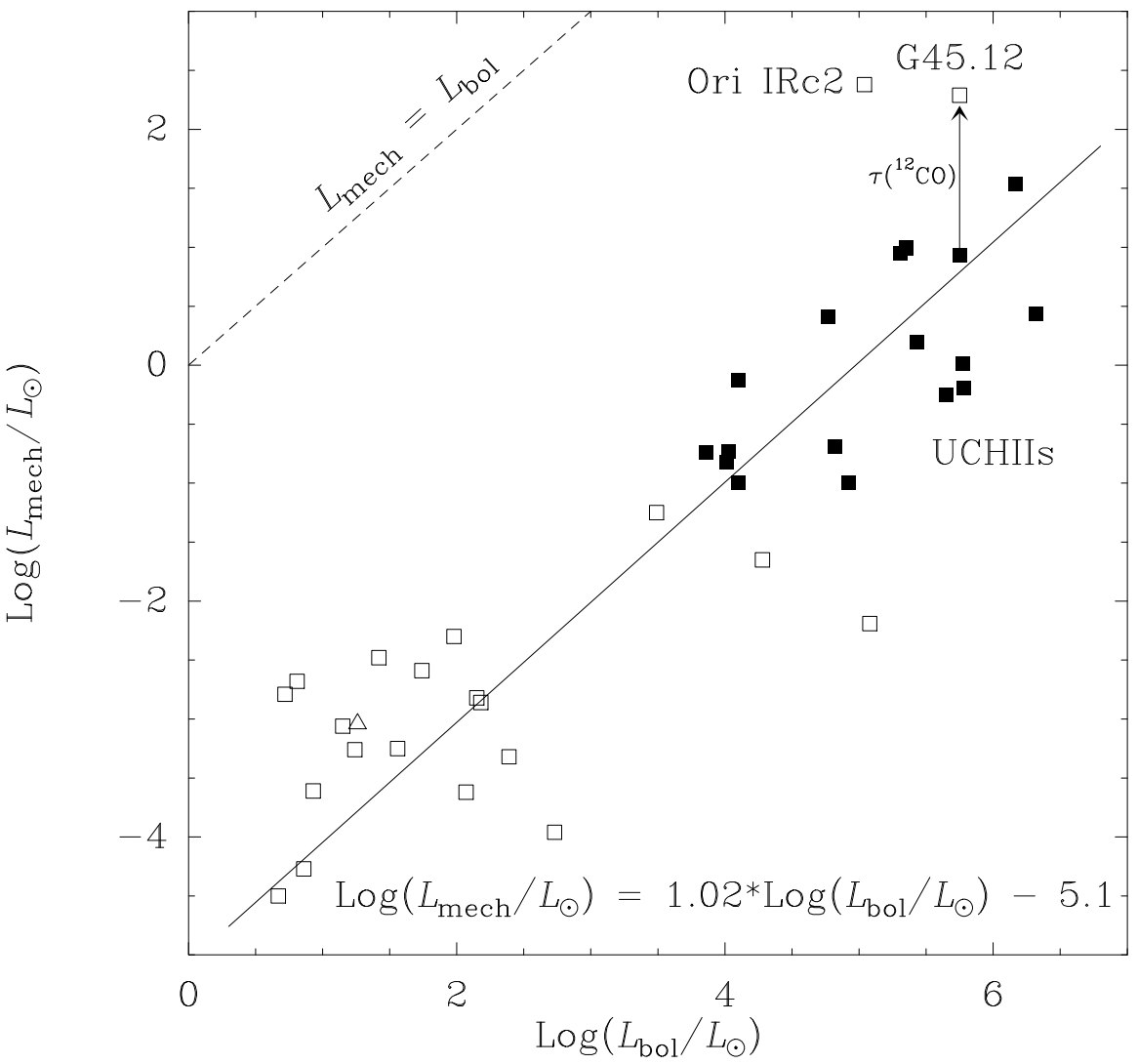

Figure 4.16: The mechanical luminosity of the outflow is plotted against the bolometric luminosity of the driving source. *Solid squares:* UCHII regions; *Open squares:* pre-main sequence stars from Levreault (1988) where the triangle represents T Tau. The linear function with the best fit to all of the data is plotted (solid line) along with the ultimate limit from the law of conservation of energy in which the two luminosities are equal (dashed line). The larger value for G45.12+0.13 comes from the ^{13}CO map presented in Chapter 5.

Shown in Fig. 4.17, the momentum supply rate required to drive the UCHII outflows scales with the 0.81 ± 0.10 power of the central source luminosity. Also plotted are outflows from lower luminosity ($L < 10^5 L_\odot$) sources from the Levreault (1988) survey which clearly cannot be driven by radiation pressure alone. However, in the case of the highest luminosity sources, the UCHII regions, the momentum supply rate available from radiation pressure becomes sufficient to drive the outflows. This crossing point reflects the simple theoretical predictions made in sections 4.2.1 that radiation pressure from the central star rivals the maximum momentum supplied by the accretion disk wind. The fact that Orion IRc2 lies so far above the curve suggests that it is a special case, or simply that it is near enough to properly resolve all of the outflowing gas. Indeed, when the correction is made for the significant optical depth in the wings of the ^{12}CO 2$\rightarrow$1 transition (see Chapter 5), the force required to drive the G45.12+0.13 outflows compares well with Orion IRc2. Further study of ^{13}CO in UCHII region outflows will be necessary to determine if all of the mass estimates should raised by a similar factor.

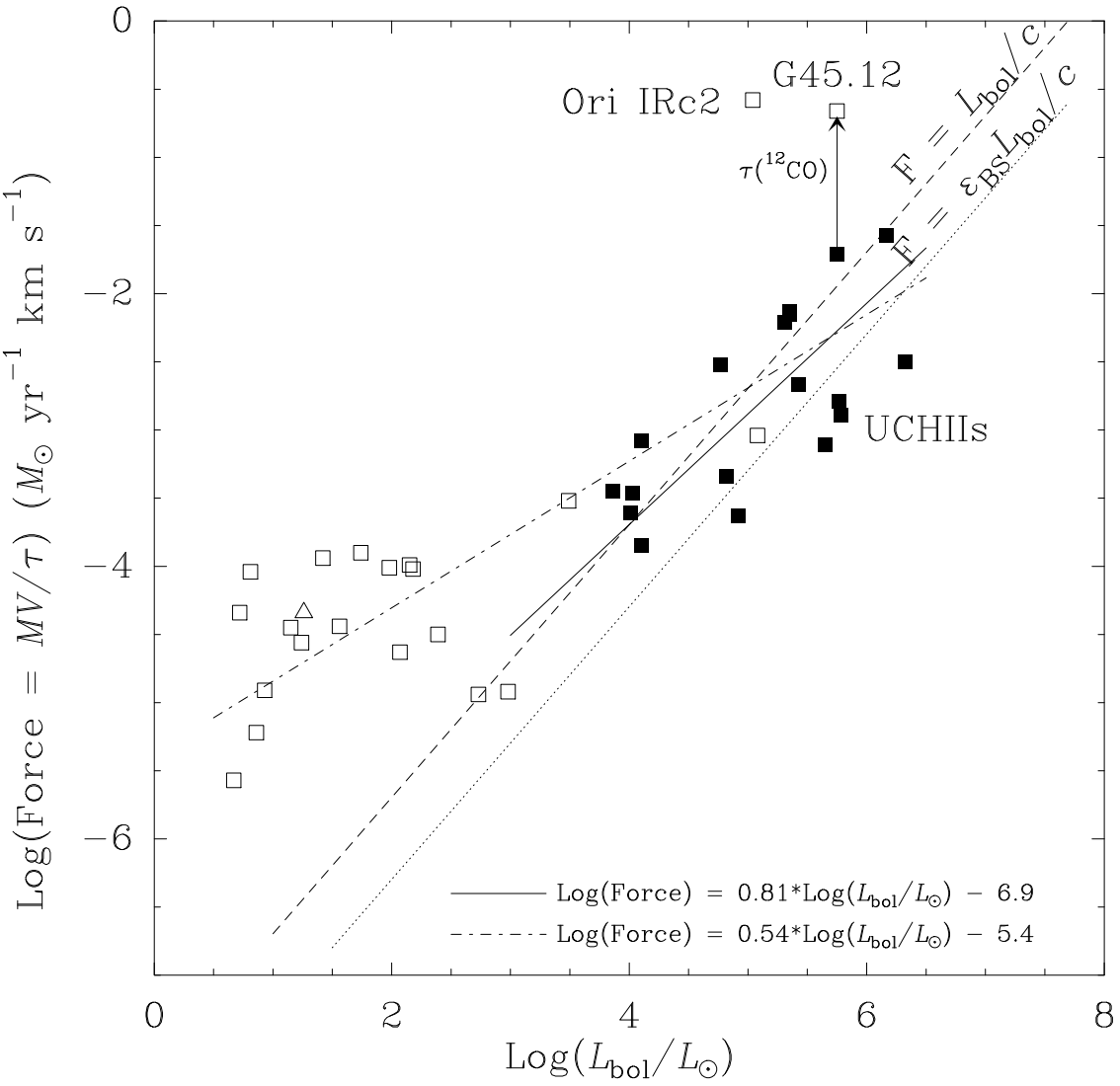

Figure 4.17: The momentum supply rate (force) required to drive the outflows is plotted against the bolometric luminosity of the central source. *Solid squares:* UCHII regions from this work; *Open squares:* pre-main sequence stars from Levreault (1988) where the triangle represents T Tau. The solid line is the linear function with the best fit to the UCHII regions and the dash-dot line is the best fit to all the data. The dashed line is the total momentum available from the radiation field and the dotted line is the reduced momentum available to a jet-driven outflow with a bow shock conversion efficiency of 25%. The larger value for G45.12+0.13 comes from the ^{13}CO map presented in Chapter 5.

For UCHII regions, the mass outflow rate of the molecular gas scales with the 0.66 ± 0.09 power of the central source luminosity as shown by the solid line in Fig. 4.18. Combining these data with those of Levreault (1988), the scaling becomes 0.87 ± 0.28 over the luminosity range from 5.6 to $10^6 L_\odot$. The extent of the correlation from sources of 5 to over $10^6 L_\odot$ speaks powerfully for a common underlying outflow mechanism.

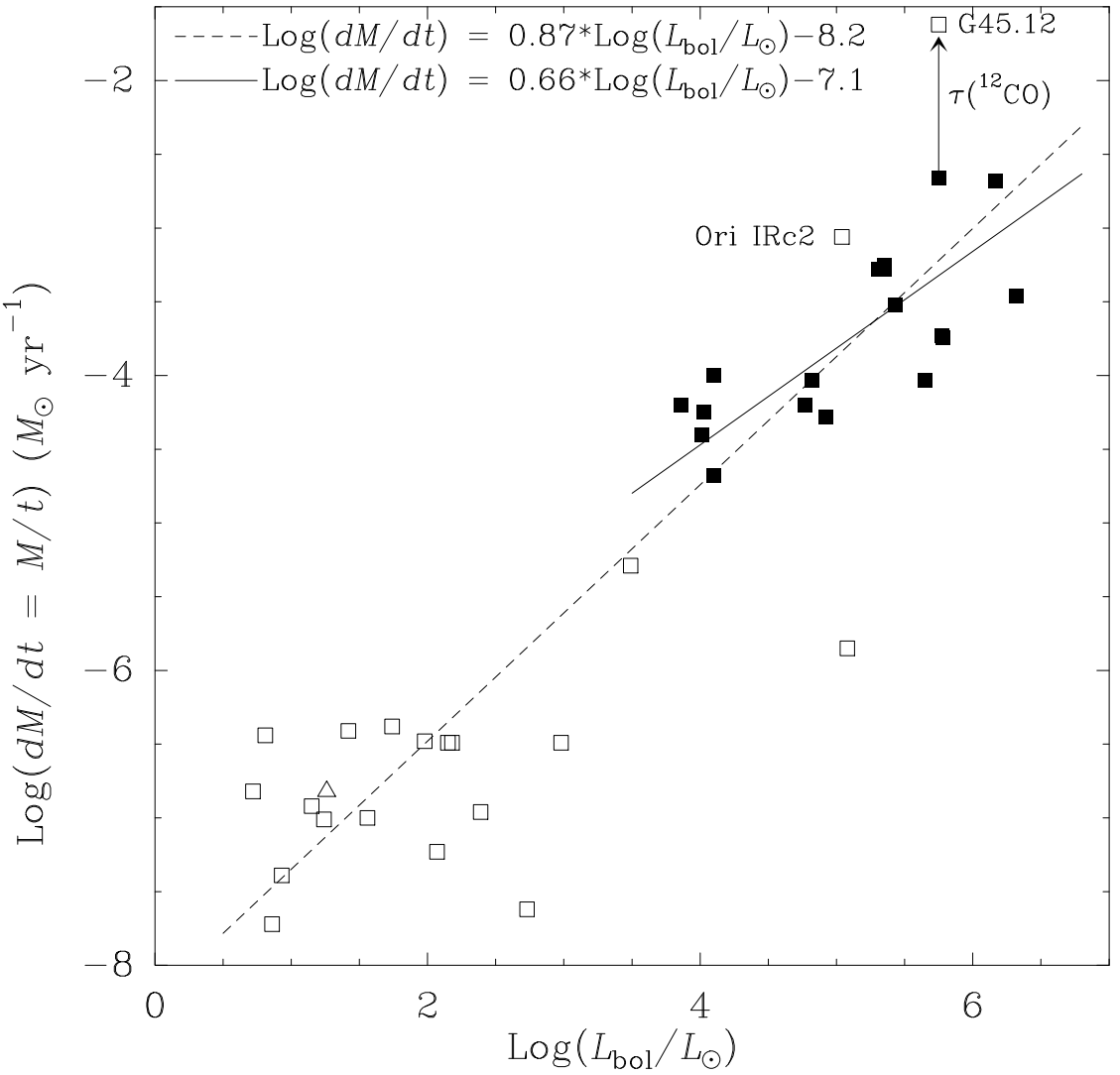

Figure 4.18: The mass outflow rate plotted against the bolometric luminosity of the driving source. *Solid squares:* UCHII regions from this work; *Open squares:* pre-main sequence stars (triangle = T Tau) from Levreault (1988). The linear functions with the best fit to the UCHII regions (solid line) and to the combined data set (dashed line) are included. The larger value for G45.12+0.13 comes from the ^{13}CO map presented in Chapter 5.

4.8 Summary

Of the 17 UCHII regions mapped, 15 show evidence for bipolar outflows in the form of a spatial offset between the redshifted and blueshifted emission centered about a position within 10″ of the peak radio position. The other two regions also show high velocity CO emission but with a non-bipolar distribution. The mass outflow rate and mechanical luminosity of the outflows both scale with the bolometric luminosity of the central source. The agreement of the scaling across the full range of protostellar luminosities suggests a common driving mechanism. In contrast to outflows from low-mass stars, radiation pressure cannot be ruled out as the ultimate source of momentum for the molecular outflows from the UCHII regions presented here. Because stellar luminosities scale steeply with stellar mass, the momentum available from the radiation pressure of an O-star rivals that from the accretion disk wind models developed to explain jet-driven outflows from low-mass stars.

Much like the submillimeter continuum images presented in Chapter 3, many of the high-velocity molecular line maps of UCHII regions show evidence for multiple sources. In G138.295+1.555, two distinct outflows can be identified with two individual radio sources. In the G75.78+0.34 complex and the S255 complex, individual outflows are seen toward a known radio source and toward an adjacent radio-quiet submillimeter source. In nearly all cases, the outflow sources coincide with areas of strong dust emission. However, in several cases including G5.97-1.18, G45.45+0.06 and K3-50A, the origin of the outflow is displaced by 10″ or more from the UCHII region, suggesting a separate driving source. When multiple outflows are present, as in Cepheus-A, G138.295+1.555 and K3-50, the most compact outflow lies closest to the center of the dust core, consistent with the idea that the youngest outflows emerge from the most deeply embedded sources.

The results presented in this chapter parallel the growing literature on multiple outflows in star-forming regions. Some examples include IRAS 20050+2720 (Bachiller, Fuente & Tafalla 1995), AFGL 5142 (Hunter et al. 1995), and DR 21 (Garden et al. 1991), all of which lie within 2 kpc of the Sun. Due to their larger dis-

tances, many of these individual outflows tentatively identified here with the UCHII regions may consist of further multiplicity like that seen in the striking dual outflow from the nearby Cepheus A core. Thus, to explore this possibility and to complete the research presented in this thesis, Chapter 5 presents a detailed high-resolution molecular line and continuum study of a complex region of outflow associated with the UCHII regions G45.12+0.13 and G45.07+0.13.

Chapter 5 Active Star Formation toward the G45.12+0.13 and G45.07+0.13 UCHII Regions

Prologue: Recently reviewed by a referee for *The Astrophysical Journal*, the results presented in this chapter have been revised for publication under the authorship of T.R. Hunter, T.G. Phillips and K.M. Menten. This paper contains a detailed study of bipolar outflows from two UCHII regions in a giant molecular cloud of high bolometric luminosity ($L > 10^6 L_\odot$) at a distance of 8.3 kpc.

Abstract

A multiwavelength study of the molecular cores containing the ultracompact HII (UCHII) regions G45.12+0.13 and G45.07+0.13 reveals a series of phenomenological differences that distinguish the age of these cores in terms of their development of high mass star formation. First, we report the discovery of massive, bipolar molecular outflows from both UCHII regions. The G45.12+0.13 UCHII region lies centered on a spatially extended, 6 km s^{-1} outflow that we have mapped in the CO J=2→1, 3→2, 6→5, ^{13}CO 2→1 and C^{18}O 2→1 transitions at the Caltech Submillimeter Observatory (CSO). The broad bipolar structure is optically-thick in the ^{12}CO line. The ^{13}CO measurements imply a large outflow mass of $4800 M_\odot$ (12% of the total cloud mass). Interferometric observations with the Owens Valley Millimeter Array in the ^{13}CO 1→0 line resolve the gas into at least two outflows, one of which emanates from the 4.0 Jy 110 GHz source identified with the UCHII region. An additional outflow is driven by an adjacent young, embedded object which contributes to the extended submillimeter continuum emission imaged with the CSO bolometer array camera. Lying in a separate core a few arcminutes away, the G45.07+0.13 UCHII region contains H_2O masers and presents higher velocity (11 km s^{-1}) yet more compact CO emission. An outflow has been detected in the CO 6→5 transition along with a compact submillimeter continuum source. OVRO observations in the CS J=2→1 transition

confirm a compact outflow centered on the 98 GHz continuum source toward which infall is also seen in the form of redshifted absorption. The multiple outflows, higher CO antenna temperatures, more extended submillimeter and radio continuum emission, and lack of H_2O masers all distinguish the core containing G45.12+0.13 as a more advanced site of massive star formation than the neighboring core containing G45.07+0.13.

5.1 Introduction

The bright, compact Galactic radio sources known as UCHII regions are thought to be powered by massive young stars still embedded in their parent molecular cloud (Wood & Churchwell 1989). Generally, the large column densities of molecular gas ($N_{\rm H_2} \sim 10^{23} - 10^{24}$ cm^{-2}) toward these objects prohibit the optical identification of their ionizing stars and hide the early stages of massive star formation (Churchwell, Walmsley & Wood 1992). While near-infrared imaging provides a deeper view of the young stars embedded in the cloud, sometimes in the form of reflection nebulae (e.g., NGC2024 FIR4, Moore & Yamashita 1995), the study of the molecular gas and dust surrounding UCHII regions at (sub)millimeter wavelengths offers the most direct tool for understanding the distribution and kinematics of the material from which stars are forming in these regions.

At some point during the accretion process of a new star, an outflow phase begins which can manifest itself in various observational forms including H_2O masers (Genzel et al. 1981; Reid et al. 1988; Gwinn, Moran & Reid 1992) and bipolar molecular outflows (Lada 1985; Bachiller & Gómez-González 1992; Tofani et al. 1995). Although most known bipolar molecular outflows have been observed in nearby, low-mass star-forming regions (Staude & Elsässer 1993), they have also been detected from young massive objects as well, such as G5.89-0.39 (Harvey & Forveille 1988), DR 21 (Garden et al. 1991), and W75N (Hunter et al. 1994). Bipolar outflow has also been seen in radio recombination lines toward the UCHII region K3-50A (DePree et al. 1994). A wider search for outflows from *massive* protostars is being pursued to determine the

rate of occurrence of outflow in high-mass star-forming regions (Shepherd & Churchwell 1996a). In recent years, multiple outflows emanating from a protostellar cluster have been identified in several star-forming regions including IRAS 20050+2720 (Bachiller, Fuente & Tafalla 1995), L 1448 (Bachiller et al. 1995), and AFGL 5142 (Hunter et al. 1995). Given that the statistical ages of the oldest outflows must be $\geq 10^5$ yr (Parker, Padman & Scott 1991), it is reasonable to expect outflows from several young embedded sources to be present simultaneously in an evolved star-forming cluster. Outflow surveys of high-mass star-forming regions should help determine the epoch of the outflow phase relative to the UCHII phase of massive stars. Also, the discovery of outflows from UCHII regions themselves are important for comparison of their energetics to outflows from lower mass objects in terms of theoretical jet-driven models (Masson & Chernin 1993).

Because most UCHII regions lie at distances of several kiloparsecs, past CO surveys have had insufficient spatial resolution to identify distinct molecular outflows. For this reason, we have performed a higher resolution ($\leq 30''$) search for molecular outflows in the submillimeter CO transitions at the CSO. Followup observations at the OVRO millimeter array are being obtained to study specific sources in greater detail. In this paper, we present a comprehensive picture including maps of molecular outflows and submillimeter continuum emission from the cores containing the luminous UCHII regions G45.12+0.13 and G45.07+0.13. Shown in Fig. 5.1 is the integrated CO 3→2 emission from these two cores. The most striking features of the map are the spoke-like structures of gas that protrude from the northern core. The southern core appears more compact. Given their proximity in the plane of the sky and similar LSR velocities, G45.12+0.13 and G45.07+0.13 probably lie at the same distance (8.3 kpc) derived from recent HI absorption studies of G45.12+0.13 (Kuchar & Bania 1994). The spectral types derived for the ionizing stars are O7 and O5.5, and the far-infrared luminosities based on the IRAS fluxes are $10^{6.02}$ and $10^{6.10} L_\odot$, respectively (Wood & Churchwell 1989).

Near-infrared photometry of G45.12+0.13 reveals a spectrum rising steeply with increasing wavelength, consistent with a deeply embedded source emitting most of

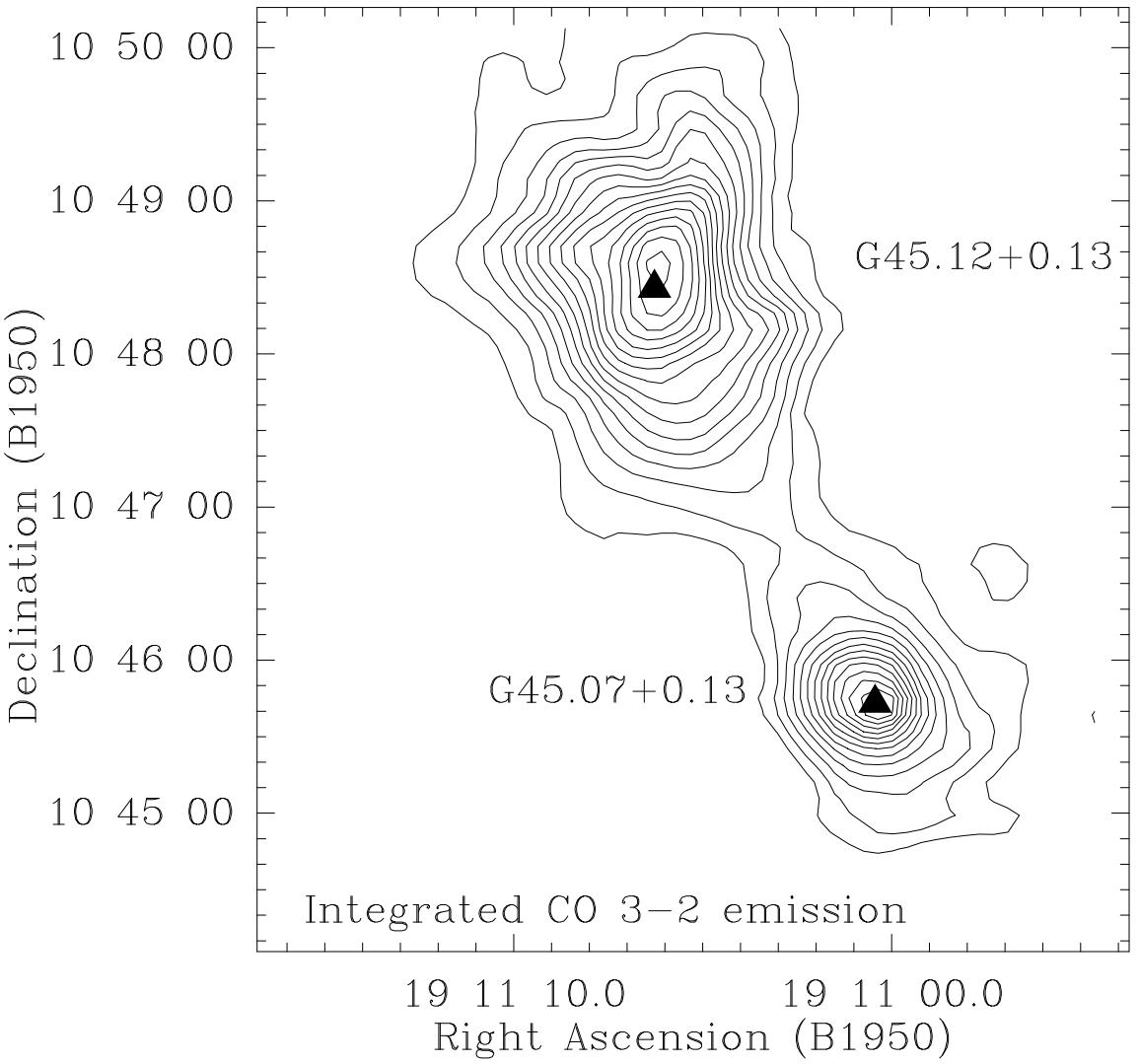

Figure 5.1: Contour map of the CO J=3→2 transition observed with a 20″ beam with levels 75 to 500 by 25 K km s^{-1}. The positions of the UCHII regions are marked by triangles (Wood & Churchwell 1989). Note the several spoke-like protrusions of gas from the core containing the UCHII region G45.12+0.13.

its energy at far-infrared wavelengths (Chini, Krügel & Wargau 1987). Imaging of the Brγ line reveals an ionized nebula extended to a scale of 10″ (Lumsden & Puxley 1996), significantly larger than the radio UCHII region. Multitransition ^{13}CO and CS observations imply large H_2 column densities toward the G45.12+0.13 core ($N_{H_2} \sim 3 \times 10^{23}$ cm^{-2}) (Churchwell, Walmsley & Wood 1992) and NH_3 observations indicate a rotational temperature of 32 K (Olmi, Cesaroni & Walmsley 1993). The millimeter continuum flux of G45.12+0.13 rises with decreasing wavelength: 4.02 Jy at 7.0 mm

in a 44″ beam (Wood et al. 1988), 6.3 Jy at 2.7 mm in a 54″ beam (Wood, Churchwell & Salter 1988) and 10.5 Jy at 1.3 mm in a 90″ beam (Chini et al. 1986), consistent with a mixture of free-free emission and dust emission. Likewise, the millimeter continuum flux of G45.07+0.13 rises steeply from 0.69 Jy at 7.0 mm, 1.15 Jy at 2.7 mm, 3.2 Jy at 1.3 mm, and 10.3 Jy at 0.8 mm (Sandell 1994) indicating a dust core. Both regions also exhibit broad near-infrared Brγ and HeI lines suggestive of outflow motion (Doherty et al. 1994).

Despite their similarities at infrared through millimeter wavelengths, these two regions exhibit rather different radio properties; thus they provide excellent targets for comparative research. The radio continuum emission from G45.07+0.13 appears "spherical or unresolved" while G45.12+0.13 appears "cometary" (Wood & Churchwell 1989). Both regions contain Type I OH masers (Goss et al. 1973), but only G45.07+0.13 contains H_2O masers (Genzel & Downes 1977) which have been resolved into several spatial and velocity components coincident with and adjacent to the UCHII region (Hofner 1996a). G45.12+0.13 has not been detected as an H_2O maser source to a 5σ level of 3 Jy (Felli 1996; Churchwell, Walmsley & Cesaroni 1990). These contrasting properties drive our interpretation of the extensive multi-wavelength observations presented here.

5.2 Observations

5.2.1 Caltech Submillimeter Observatory

Our submillimeter observations were performed with the on-the-fly mapping mode using the facility receivers and acousto-optical spectrometers (AOS) of the CSO[1]. A summary of the spectroscopic observations of G45.12+0.13 and G45.07+0.13 is given in Table 5.1. All spectra were analyzed with the CLASS software package and are

Source	molecular transition	main beam	map grid	total time per point	beam efficiency	AOS (MHz)	month of observation
G45.12+0.13	CO 2→1	30″	15″	3 sec	0.72	50	March 1994
	^{13}CO 2→1	31″	15″	9 sec	0.72	50	July 1994
	C^{18}O 2→1	31″	15″	10 sec	0.72	50	July 1994
	CO 3→2	20″	15″	5 sec	0.65	500	April 1994
	CS 7→6	20″	15″	5 sec	0.65	500	April 1994
	CO 6→5	11″	5″	17 sec	0.38	50	May 1994
G45.07+0.13	CO 4→3	15″	7.5″	30 sec	0.54	50	May 1995
	CO 6→5	11″	5″	18 sec	0.40	50	May 1995

Table 5.1: Summary of CSO spectroscopic observations of G45

presented on a main beam brightness temperature ($T_{\rm MB}$) scale. We estimate our calibration to be accurate to 30% and our pointing to ±5″.

In September 1993, we obtained an on-the-fly 800μm continuum map of both UCHII regions using the CSO single-channel bolometer equipped with a 30″ Winston cone. Repeated azimuth scans were spaced by 10″ in elevation, the chopping secondary frequency was 10 Hz and the central frequency of the filter was 380 GHz (Lis & Carlstrom 1994). Extinction correction and calibration were based on frequent observations of Saturn and Uranus at various airmasses. The zenith optical depth in the filter band was 0.66.

In March 1996, we obtained on-the-fly continuum maps of both sources at 350μm and of G45.12+0.13 at 450 μm using the new Submillimeter High Angular Resolution Camera (SHARC) at the CSO. SHARC contains a linear monolithic 24-pixel bolometer array operating at 0.3 K (Wang et al. 1996). Illuminated directly by cold optics,

[1]The Caltech Submillimeter Observatory is funded by the National Science Foundation under contract AST-9313929.

the pixels subtend $5''$ by $10''$ on the sky for a total size of $120''$ by $10''$ (Hunter, Serabyn & Benford 1996). The array was aligned in elevation and scanned in azimuth at $4''$ s^{-1} with a secondary throw of $92''$ at 4.09 Hz. 31 scans were obtained on each region, stepping by $4''$ in elevation on each subsequent scan. The relative gains of each pixel were calibrated by rapid elevation scans of Jupiter. The central frequencies of the filters were 853 and 670 GHz (for sources with $F_\nu \propto \nu^4$). The maps were smoothed to an effective angular resolution of $12''$. The zenith optical depth at 225 GHz was 0.08 as measured by the CSO tipping radiometer. Because the submillimeter optical depth was changing during the observations, a direct measurement of the optical depth in the observed filter band was not possible. Instead, the continuum flux was corrected for atmospheric extinction using an estimate of the optical depth in the filter band computed by scaling up the 225 GHz optical depth measurements by a factor of 22. Absolute calibration is based on scans of IRC+10216 during the same night (Sandell 1994) and the pointing accuracy is estimated to be $\pm 5''$.

5.2.2 Owens Valley Millimeter Array

A summary of the observations made with the six-element OVRO Millimeter Array is listed in Table 5.2. The bright, compact nature of the continuum sources associated with the UCHII regions allowed us to perform self-calibration and apply the solutions to the spectral-line data. The first few CLEAN components of the continuum source were used as an initial model for phase self-calibration using the Difmap software package (Shepherd, Pearson & Taylor 1994). After several iterations of phase self-calibration and further CLEANing, the amplitude gains for each antenna of each subarray were computed using GSCALE. Finally, the amplitude gains were allowed to vary on slowly decreasing timescales over each track in an iterative phase and amplitude self-calibration process. Due to the significant amount of extended emission, only a minimal amount of CLEANing was performed on the spectral line channels. Extended emission limits the noise achievable in most of the spectral-line channel maps.

Source	G45.12+0.13
Observing season	Fall 1994
Pointing centers	$(+6'', +15'')$ and $(-6'', -15'')$ relative to $19^h11^m06^s.227, +10°48'25''.82$ (B1950)
Transits observed	3
Total baselines	40
Phase calibrator	1923+210
Primary beam	$66''$
Synthesized beam	$2''.60 \times 2''.41''$, P.A. $-40°$
^{13}CO J=1→0 bandwidth/resolution	60 km s^{-1}/0.68 km s^{-1}
C^{18}O J=1→0 bandwidth/resolution	22 km s^{-1}/0.68 km s^{-1}
Continuum frequency/bandwidth	110 GHz / 1 GHz
Continuum sensitivity	5 mJy/beam
Continuum dynamic range	460
Source	G45.07+0.13
Observing season	Spring 1995
Pointing center	$19^h11^m00^s.397, +10°45'42''.90$ (B1950)
Transits observed	3
Total baselines	45
Phase calibrator	1749+096
Primary beam	$74''$
Synthesized beam	$2''.71 \times 2''.11''$, P.A. $-63°$
CS J=2→1 bandwidth/resolution	98 km s^{-1}/0.76 km s^{-1}
Continuum frequency/bandwidth	97.9 GHz / 1 GHz
Continuum sensitivity	1.6 mJy/beam
Continuum dynamic range	570

Table 5.2: Summary of OVRO observations of G45

5.3 Molecular outflows

5.3.1 CSO observations

5.3.1.1 CO and CS spectra

CSO spectra of the various CO transitions observed toward the central positions of G45.12+0.13 and G45.07+0.13 are presented in Fig. 5.2. Both sources exhibit high velocity emission in all of the lines, signifying molecular outflow. In G45.12+0.13, there is a rapid increase in brightness temperature with CO transition. Since all of the CO transitions are significantly extended on the scale of the beamsize, this increase cannot be due entirely to beam filling factor effects and instead indicates

the presence of a hot core. In contrast, G45.07+0.13 shows very little increase in brightness temperature with CO transition level, indicating cooler gas. Also, a steep drop in emission from the three lower J CO lines occurs in G45.07+0.13 near 65 km s^{-1}, a 5.5 km s^{-1} redshift from the LSR velocity of the molecular cloud (Cesaroni et al. 1991). No such drop is seen in the 6→5 line, suggesting that the feature is a characteristic of only the cool component of the gas.

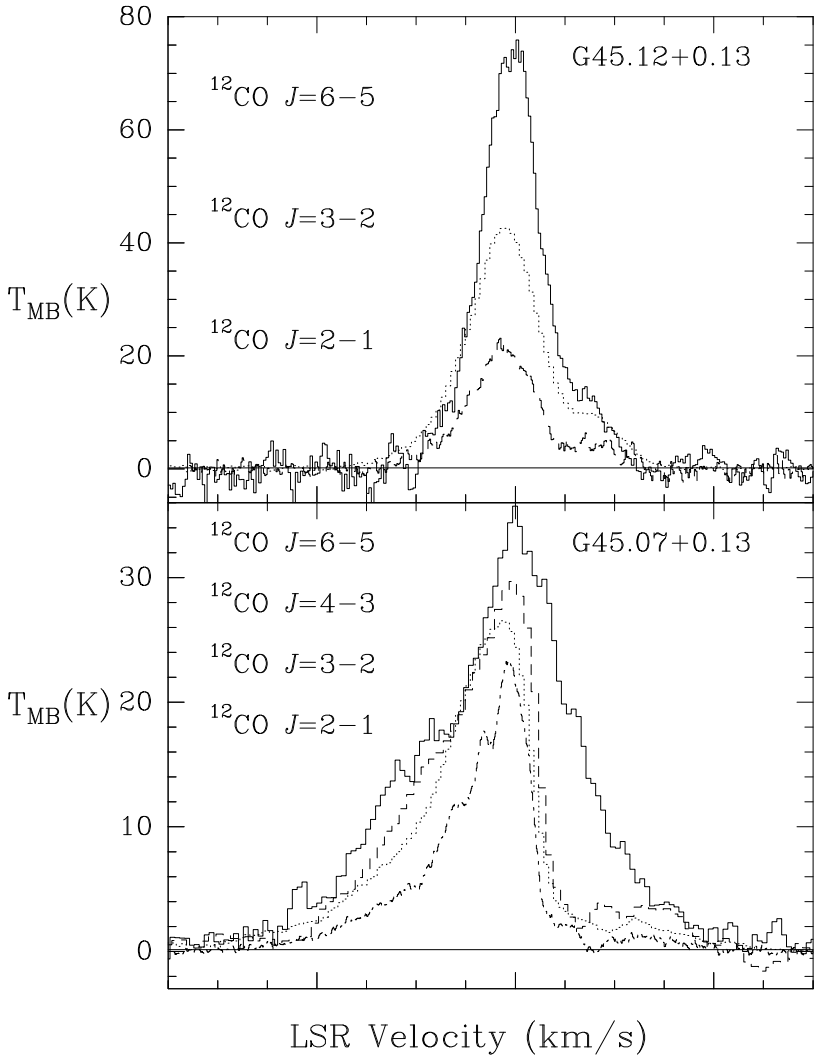

Figure 5.2: CSO spectra of several ^{12}CO transitions observed toward the UCHII regions G45.12+0.13 and G45.07+0.13 calibrated on the main beam brightness temperature scale.

Source	$v_{\rm LSR}$(km s^{-1})	Δv(km s^{-1})	$T_{\rm MB}$(K)	$I_{\rm CS}$(K km s^{-1})
G45.12+0.13	59.5	4.60	2.37	11.6
G45.07+0.13	59.7	7.33	5.75	44.9

Table 5.3: Observed properties of the CS J=7→6 transition

Spectra of the CS J=7→6 emission (observed simultaneously with the CO J=3→2) toward both sources are shown in Fig. 5.3. G45.07+0.13 exhibits significantly brighter emission than G45.12+0.13 in this high density-tracing transition. The line parameters are summarized in Table 5.3.

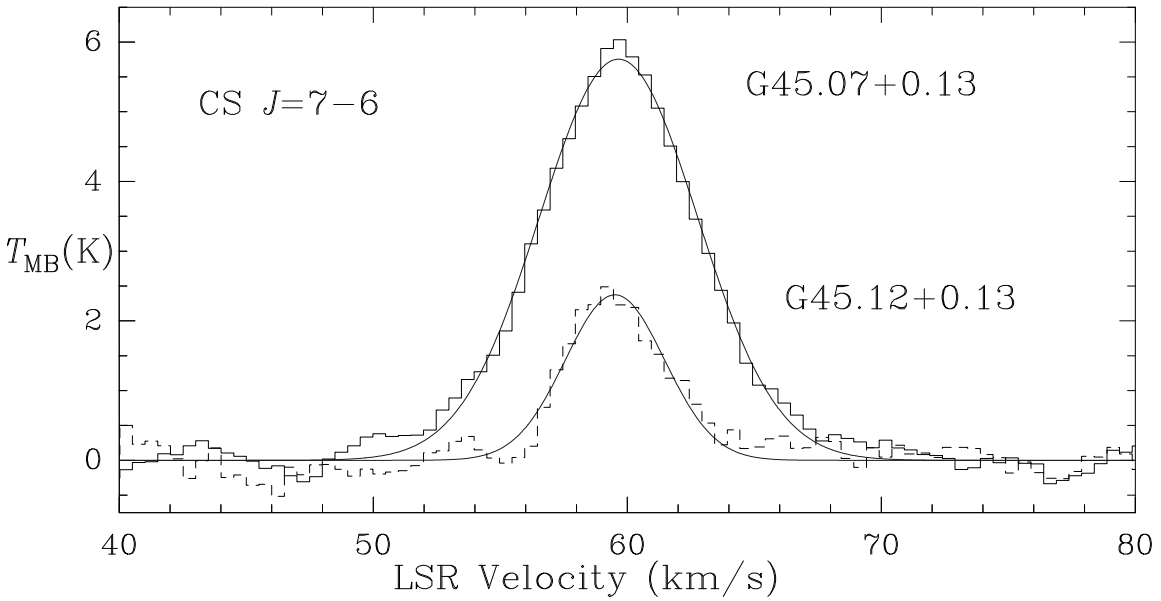

Figure 5.3: CSO spectra of the CS 7→6 transition observed toward the UCHII regions G45.12+0.13 (solid histogram) and G45.07+0.13 (dashed histogram) calibrated on the main beam brightness temperature scale.

5.3.1.2 CO maps

We now compare the spatial appearance of the CO emission toward both sources. Shown in Fig. 5.4 are contour maps of the high velocity emission from G45.12+0.13 in 3 different isotopic transitions of CO J=2→1 all at $\sim 30''$ resolution. The C^{18}O map reveals a ridge of high column density gas that peaks a few arc seconds northeast of the UCHII region. In the two more abundant species, a distinct north/south offset is present between the bulk of the redshifted and blueshifted emission. Although the

positions of the redshifted and blueshifted CO lobes are roughly symmetric about the UCHII region, the additional structure in each lobe indicates that the outflow is not a simple bipolar nebula. Furthermore, the 10″ resolution ^{12}CO J=6→5 map shown in Fig. 5.5 suggests that the outflow has a broad opening angle and may not be centered on the UCHII region.

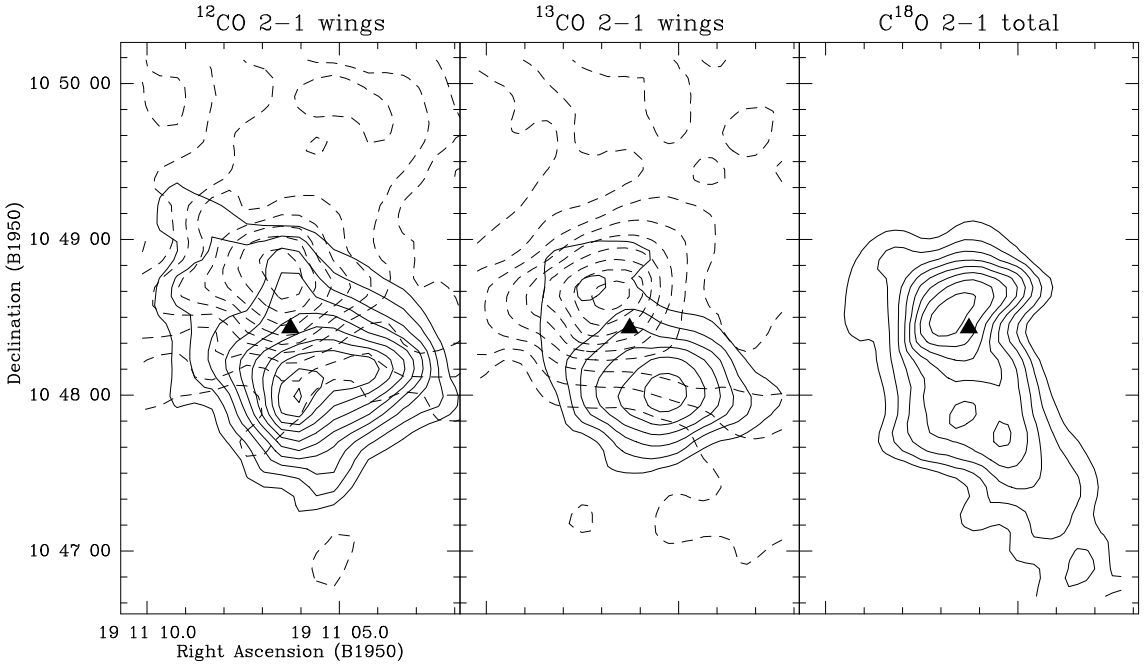

Figure 5.4: *Left panel:* Contour map of the CO J=2→1 transition toward G45.12+0.13 with the blueshifted emission (45 to 55 km s^{-1}) shown in solid contours (16 to 52 by 4 K km s^{-1}), the redshifted emission (65 to 75 km s^{-1}) shown in dashed contours and the radio peak position indicated by a triangle (Wood & Churchwell 1989). *Center panel:* Same as (a) for ^{13}CO (contours 5 to 25 by 2.5 K km s^{-1}). *Right panel:* Contour map of the integrated C^{18}O J=2→1 emission (contours: 6 to 20 by 2 K km s^{-1}).

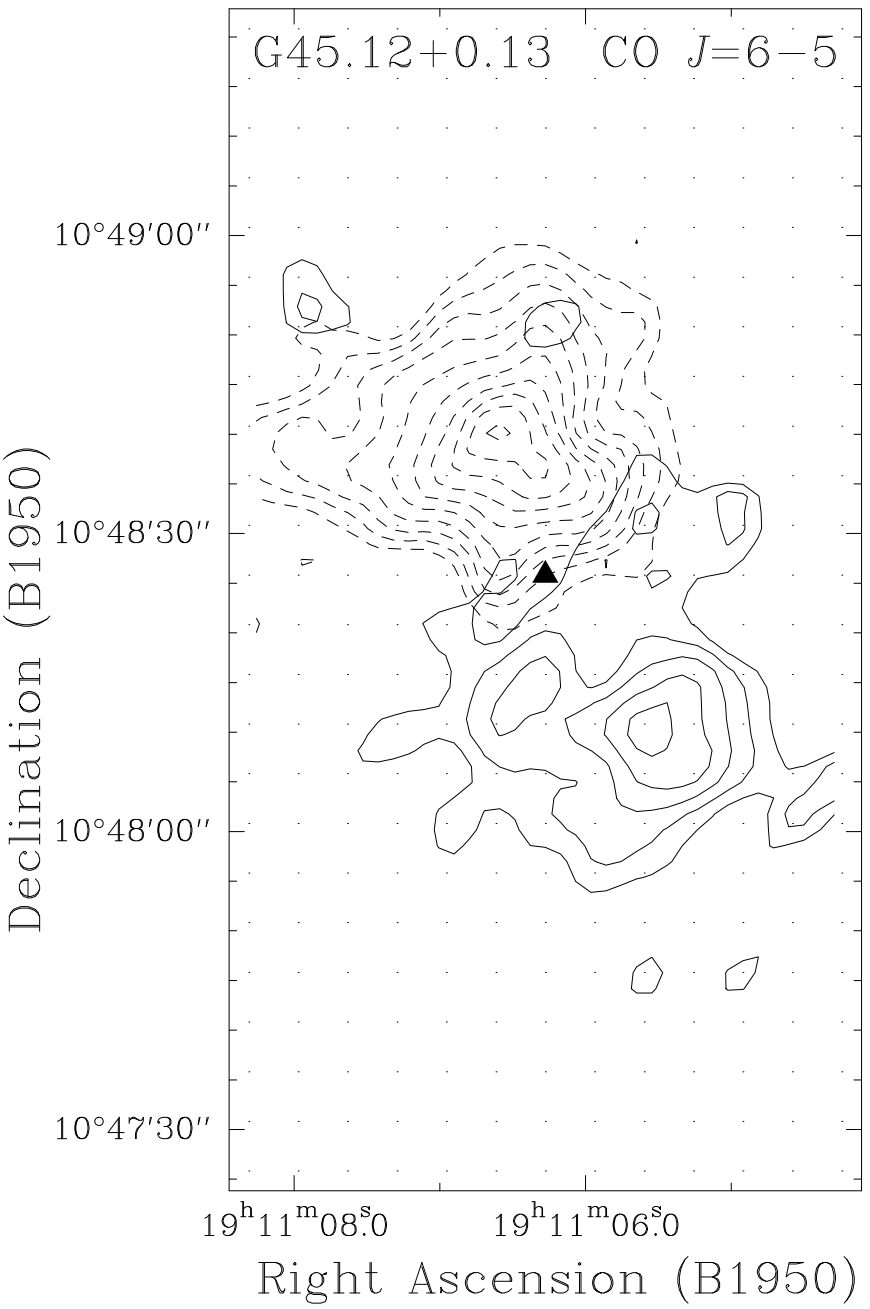

Figure 5.5: Contour map of the CO J=6→5 transition toward G45.12+0.13 with blueshifted emission (45 to 55 km s^{-1}) shown in solid contours (84 to 196 by 14 K km s^{-1}) and redshifted emission (65 to 75 km s^{-1}) shown in dashed contours (70 to 196 by 14 K km s^{-1}). The triangle marks the position of the UCHII region (Wood & Churchwell 1989).

In the case of G45.07+0.13, the CO J=2→1 map (not shown) revealed an unresolved outflow in the high velocity channels. A higher resolution (10″) followup map of the CO J=6→5 transition is presented in Fig. 5.6. In contrast to G45.12+0.13, the outflow is barely resolved in this map with the axis along a position angle of −18°. The UCHII region coincides within 3″ of the outflow origin, consistent with the absolute pointing uncertainty of the map.

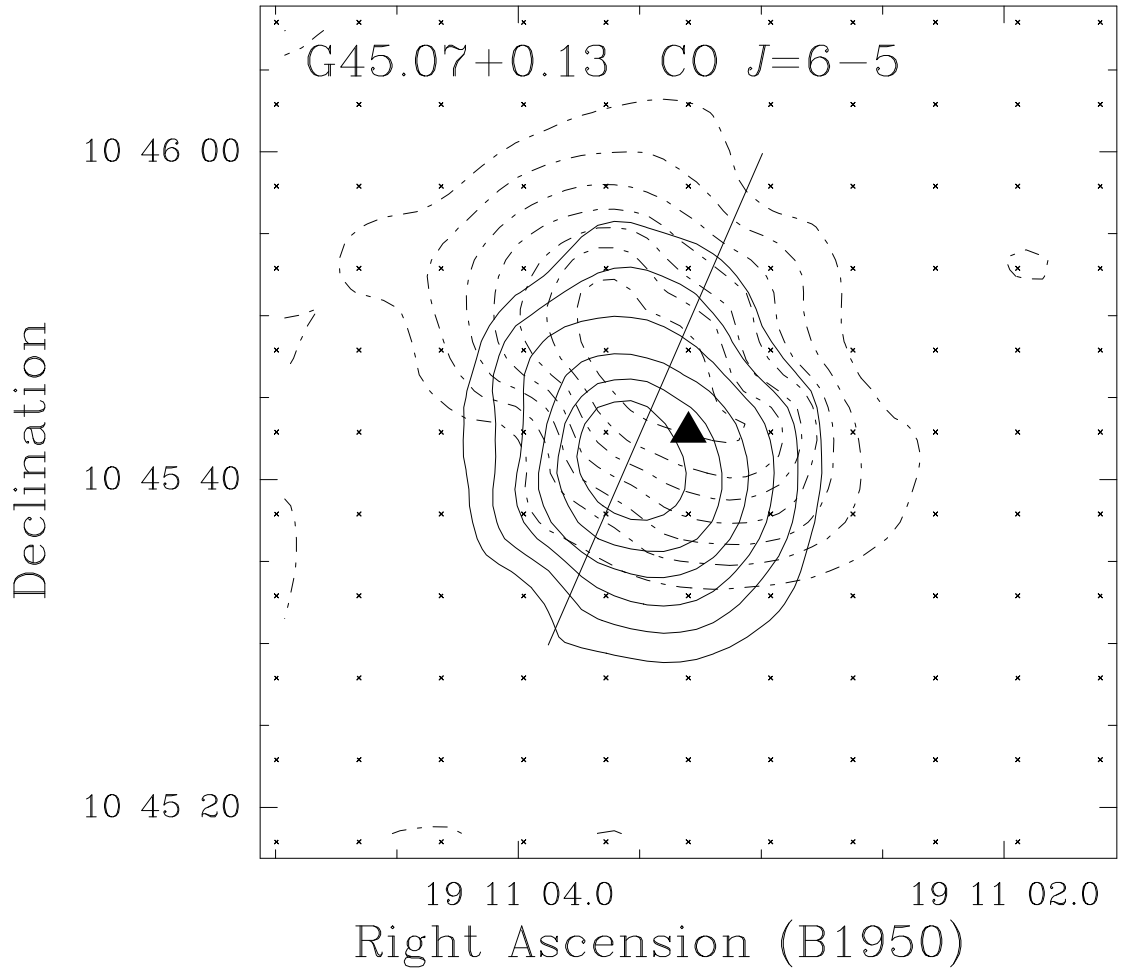

Figure 5.6: Contour map of the CO J=6→5 transition toward G45.07+0.13 with blueshifted emission (46.0 to 50.6 km s^{-1}) shown in solid contours and redshifted emission (65.0 to 70.3 km s^{-1}) shown in dashed contours 8 to 28 by 4 K km s^{-1}). The triangle marks the position of the UCHII region (Wood & Churchwell 1989).

Line	$T_{\rm exc}$	$\bar{v}$	l	$\log(t)$	$\log(M)$	$\log(\dot{M})$	$\log(\dot{M}v)$	$\log(L_{\rm m})$	$\log(Mv)$
	K	$\frac{\rm km}{\rm s}$	pc	yr	$M_\odot$	$\frac{M_\odot}{\rm yr}$	$\frac{M_\odot}{\rm yr}\frac{\rm km}{\rm s}$	$L_\odot$	$M_\odot\frac{\rm km}{\rm s}$
^{12}CO 2→1	25	6.8	1.8	5.27	3.40	-1.87	-0.88	2.07	4.38
^{13}CO 2→1	25	6.4	1.8	5.30	3.68	-1.62	-0.66	2.29	4.65
^{12}CO 3→2	40	6.4	1.8	5.30	2.40	-2.90	-1.94	0.99	3.35
^{12}CO 6→5	75	6.2	1.4	5.18	2.34	-2.84	-1.90	1.03	3.28

Table 5.4: Properties of the G45.12+0.13 molecular outflow

5.3.1.3 Outflow properties

The mass, momentum and energy contained in the molecular outflows are computed by integrating each spectrum channel by channel over the line wings (45 to 56 and 63 to 74 km s^{-1}) with the appropriate LSR velocity moment ($|v - v_{LSR}|^n$) applied (e.g., Garden et al. 1991). To properly compute the mass, the excitation temperature and the optical depth of the outflowing gas must be known. The temperature is approximated by the peak main beam brightness temperature of the ^{12}CO transition. Regarding the optical depth, it is a common practice to assume the high-velocity ^{12}CO gas to be optically thin. However, in the case of G45.12+0.13, the outflow appears prominently even in the less abundant ^{13}CO transition. To estimate the ^{12}CO optical depth, the ^{13}CO/^{12}CO line ratio was computed at each position in the maps for the redshifted and blueshifted wings separately. The ratio varies between 0.14 and 0.64 implying ^{12}CO optical depths τ between 8 and 38 (from the simple relation $T_{\rm MB}(^{13}{\rm CO})/T_{\rm MB}(^{12}{\rm CO}) = (1/60)\tau/(1-e^{-\tau})$, where (1/60) is the abundance ratio between ^{13}CO and ^{12}CO at a galactocentric distance of 6.4 kpc from Wilson & Rood (1994)). Using the appropriate factor from the optical depth at each map position, the column density measurements were increased accordingly in the calculation of the outflow parameters listed in the first row of Table 5.4. The most striking result is the large outflow mass of $2500 M_\odot$, making it one of the most massive protostellar outflows yet discovered.

A separate estimate of the outflow mass can be made by assuming the high-velocity ^{13}CO gas is optically thin. This assumption is consistent with the moderate optical depths derived for ^{12}CO and the fact that the outflow does not appear in the C^{18}O transition. The outflow mass computed in this way for the ^{13}CO line is $4800 M_\odot$,

about twice that computed from optically-thick ^{12}CO transition. We believe this larger value to be the most accurate measurement of the mass in the outflow, thus surpassing even the DR 21 outflow (Garden et al. 1991). Because ^{13}CO data are not available in the higher transitions, the values listed in rows 3 and 4 of Table 5.4 are computed for comparison under the optically-thin assumption (likewise in Table 5.5 for the G45.07+0.13 outflow).

To measure the total molecular gas mass in the cloud, we use the integrated flux in the C^{18}O line. The average C^{18}O column density over the map is 8.1×10^{15} cm^{-2}. Using the conversion formula of Frerking, Langer & Wilson (1982) for dense cores, this value corresponds to an average H_2 column density of 5.0×10^{22} cm^{-2} and hence a total mass of 3.9×10^4 $M_\odot$. The fraction of the total cloud mass participating in the outflow is 12%, similar to the 17% recently measured in the Mon R2 outflow (Tafalla et al. 1996).

Is there a precedent for such a massive bipolar outflow? To explore this question, we consider the mechanical luminosity and momentum input rate required of the driving source. These quantities require an estimate of the age of the outflow, a lower limit to which is the dynamical timescale. The dynamical timescale of the outflow is derived from the outflow half-length (half the distance between the half-power contours at the two ends of the flow) divided by the mean mass-weighted velocity. In this way, the dynamical timescale refers to an inclination angle of 45°. The wind mechanical luminosity of the outflow ($195 L_\odot$) lies below the value predicted ($655 L_\odot$) for a source of this bolometric luminosity based on the trend from lower luminosity sources (Levreault 1988):

$$\left(\frac{L_{\rm mech}}{L_{\rm bol}}\right) \approx .01 \left(\frac{L_{\rm bol}}{L_\odot}\right)^{-0.2}. \qquad (5.1)$$

Similarly, the momentum input rate (force) required to drive the outflow ($\log(\dot{M}\bar{v}) \sim -0.66$) is within the range observed in outflows from other sources with $L > 10^5 L_\odot$ (Lada 1985). As in the case of low-mass protostellar outflows (Bally & Lada 1983), this momentum input rate is nearly an order of magnitude higher than that available

Line	$T_{\rm exc}$	$\bar{v}$	l	$\log(t)$	$\log(M)$	$\log(\dot{M})$	$\log(\dot{M}v)$	$\log(L_{\rm m})$	$\log(Mv)$
	K	$\frac{\rm km}{\rm s}$	pc	yr	$M_\odot$	$\frac{M_\odot}{\rm yr}$	$\frac{M_\odot}{\rm yr}\frac{\rm km}{\rm s}$	$L_\odot$	$M_\odot\frac{\rm km}{\rm s}$
^{12}CO 4→3	30	7.9	0.3	4.60	1.65	-2.96	-2.1	0.74	2.7
^{12}CO 6→5	35	11	0.3	4.46	1.75	-2.72	-1.7	1.34	2.9

Table 5.5: Properties of the G45.07+0.13 molecular outflow

in the radiation field (-1.5) from the central source (if one assumes single scattering of photons from an O5.5 star on the basis of the the $10^{6.10}L_\odot$ bolometric luminosity from the region (Thompson 1984; Panagia 1973)).

Another physical measure of an outflow is its total kinetic energy. Past work on molecular outflows has revealed a correlation between outflow kinetic energy and the mass of the driving source (Levreault 1988). The slope (b) of the correlation is a steep function of mass: $b \propto 2.3\log(M/M_\odot)$. If we extrapolate the trend, the kinetic energy of the G45.12+0.13 outflow (5.6×10^{48} erg) implies a central mass of $210\,M_\odot$. If we use the largest slope and offset allowed by the errors in the best-fit line of Levreault, the implied mass can be as low as $110M_\odot$, not unreasonable considering the bolometric luminosity of the source. Thus, despite the large mass, it appears that the properties of the G45.12+0.13 outflow are by no means incongruent with other outflows.

5.3.2 OVRO interferometric observations

5.3.2.1 C^{18}O 1→0 absorption toward G45.12+0.13

The integrated C^{18}O 1→0 flux from G45.12+0.13 is shown in Fig. 5.7. The major feature in this field is gas seen in absorption against the UCHII region. The spatial extent of the C^{18}O absorption feature matches well with the 110 GHz continuum source (see Fig. 5.14). In addition, faint emission lies northeast of the UCHII region, matching the position of the C^{18}O 2→1 core.

5.3.2.2 ^{13}CO 1→0 emission toward G45.12+0.13

Interferometric observations of G45.12+0.13 in the ^{13}CO J=1→0 transition with a $2\farcs6$ synthesized beam are shown in channel maps in Fig. 5.8. These images provide a more detailed picture of the complex distribution of outflowing gas. Since there

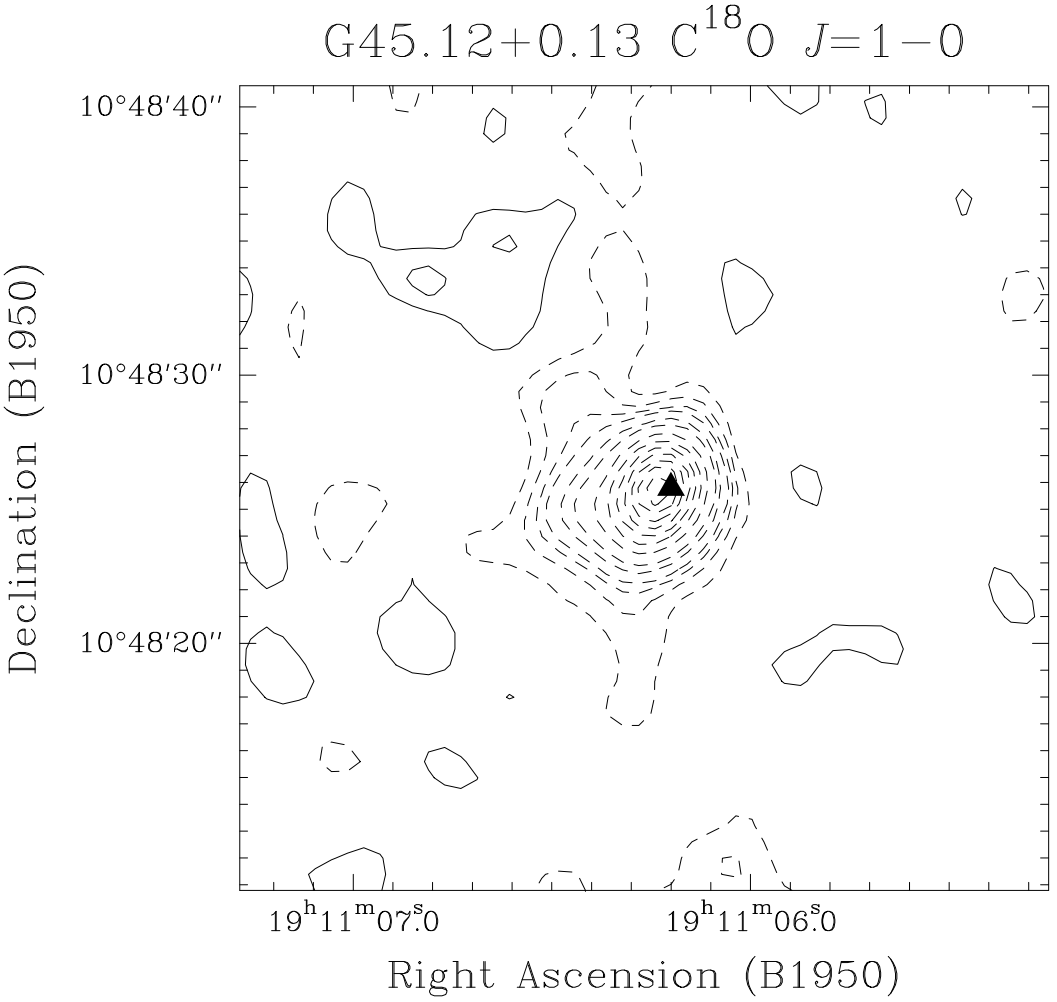

Figure 5.7: Integrated flux of the $C^{18}O$ J=1→0 transition observed toward G45.12+0.13 with a synthesized beam of $2\farcs60 \times 2\farcs41$ (contours: 50, 100, 150, 200, 300, 400 to 2000 by 200 mJy/beam with dashed contours representing negatives). The position of the 110 GHz continuum source is indicated by the triangle.

is much extended emission from this source in the ^{13}CO transition, the near-LSR velocity channels suffer from spatial filtering. Thus, only the channels from the line wings are presented. They are divided into four velocity regimes relative to the LSR velocity (59.5 km s^{-1}). In the upper panels of Fig. 5.8, the low-velocity redshifted emission is plotted next to the high-velocity blueshifted emission. A linear north-south structure appears to be symmetric about a point offset by $(-8'', -3'')$ from the UCHII region. We interpret this structure as a bipolar outflow from a separate embedded source which we designate G45.12+0.13 West. The average LSR velocity

of these velocity ranges is 58.1 km s^{-1}, blueshifted by 1.4 km s^{-1} from the bulk of the cloud. At both ends of the structure a small kink of emission extends out symmetrically on opposite sides of the main axis. This feature, along with the curved appearance of the southern lobe, suggests wandering of the outflow direction. The lack of radio continuum emission at the position of G45.12+0.13 West in the maps of Wood & Churchwell (1989) suggests that the driving source of the outflow is either a younger massive star or a cooler, lower mass star than that which powers the UCHII region.

In the lower panels of Fig. 5.8, the high-velocity redshifted emission is plotted next to the low-velocity blueshifted emission. In this case, the emission appears to be mostly symmetric about the position of the UCHII region as indicated by the conical surface drawn on the map. Therefore, we identify this emission with an outflow from the star powering the UCHII region. The average LSR velocity of these velocity ranges is 61.4 km s^{-1}, redshifted by 1.9 km s^{-1} from the bulk of the cloud.

Estimates of the individual outflow masses can be made from the ^{13}CO 1→0 maps. Assuming the same excitation temperature and abundance ratio noted in the previous section, we derive a conversion factor of $4.65 M_{\odot}$(Jy km s^{-1})$^{-1}$ for an optically-thin source at a distance of 8.3 kpc (e.g., Snell et al. 1984). By defining narrow boxes around the emission, we carefully measured the integrated flux in each of the four outflow lobes appearing in Figure 5.8. The results listed in Table 5.6 indicate that we have recovered only about 10% of the outflow emission in the interferometer maps. Nevertheless, we can conclude that the two outflows appear to be similar in mass.

Source	wing	velocity range (km s^{-1})	Integrated flux (Jy km s^{-1})	Mass ($M_{\odot}$)
G45.12+0.13	red	[61.4,64.1]	14.6	68
	blue	[49.2,54.6]	30.6	142
	total		45.2	210
G45.12+0.13 West	red	[65.5,75.0]	29.1	135
	blue	[50.6,56.0]	22.6	105
	total		51.7	240
Total			96.9	450

Table 5.6: Outflow masses derived from the ^{13}CO J=1→0 maps

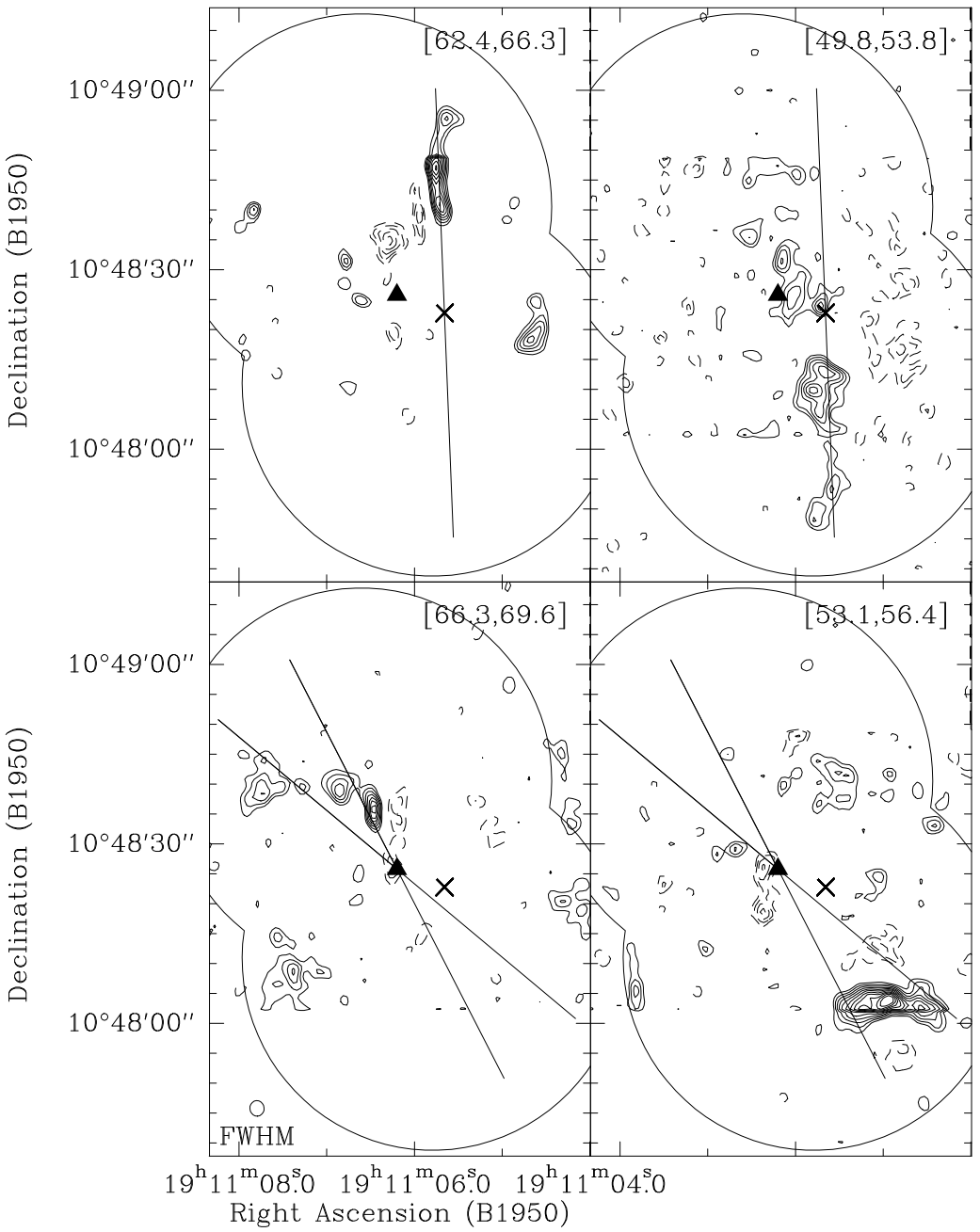

Figure 5.8: Channel maps of the ^{13}CO J=1→0 transition: *Top left panel:* Low-velocity redshifted emission (contours begin at 0.28 and increase by 0.06 Jy/beam with dashed contours representing negatives). The triangle marks the UCHII region and the cross marks the suspected origin of the outflow from G45.12+0.13 West. The large bounding circles mark the half-power primary beam; *Top right panel:* Same as left panel for the high-velocity blueshifted emission (contours: 0.09 by 0.045 Jy/beam); *Bottom left panel:* Same as top panels for the high-velocity redshifted emission (contours: 0.16 by 0.06 Jy/beam); *Bottom right panel:* Same as top panels for the low-velocity blueshifted emission (contours: 0.16 by 0.06 Jy/beam.

Having seen the interferometer maps, it is interesting to re-examine the single dish data. Channel maps of the CO J=3→2 transition observed with 20″ resolution are shown in Fig. 5.9. Also plotted are the two outflow origins and axes, identical to those in Fig. 5.8. Many of the extended ridges in the map are aligned with the axes, consistent with the multiple outflow interpretation.

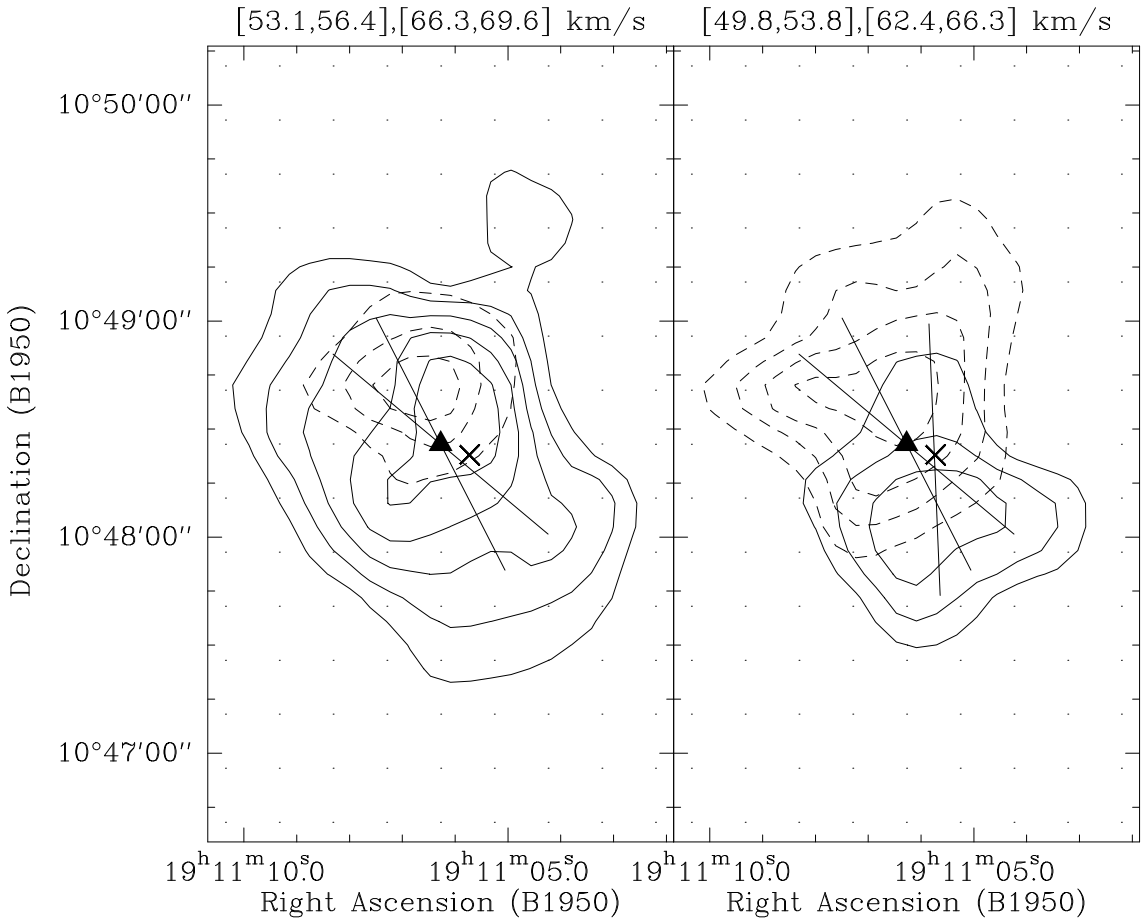

Figure 5.9: Channel maps of the CO J=3→2 transition with blueshifted emission (45 to 55 km s^{-1}) shown in solid contours and redshifted emission (65 to 75 km s^{-1}) shown in dashed contours (30 to 70 by 10 K km s^{-1}). The UCHII region G45.12+0.13 is marked by the triangle and the second outflow origin G45.12+0.13 West is marked by the cross.

The CS 7→6 map shown in Fig. 5.10 traces the warm, dense molecular core which is elongated parallel to the separation of the two outflow sources. The UCHII region G45.12+0.13 lies closest to the peak CS emission and may be the main heating source of the gas. The other outflow origin G45.12+0.13 West lies along the ridge near the edge of the core.

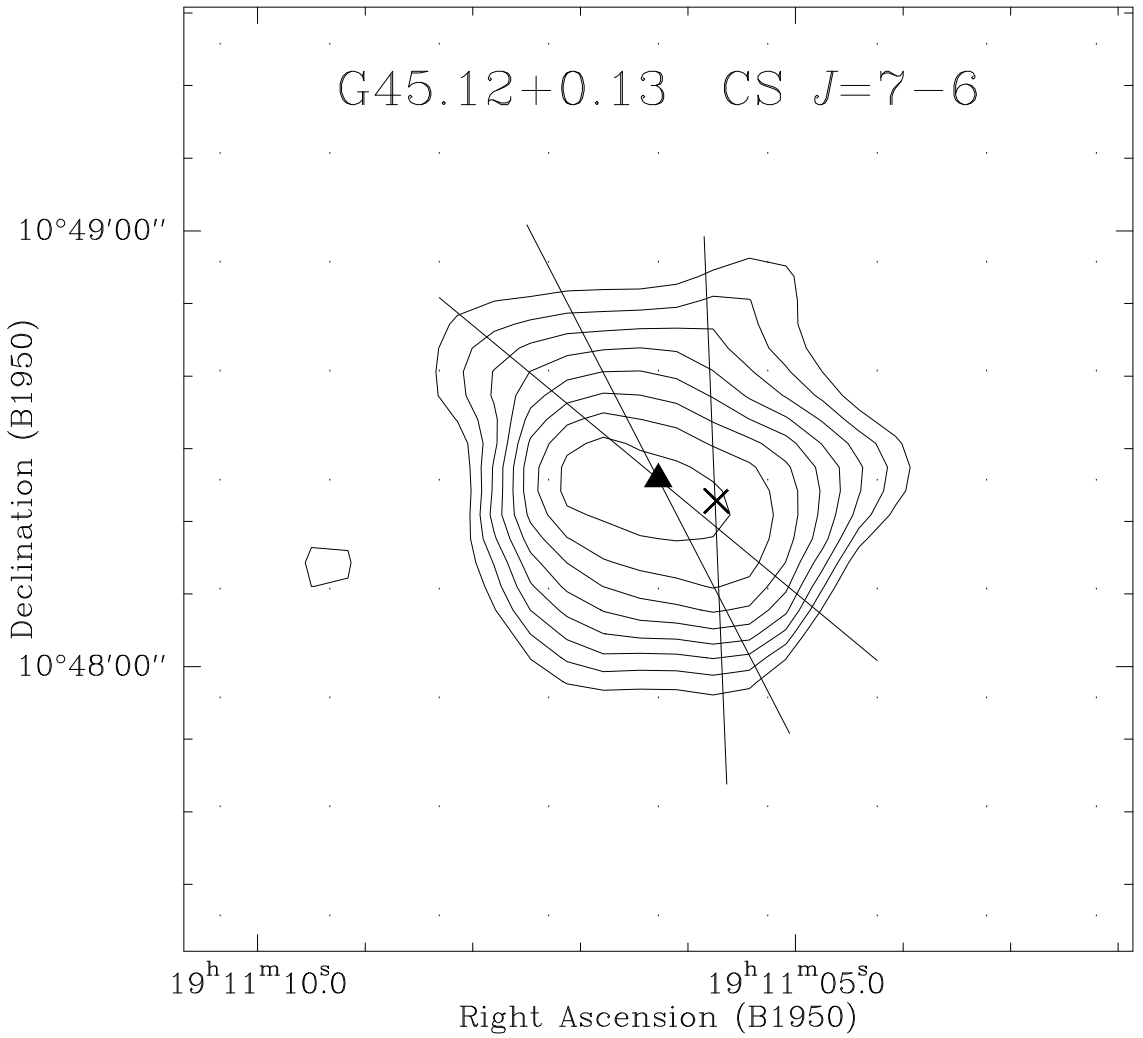

Figure 5.10: Contour map of the integrated CO J=7→6 transition with contour levels 5 to 12 by 1 km s^{-1}. The UCHII region G45.12+0.13 is marked by the triangle and the second outflow origin G45.12+0.13 West is marked by the cross.

5.3.2.3 CS 2→1 emission toward G45.07+0.13

The OVRO baseline-averaged spectrum of CS J=2→1 toward G45.07+0.13 is shown in Fig. 5.11. A broad blueshifted wing indicates molecular outflow while a redshifted absorption feature suggests infalling motion in the foreground gas.

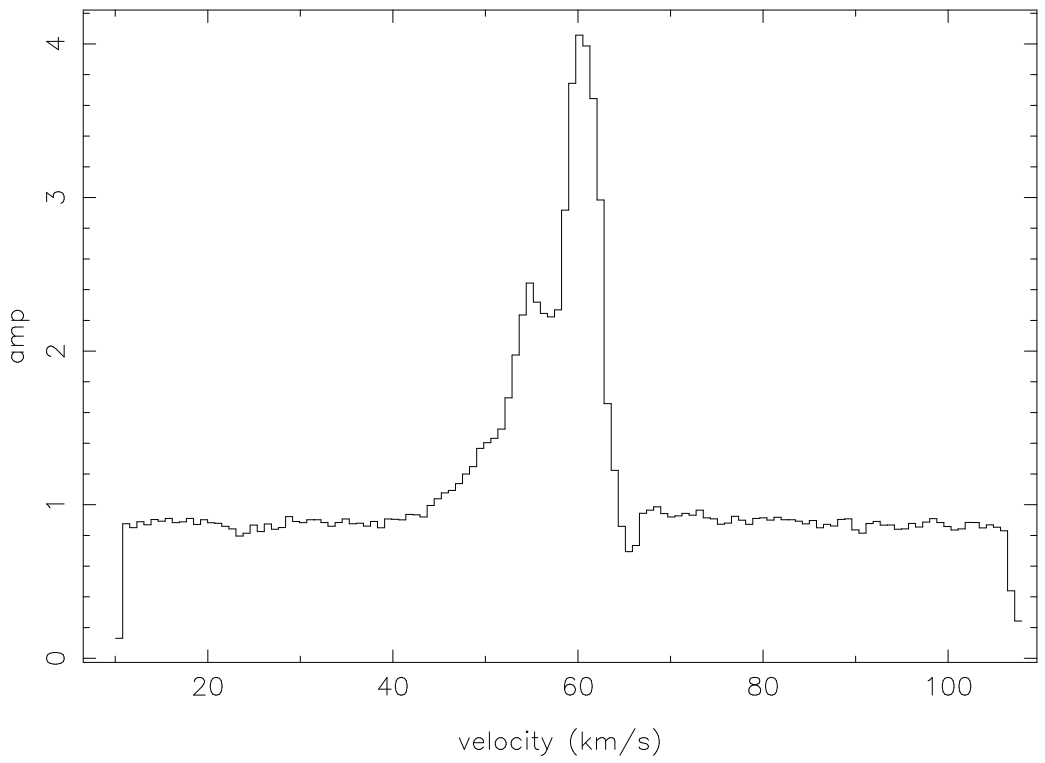

Figure 5.11: The OVRO baseline-averaged spectrum of the CS J=2→1 transition observed toward G45.07+0.13. The amplitude unit is Janskys.

Contour maps of the high velocity CS emission are shown in Fig. 5.12. The spatial offset between the red and blueshifted emission matches the structure seen in the CO J=6→5 transition and provides further evidence for molecular outflow from the UCHII region along a position angle of $-30°$. Redshifted absorption appears against the continuum source in the three channels covering 65.0 to 67.3 km s^{-1}. The curved appearance of the lowest positive contours around the UCHII region indicates that some of the redshifted CS gas lies in front of the source and is infalling. At this spatial resolution, the outflow appears to have a large opening angle. In contrast to

the outflows toward G45.12+0.13, the high velocity gas is not very extended ($\sim 6''$). The outflow dynamical timescale is 2.0×10^4 yr, nearly an order of magnitude less than the G45.12+0.13 outflows. Consequently, the outflow driving source of G45.07+0.13 is likely to be a younger object than either G45.12+0.13 or G45.12+0.13 West.

Interestingly, the velocity pattern of the H_2O masers on a $1''$ scale imaged at the VLA (Hofner 1996a) roughly matches the orientation and direction of the outflow seen here in thermal CO and CS molecular gas on a $5''$ scale. This agreement strongly supports the theoretical ideas that a protostellar jet from a massive young star can (concurrently) power H_2O masers (Mac Low et al. 1994) and drive a molecular outflow (Masson & Chernin 1993). In this case, it appears that the H_2O masers originate in the warm, dense gas located in between the jet shock and the leading bow shock (Blondin, Königl & Fryxell 1989), interior to the brightest CS J=2→1 emission.

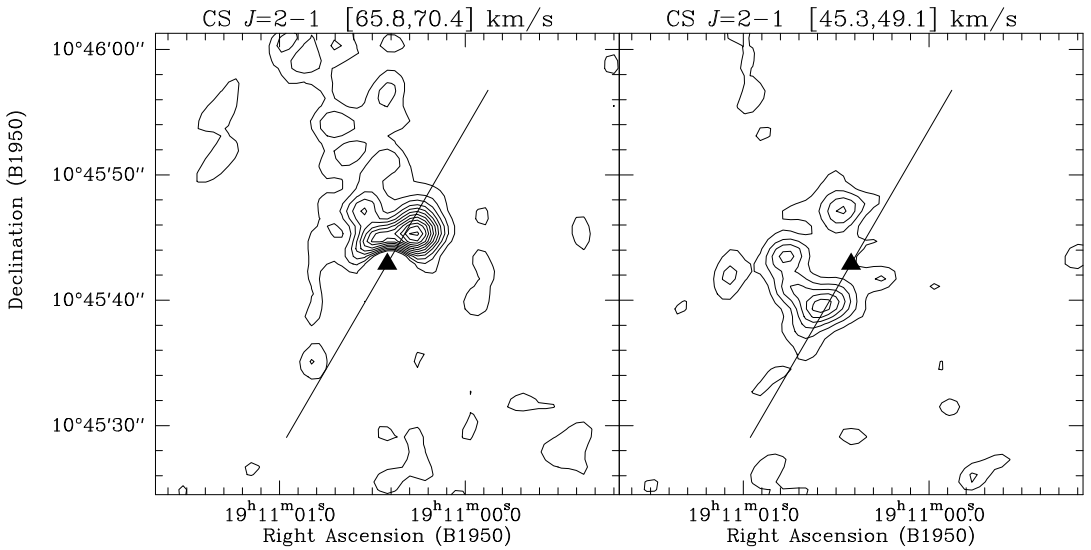

Figure 5.12: *Left panel:* redshifted (65.8-70.4 km s^{-1}) emission of the CS J=2→1 transition observed with a $2\farcs7 \times 2\farcs1$ synthesized beam. Contour levels are 0.05 to 0.60 by 0.05 Jy beam^{-1} (dashed contours represent negative emission). The outflow axis is plotted at a position angle of $-30°$. *Right panel:* Same as the left panel for the blueshifted (45.3-49.1 km s^{-1}) emission.

5.4 Continuum emission

5.4.1 CSO maps

Maps of the submillimeter continuum emission at 800, 450 and 350μm are shown in Fig. 5.13. Like the $C^{18}O$ 2→1 line, the submillimeter continuum emission from G45.12+0.13 peaks a few arcseconds northeast of the UCHII region. In the 450μm map, a ridge of emission extends to the southwest of the UCHII region and contains the outflow source G45.12+0.13 West identified in the OVRO maps, adding weight to our identification of the separate outflow source G45.12+0.13 West. Toward G45.07+0.13, the submillimeter emission is compact and coincides with the UCHII region, in agreement with the 800μm findings of Sandell (1994).

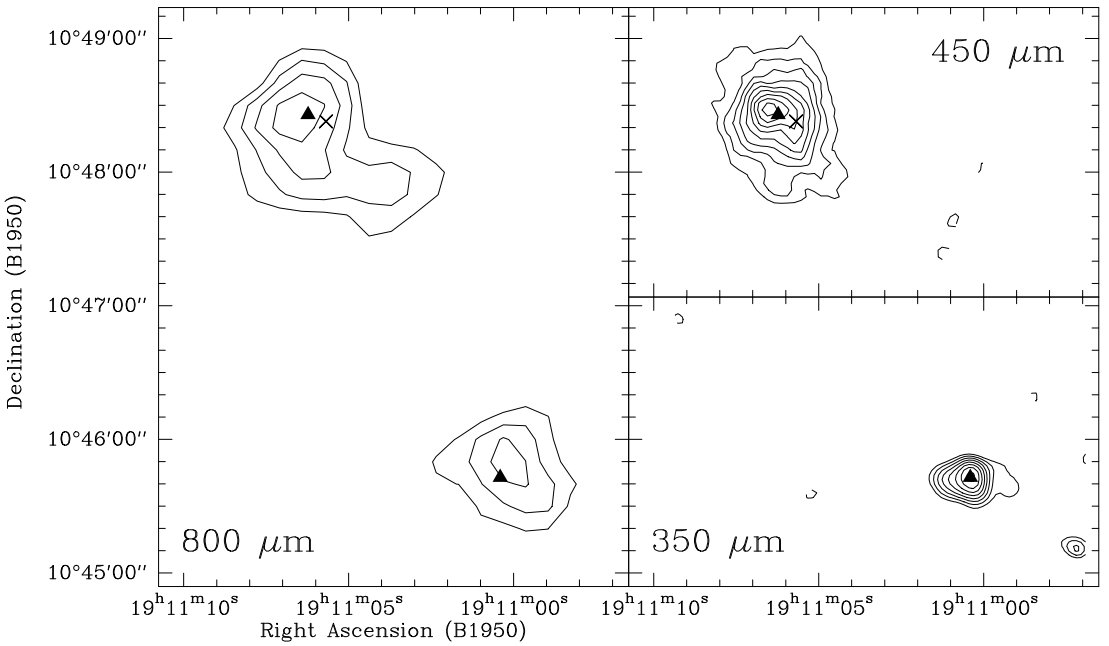

Figure 5.13: Contour maps of the 800, 450 and 350μm continuum emission of the region. Contour levels are 6 to 14 by 2 Jy at 800 μm; 12 to 44 by 4 Jy at 450μm; and 32 to 88 by 8 Jy at 350μm. The UCHII regions G45.12+0.13 and G45.07+0.12 are marked by triangles and the outflow source G45.12+0.13 West is marked by a cross.

The integrated continuum fluxes of both regions are listed in Table 5.7. Combining these fluxes with the 60 and 100μm IRAS fluxes and the 1.3 mm flux (Chini et al. 1986), a modified Planck function of some finite optical depth can be fit to the spectral energy distribution. The three free parameters in the model are the dust temperature

Source	Frequency (GHz)	Integrated Flux (Jy)	Instrument
G45.12+0.13	110	4.00 ± 0.02	OVRO
	380	31 ± 3	CSO
	851	680 ± 50	SHARC
G45.07+0.13	98	1.04 ± 0.01	OVRO
	380	21 ± 3	CSO
	851	360 ± 50	SHARC

Table 5.7: Millimeter and submillimeter continuum fluxes of G45

$T_{\rm dust}$, the grain emissivity index β, and optical depth τ at the reference wavelength of 125μm. The grain emissivity at 125μm was matched to the value of Hildebrand (1983). A summary of the best-fit models is listed in Table 5.8. The mass estimate from the dust, $3.7 \times 10^4 M_\odot$, is remarkably consistent with that derived from the $C^{18}O$ 2$\rightarrow$1 emission.

Source	$T_{\rm dust}$(K)	β	$\tau_{125\mu{\rm m}}$	$\log(M/M_\odot)$	$\log(L/L_\odot)$
G45.12+0.13	30	2.15	0.55	4.57	5.75
G45.07+0.13	42	1.90	0.73	3.89	5.77

Table 5.8: Greybody model parameters of G45.12+0.13 and G45.07+0.13

5.4.2 3 millimeter OVRO maps

The 110 GHz emission observed at OVRO is shown in Fig. 5.14. The only source reliably detected in the field is located at $\alpha = 19^h11^m06.^s239, \delta = +10°48'25.''04$, consistent with the radio position of the UCHII region (Wood & Churchwell 1989). The deconvolved size of a single two-dimensional Gaussian fit to this source is $2.''67 \times 2.''00$ at position angle 127°. The major axis of the UCHII emission is oriented roughly perpendicular to the bipolar molecular outflow axis from the UCHII region. The peak intensity is 2.13 Jy/beam and the integrated flux density is 4.00 Jy. Since the integrated flux at 15 GHz is 3.68 Jy (Wood & Churchwell 1989), the spectral index between 15 and 110 GHz is 0.04. Extrapolation from the submillimeter spectral index implies that ~ 0.4 Jy of the 110 GHz flux is from optically-thin dust emission. Subtracting this dust emission from the 110 GHz flux then implies that the spectral

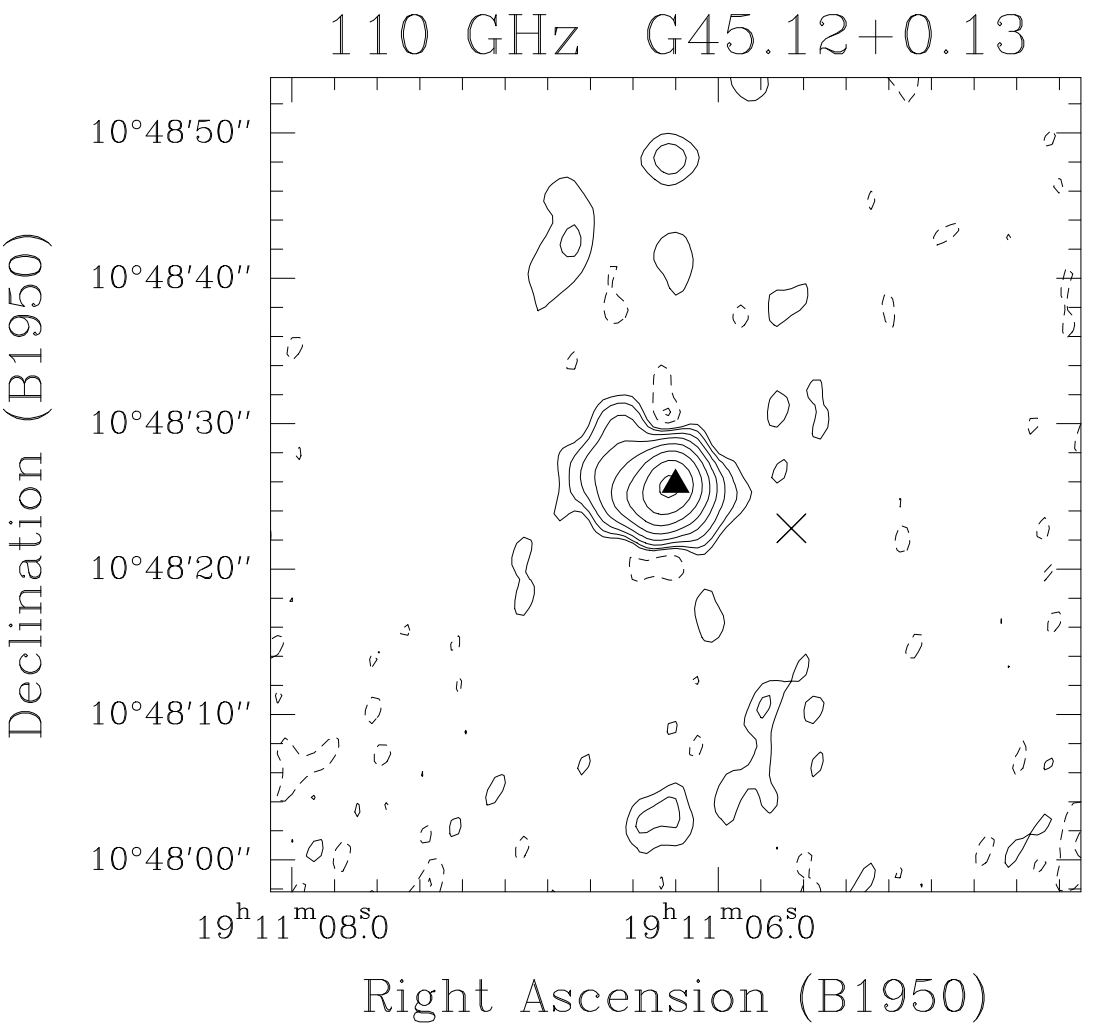

Figure 5.14: Contour map of the 110 GHz continuum emission observed toward G45.12+0.13 with a 2.″6 × 2.″4 synthesized beam. Contour levels are -10, 10, 20, 30, 120, 240, 480, 960 and 1920 mJy/beam with a peak intensity of 2.13 Jy/beam. The UCHII region G45.12+0.13 is marked by the triangle and the outflow source G45.12+0.13 West is marked by the cross.

index of the remaining emission between 15 and 110 GHz is 0.0, reasonably consistent with optically-thin free-free emission.

No emission is seen at the suspected position of the outflow source G45.12+0.13 West down to a 3σ level of 15 mJy. In the 450μm map, G45.12+0.13 West lies on the 36 Jy contour. To estimate an upper limit to the flux of a point source at this position, an elliptical Gaussian source was freely-fitted and removed from a subset of the 450μm image containing the emission around G45.12+0.13. The residual map contained a

peak intensity of 14 Jy/beam in a compact source essentially coincident with the UCHII region with a tail extending past the position of G45.12+0.13 West. Based on the model spectral energy distribution, this limit corresponds to an 8 mJy dust source at 110 GHz. Therefore, we cannot detect the source at 110 GHz with the present data. More sensitive (i.e., higher dynamic range) millimeter observations will be necessary.

The 98 GHz map of G45.07+0.13 is presented in Fig. 5.15. The peak intensity of the central source is 0.95 Jy beam^{-1} and the integrated flux density is 1.04 Jy. The fitted position of a single Gaussian model is $\alpha = 19^h11^m00.^s405, \delta = +10°45'43''.00$ with a deconvolved source size of $0''.96 \times 0''.50$ at position angle 96°. In this case, the major axis is 54° away from the axis of the CS 2→1 molecular outflow. Extrapolation from the submillimeter spectral index implies that ∼0.2 Jy of the 98 GHz flux is from optically-thin dust emission. Subtracting this flux yields 0.84 Jy of free-free emission, and a spectral index of 0.2 between 43 GHz and 98 GHz (Wood et al. 1988). Compared to G45.12+0.13, the continuum emission is three times more compact. The contrast in sizes presents another piece of evidence that G45.07+0.13 is a younger source whose central star is just beginning to ionize the molecular gas and heat the surrounding dust envelope.

5.5 Discussion

5.5.1 The nature of the multiple outflows of G45.12+0.13

In G45.12+0.13, the single dish and interferometer data show evidence for at least two separate bipolar outflows. The total mass swept up by these outflows is quite large, $M \sim 4800 M_\odot$, and their dynamical timescale is rather long at $\sim 2 \times 10^5$ yr. The age of the outflows may be even older than the dynamical timescale as rapid deceleration of the outflow may occur during the sweeping-up process of ambient gas (Masson & Chernin 1993). In fact, the absence of H_2O masers in the G45.12+0.13 cloud core suggests that both of the outflow sources have evolved beyond the H_2O maser phase.

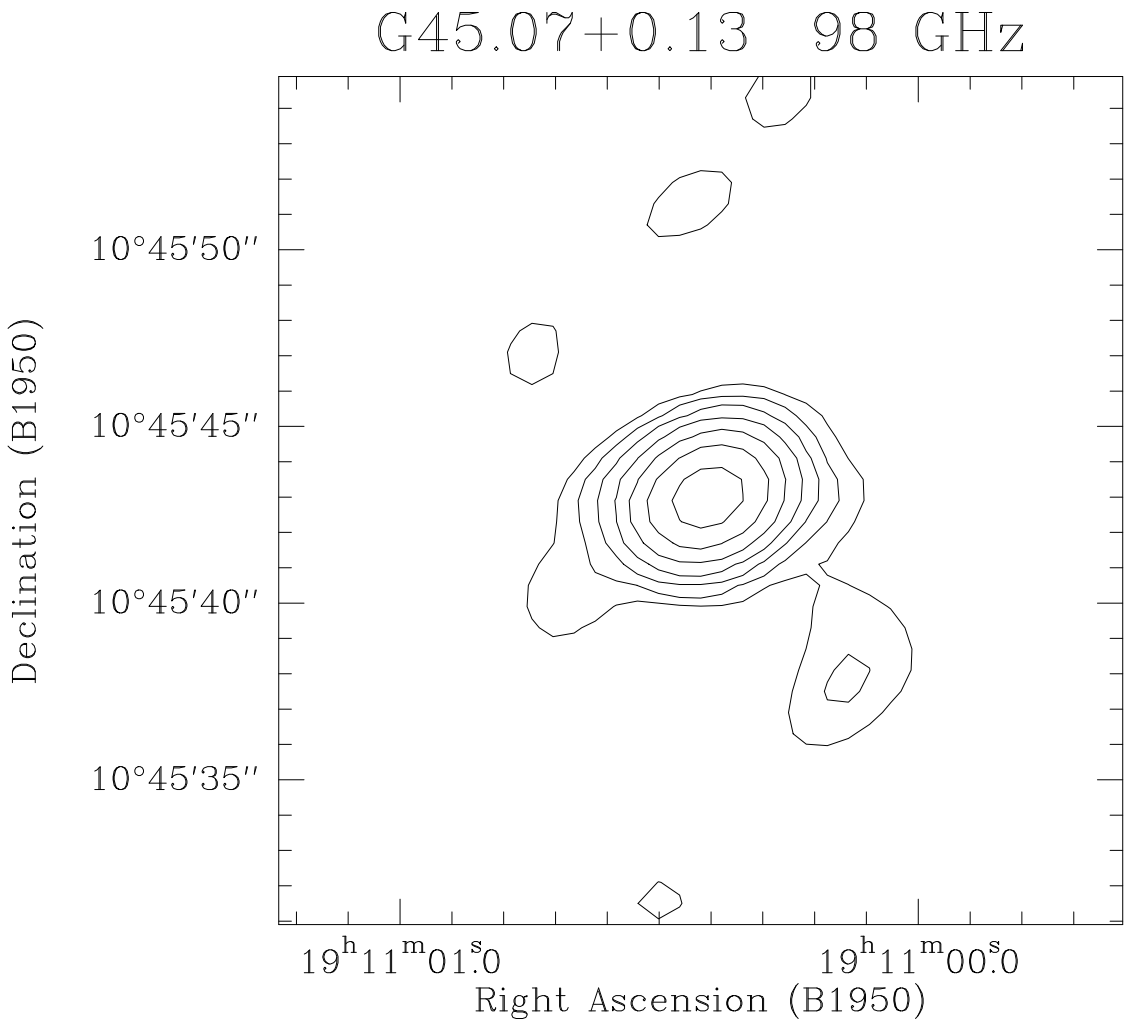

Figure 5.15: Contour map of the 98 GHz continuum emission observed toward G45.07+0.13 with a 2.″7 × 2.″1 synthesized beam. Contour levels are 10, 20, 40, 80, 160, 320 and 640 mJy/beam with a peak intensity of 950 mJy/beam.

Statistical studies of masers toward HII regions indicate that H_2O masers are much more common during the earliest phases of formation of an HII region (Codella et al. 1995) and last perhaps a few $\times 10^4$ yr (Codella, Felli & Natale 1994). Because neither of the driving sources is located exactly on the highest column density of the dust/$C^{18}O$ core, there seems to exist additional material for future star formation there. The CS 7→6 linewidth at the core of G45.12+0.13 is 5.03 km s $^{-1}$, implying a virial mass of only $2600 M_\odot$ within a 20″ beam. Since the virial mass falls a factor of 10 short of the total gas mass computed from the submillimeter dust and $C^{18}O$ 2→1 measurements, the molecular cloud is not sufficiently supported against further

collapse. The UCHII region and the outflow source G45.12+0.13 West may represent the result of the first major burst of star formation in this molecular cloud.

From the agreement of the outflow energetics with trends from lower mass examples, we can conclude that these outflows differ only in scale from lower mass outflows and likely share the same driving mechanism at the central star. Recently, theories of jet-driven molecular outflows (Masson & Chernin 1993; Raga et al. 1993) have been put forth to unify the observed phenomena of stellar jets and molecular outflows as manifestations of the same flow seen over different length scales and integrated over different timescales. As high mass analogues of low mass outflows, the outflows of G45 and other massive sources like G25.65+1.05 and G240.31+0.31 (Shepherd & Churchwell 1996a) indicate that these unified theories may apply over the entire mass range of protostellar outflows.

5.5.2 Age contrast between G45.12+0.13 and G45.07+0.13

In G45.07+0.13, both the CO 6→5 and the CS 2→1 maps indicate bipolar outflow from the UCHII region. The lower antenna temperatures from the high-J CO lines suggest that the bulk of the gas is cooler than it is in G45.12+0.13. The energy and momentum in the G45.07+0.13 outflow is significantly lower than the G45.12+0.13 outflows. Specifically, the momentum input rate in the G45.07+0.13 outflow is roughly equal to the amount available from the radiation field while the outflow mechanical luminosity ($22L_{\odot}$) is only $2 \times 10^{-6} L_{\rm bol}$. In addition, the CS 2→1 map reveals redshifted absorption toward the UCHII region. In fact, this absorption manifests itself in the low-J single-dish CO spectra as a steep drop in emission near 65 km s^{-1}. Interestingly, this drop is not present in the CO 6→5 transition despite the smaller beamsize. Apparently, very little of the absorbing gas exists in the J=5 state; therefore, it must be cooler than the outflowing gas. With this evidence, we attribute this absorption feature to cool infalling gas.

We propose that G45.07+0.13 exists in a (perhaps brief) phase in which both outflow and infall are occurring simultaneously. The smaller momentum, shorter

timescale, smaller amount of swept-up mass and the presence of H_2O masers suggest that the G45.07+0.13 outflow is younger than the outflows in the G45.12+0.13 region. Also, the agreement of the molecular outflow in both position angle and velocity with the H_2O masers imply that both phenomena are being powered concurrently in G45.07+0.13 with the masers forming at the inner edges of the outflow lobes at the site of the shocked, dense gas.

Further evidence for the age distinction between the two regions comes from the submillimeter continuum images. Toward G45.12+0.13, at least two sources are present in a region of extended dust emission with the peak emission coinciding with the $C^{18}O$ molecular core to the northeast of G45.12+0.13. In contrast, an unresolved dust core is seen toward G45.07+0.13, consistent with the conclusion that G45.12+0.13 is a more evolved region in which the dust and gas have been heated over a greater volume.

5.6 Conclusions

With extensive high resolution molecular line and (sub)millimeter continuum observations of the ultracompact HII regions G45.12+0.13 and G45.07+0.13, we present a detailed picture of massive star formation toward these regions. We have discovered bipolar molecular outflows from both sources, marking them as members of a growing class of UCHII regions observed to exhibit this phenomenon. In G45.12+0.13, the single-dish CSO maps reveal a main north/south bipolar outflow with additional complicated structure. OVRO aperture-synthesis images resolve the system into at least two outflows. The highest velocity outflow appears centered on the UCHII region which is embedded in an extended near-infrared Brγ nebula. We identify an additional bipolar outflow with a dynamical center lying offset $(-8'', -3'')$ from the UCHII region. This source, called G45.12+0.13 West, can be identified with extended 450μm emission that most likely represents dust emission from a younger or lower mass protostar that formed during the same epoch as the ionizing star of the UCHII region. From these observations it is apparent the molecular cloud core

containing G45.12+0.13 has already formed a number of stars.

In contrast, G45.07+0.13 exhibits a single, compact outflow observed in the CO 6→5 line emerging from a dense core traced by bright CS 7→6 emission. OVRO observations of the CS 2→1 line confirm that the origin of the bipolar outflow is centered on the UCHII region and that its axis is aligned spatially and kinematically with the H_2O maser spots in this source. Redshifted absorption at 6 km s^{-1} in the CS and low-J CO lines is seen toward the continuum peak which is identified with an unresolved 350μm source. These phenomena along with the more compact radio continuum emission and the presence of H_2O masers lead us to conclude that G45.07+0.13 is in an earlier evolutionary phase in which both infall and outflow are visible and only a single prominent star has been formed. More sensitive infrared images and (sub)millimeter synthesis maps of both regions will be required to confirm the identification of the young stars powering the molecular outflows and heating the dust grains.

Chapter 6 Summary

In this dissertation, I explore the phenomenon of massive star formation in the Galaxy via a submillimeter imaging survey of UCHII regions. After describing the design and performance of the bolometer array camera (SHARC) now operating at the CSO, I present submillimeter continuum images of 17 UCHII regions which show that the dust emission peaks at or near the position of the compact radio source. Often associated with H_2O masers, outlying cores of dust typically lie on the periphery of the main core. The flux measurements from the submillimeter images are combined with 800μm measurements, IRAS 100μm fluxes and millimeter fluxes from the literature to obtain greybody models of the spectral energy distribution. The average dust temperature in the 14 UCHII regions with complete wavelength coverage is 40 ± 10 K. The average grain emissivity index (β) in the 14 regions is 2.00 ± 0.25, very consistent with previous studies based solely on 1.3 mm and IRAS fluxes.

Radiative transfer simulations of dust clouds with power-law density profiles can successfully model the observed submillimeter flux profile of the UCHII regions. However, the models presented here may not be unique due to the uncertainty in the radius of the outer source boundary (which was fixed from the images rather than properly modeled). Of the 11 regions will $L_{\rm bol} > 10^{4.5} L_\odot$, three resemble the isothermal sphere profile ($n(r) \propto r^{-2}$), four exhibit the profile of dynamical collapse ($n(r) \propto r^{-3/2}$), two resemble an isothermal sphere in the outer part of the cloud and approach the collapse profile toward the inner part, and two regions exhibit a shallower profile ($n(r) \propto r^{-1}$) indicative of a cluster of sources. This evidence for collapse in more than half of the UCHII regions bolsters the collapse interpretation from spectral line observations of many UCHII regions in the literature. A good correlation exists between the density profile, the dust luminosity to mass ratio and the dust temperature. The most centrally-condensed sources exhibit the warmest dust and the high luminosity to mass ratios, indicative of a higher star formation rate.

In addition to the dust continuum images, many of the UCHII regions have been mapped in the J=3→2 or 2→1 rotational transitions of CO in search of molecular outflows. Of the 17 UCHII regions mapped in CO, 15 show evidence for bipolar outflows in the form of a spatial offset between the redshifted and blueshifted emission centered about a position within 10″ of the peak radio position. In some cases, separate outflows can be identified with different compact radio sources in the same general region. The mechanical luminosity and mass outflow rate of the outflows follow the scaling relations with bolometric luminosity established for less luminous sources by Levreault (1988). In contrast to less luminous sources, the momentum supply rate required to drive the molecular outflows from UCHII regions is comparable to that available from the radiation, field demonstrating that accretion disk winds are eventually dominated by radiation pressure.

Perhaps the most striking aspect of the data presented in this thesis is the inevitably complex appearance of massive star-forming regions due to the presence of a cluster of young stars forming from multiple dust cores and driving multiple outflows. However, the general appearance of the regions seem to be similar when observed on different size scales. Distant sources like the G34.3+0.2 complex are found to contain several molecular cores of a few hundred to a thousand solar masses. If one could observe one of these cores at higher angular resolution, it would probably look like the nearby Mon R2 core which is shown here to contain dozens of clumps of a few tens of solar masses in addition to the main core. As shown in Chapter 5, a similar hierarchy exists in the molecular outflow observations. A distant source like G45.12+0.13 appears to have a single giant outflow when observed at 30″ resolution; but when the resolution is increased by a factor of 10, the outflow breaks up into multiple individual outflows similar to those seen from nearby, isolated protostars. Both of these findings suggest a scale-invariant appearance of massive protostellar clusters. This idea will no doubt be further tested in the future by combining wide-field surveys from instruments like SHARC (and heterodyne array receivers) with high resolution studies from millimeter and submillimeter interferometers.

References

Aannestad, P.A. 1975, ApJ, 200, 30

Adams, F.C. 1991, ApJ, 382, 544

Adams, F.C., Lada, C.J. & Shu, F.H. 1987, ApJ, 312, 788

Agladze, N.I., Sievers, A.J., Jones, S.A., Burlitch, J.M. & Beckwith, S.V.W. 1996, ApJ, 462, 1026

Akeson, R.L. & Carlstrom, J.E. 1996, ApJ, in press

André, P., Ward-Thompson, D. & Motte, F. 1996, A&A, in press

André, P., Ward-Thompson, D. & Barsony, M. 1993, ApJ, 406, 122

Andriesse, C.D. 1974, A&A, 37, 257

Anglada, G., Estalella, R., Pastor, J., Rodríguez, L.F. & Haschick, A.D. 1996, ApJ, 463, 205

Armand, C., Baluteau, J.-P., Joubert, M., Gry, C. & Cox, P. 1996, A&A, 306, 593

Arquilla, R. & Goldsmith, P.F. 1984, ApJ, 279, 664

Aspin, C. & Walther, D.M. 1990, A&A, 235, 387

Aumann, H.H., Fowler, J.W. & Melnyk, M. 1990, AJ, 99, 1674

Bachiller, R. 1996, ARAA, 34, 111

Bachiller, R., Fuente, A. & Tafalla, M. 1995, ApJ, 445, L51

Bachiller, R., Guilloteau, S., Dutrey, A., Planesas, P. & Martin-Pintado, J. 1995, A&A, 299, 957

Bachiller, R., Terebey, S., Jarrett, T., Martin-Pintado, J., Beichman, C.A. & Van Buren, D. 1994, ApJ, 437, 296

Bachiller, R., & Gómez-González, J. 1992, A&A Review, 3, 257

Bachiller, & Cernicharo, 1990, A&A, 239, 276

Bally, J. & Lada, C.J. 1983, ApJ, 265, 824

Barsony, M. in Clouds, Cores, and Low Mass Stars, eds. D.P. Clemens & R. Barvainis, (San Francisco: ASP), 197

Beckwith, S., Evans II, N.J., Becklin, E.E. & Neugebauer, G.X. 1976, ApJ, 208, 390

Beech, M. & Mitalas, R. 1994, ApJS, 95, 517

Beichman, C.A., Myers, P.C., Emerson, J.P., Harris, S., Mathieu, R., Benson, P.J. & Jennings, R.E. 1986, ApJ, 307, 337

Beichman, C.A., Becklin, E.E. & Wynn-Williams, C.G. 1979, ApJ, 232, L47

Bence, S.J., Richer, J.S. & Padman, R. 1996, MNRAS, 279, 866

Benford, D.J. 1996, private communication

Benford, D.J., Hunter, T.R. & Phillips, T.G. 1996, in preparation

Benson, J.M. & Johnston, K.J. 1984, ApJ, 277, 181

Bertie, J.E., Labbé, H.J. & Whalley, E. 1969, J. Chem. Phys., 50, 10

Bevington, P.R. 1969, Data Reduction and Error Analysis for the Physical Sciences, (New York: McGraw-Hill), p. 204

Birch, J.R. 1990, Infr. Phys., v. 30, n. 2, p. 195

Birch, J.R., Dromey, J.D. & Lesurf, J. 1981, Infr. Phys., 21, 225

Blake, G.A., Sutton, E.C., Masson, C.R., & Phillips, T.G. 1987, ApJ, 315, 621

Blandford, R.D. & Rees, M.J. 1974, MNRAS, 169, 395

Blauuw, A. 1964, ARAA, 2, 261

Blondin, J.M., Königl, A. & Fryxell, B.A. 1989, ApJ, 337, L37

Bodenheimer, P., Tenorio-Tagle, G. & Yorke, H.W. 1979, ApJ, 233, 85

Bodenheimer, P. & Sweigart, A. 1968, ApJ, 152, 515

Bonnor, W.B. 1956, MNRAS, 116, 351

Boss, A.P. 1987, ApJ, 316, 721

Brand, J., Cesaroni, R., Caselli, P., Catarzi, M., Codella, C. et al. 1994, A&AS, 103, 541

Bussone, D.D. 1989, in Modern Plastics Encyclopedia 1989, (New York: McGraw-Hill), p. 66

Butner, H.M., Evans, N.J., Lester, D.F., Levreault, R.M. & Strom, S.E. 1991, ApJ, 376, 636

Cabrit, S. & Bertout, C. 1990, ApJ, 348, 530

Campbell, M.F., Lester, D.F., Harvey, P.M. & Joy, M. 1989, ApJ, 345, 298

Carpenter, J. 1996, private communication

Carpenter, J.M., Snell, R.L. & Schloerb, F.P. 1990, ApJ, 362, 147

Cato, B.T., Rönnäng, B.O., Rydbeck, O.E.H., Lewin, P.T., Yngvesson, K.S., Cardiasmenos, A.G. & Shanley, J.F. 1976, ApJ, 208, 87

Cernicharo, J. & Reipurth, B. 1996, ApJ, 460, L57

Cernicharo, J., Thum, C., Hein, H., John, D., Garcia, P. & Mattioco, F. 1990, A&A, 231, L15

Cernicharo, J., Bachiller, R. & Duvert, G. 1985, A&A, 149, 273

Cesaroni, R., Walmsley, C.M., Kompe, C. & Churchwell, E. 1991, A&A, 252, 278

Cesaroni, R., Walmsley, C.M. & Churchwell, E. 1992, A&A, 256, 618

Cesaroni, R., Churchwell, E., Hofner, P., Walmsley, C.M. & Kurtz, S. 1994, A&A, 288, 903

Cesarsky, C.J, Cesarsky, D.A., Churchwell, E. & Lequeux, J. 1978, A&A, 68, 33

Chandler, C.J., Carlstrom, J.E. & Terebey, S. 1994, in Clouds, Cores and Low Mass Stars, eds. D.P. Clemens & R. Barvainis, (San Francisco: ASP), 241

Chandler, C.J., Moore, T.J.T., Mountain, C.M., & Yamashita, T. 1993, MNRAS, 261, 694

Chernin, L., Masson, C., Gouveia Dal Pino, E.M. & Benz, W. 1994, ApJ, 426, 204

Chiosi, C., Nasi, E. & Sreenivasan, S.R. 1978, A&A, 63, 103

Chini, R., Krügel, E. & Wargau, W. 1987, A&A, 181, 378

Chini, R., Kreysa, E., Mezger, P.G. & Gemünd, H.-P. 1986, A&A, 154, L8

Chini, R., Krügel, E. & Kreysa, E. 1986, A&A, 167, 315

Churchwell, E., Walmsley, C.M. & Wood, D.O.S. 1992, A&A, 253, 541

Churchwell, E., Walmsley, C.M. & Cesaroni, R. 1990, A&AS, 83, 119

Churchwell, E., Wolfire, M.G. & Wood, D.O.S. 1990, ApJ, 354, 247

Clemens, D.P., Sanders, D.B. & Scoville, N.Z. 1988, ApJ, 327, 139

Cochise Instruments, Inc., 6304 deMello Street, Hereford, AZ 85615, (602) 378-6321

Codella, C., Felli, M., & Natale, V. 1994, A&A, 291, 261

Codella, C, Palumbo, G.G.C., Pareschi, G., Scappini, F., Caselli, P. & Attolini, M.R. 1995, MNRAS 276, 57

Cohen, R.J., Rowland, P.R. & Blair, M.M 1984, MNRAS, 210, 425

Colomé, C. & Harvey, P.M. 1995, ApJ, 449, 656

Comerón, F. & Torra, J. 1996, A&A, in press

Conti, P.S., Garmany, C.D., DeLoore, C. & Vanbeveren, D. 1983, ApJ, 274, 302

Cowan, W.D., Levan, P.D., Barnaby, D., Johnson, R.L. & Duncan, T.S. 1995, Proc. SPIE Vol. 2475, p. 236, Infrared Detectors and Instrumentation for Astronomy

Cox, P. & Mezger, P.G. 1989, A&A Rev., 1, 49

Cunningham, C.R. & Gear, W.K. 1990, in SPIE Symposium on Astronomical Telescopes and Instrumentation for the 21st Century

Davis, C.J., Mundt, R., Eisloffel, J. & Ray, T.P. 1995, AJ, 110, 766

de Geus, E.J. & Burton, W.B. 1991, A&A, 246, 559

Deharveng, L., Zavagno, A., Cruz-González, I., Salas, L., Caplan, J. & Carrasco, L. 1996, A&A, in press

DePree, C.G., Goss, W.M., Palmer, P. & Rubin, R.H. 1994, ApJ, 428, 670

DePree, C.G., Rodríguez, L.F. & Goss, W.M. 1995, RevMexAA, 31, 39

DePree, C.G. 1996, private communication

DeYoung, D.S. 1986, ApJ, 307, 62

Dickel, H.R., Lubenow, A.F., Goss, W.M. & Rots, A.H. 1984, A&A, 135, 107

Doherty, R.M., Puxley, P., Doyon, R. & Brand, P.W.J.L. 1994, MNRAS, 266, 497

Downes, D., Genzel, R., Moran, J.M., Johnston, K.J., Matveyenko, L.I., Kogan, L.R., Kostenko, V.I. & Rönnáng, B. 1979, A&A, 79, 233

Downey, P.M., Jeffries, A.D., Meyer, S.S., Weiss, R., Bachner, F.J. et al. 1984, Appl. Op., 23, 910

Draine, B.T. & McKee, C.F. 1993, ARAA, 31, 373

Draine, B.T. & Lee, H.M. 1984, ApJ, 285, 89

Dreher, J.W. & Welch, W.J. 1981, ApJ, 245, 857

Dyck, H.M. & Simon, T. 1977, ApJ, 211, 421

Egan, M.P., Leung, C.M. & Spagna, G.F. 1988, Comp. Phys. Comm., 48, 271

Eldridge, J.E. 1991, in Handbook of Optical Constants of Solids II, ed. E.D. Palik, p. 853

Elitzur, M. 1992, Astronomical Masers, (Dordrecht: Kluwer)

Elston, R., 1991, ed., Astrophysics with Infrared Arrays, ASP Conf. Ser., v. 14, (San Francicso: ASP)

Emerson, D.T., Klein, U. & Haslam, C.G.T. 1979, A&A, 76, 92

Emerson, D.T. & Payne, J.M. eds. Multi-feed systems for radio telescopes : workshop held 16-18 May 1994, Tucson, Arizona (San Francicso: Astronomical Society of the Pacific), 1995

Emerson & Cuming, Inc., Woburn, MA 01888

Evans, N.J. II 1989, Rev. Mex. A&A, 18, 21

Fellgett, P., Jones, R. Clark & Twiss, R.Q. 1959, Nature, 4691, 967

Felli, M. 1996, private communication

Fey, A.L., Gaume, R.A., Claussen, M.J. & Vrba, F.J. 1995, ApJ, 453, 308

Fey, A.L., Gaume, R.A., Nedoluha, G.E. & Claussen, M.J. 1994, ApJ, 435, 738

Fey, A.L., Claussen, M.J., Gaume, R.A., Nedoluha, G.E. & Johnston, K.J. 1992, AJ, 103, 234

Fisher Scientific 1995, Fair Lawn, NJ 07410, (201) 796-7100

Forster, J.R. & Caswell, J.L. 1989, A&A, 213 339

Foster, P.N. & Chevalier, R.A. 1993, ApJ, 416, 303

Fouquet, J.E. & Reid, M.J. 1982, AJ, 87, 691

Frerking, M.A., Langer, W.D. & Wilson, R.W. 1982, ApJ, 262, 590

Fukui, Y., Iwata, T., Mizuno, A., Bally, J. & Lane, A. 1993, in Protostars & Planets III, eds. E.H. Levy & J.I. Lunine, (Tucson: University of Arizona Press), 603

Fukui, Y., Iwata, T., Mizuno, A., Bally, J. & Lane, A.P. 1991, in Protostars and Planets III, eds. E.H. Levy & J. Lunine, (University of Arizona Press)

Fukui, Y. 1989, in ESO Workshop on Low mass star formation and pre-main sequence objects, ed. B. Reipurth

Garay, G., Reid, M.J. & Moran, J.M. 1985, ApJ, 289, 681

Garay, G., Rodríguez, L.F., Moran, J.M. & Churchwell, E. 1993, ApJ, 418, 368

Garay, G. & Rodríguez, L.F. 1990, ApJ, 362, 191

García-Segura, G. & Franco, J. 1996, ApJ, in press

Garden, R.P. & Carlstrom, J.E. 1992, ApJ, 392, 602

Garden, R.P., Hayashi, M., Gatley, I., Hasegawa, T. & Kaifu, N. 1991, ApJ, 374

Garden, R.P., Russell, A.P.G. & Burton, M. 1990, ApJ, 354, 232

Gaume, R.A., Fey, A.L. & Claussen, M.J. 1994, ApJ, 432, 648

Gaume, R.A., Claussen, M.J., DePree, C.G., Goss, W.M. & Mehringer, D.M. 1995, ApJ, 449, 663

Genzel, R., Reid, M.J., Moran, J.M. & Downes, D. 1981, ApJ, 244, 884

Genzel, R. & Downes, D. 1979, A&A, 72, 234

Genzel, R. & Downes, D. 1977, A&AS, 30, 145

Georgelin, Y.M. & Georgelin, Y.P. 1976, A&A, 49, 57

Gezari, D.Y., Schmitz, M., Pitts, P.S. & Mead, J.M. 1993, Catalog of Infrared Observations, 3rd ed., NASA Reference Publications 1294

Gezari, D.Y., Folz, W.C., Woods, L.A. & Varosi, F. 1992, PASP, 104, 191

Gezari, D.Y., Joyce, R.R. & Simon, M. 1973, ApJ, 179, L67

Giovanardi, C., Lizano, S., Natta, A., Evans, N.J. & Heiles, C. 1992, ApJ, 397, 214

Goldreich, P. & Kwan, J. 1974, ApJ, 189, 441

Gómez, J.F., Torrelles, J.M., Estalella, R., Anglada, G., Verdes-Montenegro, L. & Ho, P.T.P. 1992, ApJ, 397, 492

Gonata, C.P., Palmer, P. & Novak, G. 1992, ApJ, 398, 118

Gordon, M.A. 1988, ApJ, 331, 509

Goss, W.M., Lockhart, I.A., Fomalont, E.B. & Hardebeck, E.G. 1973, ApJ, 183, 843

Gürtler, J., Henning, Th., Krügel, E. & Chini, R. 1991, A&A, 252, 801

Güsten, R. & Marcaide, J.M. 1986, A&A, 164, 342

Güsten, R., Chini, R. & Neckel, T. 1984, A&A, 138, 205

Gwinn, C.R., Moran, J.M. & Reid, M.J. 1992, ApJ, 393, 149

Gyulbudaghian, A.L., Glushokov, Y.I. & Denisyuk, E.K. 1978, ApJ, 224, L137

Hadni, A., Claudel, J., Décamps, E., Gerbaux, X. & Strimer, P. 1962, C.R. Acad. Sci. Paris, 255, 1595

Halpern, M., Gush, H.P., Wishnow, E. & De Cosmo, V. 1986, Appl. Op., v. 25, n. 4, p. 565

Harper, D.A. 1974, ApJ, 192, 557

Hartigan, P., Morse, J. & Raymond, J. 1994, ApJ, 436, 125

Hartmann, L. & Raymond, J.C. 1984, ApJ, 276, 560

Harvey, P.M. & Forveille T. 1988, A&A, 197, L19

Harvey, P.M., Lester, D.F., Brock, D. & Joy, M. 1991, ApJ, 368, 558

Harvey, P.M., Wilking, B.A., Joy, M. & Lester, D.F. 1985, ApJ, 288, 725

Haschick, A.D. & Ho, P.T.P. 1990, ApJ, 352, 630

Haslam, C.G.T. 1974, A&AS, 15, 333

Heaton, B.D., Little, L.T. & Bishop, I.S. 1989, A&A, 213, 148

Helou, G. 1989, in Interstellar Dust, eds. L.J. Allamandola & A.G.G.M. Tielens, p. 285-301

Henning, T., Cesaroni, R., Walmsley, M. & Pfau, W. 1992, A&AS, 93, 525

Henning, Th., Chini,R. & Pfau, W. 1992, A&A, 263, 285

Heyer, M.H., Snell, R.L., Goldsmith, P.F., Strom, S.E. & Strom, K.M. 1986, ApJ, 308, 134

Hildebrand, R.H. 1986, Optical Engineering, vol. 25, no. 2, p. 323.

Hildebrand, R.H., Loewenstein, R.F., Harper, D.A., Orton, G.S., Keene, J. & Whitcomb, S.E. 1985, Icarus, 64, 64

Hildebrand, R.H. 1983, QJRAS, 24, 267

Hildebrand, R.H. & Winston, R. 1982, Appl. Op., v. 21, n. 10, p. 1844

Hillenbrand, L.A., Massey, P., Strom, S.E. & Merrill, K.M. 1993, AJ, 106, 1906

Ho, P.T.P. & Haschick, A.D. 1986, ApJ, 304, 501

Ho, P.T.P., Moran, J.M. & Rodríguez, L.F. 1982, ApJ, 262, 619

Hoare, M.G. & Garrington, S.T. 1995, ApJ, 449, 874

Hobson, M.P. & Padman, R. 1994, MNRAS, 266, 752

Hodapp, K.-W., 1994, ApJS, 94, 615

Hodapp, K.-W, 1987, A&A, 172, 304

Hofner, P. & Churchwell, E. 1993, in preparation

Hofner, P. 1996b, private communication

Hofner, P. 1996a, A&A, in press

Hollenbach, D., Johnstone, D., Lizano, S & Shu, F. 1994, ApJ, 428, 654

Howard, E.M., Pipher, J.L. & Forrest, W.J. 1994, ApJ, 425, 707

Howard, E.M., Pipher, J.L., Forrest, W.J. & DePree, C.G. 1996, ApJ, 460, 744

Howard, E.M. 1996, PhD thesis, University of Rochester

Hughes, V.A., Cohen, R.J. & Garrington, S. 1995, MNRAS, 272, 469

Hughes, V.A. & Wouterloot, J.G.A. 1984, ApJ, 276, 204

Hughes, V.A. 1993, AJ, 105, 331

Hughes, V.A. & MacLeod, G.C. 1993, AJ, 105, 1495

Humphreys, R.M. & McElroy, D.B. 1984, ApJ, 284, 565

Humphreys, R.M. 1978, ApJS, 38, 309

Hunter, T.R., Serabyn, E. & Benford, D.J. 1996, PASP, in press

Hunter, T.R., Testi, L., Taylor, G.B., Tofani, G., Felli, M., & Phillips, T.G. 1995, A&A, 302, 249

Hunter, T.R., Taylor, G.B., Felli, M., & Tofani, G. 1994, A&A, 284, 281

Hunter, C. 1977, ApJ, 218, 834

Icke, V., Gatley, I. & Israel, F.P. 1980, ApJ, 236, 808

Infrared Laboratories, 1808 E. 17th St., Tucson, AZ 85719, (602) 622-7074

Israel, F.P. 1976, A&A, 52, 175

Jaffe, D.T., Davidson, J.A., Dragovan, M. & Hildebrand, R.H. 1984, ApJ, 284, 637

James, J.F. & Sternberg, R.S. 1969, The Design of Optical Spectrometers, (Chapman and Hall Ltd.)

Jenness, T., Scott, P.F. & Padman, R. 1995, MNRAS, 276(3), 1024

Jones, R. Clark 1953, J.O.S.A., v. 43, n. 1, p. 1

Josse, M., Gerbaux, X. & Hadni, A. 1993, Int. J. of Infr. & Milli. Waves, v. 14, n. 7, p. 1381

Kaneshiro, Dave, private communication, Janos Technology Inc., 1994.

Keto, E.R., Ho, P.T.P. & Reid, M.J. 1987, ApJ, 323, L117

Keto, E.R. 1990, ApJ, 355, 190

Knacke, R.F. & Thomson, R.K. 1973, PASP, 85, 1973

Knapp, G.R., Phillips, T.G., Leighton, R.B., Lo, K.Y., Wannier, P.G., Wootten, H.A. & Huggins, P.J. 1982, ApJ, 252, 616

Koike, C., Hasegawa, H. & Hattori, T. 1987, Astr. & Sp. Sc., 134, 95

Kooi, J.W., Walker, C.K., LeDuc, H.G., Benford, D.J., Hunter, T.R. & Phillips, T.G. 1994, International Journal of Infrared and Millimeter Waves, v. 15, p. 477

Koresko, C.D., Beckwith, S, Ghez, A.M., Matthews, K., Herbst, T.M. & Smith, D.A. 1993, AJ, 105, 1481

Kraus, J.D. 1986, Radio Astronomy, 2nd ed., (Powell, Ohio: Cygnus-Quasar Books)

Kreysa, E., Haller, E.E., Gemünd, H.-P., Haslam, C.G.T., Lemke, R. & Sievers, A.W. 1993, in Fourth International Symposium on Space Terahertz Technology, p. 296

Kuchar, T.A. & Bania, T.M. 1994, ApJ, 436, 117

Kurtz, S., Churchwell, E. & Wood, D.O.S. 1994, ApJS, 91, 659

Lada, C.J. & Fich, M. 1996, ApJ, 459, 638

Lada, C.J. 1985, ARAA, 23, 267

Lada, C.J., Blitz, L., Reid, M.J. & Moran, J.M. 1981, ApJ, 243, 769

Ladd, E.F., Adams, F.C., Casey, S., Davidson, J.A., Fuller, G.A., Harper, D.A., Myers, P.C. & Padman, R. 1991, ApJ, 382, 203

Langley, S.P. 1881, Nature, 25, 14

Larson, R.B. 1969, MNRAS, 145, 271

Larson, R.B. 1972, MNRAS, 157, 121

Larson, R.B. 1981, MNRAS, 194, 809

Lay, O.P., Carlstrom, J.E., Hills, R.E. & Phillips, T.G. 1994, ApJ, 434, L75

Levreault, R.M. 1988, ApJ, 330, 897

Lewis, W.B. 1947, Proc. Phys. Soc., 59, 34

Lis, D.C., Carlstrom, J.E. & Keene, J. 1991, ApJ, 380, 429

Lis, D.C. & Carlstrom, J.E. 1994, ApJ, 424, 189

Lis, D.C., Hunter, T.R., Serabyn, E., Wang, N., Benford, D.J. & Phillips, T.G. 1996, in preparation

Little, L.T., Heaton, B.D. & Dent, W.R.F. 1990, A&A, 232, 173

Lizano, S., Heiles, C., Rodríguez, L.F., Koo, B.C., Shu, F.H., Hasegawa, T., Hayashi, S. & Mirabel, I.F. 1988, ApJ, 328, 763

Lizano, S. & Shu, F.H. 1989, ApJ, 342, 834

Loewenstein, E. V., Smith, D.R. & Morgan, R.L. 1993, Appl. Op., vol. 12, no. 2, p. 398

Lord Corporation Industrial Coatings, 2000 West Grandview Blvd., P.O. Box 10038, Erie, PA 16514-0038, (814) 868-3611

Loren, R.B., Sandqvist, Aa. & Wootten, A. 1983, ApJ, 270, 620

Loren, R.B. & Mundy, L.G. 1984, ApJ, 286, 232

Low, F.J. 1961, J.O.S.A., v. 51, n. 11, p. 1300

Low, F.J., et al. 1984, ApJ, 278, L19

Lumsden, S.L. & Hoare, M.G. 1996, ApJ, 464, 272

Lumsden, S.L. & Puxley, P.J. 1996, MNRAS, 281, 493

Lynds, B.T. 1962, ApJS, 7 ,1

Macdonald, G.H., Habing, R.J. & Millar, T.J. 1995, Astr. & Sp. Sci., 224, 177

Mac Low, M.-M., Elitzur, M., Stone, J.M. & Königl, A. 1994, ApJ, 427, 914

Mac Low, M.-M. & Elitzur, M. 1992, ApJ, 393, L33

Mac Low, M.-M., Van Buren, D., Wood, D.O.S. & Churchwell, E. 1991, ApJ, 369, 395

Mangum, J.G. & Wootten, A. 1993, ApJS, 89, 123

Massey, P., Johnson, K.E. & Degioia-Eastwood, K. 1995, ApJ, 454, 151

Massi, M., Felli, M. & Simon, M. 1985, A&A, 152, 387

Masson, C.R., Mundy, L.G. & Keene, J.B. 1990, ApJ, 357, L25

Masson, C.R. & Chernin, L.M. 1994, in Clouds, Cores and Low Mass Stars, eds. D.P. Clemens & R. Barvainis, (San Francisco: ASP), 350

Masson, C.R. & Chernin, L.M. 1993, ApJ, 414, 230

Mather, J.C. 1981, Appl. Op., v. 21, n. 6, p. 1125

Mather, J.C. 1984, Appl. Op., v. 23, n. 4, p. 584

Mathis, J.S. 1990, ARAA, 28, 37

Mathis, J.S., Rumpl, W. & Nordsieck, K.H. 1977, ApJ, 217, 425

Mathis, J.S., Mezger, P.G. & Panagia, N. 1983, A&A, 128, 212

Matthews, N., Little, L.T., Macdonald, G.H., Andersson, M., Davies, S.R., Riley, P.W., Dent, W.R.F. & Vizard, D., A&A, 184, 284

Matthews, H.E., Goss, W.M., Winnberg, A. & Habing, H.J. 1973, A&A, 29, 309

Mattila, K., Holsti, N., Toriseva, M., Anttila, R. & Malkamäki, L. 1985, A&A, 145, 192

McCammon, D., Edwards, B., Juda, M., Plucinsky, P., Zhang, J., Kelley, R., Holt, S., Madejski, G., Moseley, S. & Szymkowiak, A. 1989, in Low Temperature Detectors for Neutrinos and Dark Matter III, (Edition Fronteres: Gif sur Yvette Cedex)

McCammon, D., Juda, M., Zhang, J., Holt, S.S., Kelley, R.L., Moseley, S.H. & Szymkowiak, A.E. 1987, Japanese. J. of Appl. Phys., 26 Suppl 26-3, 208

McCutcheon, W.H., Sato, T., Purton, C.R., Matthews, H.E. & Dewdney, P.E. 1995, AJ, 110, 1762

McLean, I.S. 1994, ed., Infrared Astronomy with Arrays: The Next Generation, (Dordrecht: Kluwer)

Megeath, S.T., Herter, T., Gull, G.E. & Houck, J.R. 1990, ApJ, 356, 534

Mehringer, D.M. & Synder, L.E. 1996, ApJ, in press

Melnick, G., Menten, K.M., Phillips, T.G., & Hunter, T. 1993, ApJ, 416, L37

Menten, K.M., Reid, M.J., Pratap, P., Moran, J.M. & Wilson, T.L. 1992, ApJ, 401, L39

Menten, K.M., Melnick, G.J. & Phillips, T.G. 1990, ApJ, 350, L41

Mestel, L. 1965, QJRAS, 6, 161

Mezger, P.G. 1994a, A&SS, 212, 197

Mezger, P.G. 1994b, Infrared Phys. Technol., 35(2/3), 337

Mezger, P.G., Chini, R., Kreysa, E., Wink, J.E. & Salter, C.J. 1988, A&A, 191, 44

Meyers-Rice, B. & Lada, C.J. 1991, ApJ, 368, 445

Mihalas, D. & Binney, J. 1981, "Galactic Astronomy," San Francisco: Freeman

Mitchell, G., Hasegawa, T., Schella, J., 1992, ApJ, 386, 604

Mitsuishi, A., Yamada, Y., & Yoshinaga, H. 1962, J.O.S.A., 52(1), 14

Mooney, T.J. & Solomon, P.M. 1988, ApJ, 334, L51

Moore, T.J.T. & Yamashita, T. 1995, ApJ440, 722

Moriarty-Schieven, G.H., Snell, R.L. & Hughes, V.A. 1991, ApJ, 374, 169

Moriarty-Schieven, G.H. & Snell, R.L. 1988, ApJ, 332, 364

Moseley, S.H. & Allen, C. 1996, private communication

Moseley, H. 1995, in New Developments in Array Technology and Applications, eds. A.G. Davis Philip et al., (Netherlands: International Astronomical Union), 95

Moseley, S.H., Mather, J.C. & D.J. McCammon, 1984, J. Appl Phys., 56(5), 1257

Motte, F., André, P. & Neri, R. 1996, Proc. of ESO Workshop: The Role of Dust in the Formation of Stars

Mozurkewich, D., Schwartz, P.R. & Smith, H.A. 1986, /apj, 311, 371

Mundt, R., Brugel, E.W. & Bührke, E. 1987, ApJ, 319, 275

Mundy, L.G., Blake, G.A., Men'shchikov, A., Sandell, G. & McMullin, J. 1996, preprint

Myers, P.C., Bachiller, R. & Caselli, P. 1995, ApJ, 449, L65

Myers, P.C., Fuller, G.A., Mathieu, R.D., Beichman, C.A., Benson, P.J., Schild, R.E. & Emerson, J.P. 1987, ApJ, 319, 340

Najita, J.R. & Shu, F.H. 1994, ApJ, 429, 808

National Instruments, Inc. 6504 Bridge Point Parkway, Austin, TX 78730-5039

Neugebauer, G.X. & Garmire, G. 1970, ApJ, 161, L91

Nishioka, N.S., Richards, P.L. & Woody, D.P. 1978, Appl. Op., 17, 1562

Norris, R.P., Booth, R.S. & Diamond, P,J. 1982, MNRAS, 201, 209

Olmi, L., Cesaroni, R., & Walmsley, C.M. 1993, A&A, 276, 489

Optical Research Associates, 3280 East Foothill Blvd., Pasadena, CA 91107, (818) 795-9101

Orton, G.S., Griffin, M.J., Ade, P.A.R., Nolt, I.G., Radostitz, J.V., Robson, E.I. & Gear, W.K. 1986, Icarus, 67, 289

Padman, R. & Richer, J.S. 1994 Ap. & Sp. Sci., 216, 129

Padman, R. 1994, in Multi-Feed Systems for Radio Telescopes, eds. D.T. Emerson & J.M. Payne, ASP Conf. Ser., v. 75, (San Francisco: ASP)

Pajot, F., Boissé, P., Gispert, R., Lamarre, J.M., Puget, J.L. & Serra, G. 1986, A&A, 157, 393

Palla, F., Brand, J., Cesaroni, R., Comoretto, G. & Felli, M. 1991, A&A, 246, 249

Palla, F. & Stahler, S.W. 1993, ApJ, 418, 414

Panagia, N. 1973, AJ, 78, 929

Parker, N.D., Padman, R. & Scott, P.F. 1991, MNRAS, 252, 442

Penston, M.V. 1971, Contemp. Phys, v. 12, n. 4, p. 379

Phillips, J.P. & Mampaso, A. 1991, A&AS, 88, 189

Phillips, T.G. 1988, in *Millimetre and Submillimetre Astronomy*, eds. Wolstencroft & Burton, p. 1

Pignatel, G.U., Pedrolli, F., Cavalleri, A., Bonaldi, M. & Vitale, S. 1994, Physica B, 194-196, 1183

Pipher, J.L., Soifer, B.T. & Krassner, J. 1979, A&A, 74, 302

Plume, R., Jaffe, D.T. & Evans, N.J. 1992, ApJS, 78, 505

Pollack, J.B., Hollenbach, D., Beckwith, S., Simonelli, D.P., Roush, T. & Fong, W. 1994, ApJ, 421, 615

Pompea, S.M., Bergener, D.W., Shepard, D.F. & Russak, S. 1984, Optical Eng., v. 23, n. 2, p. 149

Potters Industries, Inc., Waterview Corporate Center, 20 Waterview Blvd., Parsippany, NJ 07054-1282, (201) 229-2900. Part number A-glass 1922 and 2024

Pratap, P., Menten, K.M. & Snyder, L.E. 1994, ApJ, 430, L129

Price, S.D. & Murdock, T.L. 1983, The Revised AFGL Infrared Sky Survey Catalog, AFSG report number 442

Pringle, J.E. 1981, ARAA, 19, 137

Pudritz, R.E. 1988, in Galactic and Extragalactic Star Formation, eds. R.E. Pudritz & M. Fich, (Dordrecht: Kluwer), 135

Pudritz, R.E. & Norman, C.A. 1983, ApJ, 274, 677

Purcell, E.M. 1969, ApJ, 158, 433

Raga, A.C., Binette, L. & Cantó, J. ApJ, 360, 612

Raga, A.C. 1991, AJ, 101, 1472

Raga, A. & Cabrit, S. 1993, A&A, 278, 267

Raga, A.C., Cantó, J., Calvet, N., Rodríguez, L.F. & Torrelles, J.M. 1993, A&A, 276, 539

Randall, C.M. & Rawcliffe, R.D. 1967, Appl. Op., v. 6, n. 11, p. 1889

Redman, M.P., R.J.R. Williams, & Dyson, J.E. 1996, MNRAS, 280, 661

Reid, M.J. & Moran, J.M. 1988, in Galactic and Extragalactic Radio Astronomy, 2nd edition, eds. G.L. Verschuur & K.I. Kellermann, (New York: Springer-Verlag), 255

Reid, M.J., Schneps, M.H., Moran, J.M., Gwinn, C.R., Genzel, R., Downes, D. & Rönnáng 1988, ApJ, 330, 809

Reid, M.J., Myers, P.C. & Bieging, J.H. 1987, ApJ, 312, 830

Reid, M.J. & Ho, P.T.P. 1985, ApJ, 288, L17

Reid, M.J., Haschick, A.D., Burke, B.F., Moran, J.M., Johnston, K.J. & Swenson, G.N. 1980, ApJ, 239, 89

Reipurth, B. & Heathcote, S. 1993, in Astrophysical Jets, (Cambridge: University of Cambridge Press), 35

Rengarajan, T.N. & Ho, P.T.P. 1996, ApJ, 465, 363

Richards, P.L & Greenberg, L.T. 1982, Infrared And Millimeter Waves, Volume 6, Chapter 3, Academic Press, Inc.

Richardson, K.J., White, G.J., Gee, G., Griffin, M.J., Cunningham, C.T., Ade, P.A.R. & Avery, L.W. 1985, MNRAS, 216, 713

Richer, J.S., Hills, R.E. & Padman, R. 1992, MNRAS, 254, 525

Rodríguez, L.F., Garay, G., Curiel, S., Ramírez, S., Torrelles, J.M., Gómez, Y. & Velázquez, A. 1994, ApJ, 430, L65

Rodríguez, L.F. & Cantó, J. 1983, Rev. Mexicana Astron. Astrof., 8, 163

Rodríguez, L.F., Cantó, J. & Torrelles, J.M. 1982, ApJ, 260, 635

Rodríguez, L.F., Moran, J.M., Ho, P.T.P. & Gottlieb, E.W. 1980, ApJ, 235, 845

Roelfsema, P.R., Goss, W.M. & Geballe, T.R. 1988, A&A, 207, 132

Rudolph, A., Welch, W.J., Palmer, P. & Dubrulle, B. 1990, ApJ, 363, 528

Ruiz, A., Rodríguez, L.F., Cantó, J. & Mirabel, I.F. 1992, ApJ, 398, 139

Rybicki, G.B. & Lightman, A.P. 1979, Radiative Processes in Astrophysics, (New York: John Wiley & Sons), 47

Sams, B.J. III, Moran, J.M. & Reid, M.J. 1996, ApJ, 459, 632

Sandell, G. 1994, MNRAS, 271, 75

Sandell, G. 1995, private communication via E.F. van Dishoeck

Sarcander, M., Neckel, T. & Elsässer, H. 1985, ApJ, 288, L51

Sato, S., Hayakawa, S., Matsumoto, T., Matsuo, H., Murakami, H., Sakai, K., Lange, A.E. & Richards, P.L. 1989, Appl. Op., v. 28, n. 20, p. 4478

Schraml, J. & Mezger, P.G. 1969, ApJ, 156, 269

Schroeder, D.J. 1987, Astronomical Optics, (San Diego: Academic Press)

Schwartz, P.R. 1982, ApJ, 252, 589

Schwartz, R.D. 1983, ARAA, 21, 209

Scoville, N.Z. & Good, J.C. 1989, ApJ, 339, 149

Scoville, N.Z. & Kwan, J. 1976, ApJ, 206, 718

Scoville, N.Z. & Solomon, P.M. 1975, ApJ, 199, L105

Seki, J. & Yamamoto, T. 1980, Astr. Sp. Sc., 72, 79

Serabyn, E. & Weisstein, E.W. 1996, Appl. Opt., v. 35, n. 16, p. 2752

Serabyn, E. 1994, in Multi-Feed Systems for Radio Telescopes, eds. D.T. Emerson & J.M. Payne, ASP Conf. Ser., v. 75, (San Francisco: ASP)

Serabyn, E. 1996, Int. J. of IR & mm Waves, in press

Sharpless, S. 1959, ApJS, 4, 257

Shepherd, D.S. & Churchwell, E. 1996a, ApJ, 457, 267

Shepherd, D.S. & Churchwell, E. 1996b, in preparation

Shepherd, M. C., Pearson, T. J., Taylor, G. B., 1994, BAAS, 26, 987

Shu, F., Najita, J., Ostriker, E., Wilkin, F., Ruden, S. & Lizano, S. 1994, ApJ, 429, 781

Shu, F.H., Ruden, S.P., Lada, C.J. & Lizano, S. 1991, ApJ, 370, L31

Shu, F.H., Lizano, S., Ruden, S.P. & Najita, J. 1988, ApJ, 328, L19

Shu, F.H., Adams, F.C., & Lizano, S. 1987, ARAA, 25, 23

Shu, F.H. 1977, ApJ, 214, 488

Shull, J.M. 1977, ApJ, 215, 805

Silk, J. 1995, ApJ, 438, L41

Smith, S.M. 1984, Appl. Op., v. 23, n. 14, p. 2311

Snell, R.L., Huang, Y.-L., Dickman, R.L. & Claussen, M.J. 1988, ApJ, 325, 853

Snell, R.L. & Bally J. 1986, ApJ, 303, 683

Snell, R.L. et al. 1984, ApJ, 284, 176

Snell, R.L., Loren, R.B. & Plambeck, R.L. 1980, ApJ, 239, L17

Soifer, B.T., Russell, R.W. & Merrill, K.M. 1976, ApJ, 210, 334

Spitzer, L., 1978, Physical Processes in the Interstellar Medium, (New York: John Wiley & Sons),

Staude, H.J., Elsässer, H. 1993, A&AR, 5, 16937

Stecklum, B., Henning, T., Eckart, A., Howell, R.R. & Hoare, M.G. 1995, ApJ, 445, L153

Stützel, P., Tegtmeier, H.D. & Tacke, M. 1988, Infr. Phys., v. 28, n. 2, p. 67

Stüwe, J.A. 1990, A&A, 237, 178

Sutton, E.C., Blake, G.A., Genzel, R., Masson, C.R., & Phillips, T.G. 1986, ApJ, 311, 921

Tafalla, M., Bachiller, R., Wright, M.C.H. & Welch, W.J. 1996, ApJ, in press

Tafalla, M., Bachiller, R. & Wright, M.C.H. 1994, ApJ, 432, L127

Taft, E.A. & Philipp, H.R. 1965, Phys. Rev., 138A, 197

Takano, T. 1986, ApJ, 303, 349

Takano, T., Fukui, Y., Ogawa, H., Takaba, H., Kawabe, R., Fujimoto, Y., Sugitani, K. & Fujimoto, M. 1984, ApJ, 282, L69

Tamura, M., Gatley, I., Joyce, R.R., Ueno, M., Suto, H. & Sekiguchi, M. 1991, ApJ, 378, 611

Tatematsu, K., Umemoto, T., Kameya, O., Hirano, N., Hasegawa, T., Hayashi, M., Iwata, T., Kaifu, N., Mikami, H. et al. 1993, ApJ, 404, 643

Tenorio-Tagle, G. 1979, A&A, 71, 59

Terebey, S., Shu, F.H. & Cassen, P. 1984, ApJ, 286, 529

Testi, L., Felli, M., Persi, P. & Roth, M. 1994, A&A, 288, 634

TGV, Inc., 603 Mission St., Santa Cruz, CA 95060-3653

Thompson, R.I. 1984, ApJ, 283, 165

Thronson, H.A., Gatley, I., Harvey, P.M., Sellgren, K., Werner, M.W. 1980, ApJ, 237, 66

Thronson, H.A. & Harper, D.A. 1979, ApJ, 230, 133

Tieftrunk, A.R., Gaume, R.A., Claussen, M.J., Wilson, T.L. & Johnston, K.J. 1996, A&A, in press

Tielens, A.G.G.M. 1989, in IAU Symposium 135 "Interstellar Dust" ed. L.J. Allamandola & A.G.G.M. Tielens, p. 285

Tofani, G., Felli, M., Taylor, G.B. & Hunter, T.R. 1995, A&AS, 112, 299

Torrelles, J.M., Gómez, J.F., Rodríguez, L.F., Curiel, S., Ho, P.T.P. & Garay, G. 1996, ApJ, 457, L107

Torrelles, J.M., Verdes-Montenegro, L., Ho, P.T.P., Rodríguez, L.F. & Cantó, J. 1993, ApJ, 410, 202

Torrelles, J.M., Gómez, J.F., Anglada, G., Estalella, R., Mauersberger, R. & Eiroa, C. 1992, ApJ, 392, 616

Torrelles, J.M., Ho, P.T.P., Rodríguez, L.F. & Cantó, J. 1986, ApJ, 305, 721

Torrelles, J.M., Rodríguez, L.F., Cantó, J., Carral, P., Marcaide, J., Moran, J.M. & Ho, P.T.P. 1983, ApJ, 274, 214

Tosatti, E. & Bassani, F. 1970, Nuovo Cimento, 65B, 161

Townes, C.H. & Schawlow, A.L. 1975, Microwave Spectroscopy, (New York: Dover Publications, Inc.

Trinchieri, G., Fabbiano, G. & Bandiera, R. 1990, ApJ, 342, 766

Turner, B.E. & Matthews, H.E. 1984, ApJ, 277, 164

Turner, J.L. & Welch, W.J. 1984, ApJ, 287, L81

Ulich, B.L. 1981, AJ, 86, 1619

Van Buren, D. & Mac Low, M.-M. 1992, ApJ, 394, 534

van de Hulst, H.C. 1957, Light Scattering by Small Particles, (New York: Wiley)

Walker, R.C., Burke, B.F., Haschick, A.D., Crane, P.C., Moran, J.M., Johnston, K.J., Lo, K.Y., Yen, J.L., Broten, N.W., Legg, T.H., Greisen, E.W. & Hansen, S.S. 1978, ApJ, 226, 95

Wang, N., Hunter, T.R., Benford, D.J., Serabyn, E., Lis, D.C., Phillips, T.G., Moseley, S.H. et al. 1996, Appl. Op., in press

Wang, Y.S., Evans II, N.J., Zhou, S.D. & Clemens, D.P. 1995, ApJ, 454, 217

Wang, N. 1994, private communication

Weintraub, D.A. & Kastner, J.H. 1996, ApJ, 458, 670

Weintraub, D.A., Kastner, J.H, Gatley, I. & Merrill, K.M. 1996, ApJ, in press

Wells, D.C., Greisen, E.W. & Harten, R.H. 1981, A&AS, 44, 363

Westerhout, G. 1958, Bull. Astron. Inst. Netherlands, 14, 215

Whalley, E. & Labbé, H.J. 1969, J. Chem. Phys., 51, 3120

Williams, R.J.R., Dyson, J.E. & Redman, M.P. 1996, MNRAS, 280, 667

Wilner, D.J., Ho, P.T.P. & Zhang, Q. 1996, ApJ, 462, 339

Wilner, D.J., Welch, W.J. & Forster, J.R. 1995, ApJ, 449, L73

Wilson, T.L., Johnston, K.J. & Mauersberger, R. 1991, A&A, 251, 220

Wilson, T.L., Gaume, R.A. & Johnston, K.J. 1993, ApJ, 402, 230

Wilson, T.L. & Rood, R.T. 1994, ARAA, 32, 191

Wink, J.E., Duvert, G., Guilloteau, S., Güsten, R. Walmsley, C.M & Wilson, T.L. 1994, A&A, 281, 505

Wink, J.E., Altenhoff, W.J. & Mezger, P.G. 1982, A&A, 108, 227

Winston, R. 1970, J. Opt. Soc. Am. 60, 245

Wiseman, J.J. & Ho, P.T.P. 1996, Nature, 382, 139

Wolf, G.A., Lada, C.J. & Bally, J. 1990, AJ, 100(6), 1892

Wolfire, M.G. & Königl, A. 1991, ApJ, 383, 205

Wood, D.O.S. & Churchwell, E. 1989a, ApJ, 340, 265

Wood, D.O.S. & Churchwell, E. 1989b, ApJS, 69, 831

Wood, D.O.S., Handa, T., Fukui, Y., Churchwell, E., Sofue, Y. & Iwata, T. 1988, ApJ, 326, 884

Wood, D.O.S., Churchwell, E. & Salter, C.J. 1988, ApJ, 325, 694

Wright, E.L. 1982, ApJ, 255, 401

Wright, E.L. 1987, ApJ, 320, 818

Wynn-Williams, C.G., Werner, M.W. & Wilson, T.L. 1974, ApJ, 187, 41

Wynn-Williams, C.G., Becklin, E.E., Matthews, K., Neugebauer, G.X., Werner, M.W. 1977, MNRAS, 179, 255

Xiang, D. & Turner, B.E. 1995, ApJS, 99, 121

Xie, T., Goldsmith, P.F., Snell, R.L. & Zhou, W. 1993, ApJ, 402, 216

Yorke, H.W. & Krügel, E. 1977, A&A, 54, 183

Young, J.S. 1986, in The Interstellar Medium in Galaxies, eds. H.A. Thronson & J.M. Shull, (Dordrecht: Kluwer), p. 67

Young, J.S., Schloerb, F.P., Kenney, J.D. & Lord, S.D. 1986, ApJ, 304, 443

Yun, J.L. & Clemens, D.P. 1991, ApJ, 381, 474

Zhang, J., Cui, W., Juda, M., McCammon, D., Kelley, R.L., Moseley, S.H., Stahle, C.K., Szymkowiak, A.E. 1993, Phys. Rev. B, 48, 2312

Zhou, S. & Evans, N.J. 1994, in Clouds, Cores and Low Mass Stars, eds. D.P. Clemens & R. Barvainis, (San Francisco: ASP), 183

Appendix A: SHARC Cryostat Manual

Last revised on August 7, 1996

Pumping the cryostat to vacuum

1. Connect the vacuum gauge controller to the blue sensor on the top plate of the dewar.

2. Start the rough pump and pump out the line in front of the dewar valve.

   If the dewar has NOT been opened since the last time it was cold, then turn on the turbopump and wait until the pump gauge goes below the current dewar pressure before opening the dewar valve.

   Else (if the dewar has been opened), then don't turn on the turbo pump yet. First slowly open the dewar valve and rough out the dewar with the rough pump. Due to the large diameter of the bandpass filters, you should pump slowly, **no more than 1 torr/sec**. Once the dewar gauge reads less than 1 torr, you can fully open the valve. When the pressure reaches about 0.1 torr, you can turn on the turbo pump.

3. Let the turbopump run for $\sim$ 12 hours (until pressure is below 1 mTorr on the dewar gauge).

Initial Cooldown to 77 K

1. Open both heat switches (counterclockwise). They jam if left closed while cooling from room temperature! They have about 60 turns of travel.

2. Open the knurled green valve (counterclockwise) on the ^{3}He tank (about 1.25 turns), but not so far as to have it come loose in your hand!

3. Pour LN_2 with a funnel into the nitrogen can. Be careful not to scrape the sides of the fill tube when you insert and remove the funnel. Filling this jacket first causes any remaining water and hydrocarbons to condense on the nitrogen jacket rather than the helium jacket (hence less helium will be required to cool the helium jacket).

4. Pour LN_2 into the helium can. It will take $\sim$ 24 liters (l) and $\sim$ 1 hour to fill both tanks.

5. Plug **separate** rubber hoses onto both fill tubes to prevent ice plugs from forming.

6. About 2 hours later, close both heat switches (clockwise).

7. It takes another 6 hours to get everything inside down to 77 K. The longer you wait, the less helium you will use later.

Cooling to 4 K

1. Close the dewar vacuum valve and disconnect and power off the turbopump.

2. Dump out the LN_2 by flipping the dewar upside down on the cart. Have 2 containers ready to catch the liquid. You can raise the elevator to the highest position for convenience.

3. Rock the dewar a couple times to get the last drops out.

4. Right the dewar, re-tighten the rotation stage, plug He fill tube with the stopper and refill the nitrogen can with LN_2.

5. Hook up the 32-pin military connector cable from the Housekeeping port on SHARC to the aluminum BNC/IEEE housekeeping breakout box.

6. Connect an ohm-meter across pins gj which reads the charcoal pump heater resistor.

7. Connect the IEEE cable to the Lakeshore thermometer readout.

8. Set the Lakeshore to position B and the rotating switch on the breakout box to DE. This selects the DT-470 thermometer on the filter wheel which is quite far from the helium cold plate and thus will lag a lot in temperature during the cooling process. It should read around 1 volt.

9. Connect a voltmeter in parallel with the small blue 10 microamp current source across pins NP (using a BNC tee and 2 cables). This selects the diode thermometer mounted directly on the helium cold plate which gives a good measure of the instantaneous cold plate temperature. If you reverse the cables by mistake, this will read 14 volts, otherwise it should read about 1 volt.

10. Unstopper the He fill tube and start a slow transfer of liquid He. Immediately after removing the stopper, use the initial warm gas from the transfer tube to blow out any remaining LN_2 in the helium can. Remove the transfer tube from the fill tube after a few seconds. When you see a liquid flame, reinsert it to the bottom.

11. It takes 12 l to pre-cool the ^{4}He tank to 4K and another 5 to get it full the first time, for a total of 17 l on the initial transfer. In the following section is a typical log for the cooling process to use as a guide to see how it is going.

Typical log for the initial cooldown to 4 K

9:40 AM: Blow out any remaining LN_2 with warm He.

9:41 AM: Begin LHe transfer at $\sim$ 1 psi pressure. Prevent LHe transfer tube from resting on the bottom of the can or else things may stop cooling at some point. Rub ice off the tip of the transfer tube if necessary before inserting it.

Time	Transfer	Thermometer readings		
AM	rate	NP	gj	DE (filter wheel)
(HST)	(psi)	(^{4}He plate)	charcoal pump	(Lakeshore channel B)
9:42	1	0.95V	1780Ω	
9:56		1.117	2116	1.016 V
9:59		1.77	2300	
10:00		1.88	2536	
10:02		1.927	2740	
10:04		1.997	2965	1.020
10:05		2.026	3110	
10:10		2.20	4.09 kΩ	
10:14		2.44	7.67	
10:17		2.64	13.0	
10:20	3	3.10	16.4	
10:23		3.36	18.0	
10:25		3.417	19.0	
10:26	FULL	3.42	19.5	1.038

(This should have taken $\sim$ 45 minutes and 17-20 L of ^{4}He.)

If it is humid, then place the long rubber hose on ^{4}He fill tube.

Disconnect the 32-pin military connector cable and mount dewar on telescope.

11:52		3.56	29.5	1.556

1. After it is full, leave at 4 K for 4 hours to equilibrate. The hold time will be less if you allow less time before starting the cycling of the ^{3}He. The dewar can be mounted on the telescope during this equilibration period.

2. After the dewar has been mounted on the telescope, rotate the stage until the small red indicia are aligned correctly with the bolt heads on the mounting plate and the preamp box facing front. Connect the small housekeeping breakout box to the dewar where the 32-pin military cable used to be. (It will rotate freely a bit when it is on because I didn't make the thread depth exactly right).

3. Mount the blue A/D box on the relay optics in front of the dewar by placing the 2 long screws through the 2 available holes and fastening them with the nuts supplied.

4. Attach the 2 3-pin military cables hanging from the hex plate to the Analog and Digital power input ports on the A/D box. It doesn't matter which is which. Attach the 2 shield ground lines from the cables under one of the screws holding the A/D power input ports.

5. Attach the DB-9 connector to the preamp power input port, screwing down the connector. The ground does not need to be attached. Don't loosen any screws on the top of the preamp box because there are nuts on them inside the box!

6. Detach the silver fiber optic hose from the railing and undo the duct tape holding the end section on. Carefully pull this section off, revealing the ends of the fiber. Place the fibers through the shorter green hose for protection and re-tape the joint.

7. Cable tie the silver hose to one of the lower relay optics struts. Cable tie the green hose to the black bracket on top of the relay optics so that the fibers emerge near their ports on the A/D box.

8. Pull off the plastic fiber end protectors and screw them into the ports. The fibers are labelled "1" and "2" and should be attached to the proper numbered port. Keep the plastic protectors in a safe place.

9. Attach the 2 black DB25 cables from the preamp box to the A/D input. They are labelled "1-12" and "13-24."

Pumping on liquid ^{4}He (start here on succeeding afternoons)

1. Make sure both the pot and the pump heat switches are closed (clockwise).

2. Tilt the telescope to $\sim 40^\circ$ zenith angle for convenience. If the observatory is running low on liquid ^{4}He, or you want the longest possible hold time, leave the telescope at 53° zenith angle to keep the dewar vertical during transfer and pumping.

3. Turn on the Lakeshore thermometer and attach the IEEE cable from it to the housekeeping breakout box on the back topside of the dewar. In this mode, the Lakeshore reads the temperature of a germanium resistor on the ^{3}He pot.

4. Move a ≥ 5 foot step ladder next to the relay optics.

5. Move the LHe storage dewar on the gold cart into position next to the ladder.

6. Tighten the extension on the transfer tube before inserting it into the storage dewar. You may have to use one of the 2 longer transfer tubes. To conserve helium, use the shortest one that isn't soft.

7. Re-top the ^{4}He can of the dewar from the storage dewar until it is full (audible pluming). It may take about 15 minutes depending on the transfer rate. Prevent the LHe transfer tube from resting on the bottom of the can or else ice may form on the tip and the transfer rate may slow way down.

8. Put away the transfer tube and move the storage dewar out of the way.

9. Tilt the dish back to 53° zenith angle so the dewar is vertical while pumping.

10. Be sure the roughing pump next to the CTI compressors is powered on and the red ball valve next to it is open. Be sure the small valve on the pumping assembly is closed (the valve on the port you use to re-pressurize the ^{4}He tank with ^{4}He gas).

11. Put the pump fitting on the ^{4}He fill tube. You may have to align the O-ring in the bottom section if it does not fit easily (don't force it too hard!). Tighten the base.

12. Begin pumping by cracking open the large ball valve on the pumping assembly while monitoring the Lakeshore thermometer. At LHe temperature, the Lakeshore should read $\sim 54\Omega$. Crack the valve slowly until the Lakeshore reading rises at a rate of 0.02Ω to 0.04Ω per update. 0.02Ω will give the best holdtime; use 0.04Ω if you are in a hurry.

13. Monitor this rate every 5-10 minutes and continue opening the valve to maintain this rate. You can watch from the control room. If it is humid, use the heat gun to de-ice the pump fitting if it gets heavy ice on it. Wipe away the resulting water with a Kimwipe.

14. Re-top the LN_2 jacket while you wait. After it is full, place the long hose over the tip of the fill tube so that LN_2 won't spill onto the fiber optics when you start observing near the zenith later. It is easier to put the hose on if you wait a couple of minutes until the fill tube has warmed up a bit.

15. After $\sim$ 45 minutes of monitoring the thermometer and opening the pump valve, you will reach a pressure of 38 torr (the lambda point). At this point the Lakeshore reads $\sim 90\Omega$. Open the pump valve all the way!

16. After another $\sim$ 15 minutes, the Lakeshore thermometer will rise above 105.00Ω. The ^{4}He pump pressure will probably be below 15 torr. At this point all the ^{3}He should be condensed in the charcoal sorption pump. The ^{4}He pump pressure will eventually go down to $\sim$ 7 torr.

Condensing ^{3}He

1. Connect an ohm-meter with a BNC cable to the pump thermometer port on the housekeeping breakout box. The pump thermometer will be about 65-70 kΩ.

2. Connect a BNC between the JFET thermometer port on top of the preamp box to the small blue 10 microamp current source. Put a BNC tee to the Fluke meter. Voltage will be $\sim$ 1.9V.

3. Close the knurled green valve (clockwise) on the ^{3}He tank outside the dewar.

4. Be sure the pot heat switch is closed (clockwise). Open the pump heat switch counterclockwise. The pump thermometer will drop quickly to ~ 25kΩ.

5. Connect the long BNC from the battery box (hanging from the hex plate) to the pump heater BNC port on the housekeeping breakout box on the backside of the dewar.

6. Connect the other end of this long BNC to the BNC port on the battery box labelled "Heater 2: Charcoal pump."

7. Be sure the AC line is plugged into the battery box and press the big green "1" button on the battery box to switch into operation mode. Unplug the AC line.

8. Turn on the preamp switch and A/D switch on the battery box (near the top center and top right of the front panel). The preamp takes the raw +12 and −12V from the batteries. The A/D voltages are pre-set through a regulator to +6.00 and −7.00 volts. They can be read with the lower voltmeter on the battery box.

9. Turn on the meter and meter backlights on the battery box. Set the lower meter rotary switch to "Pump heater." The lower meter then displays the pump heater voltage.

10. Turn on the pump heater switch on the battery box and adjust voltage to 8.0 Volts.

11. After about 8-9 minutes, the pump thermometer will drop to 2400Ω. You will notice that the ^{3}He stage thermometer (Lakeshore) will have dropped to $\sim 30-40\Omega$ (due to thermal conduction from the pump heater). IMMEDIATELY turn off the pump heater switch on the battery box.

12. Disconnect the pump thermometer cable and ohm-meter from the dewar to prevent noise pickup.

13. Move the long BNC cable from the pump heater to the JFET heater port on the housekeeping breakout box on the top backside of the dewar.

14. Wait for $\sim$ 30 minutes until the Lakeshore thermometer again reads $\geq 105\Omega$. At this point, all the ^{3}He will be liquefied in the pot.

15. Open the pot heat switch (counterclockwise).

16. Close the pump heat switch (clockwise). The Lakeshore reading will now rise.

17. While you are still on the ladder, turn on the preamp power switch on the top of the preamp box bolted to the dewar. The JFET thermometer reading drops as the JFETs warm up from bias current.

Setting up the electronics

1. Move the BNC from the pump heater output on battery box to the JFETs heater output.

2. Set the lower meter rotary 6-position switch to read the "heater 1" voltage = JFET heater.

3. Turn on the JFET heater switch on the battery box and adjust the meter voltage to 8 V to start with.

4. When the JFET thermometer reaches 0.87 after a few minutes, immediately turn the JFET heater voltage down to 6.25 V. This will give a stable temperature reading near 0.87 V. If you overshoot and drop below 0.87V, turn off the JFET heater and allow it to rise to 0.87 before turning it back on.

5. Turn off the meter switch and the meter backlight switch on the battery box.

6. Turn off the 10 microamp current source and the Fluke meter to prevent noise pickup.

7. Unplug the JFET thermometer cable from the preamp box to prevent pickup.

8. When the Lakeshore thermometer reading goes above $\sim 5000\Omega$ (in about an hour) the array will be at operating temperature. Turn off the Lakeshore thermometer and unplug (at the dewar side) the IEEE cable going from the dewar to the thermometer.

   Note: If you turn on the A/D while the Lakeshore is still on, a strange ground loop will cause the Lakeshore reading to plateau at $\sim 1200\Omega$. This is OK, it is just an anomalous reading.

9. The only cable plugged into the dewar housekeeping port at this point should be the JFET heater.

10. For safety, open (counterclockwise) the knurled green ^{3}He valve on the dewar (about 1.25 turns), but not so far as to have it come loose in your hand.

11. Turn on the A/D power switch on the A/D box mounted on the relay optics. Don't bother turning on the A/D heater switch as it is not needed. Note that the chopping secondary TTL signal is ultimately generated on the logic board in the A/D box, so powering it on starts the chopping secondary if the BNC cables are connected in the control room.

12. If it is humid, be sure the fan is running to keep ice off the dewar window (1 mm polyethylene). If there is ice, gently melt it with your fingers and wipe the water away with a Kimwipe.

13. Uncover the flat tertiary mirror and the big ellipsoidal mirror before observing.

14. During your first ZA slew, monitor the movement of the fiber optic cable conduit to ensure that it never gets caught on anything or gets too tight.

At the end of the night (or when the helium runs out)

1. If properly cycled, the limiting cryogen in the dewar will be the ^{4}He. When the ^{4}He has all boiled, the ^{3}He will quickly follow and you will no longer detect sources. The data will look much less noisy since the bolometers are no longer sensitive to radiation as they warm up. Also, the pump gauge will be pegged below 1 mTorr, essentially at 0, meaning that all the ^{4}He has been pumped out. The ^{4}He will typically last 16-18 hours from when you start pumping (in the early afternoon). On the first night, it may only last 13 hours.

2. Cover the flat tertiary mirror with the plexiglass cover and cover the ellipsoidal mirror with the foam pad.

3. Turn off the preamp switch on the preamp box on the side of the dewar.

4. Turn off the A/D power switch on the A/D box on the relay optics.

5. Turn off the preamp switch on the battery box.

6. Turn off the FET heater switch on the battery box.

7. Turn off the A/D power switch on the battery box.

8. Plug the AC line back into the battery box and switch it to recharge by pressing the big red zero button.

9. If it is the last night observing with SHARC, you can simply leave the ^{4}He can on the pump and let the day crew deal with it. Open the pump heat switch (counterclockwise) and press the telescope STOP button before you leave. Be sure the green ^{3}He valve is open before you leave!

10. If the dewar is to be used tomorrow, then you must immediately backfill it with warm ^{4}He gas and refill the can with liquid ^{4}He as described below:

11. Tilt the telescope to $\sim 40^\circ$ zenith angle

12. Connect the hose from the ^{4}He gas bottle to the inlet valve to the pumping line, being sure to blow out the hose with ^{4}He gas first and have some pressure on the line.

13. Close the big pump valve.

14. Slowly open the small inlet valve and watch the pressure gauge.

15. Bring the pressure up slowly, over the course of ~ 1 minute to between 450 and 600 torr on the vacuum gauge next to the big valve.

16. Close the small inlet valve.
17. Move a ≥ 5 foot step ladder next to the relay optics.
18. Get the helium storage dewar in transfer position next to the ladder.
19. If it is humid, use a heat gun to de-ice the pumping fixture on the helium fill tube.
20. Unscrew the base of the pumping fixture enough so that you can lift it off as 1 unit. (you may get a blast of helium overpressure when you do this, which is fine–this actually prevents air being sucked in and causing an ice plug.)
21. Tighten the extension on the transfer tube before inserting into the storage dewar.
22. Immediately transfer helium into the dewar until it is full (pluming out of the fill tube).
23. Put away the transfer tube carefully and move the storage dewar out of the way.
24. Put the short rubber hose over the helium fill tube.
25. Fill the nitrogen can with LN_2.
26. Put the long rubber hose over the nitrogen fill tube.
27. Close the pot heat switch (clockwise).
28. A few minutes after it is full, put the short rubber hose onto the nitrogen fill tube.
29. Tilt the telescope to 45° zenith angle to conserve cryogen.
30. Be sure the knurled green ^{3}He valve is open before you leave!
31. Press the STOP button and you can safely leave.

Appendix B: SHARC Software Manual

This manual describes the function and operation of the system hardware and Labview and VAX software required to perform the proper instrument setup for astronomical observing at the CSO.

Goddard Space Flight Center A/D and DSP Hardware

The A/D unit consists of a logic board and A/D boards each with up to 16 channels contained in an isolated electronics box. DC power (+6 and -7V) is connected via two 3-pin cables from the battery box containing four 12V deep cycle marine batteries. The A/D inputs are two 25-pin cables from the dewar preamp box. The A/D output is sent via two 15-meter fiber optic cables (encased in a wire-reinforced plastic hose) to the control room where they connect to a small interface box attached to the Macintosh Quadra 950. The interface box connects via a short cable to the DB-37 input port on the DSP NuBus board in the Quadra. In order to eliminate capacitive coupling in the particular fibers and detectors, 3 flat washers are inserted such that the fibers attach only through a single screw thread. Also located on the interface box are BNC ports for "Chop Out"–the output TTL chopping signal from the DSP board and "Chop In"–the input TTL chopping signal. Typically, these two ports are connected together via a short BNC cable such that the output signal is piped right back in as the input. A BNC-Tee is added so that the Chop Out signal can be sent to Martin Houde's chopping secondary control box (to the TTL input port). Another Tee can be added to monitor the TTL signal on the HP digital oscilloscope.

Labview on the Macintosh

Labview is an object-oriented, graphical programming language designed to simulate a multitude of scientific instruments. The building blocks of the language are called Virtual Instruments (VIs) and are analogous to functions or subroutines in other programming languages like C or FORTRAN. Each Labview VI consists of a

front-panel display and a programming diagram. The front-panel is a window that can be used to display data in the form of numbers, graphs, strip charts, lights etc. and/or to accept input from the user in the form of data, control switches, dials, etc. VIs have the handy feature that they can be embedded as subVIs with their input and output parameters wired into other VIs. Thus each VI can be run "standalone" or can be called and executed by other VIs. The programming diagram for a VI is a separate window that is configured by the application programmer to perform the appropriate tasks (including arithmetic, file I/O, etc.) required of the VI. Diagrams can contain typical programming structures such as FOR and While loops and Case and Sequence structures. Operations and conversions on all common datatypes (integer, long integer, float, double, extended precision, string, array, bundle, etc.) are provided. Communication over GPIB, Serial and TCP/IP networks is simplified with the use of built-in VIs.

Getting Started: SHARC Server

Many of the Labview VIs for SHARC based upon similar VIs written by Kevin Boyce for the Kuiper Airborne Observatory infrared bolometer spectrometer instrument. Small modifications have been made to suit our needs at the CSO. The main VI for the bolometer array system is called "SHARC Server". Currently, this VI must be started manually on the Macintosh by clicking on the desktop alias "SHARC Server" in the top righthand corner of the display. Alternatively, it can be started by pulling down the Apple menu to "Todd's Labview", moving right and releasing on "SHARC Server 9/15." The 9/15 refers to the date of the last major revision of the code. (It is possible to place this VI in the Startup Folder of the System Folder so that it will be started upon reboot of the Macintosh. But because the Macintosh is a multi-purpose machine and Labview takes a significant amount of resources, this is not advised on a permanent basis.) When this VI is executed, it goes into a wait mode and listens for a TCP/IP communication request from the CSO control computer Poliahu (VAXStation 3100). This request is issued by a client routine activated on the VAX by the UIP command "SHARC." Like all UIP commands, the SHARC command is

implemented by a Pascal subroutine. When the request is received (from port 5000 on the VAX), "SHARC Server" in effect becomes a server program running on the Mac which in turn opens 3 new TCP/IP connections to the VAX for clearing event flags (port 5001), displaying error messages on the operator terminal (port 5002) and sending scan data (port 5003). All commands sent to the Mac must have a standard length due to the apparent constraints of the TCP/IP software available within Labview. Currently, 80 characters is the standard length that I have chosen. The ":" character serves as a command delimiter and the "~" character serves as a command terminator. See "HELP SHARC" from within the CSO UIP program for a description of the available commands. When in the default PRINT mode, the SHARC command will send any new values to the Mac, then immediately re-query it for all of the current values and print them on the control terminal so the user knows the current configuration. Occasionally, one of the values printed will be bizarre, perhaps to do some communication glitch. In this case, reissuing the command usually clears up the problem. On rare occasions, the DSP will get screwed up and report an error during a SHARC command. If it continues to do this, try turning the setup display on and off with the commands SHARC/SETUP followed by SHARC/NOSETUP. This should reset the DSP.

Bad and/or Dark pixels

As in all array detectors, not all of the pixels are working. In SHARC, pixels 1,5,15 and 16 are dead. These are defined as dead by running the subVI SHARC Set Bad Pixels which updates a file on the Mac containing the current array configuration. When data are taken, the subVI SHARC Read Bad Pixels returns the numbers of the dead channels which are subsequently flagged in the header of the data file so that the data reduction software will ignore them. Also, we have a different field stop slit that darkens pixel 24 in case you would like to get an idea of the level and nature of the correlated pixel noise not associated with sky radiation. Dark pixels are also defined in the subVI SHARC Set Bad Pixels. Once you know the current array configuration you should run this routine to store any changes in the configuration.

Pointing

Perhaps the first thing to do at the beginning of the night is to locate and point on a bright source like a planet. Partly for this purpose, the VI SHARC Setup Display has been written. Essentially, it performs the duties of an analog strip-chart while you point up on a source and center the beams using the JOYSTICK command in UIP. Fixed pointing offsets and the nominal focus offset have been measured with SHARC mounted on the righthand port of the Cassegrain relay optics of CSO and the array aligned in zenith angle with pixel 1 the highest in the sky. These offsets are stored in a standard UIP pointing file called "SHARC" and can be loaded with the UIP command "POINT SHARC". (Rough values are -10 for FAZO and -70 for FZAO for reference pixel 12.) Although a stepper motor controls the rotation of the dewar plate, so far we have always manually aligned the dewar in elevation by using fiducial marks on the relay optics which should be set by the day crew that mounts the dewar. These fiducial marks apply only to the righthand port of the relay optics. (WARNING: If the dewar is ever mounted on the lefthand side, then the dewar rotation will have to be readjusted. Repointing and refocus would also be recommended in this case.) Generally only small adjustments of a few arc seconds are needed to optimize the pointing during the night. As a superior alternative to JOYSTICK for OTF aficionados, pointing can be done rapidly by making a single-row OTF map of the calibrator and displaying the resulting map in "pointing mode" in the CAMERA software written by Darek Lis. The pointing corrections can then be read from the peak position of the planet in the map.

Focus

The nominal focus of the array (+0.25) is stored in the SHARC point file but should be checked occasionally (especially if people or other instruments have been standing on the relay optics.) The peak intensity of the image is fairly insensitive to focus offset changes of ± 0.25. However the shape of the image due to aberrations does vary noticeably over such a range. Thus it is best to optimize the focus for the roundest image and hence the best beamshape. At proper focus, the observed half-

power contour of a resolved planet matches well with the almanac values, with the polar flattening of the Jovian planets easily visible. The half-power contour on point sources should be close to the diffraction beamsize. Note: if someone ever removes the secondary mirror, get them to verify the XPOS and YPOS before your observing run!

Phasing the pixels

After pointing, it is wise to phase the pixels individually on a bright source. From the UIP, executable command files have been created to perform this task automatically in communication with the Macintosh. They are stored in the directory USER:[HUNTER.NEWUIP] and are named using the format PHASE_*.COM where * indicates the reference pixel being used. A different .COM file is needed for each choice of reference pixel. For obvious reasons, it is useful (especially for mapping an extended source) to choose a pixel near the center of the array as the reference pixel (i.e. the pixel whose lock-in signal is used to point the telescope). These .COM files command the telescope to move to one pixel after another. At each point, the Macintosh gathers a data sample and computes the arc tangent of the in-phase and quadrature data and determines the phase. This process is accomplished by the subVI SHARC Phases All-or-1. The computed phase is stored in the DSP memory for subsequent lock-in detection. It is important to remember that this calculation is valid only for a sine-wave template (the current default). If a different template function is loaded (such as the modified square wave that we have created), the results of this calculation will not be as accurate. A manual switch on the VI allows you to select a different calculation path for the modified square wave.

After phasing, one should make at least two more scans on the calibrator source at different airmasses in order to measure a good millivolts to Janskys conversion factor for the night. Also, you should consider issuing the useful UIP command SHARC/SAVE_PHASE in order to save your current phases to disk on the Mac in case the Mac crashes and needs to be rebooted. If this happens, the UIP command SHARC/LOAD_PHASE can be used to reload the last phases that were saved.

Pixel Gain Calibration

After phasing, it is necessary to measure the relative gains of the pixels. The pixels vary in their responsivity to astronomical sources for several reasons: differing thermal conductivity of the pixel support legs, varying quality of the optical focal plane, diffraction effects near the ends of the field stop, and possible misalignment effects. The method for removing these effects from imaging data is referred to as flat-fielding. Our method for flat-fielding is to perform scans through a bright calibrator (i.e. Saturn), measure the relative signals among the pixels and create a gain file to be used in data reduction of subsequent target source observations. There are of course several methods to accomplish this goal. In the OTF mapping mode, zenith angle scans are used for gain calibration because the array is aligned in zenith angle and scanned in azimuth in OTF mode. These calibration scans are accomplished using the /SIDEWAYS/ALTAZ option of OTF_MAP in UIP and provide a rapid comparison of the signal from each pixel, thus minimizing sky changes during the time of the measurement.

On-the-Fly Mapping

On-the-fly mapping is a useful procedure that allows you to point, perform gain calibration and observe real sources. The preferred method for observing of the CSO bolometer crew is OTF (On-The-Fly) mapping. The OTF procedure is similar to that used in heterodyne spectroscopy with the main difference being that continuum OTF is performed in altitude-azimuth coordinates to optimize the sky subtraction performance of an azimuth chopper. See HELP OTF under UIP for details on the UIP command parameters. A minor difference between heterodyne OTF mapping and SHARC OTF mapping is in the definition of the longitude resolution of the map. Because the chopping secondary is run during bolometer mapping, the data are quantized in units of 1 chopper cycle (typically 4 Hz). Then, the longitude resolution is calculated from the current values of the chopping frequency and the number of chops per integration. The calculated value is displayed when the OTF command is issued. Occasionally, the Mac will speeze and return a 0 for one of the important

OTF parameters. The OTF command now traps this case instead of dying with a divide-by-zero error. Simply reissue the OTF command and it will work properly.

On the Macintosh, the subVI SHARC OTF Accumulate handles the data-taking. At the beginning of each row, the Mac awaits the IDLE bit from the antenna computer which indicates that the antenna has reached the beginning of the map (after the ramp up period). The Mac then takes data and sends it to the VAX over the data socket until it has acquired the proper number of data points. Even when sampling each chop cycle at 4 Hz, the Mac can keep up with the data rate. If the map is aborted by issuing Control-C under UIP, the Mac does not know this and will continue to finish the row. Once it finishes, it should be in a healthy state ready for the next UIP command.

There is one remaining (known) bug in the OTF command. Actually, the problem seems to be in the TCP data channel but so far has only been seen during the rapid data rate of OTF maps. After a couple of hours of mapping, the antenna computer will die at the end of an OTF row. To recover from this situation, you must stop the main SHARC Server VI on the Mac by clicking on the little STOP sign on the window menu bar. Then restart the VI by clicking on the right-arrow button. On the VAX, control-Y out of the UIP and type EXIT to kill the image. Finally, re-enter the UIP and type the SHARC/RESTART command to restart the connections. If this command hangs (goes more than 30 seconds without a response) then the SHARC Client on the VAX was not killed properly. Just control-Y out of UIP, type EXIT and go back in and issue the SHARC command, which should now work. As always, be sure to issue the SHARC command before trying to open a new data file because this requires that the Mac connection already be established.

Pointed Observing

For those observers who are interested in making deep integrations on point sources, the routine CHOP_SLEWY is available. In this mode, the telescope executes a sequence of chops and nods in the form $+--+$. In other words, a specified number of chop periods are integrated in the positive beam, then in the negative

beam, the negative beam and back to the positive beam. This sequence is repeated for the number of CHOP_SLEWY cycles specified. The data file format is different from the OTF map files (which is why you must always specify which type of file you wish to open in the UIP DATA_FILE command). The data reduction package for CHOP_SLEWY data is the Bolometer Array Data Analysis Software (BADAS) written by Dominic Benford. Resembling the CLASS package developed at IRAM for heterodyne spectroscopy, BADAS will read, sum, calibrate and plot scans. For pointed observing, the option exists to align the array in azimuth or elevation, or to track the parallactic angle of the source. Tracking the rotation has not yet been tested.

Appendix C: Input parameters for the OUTFLOW program

The FORTRAN program OUTFLOW reads the input parameters from a text file with the following example format. The "!" mark simply represents the VMS comment delimiter.

K3-50 ! source name
12 ! CO isotope (12, 13 or 18 for ^{12}CO, ^{13}CO or C^{18}O)
3 ! upper J level of the transition
90 ! number of spectra to be summed
-24 ! LSR velocity in kilometers/second
-42 -28 ! lower and upper velocities of blue wing
-20 -8 ! lower and upper velocities of red wing
8.7 ! distance in kiloparsecs
40 40 ! angular size in arcseconds of the red lobe and blue lobe
0.0 ! optical depth
33 ! excitation temperature in Kelvin
45 ! inclination angle in degrees (0 = pole-on)
k3-50.spectrum01 ! filename of spectrum 1
k3-50.spectrum02 ! filename of spectrum 2
.
.
k3-50.spectrum90 ! filename of spectrum 90

The list of filenames included at the end identify the files containing the spectral line data in ASCII format where the first column is the channel velocity and the second column is the line strength in Kelvin at that velocity. The columns are delimited by spaces. Such files can be created with the following CLASS command:

CLASS> GREG filename /FORMATTED

Column densities are computed by assuming that the spectra have been obtained on a regular grid corresponding to half the beamsize.